Quantum Link and Quantum Dimer Models: From Classical to Quantum Simulation

Inauguraldissertation
der Philosophisch-naturwissenschaftlichen Fakultät
der Universität Bern

vorgelegt von

Pascal Stebler

von Nunningen/SO

Leiter der Arbeit:
Prof. Dr. U.-J. Wiese
Albert Einstein Center for Fundamental Physics
Institut für Theoretische Physik, Universität Bern

Quantum Link and Quantum Dimer Models: From Classical to Quantum Simulation

Inauguraldissertation
der Philosophisch-naturwissenschaftlichen Fakultät
der Universität Bern

vorgelegt von

Pascal Stebler

von Nunningen/SO

Leiter der Arbeit:
Prof. Dr. U.-J. Wiese
Albert Einstein Center for Fundamental Physics
Institut für Theoretische Physik, Universität Bern

Von der Philosophisch-naturwissenschaftlichen Fakultät angenommen.

Bern, 5. Februar 2016

Der Dekan:
Prof. Dr. G. Colangelo

Abstract

The first part of this thesis is about the Abelian $U(1)$ and non-Abelian $U(N)$ or $SU(N)$ quantum link model with staggered fermions and a proposal for its implementation on a quantum simulator consisting of ultracold atoms trapped in an optical lattice.

The first quantum simulator is for the $(1 + 1)$-dimensional $U(1)$ gauge theory. Exact diagonalization studies of string breaking and its real-time evolution were performed to serve as a benchmark.

The second quantum simulator is for the $(1+1)$, the $(2+1)$, and the $(3+1)$-dimensional Abelian $U(N)$ and with extensions also for the non-Abelian $SU(N)$ gauge theory. Exact diagonalization studies of chiral symmetry breaking and real-time evolution mimicking the expansion of a "quark-gluon plasma" were performed to serve as a benchmark.

The main emphasis of the first part of this thesis is placed on the review of the quantum link model and on the exact diagonalization studies.

The second part of this thesis concerns a modified Rokhsar-Kivelson ground state wave function for the quantum dimer model which can be rewritten as a $(2 + 1)$-dimensional $U(1)$ pure gauge quantum link model with staggered background charges and spin $1/2$ degrees of freedom on the links.

The ground state wave function can be efficiently sampled in individual flux sectors by the Metropolis Monte Carlo method for moderately large system sizes at temperature exactly zero.

The phase structure and the local electric flux patterns created by a static charge-anti-charge pair are investigated and the spectrum is calculated with exact diagonalization.

Contents

1. Introduction **1**

2. Quantum simulation of string breaking and evolution after a quench in a $U(1)$ gauge theory **5**
2.1. $(1+1)$-dimensional $U(1)$ quantum link model with staggered fermions . . . 10
2.2. Implementation of the exact diagonalization and the real-time evolution . . 14
2.3. Real-time evolution of string breaking for spin $S = 1$ 16
2.4. Real-time evolution after a quench for spin $S = 1/2$ 23
2.5. Implementation on a quantum simulator 25
2.6. Conclusions 33

3. Expansion of a "quark-gluon plasma" in a $U(2)$ gauge theory **35**
3.1. Extending the quantum link model to $U(N)$ and $SU(N)$ 35
3.2. Representing quantum links with rishons 46
3.3. Color-neutral bosonic $U(N)$ gauge invariant operators 53
3.4. Implementation of exact diagonalization studies 58
3.5. Spontaneous chiral symmetry breaking 64
3.6. Real-time evolution of expansions 68
3.7. Implementation on a quantum simulator 71
3.8. Conclusions 72

4. Ground state Rokhsar-Kivelson wave function for a quantum dimer model **75**
4.1. Introduction 75
4.2. Quantum dimer model as a special case of the more general (2+1)-d quantum link model 76
4.3. Candidate phases 81
4.4. Four-component order parameter 84
4.5. The Rokhsar-Kivelson point $\lambda = 1$ 96
4.6. Previous results 98
4.7. Modified ground state Rokhsar-Kivelson wave function 101
4.8. Observables 104
4.9. Effective theory 105
4.10. Algorithms 114
4.11. Results 117
4.11.1. Statistics of the order parameter 117
4.11.2. Local phase structure with static external charges 123
4.11.3. Electric fluxes 127

4.11.4. Exact diagonalization 132
4.12. Conclusions 136

5. Summary and Outlook **139**

Acknowledgements **141**

A. Plaquette operator of the quantum dimer model in dimer and flux bases **143**

B. Check of the height symmetries in the quantum dimer model **145**

C. Empiric blocking and averaging of the electric fluxes in the quantum dimer model **149**

Bibliography **157**

Declaration **161**

Curriculum Vitae **163**

1. Introduction

The effort to simulate a general quantum system on a classical system like a universal computer grows exponentially with the size of the quantum system. A very important method which circumvents these problems is lattice quantum Monte Carlo. With this method the effort grows essentially with the space-time volume of the system. In many situations the Monte Carlo weights are negative or even complex and this method fails. This is known as a sign-problem.

Already in 1982, Richard Feynman formulated the idea of using quantum degrees of freedom to compute a quantum system [1]. Seth Lloyd showed that such a quantum computer can simulate quantum systems efficiently [2]. Ignacio Cirac and Peter Zoller proposed a first implementation of a quantum device in which cold ions are trapped along a line to form a quantum register of entangled quantum bits (qubits) [3]. Discrete quantum gate operations are performed on the quantum register by a controlled manipulation of one or several qubits e.g. by stroboscopic laser pulses. This concept is known as "digital" quantum computing. A quantum register with eight and later on fourteen quantum bits was realized in the laboratory by the group of Rainer Blatt [4, 5].

Another type of quantum computing, the so-called "analog" quantum simulation was introduced again by a group around Ignacio Cirac and Peter Zoller [6]. There a cloud of ultracold bosonic atoms is trapped in an optical lattice. The system is described by a Bose-Hubbard model. It possesses a huge number of degrees of freedom but the single atoms are not controlled individually. The interactions between the atoms are tunable and super-lattices are used to create non-trivial potential terms. Such a system was first realized in the laboratory by a group around Theodor Hänsch and Immanuel Bloch to measure the quantum phase transition from a superfluid to a Mott insulator [7].

On classical computers lattice gauge theory allowed to address many non-perturbative problems. As an example the masses of light hadrons were calculated with lattice quantum chromodynamics (QCD) [8]. However, many problems are inaccessible due to strong sign problems or a complex action. This prevents the progress on topics like high temperature superconductors, the dense core of neutron stars, heavy ion collisions, or the QCD phase diagram.

In contrast to Wilson's formulation of lattice gauge theory [9] with continuous degrees of freedom on gauge links the degrees of freedom of the above quantum simulators are discrete. An alternative formulation of gauge theories are the so-called quantum link models (QLM) which appeared several times in the literature [10–12]. There the continuous degrees of freedom are replaced by discrete quantum variables in a gauge covariant manner.

Therefore, quantum link models are very good candidates for quantum simulation.

The quantum links are generalized quantum spins living in a finite-dimensional Hilbert space. They are non-commuting operators which realize dynamical gauge fields and they replace the parallel transporters in Wilson's lattice gauge theory. While the latter resembles a 4-dimensional classical statistical mechanics system, quantum link models resemble (4+1)-dimensional quantum statistical problems. They are more closely related to quantum mechanical problems. There the quantum spins undergo collective spin wave excitations. In quantum link models the quantum links undergo excitations in an extra dimension which leads to an emergent gluon field. When the quantum link is represented by an $SU(2)$ quantum spin, this leads to a $U(1)$ gauge theory. The links can be non-Abelian as well. Quantum link models are usually constructed in the Hamiltonian formulation.

Quantum chromodynamics can be formulated with quantum link models [13], via dimensional reduction [14]. Quantum link models also serve as toy models which share qualitative phenomena with QCD and condensed matter physics. Furthermore, the study of quantum link models is a potential source of new ideas for efficient simulation algorithms.

Cold quantum gases realize many-body dynamics of isolated quantum systems. Putting bosonic or fermionic ultracold atoms in an optical lattice they realize Hubbard-type dynamics. The interactions are tunable by external fields with high experimental precision. There are experimental designs and techniques available to create various effects together with optical lattices, namely ring exchange interactions [15], artificial photons [16], control of strong spin interaction [17], laser-excited Rydberg atoms in large-spacing optical or magnetic lattices [18], emerging Dirac fermions [19], whole Hamiltonians for quantum electrodynamics [20], and an experimental method that yields the equation of state of a uniform gas [21]. Various experiments were already performed, namely the comparison between experiments and quantum Monte Carlo simulations for strongly interacting Bose gases [22], cross-validation between a new theoretical approach (bold diagrammatic Monte Carlo), and precision experiments on ultracold atoms [23], observation of quantum criticality [24] and observation of the non-equilibrium dynamics of a density wave in the regime of strong correlations [25]. However, it remains a challenge to implement gauge theories with cold atoms, especially for fermionic fields coupled to dynamical gauge fields. First quantum simulators were already constructed theoretically for $U(1)$ quantum link models using Rydberg atoms in an optical lattice.

Our group together with the group of Peter Zoller in Innsbruck has proposed realizations of quantum link models in optical lattices, first for $U(1)$ (Abelian) theories [26], and shortly after that for $U(N)$ and $SU(N)$ (non-Abelian) theories [27]. Personal contributions to this work will be discussed in this thesis.

As a benchmark for the proposed quantum simulators we performed exact diagonalization studies of string breaking and real-time evolution after a quench in a $U(1)$ gauge theory and of spontaneous chiral symmetry breaking and real-time evolution in a $U(2)$ gauge theory. The systems accessible on classical computers are rather small. A quantum

simulator would allow to simulate systems in up (3+1) dimensions with higher-dimensional representations and therefore with much richer expected phenomenology.

The study of the $(2+1)$-dimensional $U(1)$ quantum link model without fermions with a novel cluster algorithm showed a surprisingly rich phase diagram. Putting a static charge-anti-charge pair into the periodic system split the flux between the charges into fractionalized flux 1/2 strands [28].

The same model but with staggered background charges is equivalent to the so-called quantum dimer model (QDM) [29]. This model serves as an attempt to understand high-T_c superconductivity. It models the low-energy effective theory of systems with resonating valence bond (RVB) ground states [30]. It is hoped that such systems are related to Cooper pair formation.

There were only limited quantum Monte Carlo calculations which lead to long-standing debates about the phase structure [31, 32]. In [33] a four-component order parameter was introduced together with a new Monte Carlo method. These developments clarified the phase diagram of the quantum dimer model. Putting a static charge-anti-charge pair into the periodic system split the flux between the charges into fractionalized flux 1/4 strands.

At the so-called Rokhsar-Kivelson point, which corresponds to a distinct set of Hamiltonian parameters, the ground state of the model can be constructed analytically [29]. The local energy density is exactly zero. Hence, approaching the Rokhsar-Kivelson point, electric fluxes condense in the vacuum. This leads to deconfinement even for $(2+1)$ dimensions at zero temperature and a massless Goldstone boson appears.

The construction of the ground state wave function can be varied in a very general way [34]. We construct a parameterizable ground state wave function which at one point coincides with the standard Rokhsar-Kivelson point. The result is a whole line of Rokhsar-Kivelson points which allows us to drive the model from a so-called staggered phase through the phase with the massless Goldstone boson mode and further deep into the so-called columnar phase. For the whole Rokhsar-Kivelson line the local energy density remains zero and the system remains deconfined at zero temperature.

Since the ground state wave function is analytically known, it can be evaluated explicitly. In other words, the properties of the system are accessible even exactly at zero temperature without the need of a path integral method. However, it still can't be computed analytically since the Hilbert space is exponentially large. The model is investigated with a very simple Metropolis algorithm which probes the ground state wave function even for moderately large system sizes.

Due to the zero local energy density the electric flux sectors of the system all have ground state energy zero. However, we evaluate the system in separate flux sectors. This is to our knowledge in contrast to existing literature. Thanks to the four-component order parameter I came to the conclusion that there is no plaquette phase on the whole Rokhsar-Kivelson line, at least in the zero-flux sector.

In the standard quantum dimer model, away from the Rokhsar-Kivelson point, fluxes cost energy and the flux strands are visible in the local energy density. However, on the whole Rokhsar-Kivelson line the local energy density is strictly zero and the local electric flux has to be investigated directly.

However, the staggered background charges create a strong staggered flux pattern which hinders the evaluation of the superposed net flux which is created by the static charge-anti-charge pair Hence, an empiric blocking and averaging was developed to properly uncover the underlying flux structure.

As a result of this work, I found that there are no flux strands for the whole Rokhsar-Kivelson line even deep in the deconfined columnar phase.

The spectrum of the modified ground state wave function is examined by exact diagonalization of small systems. As an outlook, I propose an interpolation between standard quantum dimer model and modified ground state wave function. However for this interpolation, the ground state wave function can no longer be described analytically.

2. Quantum simulation of string breaking and evolution after a quench in a $U(1)$ gauge theory

This project concerns about a concept for atomic quantum simulation of an Abelian quantum link model in one dimension. It aims at future atomic experiments which would allow to simulate real-time dynamics in gauge theories. In contrast, the classical (computer) simulation of quantum systems is in general exponentially hard [35].

We will address dynamical string breaking and real-time evolution after a quench. Both examples are also relevant for quantum chromodynamics. For a small number of degrees of freedom, the real-time evolution in dynamical gauge theories is studied by exact diagonalization of specific $(1+1)$-dimensional quantum link models. These results serve as motivation and validation of future implementations of such systems with a much larger number of degrees of freedom on quantum simulators.

We use quantum link models as an alternative formulation of gauge theories with discrete degrees of freedom to realize continuous gauge symmetry. By exact diagonalization we study the real-time evolution of a $(1+1)$-dimensional $U(1)$ quantum link model with staggered fermions which resembles the Schwinger model. The computational resources needed to diagonalize such systems on classical computers grow exponentially with the size of the system.

We consider spinless fermions which hop on a lattice with sites x. The fermion creation $(\psi_x^\dagger)$ and annihilation (ψ_x) operators obey the usual anti-commutation relations

$$\begin{aligned} \{\psi_x, \psi_y^\dagger\} &= \delta_{xy}\,, \\ \{\psi_x, \psi_y\} &= \{\psi_x^\dagger, \psi_y^\dagger\} = 0\,. \end{aligned} \tag{2.1}$$

For the moment, let's assume that the fermions are moving in a classical background magnetic field described by the vector potential $\vec{A}$ with

$$\vec{B} = \vec{\nabla} \times \vec{A}\,. \tag{2.2}$$

A site x is connected to its nearest-neighbor site y by a link (x, y). The hopping from site y to site x has to be gauge covariant and is described by

$$\psi_x^\dagger u_{xy} \psi_y\,. \tag{2.3}$$

Here

$$u_{xy} = \exp(i\varphi_{xy}) = \cos\varphi_{xy} + i\sin\varphi_{xy} \tag{2.4}$$

is the classical $U(1)$ gauge parallel transporter associated with the link (x, y), and we are still working in the standard Wilson formulation. The phase φ_{xy} is

$$\varphi_{xy} = \int_x^y d\vec{l} \cdot \vec{A} \,. \tag{2.5}$$

Performing a gauge transformation of the classical background field

$$\vec{A}' = \vec{A} - \vec{\nabla}\alpha \tag{2.6}$$

leads to

$$\varphi'_{xy} = \varphi_{xy} + \alpha_x - \alpha_y \,. \tag{2.7}$$

Hence,

$$u'_{xy} = \exp(i\varphi'_{xy}) = \exp(i\alpha_x) u_{xy} \exp(-i\alpha_y) \,. \tag{2.8}$$

The fermion operators transform as

$$\begin{aligned} \psi'_x &= \exp(i\alpha_x)\psi_x \,, \\ \psi_x^{\dagger\prime} &= \exp(i\alpha_x)\psi_x^\dagger \,, \end{aligned} \tag{2.9}$$

such that the hopping term

$$\psi_x^\dagger u_{xy} \psi_y \tag{2.10}$$

becomes gauge invariant. The anti-commutation relations in eq. (2.1) remain valid.

We are interested in charged particles. As they move, they create dynamical magnetic fields. Hence, instead of a static background magnetic field, we are interested in dynamical gauge fields. Now the link variable becomes an independent quantum degree of freedom in form of a dynamical bosonic lattice gauge field u_{xy}. The gauge field again transforms as described in eq. (2.8). The electric field

$$E_{xy} = -i\partial/\partial\varphi_{xy} \tag{2.11}$$

associated to the link (x, y) then is the canonical conjugate of u_{xy} with commutation relation

$$[E_{xy}, u_{xy}] = -i\frac{\partial}{\partial\varphi_{xy}} \exp(i\varphi_{xy}) = u_{xy} \,. \tag{2.12}$$

In a gauge theory, to describe gauge invariant physical states $|\Psi\rangle$, redundant gauge variant variables are needed. To remove the unphysical gauge redundant states, the Gauss law is imposed, i.e.

$$G_x|\Psi\rangle = 0 \,. \tag{2.13}$$

In our case with spinless fermions, the generator of gauge transformations has the form

$$G_x = \psi_x^\dagger \psi_x - \sum_i (E_{x,x+\hat{i}} - E_{x-\hat{i},x}) \,. \tag{2.14}$$

This is the lattice variant of $\rho - \vec{\nabla} \cdot \vec{E}$. A general non-infinitesimal local gauge transformation is described by the unitary transformation

$$V = \prod_x \exp(i\alpha_x G_x) \,. \tag{2.15}$$

For a gauge theory, the Hamiltonian has to be invariant under gauge transformations. For this, the gauge generator has to commute with the Hamiltonian

$$[G_x, H] = 0\,. \tag{2.16}$$

Just as a reminder, if some general operator commutes with the local gauge generator in eq. (2.14)

$$[O_{xy}, G_z] = 0\,, \tag{2.17}$$

then it is gauge invariant

$$O'_{xy} = V^\dagger O_{xy} V = \exp(-i\alpha_x G_x^\dagger - i\alpha_y G_y^\dagger) O_{xy} \exp(i\alpha_x G_x + i\alpha_y G_y) = O_{xy}\,. \tag{2.18}$$

We used the fact that the gauge generator is Hermitean. The electric field and the local number of fermions commute with the gauge generator, they are physical observables. The fermions transform as

$$\begin{aligned}\psi'_x &= V^\dagger \psi_x V = \exp(-i\alpha_x G_x^\dagger)\psi_x \exp(i\alpha_x G_x) = \exp(-i\alpha_x \psi_x^\dagger \psi_x)\psi_x \exp(i\alpha_x \psi_x^\dagger \psi_x) \\ &= \sum_{k,l} \frac{(-1)^k (i\alpha_x)^{k+l}}{k!l!} (\psi_x^\dagger \psi_x)^k \psi_x (\psi_x^\dagger \psi_x)^l = \sum_l \frac{(i\alpha_x)^l}{l!} \psi_x \\ &= \exp(i\alpha_x)\psi_x \end{aligned} \tag{2.19}$$

and

$$\psi_x^{\dagger\prime} = \sum_{k,l} \frac{(-1)^k (i\alpha_x)^{k+l}}{k!l!} (\psi_x^\dagger \psi_x)^k \psi_x^\dagger (\psi_x^\dagger \psi_x)^l = \psi_x^\dagger \exp(-i\alpha_x)\,, \tag{2.20}$$

in agreement with eq. (2.9). Here we used $\psi_x \psi_x = \psi_x^\dagger \psi_x^\dagger = 0$, $\psi_x \psi_x^\dagger \psi_x = \psi_x$, and $\psi_x^\dagger \psi_x \psi_x^\dagger = \psi_x^\dagger$.

In [36], Wilson's $U(1)$ lattice gauge theory was cast into the Hamilton formalism. The Hamiltonian of a lattice gauge theory with a dynamical $U(1)$ gauge field coupled to dynamical fermions is

$$H = -t \sum_{\langle x,y \rangle} (\psi_x^\dagger u_{xy} \psi_y + \text{H.c.}) + \frac{g^2}{2} \sum_{\langle x,y \rangle} E_{xy}^2 - \frac{1}{4g^2} \sum_{\langle wxyz \rangle} (u_{wx} u_{xy} u_{yz} u_{zw} + \text{H.c.}) \tag{2.21}$$

with t the hopping amplitude and g the gauge coupling. The last term is known as a plaquette term and its sum over $\langle wxyz \rangle$ is meant as a sum over lattice plaquettes with the corners w, x, y, and z in counter-clockwise order. The link variable $u_{x,\mu}$ is still a complex phase and therefore a continuous degree of freedom. Hence, there is an infinite-dimensional Hilbert space for each link. This is in contrast to the usually discrete degrees of freedom in ultracold matter systems which we would like to use for quantum simulation. As proposed in [12], we replace the classical gauge parallel transporters u_{xy} by quantum link operators U_{xy} with a finite-dimensional Hilbert space per link. We set

$$U_{x,\mu} = C_{x,\mu} + iS_{x,\mu}\,, \tag{2.22}$$

analogous to eq. (2.4). The gauge generator has the same form as in eq. (2.14).

For the hopping term and the plaquette term of the Hamiltonian to be gauge invariant, the quantum link operator has to transform as

$$U'_{xy} = V^\dagger U_{xy} V = \exp(i\alpha_x) U_{xy} \exp(-i\alpha_y)\,. \tag{2.23}$$

This required gauge covariance can be obtained by imposing

$$[E_{xy}, U_{vw}] = \delta_{xv}\delta_{yw} U_{xy}\,, \tag{2.24}$$

which is the same relation as eq. (2.12). We use the Hadamard-Lemma

$$\exp(X) Y \exp(-X) = \sum_{m=0}^{\infty} \frac{1}{m!} [X, Y]_m\,, \tag{2.25}$$

with $[X,Y]_m = [X,[X,Y]_{m-1}]$ and $[X,Y]_0 = Y$ to get

$$\begin{aligned}
[i\alpha_x E_{xy} - i\alpha_y E_{xy}, U_{xy}]_0 &= U_{xy}\,,\\
[i\alpha_x E_{xy} - i\alpha_y E_{xy}, U_{xy}]_1 &= i(\alpha_x - \alpha_y) U_{xy}\,,\\
[i\alpha_x E_{xy} - i\alpha_y E_{xy}, U_{xy}]_m &= [i\alpha_x E_{xy} - i\alpha_y E_{xy}, i^{m-1}(\alpha_x - \alpha_y)^{m-1} U_{xy}]\\
&= i^m (\alpha_x - \alpha_y)^m U_{xy}\,,
\end{aligned} \tag{2.26}$$

and so, using the abbreviation

$$F_x = \sum_i (E_{x,x+\hat{i}} - E_{x-\hat{i},x})\,, \tag{2.27}$$

we obtain

$$\begin{aligned}
U'_{xy} &= V^\dagger U_{xy} V = \exp(i\alpha_x F_x + i\alpha_y F_y) U_{xy} \exp(-i\alpha_x F_x - i\alpha_y F_y)\\
&= \sum_m \frac{1}{m!} [i\alpha_x F_x + i\alpha_y F_y, U_{xy}]_m = \sum_m \frac{1}{m!} [i\alpha_x E_{xy} - i\alpha_y E_{xy}, U_{xy}]_m\\
&= \exp(i\alpha_x) U_{xy} \exp(-i\alpha_y)\,,
\end{aligned} \tag{2.28}$$

which validates the choice of eq. (2.24).

Taking the Hermitean conjugate of eq. (2.24) amounts in

$$[E_{xy}, U^\dagger_{vw}] = -\delta_{xv}\delta_{yw} U^\dagger_{xy}\,. \tag{2.29}$$

Using the definition in eq. (2.22) the commutation relations can be rewritten as

$$\begin{aligned}
[E_{xy}, C_{vw}] &= i\delta_{xv}\delta_{yw} S_{xy}\,,\\
[E_{xy}, S^\dagger_{vw}] &= -i\delta_{xv}\delta_{yw} C^\dagger_{xy}\,,
\end{aligned} \tag{2.30}$$

which is fulfilled for

$$\begin{aligned}
C_{xy} &= S^1_{xy}\,,\\
S_{xy} &= S^2_{xy}\,,\\
E_{xy} &= S^3_{xy}\,.
\end{aligned} \tag{2.31}$$

Here, $\vec{S}_{xy} = (S^1_{xy}, S^2_{xy}, S^3_{xy})$ is nothing else than the standard angular momentum operator with

$$[S^i_{xy}, S^j_{vw}] = i\delta_{xv}\delta_{yw}\epsilon_{ijk}S^k_{xy}\,. \tag{2.32}$$

Now we can write the quantum link operator as

$$\begin{aligned} U_{xy} &= C_{xy} + iS_{xy} = S^1_{xy} + iS^2_{xy} = S^+_{xy}\,, \\ U^\dagger_{xy} &= C_{xy} - iS_{xy} = S^1_{xy} - iS^2_{xy} = S^-_{xy}\,, \end{aligned} \tag{2.33}$$

so the link variables are represented by raising operators S^+_{xy} of a quantum spin. The standard angular commutation relations can be realized with any representation of the $SU(2)$ algebra. The Hilbert space of the gauge part of the model then is a direct product of $(2S+1)$-dimensional link Hilbert spaces. We will consider quantum links with $S = 1/2$ or 1, for which the electric flux is $E_{xy} = \pm 1/2$ or $E_{xy} \in \{-1, 0, 1\}$. In the classical limit $S \to \infty$, with integer S, this quantum link model reduces to the Hamilton formulation of Wilson's lattice gauge theory [36].

Using the facts that

$$\begin{aligned} [G_x, H] &= 0\,, \\ [G_x, G_y] &= 0 \end{aligned} \tag{2.34}$$

allows us to express the eigenstates of the Hamiltonian as eigenstates of the gauge generator. A complete set of latter eigenstates is constructed by a systematical search of all states which fulfill the Gauss law.

Beside the gauge symmetry, there are other global symmetries, namely translations by one or several lattice spacings, rotations by 90 degrees, reflections, parity, charge conjugation, and the center symmetry. Physical states may break some of them. The conserved quantity associated with translation invariance is the lattice momentum $p = (p_1, p_2, \ldots, p_d)$ in the d-dimensional Brillouin zone $B =]-\pi/a, \pi/a]^d$.

In the Wilson formulation the charge conjugation C is a $\mathbb{Z}(2)$ symmetry which corresponds to a complex conjugation of u_{xy} and a change of sign of the electric field E_{xy}. In the quantum link model the charge conjugation C corresponds to a Hermitean conjugation of U_{xy} and again a change of sign of the electric field. The quantum spins residing on the links undergo a unitary transformation, where $\vec{S}_{x,\mu} = (S^1_{x,\mu}, S^2_{x,\mu}, S^3_{x,\mu})$ gets replaced by $\vec{S}_{x,\mu} = (S^1_{x,\mu}, -S^2_{x,\mu}, -S^3_{x,\mu})$, which leaves the commutation relations invariant.

The center symmetry is associated with gauge transformations in a periodic volume and can't be expressed by eq. (2.15). For the non-Abelian $SU(N)$ gauge group, the center is $\mathbb{Z}(N)$. For the Abelian $U(1)$ gauge group used in this chapter the center is $U(1)$ too and all gauge transformations commute with each other. The infinitesimal generators of the $U(1)^d$ center transformations on a $L_1 \times L_2 \times \ldots \times L_d$ lattice with periodic boundary conditions are total fluxes

$$E_i = \frac{1}{L_i}\sum_x E_{x,x+i}\,. \tag{2.35}$$

The Hamiltonian is block diagonal in the associated flux sectors.

In [26] we present a general procedure to generate a $U(1)$ quantum link model coupled to fermionic matter realizable in an optical lattice setup. This method will be summarized in a latter section.

2.1. $(1+1)$-dimensional $U(1)$ quantum link model with staggered fermions

To illustrate the possibilities of the $U(1)$ quantum link model, we treat a simple example restricted to $(1+1)$ space-time dimensions minimally coupled to a single species of so-called staggered fermions, which represent one degree of freedom per lattice site. It is a strong coupling model, and it is inspired by the Schwinger model, which describes quantum electrodynamics in $(1+1)$ dimensions. The lattice version of the massive Schwinger model was studied in [37].

The Hamiltonian is

$$H = -t \sum_x \left[\psi_x^\dagger U_{x,x+1} \psi_{x+1} + \text{H.c.} \right] + m \sum_x (-1)^x \psi_x^\dagger \psi_x$$
$$+ \frac{g^2}{2} \sum_x E_{x,x+1}^2 - \delta_F \sum_x \psi_x^\dagger \psi_x \left(1 - \psi_{x+1}^\dagger \psi_{x+1} \right) . \tag{2.36}$$

Here t is the hopping amplitude, m the staggered fermion mass, g the gauge coupling, and δ_F is a 4-Fermi interaction (also referenced as fermion repulsion for $\delta_F > 0$). Since we consider one spacial dimension, there is no magnetic field and no plaquette term.

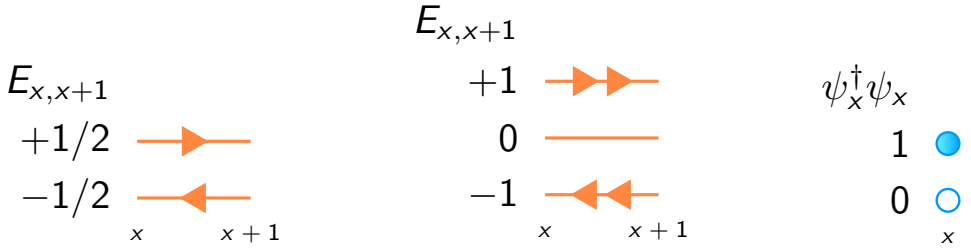

Figure 2.1.: *Graphical representation of the degrees of freedom of the $U(1)$ quantum link model.* Left panel: *Spin $1/2$ link in the flux basis. There are two possible spin projections, which correspond to a flux $+1/2$ which is flowing from left to right, and a flux denoted as $-1/2$ which is flowing from right to left.* Center panel: *Spin 1 link in the flux basis. There are three possible spin projections, which correspond to a flux $+1$ which is flowing from left to right, a state with flux zero, and a flux denoted as -1 which is flowing from right to left.* Right panel: *Site with one positively charged staggered fermionic degree of freedom in the occupation number basis. There are two states (fermion present or absent).*

Figure 2.1 shows the pictorial representation of the fermionic degrees of freedom at each lattice site and the quantum spin degrees of freedom on each gauge link. The positively

charged fermions satisfy the usual commutation relations in eq. (2.1). The staggered fermions are analogous to spinless fermions at half-filling. The definitions of the electric flux operator and the gauge field, which is represented by the quantum links, were already given in eqs. (2.31) and (2.33) as

$$\begin{aligned} E_{x,x+1} &= S^3_{x,x+1}\,, \\ U_{x,x+1} &= S^+_{x,x+1}\,, \\ U^\dagger_{x,x+1} &= S^-_{x,x+1}\,. \end{aligned} \tag{2.37}$$

A quantum state $|\Psi\rangle$ of the system can be described by a superposition of so-called cartoon states which consists of the fermion occupation numbers

$$n_x = \psi^\dagger_x \psi_x \tag{2.38}$$

and the electric fluxes $E_{x,x+1}$. The local fermion occupation number operator n_x commutes with the gauge generator

$$[G_x, n_y] = 0\,, \tag{2.39}$$

and with all the terms of the Hamiltonian, except for the hopping term. However, the total number of fermions

$$N = \sum_x n_x \tag{2.40}$$

commutes with the Hamiltonian

$$[H, N] = 0\,, \tag{2.41}$$

since

$$\begin{aligned} [\psi^\dagger_x U_{x,x+1}\psi_{x+1}, N] &= U_{x,x+1}\sum_y [\psi^\dagger_x\psi_{x+1}, \psi^\dagger_y\psi_y] \\ &= U_{x,x+1}\sum_y \left(\delta_{x+1,y}\psi^\dagger_x\psi_y - \delta_{xy}\psi^\dagger_y\psi_{x+1}\right) \\ &= 0\,. \end{aligned} \tag{2.42}$$

This also means, that the 1 in the bracket of the 4-Fermi term in the Hamiltonian in eq. (2.36) proportional to δ_F

$$\sum_x n_x\,(1 - n_{x+1}) \tag{2.43}$$

leads to a constant, which has no further influence on the eigenstates of the system, than shifting all energies.

The quantum links obey the commutation relation in eq. (2.24). The factor $(-1)^x$ in the mass term of the Hamiltonian is due to the use of staggered fermions. It breaks translation symmetry by one lattice spacing and therefore chiral symmetry explicitly. The term proportional to the gauge coupling g^2 has a trivial contribution in case of spin 1/2. The kinetic term with hopping amplitude t describes the hop of a fermion along a link correlated with the change of the flux through the link, such that the Gauss law is satisfied. Such a hop is illustrated in Figure 2.2.

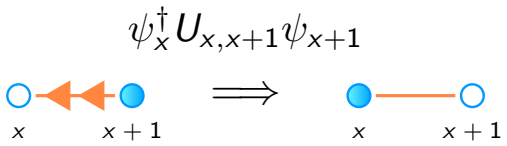

Figure 2.2.: *Example of a correlated hop for spin $S = 1$. The positively charged fermion hops from right to left. This is correlated with the increase of the spin projection (read from left to right), and respects the Gauss law. The part of the hopping term which mediates this process is denoted on top of the process.*

In the absence of a staggered fermion mass ($m = 0$), the Hamiltonian is obviously invariant against the $\mathbb{Z}(2)$ chiral symmetry χ, which corresponds to a shift by one lattice spacing

$$\begin{aligned} {}^{\chi}\psi_x &= \psi_{x+1}\,, \\ {}^{\chi}\psi_x^\dagger &= \psi_{x+1}^\dagger\,, \\ {}^{\chi}U_{x,x+1} &= U_{x+1,x+2}\,, \\ {}^{\chi}E_{x,x+1} &= E_{x+1,x+2}\,. \end{aligned} \tag{2.44}$$

This symmetry is explicitly broken in the presence of a staggered fermion mass. For large positive m, the fermions would prefer to sit at sites with odd x. Let's call the cartoon of such a state $|\Psi_{+m}\rangle$. The staggered fermion occupation numbers of this cartoon state correspond to a filled Dirac sea. For large negative m, the fermions in a cartoon $|\Psi_{-m}\rangle$ of the ground state would sit at the sites with even x. Under a shift by one lattice spacing, these ground states obey

$$\begin{aligned} {}^{\chi}|\Psi_{+m}\rangle &= |\Psi_{-m}\rangle\,, \\ {}^{\chi}|\Psi_{-m}\rangle &= |\Psi_{+m}\rangle\,. \end{aligned} \tag{2.45}$$

However, the mass term and therefore the whole Hamiltonian commutes with an even number of shifts. Therefore, applying χ two times corresponds to the ordinary translation.

Another important symmetry of the Hamiltonian is the charge conjugation CT, which is combined with a shift by one lattice spacing

$$\begin{aligned} {}^{CT}\psi_x &= (-1)^{x+1}\psi_{x+1}^\dagger\,, \\ {}^{CT}\psi_x^\dagger &= (-1)^{x+1}\psi_{x+1}\,, \\ {}^{CT}U_{x,x+1} &= U_{x+1,x+2}^\dagger\,, \\ {}^{CT}E_{x,x+1} &= -E_{x+1,x+2}\,. \end{aligned} \tag{2.46}$$

The sign factor for charge conjugated fermions ensures the invariance of the hopping term

$${}^{CT}\left(\psi_x^\dagger U_{x,x+1}\psi_{x+1}\right) = -\psi_{x+1}U_{x+1,x+2}^\dagger\psi_{x+2}^\dagger = \left(\psi_{x+1}^\dagger U_{x+1,x+2}\psi_{x+2}\right)^\dagger\,. \tag{2.47}$$

The staggered mass term remains unbroken up to a trivial constant:

$${}^{CT}\left((-1)^x\psi_x^\dagger\psi_x\right) = -(-1)^{x+1}\psi_{x+1}\psi_{x+1}^\dagger = (-1)^{x+1}\left(\psi_{x+1}^\dagger\psi_{x+1} - 1\right)\,. \tag{2.48}$$

The charge conjugation of the gauge transformation in eq. (2.14) is

$$^{CT}G_x = \psi_{x+1}\psi^\dagger_{x+1} + E_{x+1,x+2} - E_{x,x+1} = 1 - G_{x+1}\,. \tag{2.49}$$

We would like to obtain charge conjugation as well as gauge invariant states. Therefore, we modify the gauge generator

$$\begin{aligned}\widetilde{G}_x &\doteq G_x + \frac{1}{2}\left[(-1)^x - 1\right] \\ &= n_x - E_{x,x+1} + E_{x-1,x} + \frac{1}{2}\left[(-1)^x - 1\right]\,.\end{aligned} \tag{2.50}$$

With this modified gauge generator, the gauge invariant states defined by

$$\widetilde{G}_x|\Psi\rangle = 0 \tag{2.51}$$

are symmetric under charge conjugation. The form of the Gauss law now depends on whether a site is even or odd. Hence, gauge invariant states are no longer symmetric under the chiral transformation χ.

Under charge conjugation, the number of fermions in the system transforms as

$$^{CT}N = \sum_x (1 - n_{x+1}) = L - N\,, \tag{2.52}$$

where L is the length of the system. Hence, we fix the number of fermions in the system to

$$N = \frac{L}{2}\,. \tag{2.53}$$

There are two further symmetries under which the Hamiltonian, the gauge invariant states, and the total number of fermions are invariant. The parity P,

$$\begin{aligned}^{P}\psi_x &= \psi_{-x}\,, \\ ^{P}\psi^\dagger_x &= \psi^\dagger_{-x}\,, \\ ^{P}U_{x,x+1} &= U^\dagger_{-x-1,-x}\,, \\ ^{P}E_{x,x+1} &= -E_{-x-1,-x}\,,\end{aligned} \tag{2.54}$$

for which we check the invariance of the hopping term

$$^{P}\left(\psi^\dagger_x U_{x,x+1}\psi_{x+1}\right) = \psi^\dagger_{-x}U^\dagger_{-x-1,-x}\psi_{-x-1} = \left(\psi^\dagger_{-x-1}U_{-x-1,-x}\psi_{-x}\right)\,, \tag{2.55}$$

of the 4-Fermi term

$$^{P}\left(\sum_x n_x\,(1 - n_{x+1})\right) = N - \sum_x n_{-x}n_{-x-1} = \sum_x n_x\,(1 - n_{x+1})\,, \tag{2.56}$$

and of the gauge generator

$$^{P}\widetilde{G}_x = n_{-x} + E_{-x-1,-x} - E_{-x,-x+1} + \frac{1}{2}\left[(-1)^x - 1\right] = \widetilde{G}_{-x}\,. \tag{2.57}$$

Finally, there is the combined CP symmetry

$$\begin{aligned} {}^{CP}\psi_x &= (-1)^{-x+1}\psi^\dagger_{-x+1}\,, \\ {}^{CP}\psi^\dagger_x &= (-1)^{-x+1}\psi_{-x+1}\,, \\ {}^{CP}U_{x,x+1} &= U_{-x,-x+1}\,, \\ {}^{CP}E_{x,x+1} &= E_{-x,-x+1}\,. \end{aligned} \tag{2.58}$$

We also check the total number of fermions

$${}^{CP}N = \sum_x \psi_{-x+1}\psi^\dagger_{-x+1} = L - N = \frac{L}{2}\,, \tag{2.59}$$

the hopping term

$${}^{CP}\left(\psi^\dagger_x U_{x,x+1}\psi_{x+1}\right) = -\psi_{-x+1}U_{-x,-x+1}\psi^\dagger_{-x} = \psi^\dagger_{-x}U_{-x,-x+1}\psi_{-x+1}\,, \tag{2.60}$$

the 4-Fermi term

$${}^{CP}\left(n_x\left(1-n_{x+1}\right)\right) = \left(1-n_{-x+1}\right)n_{-x}\,, \tag{2.61}$$

and the gauge generator

$$\begin{aligned} {}^{CP}\widetilde{G}_x &= 1 - n_{-x+1} - E_{-x,-x+1} + E_{-x+1,-x+2} + \frac{1}{2}\left[(-1)^x - 1\right] \\ &= 1 - n_{-x+1} + E_{-x+1,-x+2} - E_{-x,-x+1} - \frac{1}{2}\left[(-1)^{-x+1} + 1\right] \\ &= -\widetilde{G}_{-x+1}\,. \end{aligned} \tag{2.62}$$

2.2. Implementation of the exact diagonalization and the real-time evolution

Exact diagonalizations were performed in the cartoon basis. To describe a gauge invariant cartoon state of an open boundary system it is sufficient to give the fermion occupation numbers n_x and the static external charge at one end of the system. The fluxes and the other static external charge are then fully constrained by the Gauss law. In the performed exact diagonalization studies the external static charges were fixed. The fermion occupation numbers have two states (0 or 1) independent of the actual spin S. This allowed us to encode a cartoon state as an integer number i, where the encoding was

$$i = \sum_{x=1}^{L} 2^{x-1} n_x \in \{0, 1, \ldots, 2^L - 1\}\,. \tag{2.63}$$

Using 64-bit integers allows to handle systems up to $L = 64$ which is way beyond what actual classical technologies could handle for exact diagonalizations.

Most of the possible fermion occupations encoded by i result in gauge variant states. We are only interested in gauge invariant ones. Explicitly finding them by counting up i and

testing if i results in a gauge invariant state would be inefficient, since the range of i grows exponentially with the system size. The chosen strategy was to divide a system of size L and external charges Q_L, Q_R into a left subsystem l of size L_l and a right subsystem r of size $L_r = L - L_l$ such that $|L_l - L/2| = |L_r - L/2|$ is minimal. Then the flux $E_{L/2,L/2+1}$ on the link between the two subsystems is iteratively fixed to all of its allowed states

$$E_{L/2,L/2+1} = -S, -S+1, \ldots, S-1, S\,, \tag{2.64}$$

and is interpreted as external charges for the subsystems

$$\begin{aligned} Q_{l,L} &= Q_L\,, \\ Q_{l,R} &= -E_{L/2,L/2+1}\,, \\ Q_{r,L} &= E_{L/2,L/2+1}\,, \\ Q_{r,R} &= Q_R\,. \end{aligned} \tag{2.65}$$

Then the gauge invariant configurations in both subsystems are searched and combined in all possible ways. Assume we call the N_l codes of the gauge invariant states of the left subsystem j_{l,m_l} with $m_l \in \{1, 2, \ldots, N_l\}$. For the right subsystem we use the same notation N_r, j_{r,m_r}, $m_r \in \{1, 2, \ldots, N_r\}$. If we start the procedure with a flux between the subsystems of $E_{L/2,L/2+1} = -S$, the codes of the combined system with fixed flux $E_{L/2,L/2+1} = E$ are added to those which were already found for $E_{L/2,L/2+1} \in \{-S, -S+1, \ldots, E-1\}$. If we define the number of above already found gauge invariant states as n_{E-1}, the new codes to add to a list of found states are defined as

$$i_{N_r m_l + m_r + n_{E-1}} = 2^{L_r} j_{l,m_l} + j_{r,m_r}\,. \tag{2.66}$$

The same procedure was recursively applied on the left and the right subsystems until a critical size L_c was reached. For subsystems smaller than L_c the simple trial and error method was faster than the described method of dividing the subsystems into pieces. In fact, some additional tricks were applied on subsystems smaller than L_c to speed up the procedure. The final result is an ordered list of integer numbers i_k, with $i_k < i_{k+1}$, which represent gauge invariant cartoon states.

The Hamiltonian to be diagonalized is represented by a sparse matrix whose indices correspond to the indices in the list of gauge invariant states described above

$$\mathrm{H}_{jk} = (\mathbf{H})_{jk} = \langle i_j | H | i_k \rangle\,, \tag{2.67}$$

where $|i\rangle$ corresponds to the cartoon state whose fermion occupation numbers are encoded by the integer number i defined in eq. (2.63).

The numerical result of the exact diagonalization procedure are eigenvectors $\vec{\Psi}_n$ and eigenvalues E_n (the energies of the system) solving the eigenvalue equation

$$\mathbf{H}\vec{\Psi}_n = E_n \vec{\Psi}_n\,. \tag{2.68}$$

The eigenvectors describe the eigenstates of the system by

$$|\Psi_n\rangle = \sum_k \Psi_{n,k} |i_k\rangle\,, \tag{2.69}$$

such that

$$H|\Psi_n\rangle = \sum_{k,l} |i_l\rangle\langle i_l|H|i_k\rangle\langle i_k|\Psi_n\rangle = \sum_{k,l} \mathrm{H}_{lk}\Psi_{n,k}|i_l\rangle = E_n \sum_l \Psi_{n,l}|i_l\rangle = E_n|\Psi_n\rangle\,, \quad (2.70)$$

as intended.

While the above eigenstates are solutions of the time-independent Schrödinger equation, up to an arbitrary static phase, their real-time behavior is described by

$$|\psi(t)\rangle = \exp(-\frac{i}{\hbar}E_n t)|\Psi_n\rangle\,, \quad (2.71)$$

which satisfies the time-dependent Schrödinger equation

$$i\hbar\partial_t|\psi(t)\rangle = H|\psi(t)\rangle\,. \quad (2.72)$$

Given a general initial state $|\psi(0)\rangle$ its real-time evolution is calculated by

$$\begin{aligned} |\psi(t)\rangle &= \exp(-\frac{i}{\hbar}Ht)|\psi(0)\rangle \\ &= \sum_n \exp(-\frac{i}{\hbar}Ht)|\Psi_n\rangle\langle\Psi_n|\psi(0)\rangle \\ &= \sum_n \langle\Psi_n|\psi(0)\rangle \exp(-\frac{i}{\hbar}E_n t)|\Psi_n\rangle\,. \end{aligned} \quad (2.73)$$

We will set $\hbar = 1$ in our calculations. Obviously the whole spectrum is needed to calculate the real-time evolution of a general initial state of the system.

The exact diagonalization was performed by a call of a corresponding function of the GNU Octave software package which is an open source clone of the known MATLAB numerical computing environment. Behind the scenes Octave uses different popular libraries to store the sparse matrices and to perform the exact diagonalization. If not all the eigenvalues and eigenstates are demanded, Octave, like MATLAB, calls functions which are based on the well-known ARPACK software package originally written by R. B. Lehoucq, D. C. Sorensen, and C. Yang. Depending on the structure of the matrix, ARPACK itself uses the Implicitly Restarted Arnoldi Method [38] which is an improved Arnoldi iteration method [39] or, for symmetric matrices, an implicitly restarted Lanczos [40] algorithm.

2.3. Real-time evolution of string breaking for spin $S = 1$

In quantum chromodynamics, when a quark and an anti-quark are separated by a distance r, then a string of color electric flux is formed which connects them. This is an interesting physical object. The string costs energy in proportion to its length, which amounts into a linear quark-anti-quark potential

$$V(r) = \rho r\,. \quad (2.74)$$

Here, ρ is the string tension. In QCD with dynamical charges, the string can break by pair creation of quark-anti-quark. This dynamics (the evolution in real-time) is inaccessible to classical simulation methods. In one spatial dimension, string breaking by pair creation and false vacuum decay are similar phenomena. The dynamical quark-anti-quark pairs play the role of domain walls in the true vacuum.

In contrast, our $U(1)$ quantum link model is a toy model for electrodynamics in 1 dimension. In the case of spin 1 quantum links ($S = 1$), the Hamiltonian in eq. (2.36) realizes a string breaking by dynamical creation of charge-anti-charge pairs $q\bar{q}$ [41]. The vacuum state for $t = d_F = 0$ and $m > 0$ is illustrated in Figure 2.3 and is described by

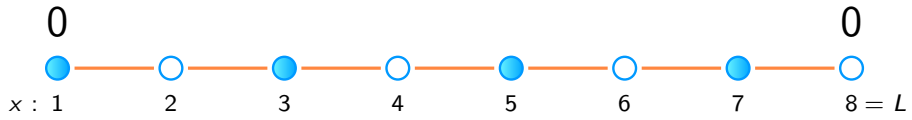

Figure 2.3.: *Cartoon of the candidate vacuum state of the spin $S = 1$ system without external charges and without flux.*

$$\begin{aligned} E_{x,x+1} &= 0\,, \\ \psi_x^\dagger \psi_x &= \frac{1}{2}[1 - (-1)^x]\,. \end{aligned} \tag{2.75}$$

Here we assumed that the leftmost site has an odd coordinate x. The vacuum state obeys the Gauss law. The latter one enforces the particular staggering in eq. (2.75) for zero flux. The corresponding energy of an open system with L lattice sites is

$$E_{\text{ref}} = -\frac{(m + d_F)L}{2}\,. \tag{2.76}$$

Figure 2.4 shows how a string connecting a static $\bar{Q}Q$ pair breaks into two mesons by pair creation of $q\bar{q}$ pairs in intermediate steps of cartoon states. The Gauss law is fulfilled at each site including the boundaries. The external static charge-anti-charge pair $\bar{Q}Q$ generates a confining electric flux string as shown in the first row of the figure. This leads to large total electric flux. For $t = 0$ (static limit) the energy of this configuration relative to the vacuum without external charges is

$$E_{\text{string}} - E_{\text{ref}} = \frac{g^2(L-1)}{2}\,. \tag{2.77}$$

The tension of the string is

$$\rho = \frac{\partial}{\partial L}(E_{\text{string}} - E_{\text{ref}}) = \frac{g^2}{2}\,. \tag{2.78}$$

The value of the total flux is

$$\langle \sum_x E_{x,x+1} \rangle_{\text{string}} = -L + 1\,. \tag{2.79}$$

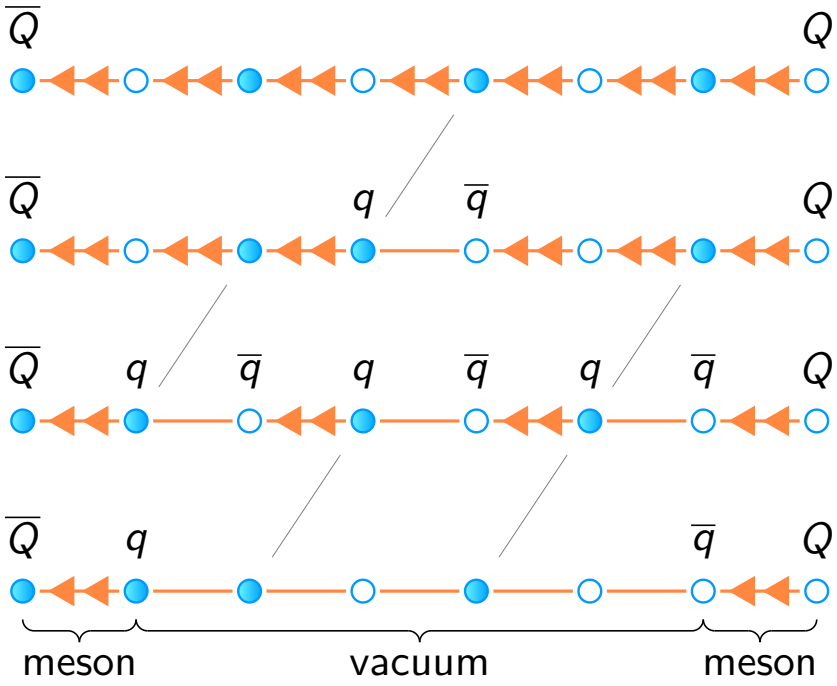

Figure 2.4.: *Cartoon states of the string breaking in the spin $S = 1$ system with static external charges $\bar{Q}Q$. The thin diagonal lines serve as a guide to the eye to emphasize the hopping of the fermions.* Top row: *An electric flux string connects the static $\bar{Q}Q$ pair and has its minimal possible value $\sum_x E_{x,x+1} = -7$.* Mid rows: *Fermion hopping correlated with increase of the flux on the links, creation of dynamical $q\bar{q}$ pairs, and annihilation of dynamical $\bar{q}q$ pairs.* Bottom row: *The term $\sum_x E^2_{x,x+1}$ is minimized to 2. The total electric flux is now $\sum_x E_{x,x+1} = -2$. There are two mesons at the end of the system with a vacuum in the middle of the system.*

If the static charges are separated by a sufficiently large number of lattice sites L, then the potential energy of the string converts to fermion hopping (kinetic energy). This results in the creation of dynamical charge-anti-charge pairs $q\bar{q}$, a process known as string breaking. Finally, fermions are formed by pairing of Q with $\bar{q}$ and of $\bar{Q}$ with q. The resulting state is shown in the last row of Figure 2.4. The energy of the state for $t = 0$ is

$$E_{\text{mesons}} - E_{\text{ref}} = g^2 + 2(m + d_F)\,. \tag{2.80}$$

It has the small total flux

$$\langle \sum_x E_{x,x+1} \rangle_{\text{mesons}} = -2\,. \tag{2.81}$$

The energy difference between the initial and the final state is ($t = 0$)

$$E_{\text{string}} - E_{\text{mesons}} = \frac{g^2(L-3)}{2} - 2(m + d_F)\,. \tag{2.82}$$

Hence, for $t = 0$, the critical length L_c at which the string breaks can be read off:

$$L_c = \frac{4(m + d_F)}{g^2} + 3\,. \tag{2.83}$$

With exact diagonalization, I calculated the difference of the ground state energy E of a 1-dimensional open system of length L with static external charges $\bar{Q}Q$ to the ground state energy E_{ref} of the same system without external charges. This difference is shown in Figure 2.5 for system lengths $L = 4,\ 6, \ldots, 24$ and varying staggered fermion mass parameter m. The hopping parameter and the gauge coupling were both set to $t = g = 1$, the 4-Fermi coupling was set to $d_F = 0$. In the static limit $t = 0$, again with $g = 1$, $d_F = 0$ and with $m = 0, 0.5, \ldots, 5$ the string will break at $L_c = 3, 5, \ldots, 23$. This is in good agreement with the results shown in latter figure, where the quantum hopping was allowed ($t = 1$). The slope of the graphs of the unbroken strings correspond to the string tension ρ. For e.g. $m = 5$, it can be calculated as

$$\rho = \triangle(E - E_{\text{ref}})/\triangle L \approx (11.09 - 1.84)/(20 - 4) = 0.578\,. \tag{2.84}$$

This is in good agreement with the string tension $\rho = 0.5$ in the static limit $t = 0$.

Figures 2.6 and 2.7 show the expectation values of the flux and the fermion number density on each individual quantum link. The parameters of the Hamiltonian were the same as in Figure 2.5, except for the system length, which was fixed to $L = 24$ and the staggered fermion mass parameter m. For large staggered fermion mass $m \geq 6$ the patterns correspond to the unbroken string cartoon state, as expected. For $m = 3$ and $m = 5$ the patterns correspond to the broken string cartoon state with two mesons $\bar{Q}q$ and $\bar{q}Q$ at the ends of the system. This is again in agreement with the previous derivations. For $m = 0$ a mildly staggered flux with delocalized fermions is realized. The hopping is strong enough to create fluctuating charge-anti-charge pairs in the system.

Figure 2.8 shows the dynamic real-time evolution of the expectation value of the total electric flux $\sum_x E_{x,x+1}$ for the same system. Since, to calculate the real-time evolution,

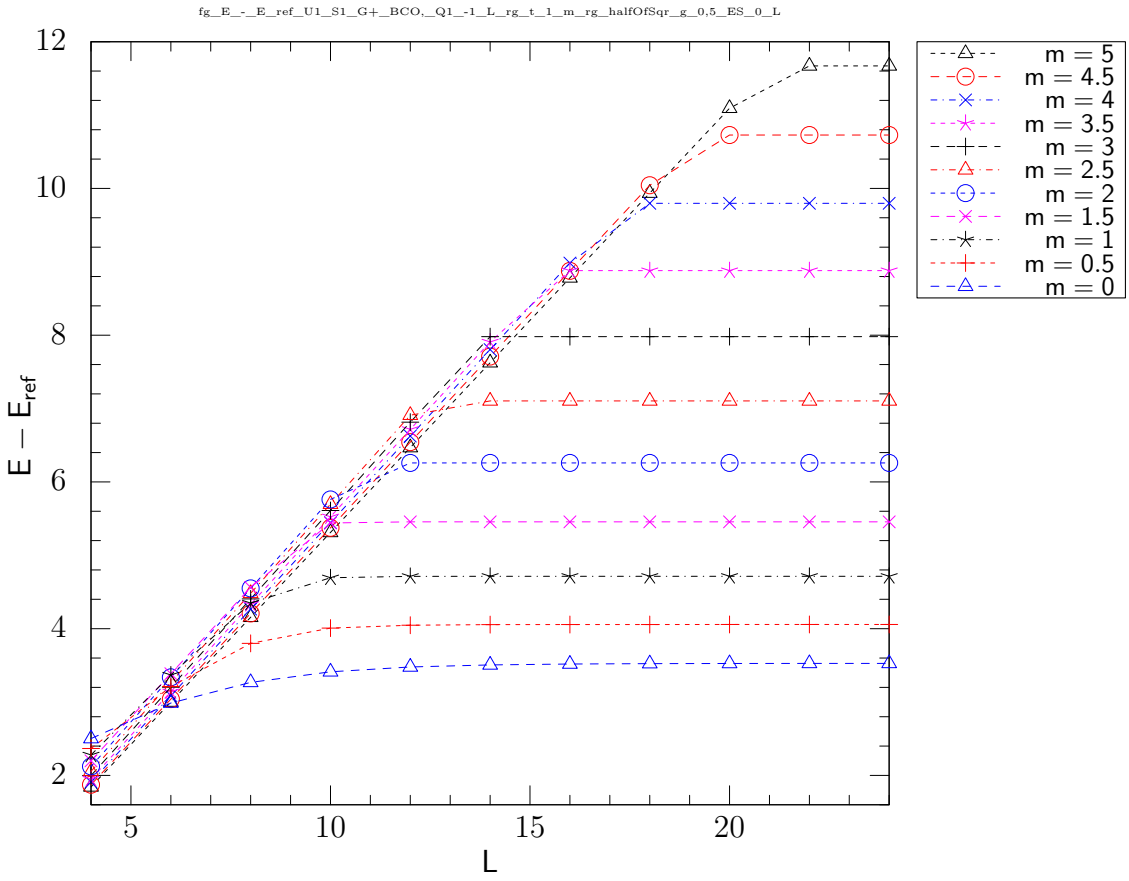

Figure 2.5.: *The vertical axis shows the energy difference $E - E_{ref}$ of an open system with spin $S = 1$ quantum links where E belongs to the system with static external charges $\bar{Q}Q$ (compare Figure 2.4). E_{ref} belongs to the same system but one without external charges (compare the vacuum state in Figure 2.3). The hopping parameter and the gauge coupling are $t = g = 1$, the system length is $L = 4, 6, \ldots, 24$ (horizontal axis), and the staggered fermion mass is $m = 0, 0.5, \ldots, 5$ (see legend). There is no 4-Fermi coupling involved ($d_F = 0$). The lines between the data points are linear interpolations and shall serve as a guide of the eye. The energy of two charges separated by the distance L first grows, as the induced total electric flux $\sum_x E_{x,x+1}$ (and thereby the total energy) gets larger (compare top row of Figure 2.4). The plateaus indicate broken strings (compare bottom row of Figure 2.4). There the electric flux is no more maintained over the whole system length and charge-anti-charge pairs are generated.*

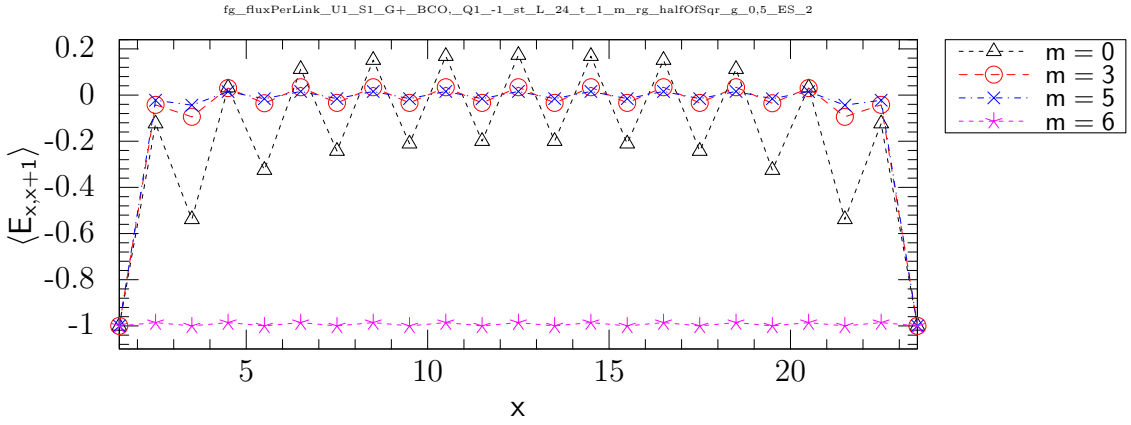

Figure 2.6.: *The vertical axis shows the expectation value $\langle E_{x,x+1} \rangle$ of the flux on each individual quantum link between site x and $x+1$ (horizontal axis) with spin $S = 1$ for an open system with static external charges $\bar{Q}Q$. The hopping parameter and the gauge coupling are $t = g = 1$, the system length is $L = 24$ and the staggered fermion mass is $m = 0, 3, 5, 6$ (see legend). There is no 4-Fermi coupling involved ($d_F = 0$). For $m = 3$ and $m = 5$ the flux pattern corresponds almost to the cartoon state with broken string and two mesons depicted in the bottom row of Figure 2.4. For $m = 6$ it corresponds to the fully restored string depicted in the top row of Figure 2.4.*

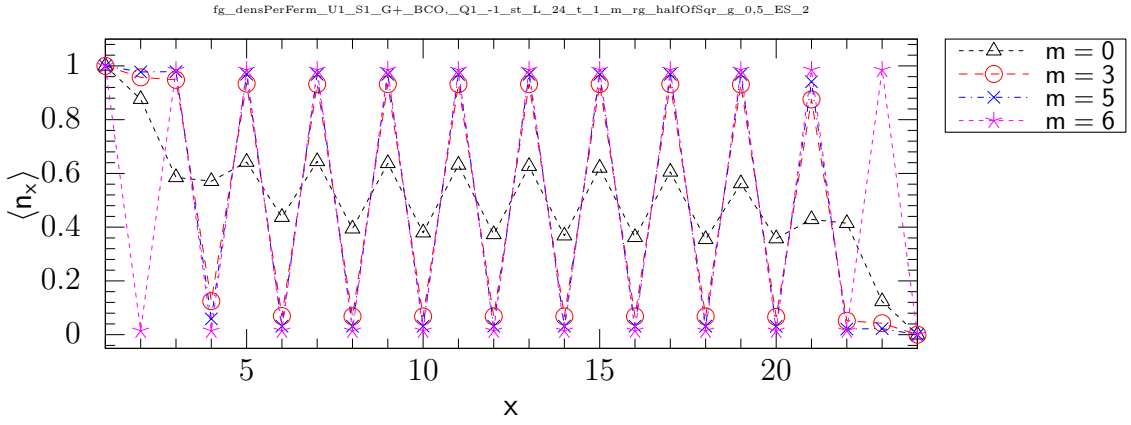

Figure 2.7.: *The vertical axis shows the expectation value $\langle n_x \rangle$ of the fermion number density on each site x (horizontal axis) for an open system with spin $S = 1$ quantum links and static external charges $\bar{Q}Q$. The hopping parameter and the gauge coupling are $t = g = 1$, the system length is $L = 24$ and the staggered fermion mass is $m = 0, 3, 5, 6$ (see legend). There is no 4-Fermi coupling involved ($d_F = 0$). For $m = 3$ and $m = 5$ the fermion number density pattern corresponds almost to the cartoon state with broken string and two mesons depicted in the bottom row of Figure 2.4. For $m = 6$ it corresponds to the fully restored string depicted in the top row of Figure 2.4.*

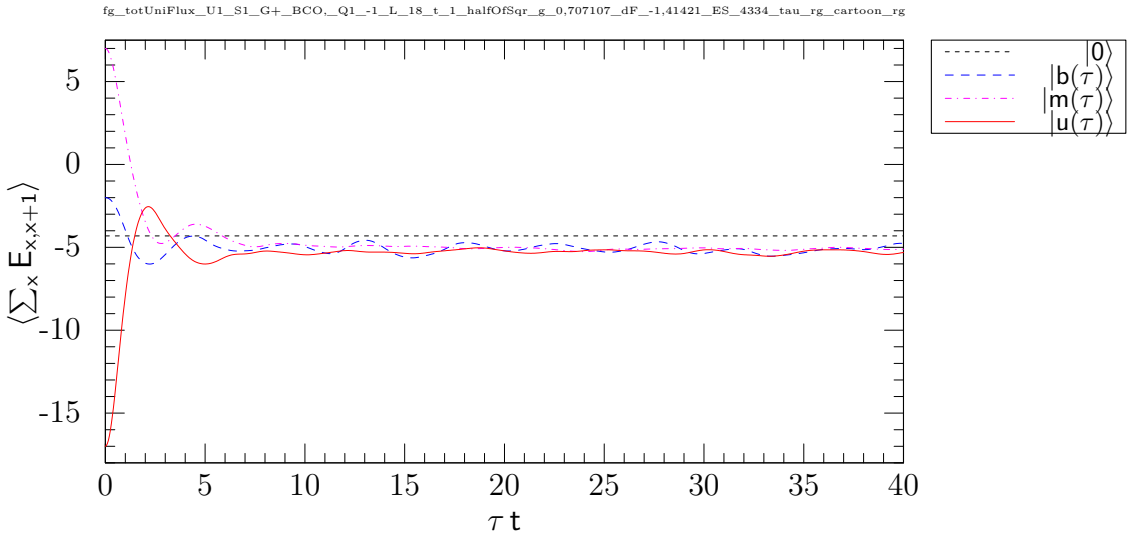

Figure 2.8.: *The vertical axis shows the dynamic real-time evolution of the expectation value* $\langle \sum_x E_{x,x+1} \rangle$ *of the total electric flux in an open system with quantum links of spin* $S = 1$ *and static external charges* $\bar{Q}Q$ *after preparing different initial conditions* $|0\rangle$, $|b(0)\rangle$, $|m(0)\rangle$, *and* $|u(0)\rangle$. *The system length is* $L = 18$, *and the parameters of the Hamiltonian are* $m = 0$, $g^2 = \sqrt{2}t$, *and* $d_F = -\sqrt{2}t$. *The initial condition* $|u(0)\rangle$ *of the solid red line corresponds to the situation with the largest possible negative total electric flux* $\sum_x E_{x,x+1} = -17$, *which corresponds to the unbroken string (see top row of Figure 2.4). The initial condition* $|b(0)\rangle$ *of the dashed blue line corresponds to the situation with a total electric flux* $\sum_x E_{x,x+1} = -2$ *which corresponds to the broken string with two mesons (see bottom row of Figure 2.4). Finally, the initial condition* $|m(0)\rangle$ *of the dash dotted magenta line corresponds to the situation with the largest possible positive total electric flux* $\sum_x E_{x,x+1} = 7$. *The thin black dotted line corresponds to the electric flux expectation value in the vacuum* $|0\rangle$.

all eigenstates are needed, the system size $L = 18$, which results in 4334 eigenstates, is smaller than for the calculation of previous ground state properties. The Hamiltonian parameters are $m = 0$, $g^2 = \sqrt{2}t$, and $d_F = -\sqrt{2}t$. With these parameters, the critical length in eq. (2.83) is $L_c = -1$. Hence, the string is broken. The solid red line illustrates the situation with an unbroken string as its initial condition. The string breaks for sufficiently large positive real-time and it remains broken afterwards. Due to the choice of the Hamiltonian parameters, other initial conditions lead to similar long-term behavior of the total electric flux. As explained in the introduction, the initial states are projected on the whole spectrum to obtain the real-time evolution. Hence, the initial conditions lead to some excitations in the system and therefore, the mean long term-value of total electric fluxes with other initial conditions than the ground state are slightly different from the vacuum expectation value.

2.4. Real-time evolution after a quench for spin $S = 1/2$

The simplest model realizable with the Hamiltonian in eq. (2.36) is the spin $S = 1/2$ quantum link model. From a particle physics point of view the fact that there are no zero flux states seems unnatural. Nevertheless this model already undergoes spontaneous symmetry breaking and is able to describe the real-time evolution after a quench. This is a non-perturbative process. Again, its dynamics is inaccessible to classical simulation methods. However, in a quantum simulator the real-time evolution after a quench could be performed.

Note, that in the case of spin $S = 1/2$, the electric term in the Hamiltonian is a trivial constant. Therefore, the value of the gauge coupling g is not important and is set to zero. One could add the additional term

$$-2\sigma \sum_x (-1)^x E_{x,x+1} \tag{2.85}$$

to the Hamiltonian. This term is C and P invariant and leads to a staggered flux pattern. Like the Gauss law it explicitly breaks the chiral symmetry. However, for gauge invariant states in the case of spin $S = 1/2$, since

$$0 = \sum_x (-1)^x \widetilde{G}_x |\Psi\rangle = \sum_x (-1)^x \left(\psi_x^\dagger \psi_x - 2E_{x,x+1}\right) |\Psi\rangle \,, \tag{2.86}$$

the σ term can be absorbed by a renormalized staggered fermion mass term

$$m_{\text{eff}} = m - \sigma \,, \tag{2.87}$$

Therefore, we ignore this staggered flux term.

There are three candidate vacuum states for $t = 0$ which respect the Gauss law $\widetilde{G}_x |\Psi\rangle = 0$ with the gauge generator defined in eq. (2.50). For $m < 0$ charge conjugation (C) and

parity (P) are restored. This vacuum state, depicted in Figure 2.9, is described by

$$E_{x,x+1} = \frac{1}{2}(-1)^x\,,$$
$$\psi_x^\dagger \psi_x = \frac{1}{2}[1 + (-1)^x]\,. \tag{2.88}$$

For $m > 0$ charge conjugation (C) and parity (P) are spontaneously broken. Those competing vacuum states are depicted in Figure 2.10. The fermion occupation for those broken vacua is

$$\psi_x^\dagger \psi_x = \frac{1}{2}[1 - (-1)^x]\,. \tag{2.89}$$

For $|t|, |d_F| \ll |m|$ the vacuum states are very close to the above described cartoon vacuum states.

Figure 2.9.: *Cartoon of a candidate vacuum state of the spin $S = 1/2$ system. The state is charge conjugation (C) and parity (P) invariant. The total electric flux has its minimal possible absolute value $|\sum_x E_{x,x+1}| = 1/2$.*

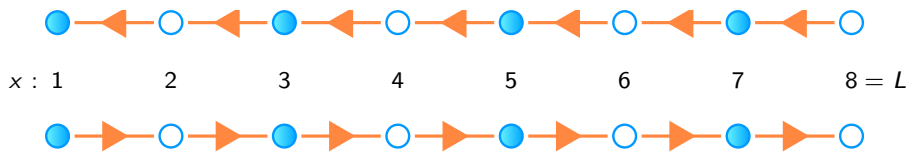

Figure 2.10.: *Cartoons of competing candidate vacuum states of the spin $S = 1/2$ system The states are C and P partners of each other. In both cases, the total electric flux has its maximal possible absolute value $|\sum_x E_{x,x+1}| = 7/2$.*

Figure 2.11 illustrates the spontaneous symmetry breaking of a charge conjugation and parity invariant phase after a quench. The Gauss law is fulfilled at each site. For open boundary conditions external static charges or equivalently external static fluxes have to be imposed to fulfill the Gauss law at the boundaries. The choice of those external static charges decides about which of the competing C and P invariant vacua is realized. The total electric flux

$$\sum_x E_{x,x+1} \tag{2.90}$$

is an order parameter for the combined charge conjugation and parity breaking.

With exact diagonalization, I calculated the expectation values of the flux and the fermion number density on each individual quantum link. The results are shown in Figures 2.12 and 2.13 for a system size of $L = 26$ with a static charge $+1/2$ at site 1 and a static charge $-1/2$ at site $L = 26$. The hopping parameter was set to $t = 1$, the 4-Fermi coupling was set to $d_F = 0$ and the electric term proportional to the gauge coupling g is

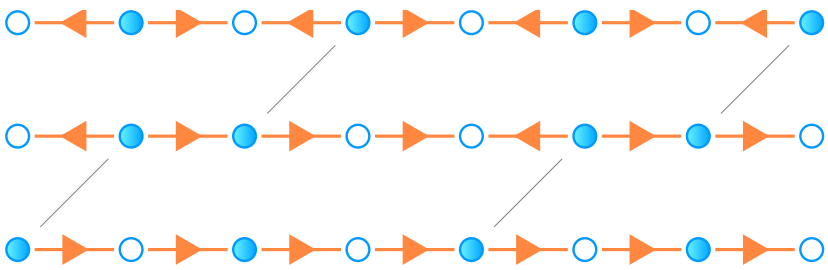

Figure 2.11.: *Cartoon states mimicking the spontaneous symmetry breaking of a charge conjugation (C) and parity (P) invariant phase after a quench in the spin $S = 1/2$ system. The thin diagonal lines serve as a guide to the eye to emphasize the hopping of the fermions.* Top row: *This is the same charge conjugation and parity invariant quenched state with staggered flux as shown in Figure 2.9. The total electric flux is $\sum_x E_{x,x+1} = -1/2$.* Center row: *Fermion hopping correlated with spin flips.* Bottom row: *Vacuum with spontaneous parity and charge conjugation breaking. The same state is shown in the bottom row of Figure 2.10. The total electric flux has its maximal possible value $\sum_x E_{x,x+1} = +7/2$.*

a trivial constant. For a sufficiently large negative staggered fermion mass $m < -8$ the patterns correspond to the charge conjugation C and the parity P invariant cartoon state depicted in Figure 2.9, as expected. For a sufficiently large positive staggered mass $m > 8$ the patterns correspond to the spontaneously broken cartoon state depicted in bottom row of Figure 2.10.

Figure 2.14 shows the dynamic real-time evolution of the expectation value of the total electric flux $\sum_x E_{x,x+1}$ which is an order parameter for the symmetry breaking. Again, for the real-time evolution, all eigenstates were accounted and the system was therefore limited to $L = 16$, which results in 1597 eigenstates. The 4-Fermi coupling was set to $d_F = -10t$. The initial condition at $\tau = 0$ corresponds to the situation of the charge conjugation C and parity P unbroken state illustrated in Figure 2.9. The figure shows coherent oscillations, which depend on the staggered fermion mass parameter m/t.

2.5. Implementation on a quantum simulator

In [26] we proposed the implementation of a $U(1)$ gauge theory coupled to fermionic matter on a quantum simulator which consists of a Fermi-Bose mixture of ultracold atoms confined in an optical lattice. The construction is based on quantum links. While the gauge fields are represented by two-component bosons in form of bosonic atoms, the matter fields are represented by fermionic atoms. The fermions hop between the lattice sites and interact with the dynamical gauge fields on the links.

The underlying microscopic Hamiltonian which describes the concrete system realized

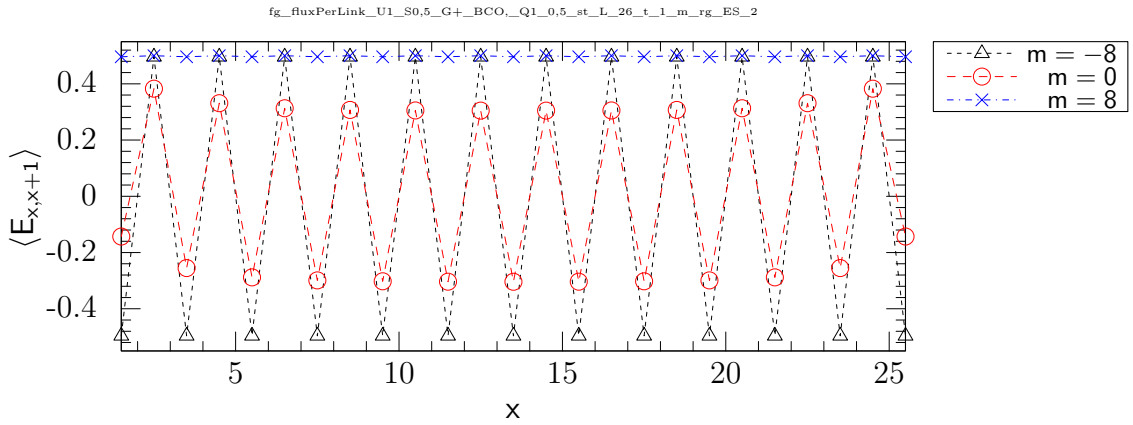

Figure 2.12.: *The vertical axis shows the expectation value $\langle E_{x,x+1}\rangle$ of the flux on each individual quantum link between site x and $x+1$ (horizontal axis) with spin $S = 1/2$ for an open system. The hopping parameter is $t = 1$, the system length is $L = 26$ and the staggered fermion mass is $m = -8, 0, 8$ (see legend). There is no 4-Fermi coupling involved ($d_F = 0$) and the gauge coupling is irrelevant. For $m = -8$ the flux pattern corresponds to the C and P invariant cartoon state depicted in Figure 2.9. For $m = 8$ it corresponds to the C and P broken cartoon state depicted in the bottom row of Figure 2.10.*

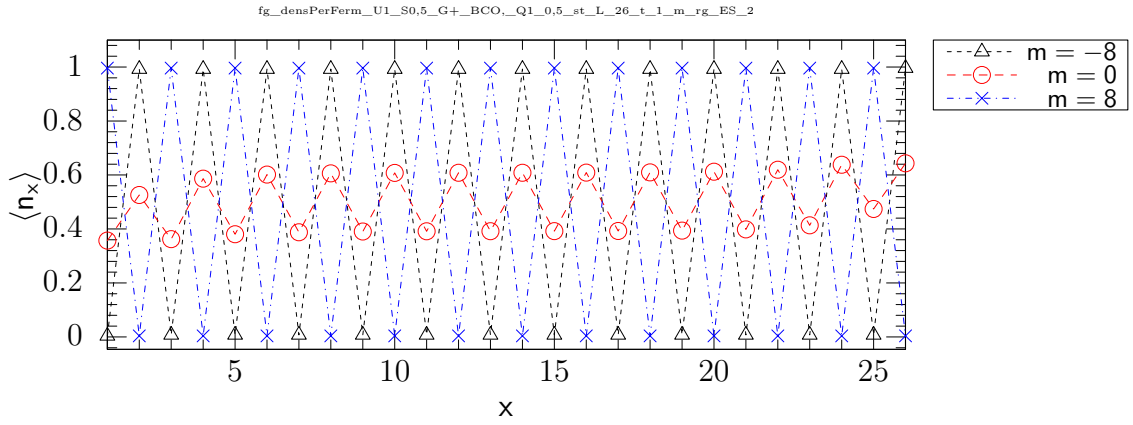

Figure 2.13.: *The vertical axis shows the expectation value $\langle n_x\rangle$ of the fermion number density on each site x (horizontal axis) for an open system with spin $S = 1/2$ quantum links. The hopping parameter is $t = 1$, the system length is $L = 26$ and the staggered fermion mass is $m = -8, 0, 8$ (see legend). There is no 4-Fermi coupling involved ($d_F = 0$) and the gauge coupling g has no influence. For $m = -8$ the fermion number density pattern corresponds to the C and P invariant cartoon state depicted in Figure 2.9. For $m = 8$ it corresponds to the C and P broken cartoon state depicted in the bottom row of Figure 2.10.*

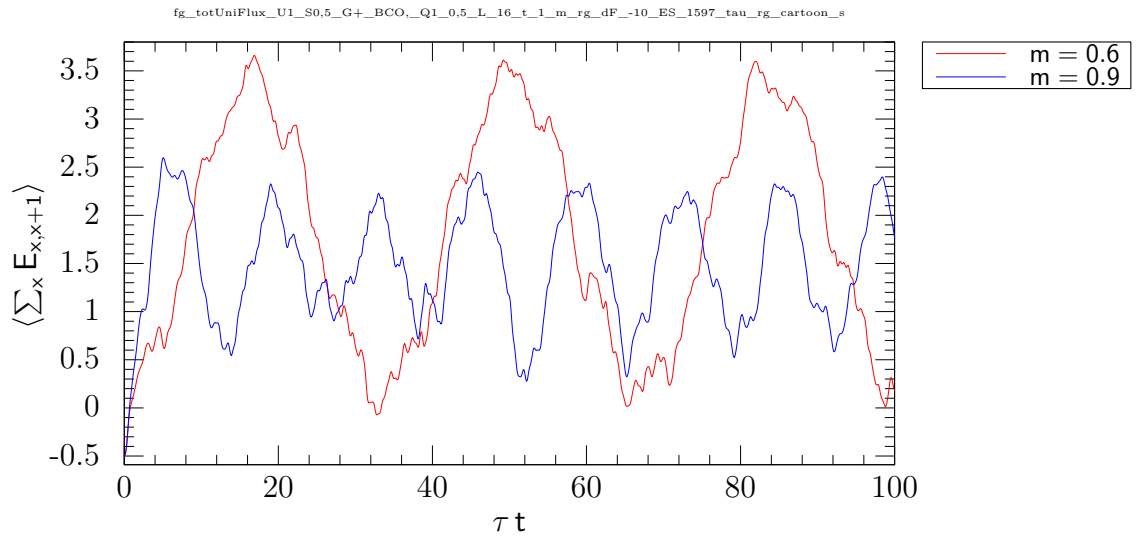

Figure 2.14.: *The vertical axis shows the dynamical real-time evolution of the expectation value* $\langle \sum_x E_{x,x+1} \rangle$ *of total electric flux in an open system with quantum links of spin* $S = \frac{1}{2}$ *for two different values of the staggered fermion mass parameter* $m = 0.6t, 0.9t$*. The system length is* $L = 16$*, the 4-Fermi coupling is* $d_F = -10t$*, and the gauge coupling* g *has no influence. The initial condition at* $\tau = 0$ *corresponds to the situation of the* C *and* P *invariant cartoon state illustrated in Figure 2.9 with total electric flux* $\sum_x E_{x,x+1} = -1/2$*. The flux performs coherent oscillations whose strength depends on* m/t*.*

by the quantum simulator is a Hubbard type model. By tuning the system parameters of the optical lattice, the quantum link model with staggered fermions emerges as a low energy effective theory. Its target effective Hamiltonian is gauge invariant and we had to find a way to remove the gauge variant states to fulfill the Gauss law.

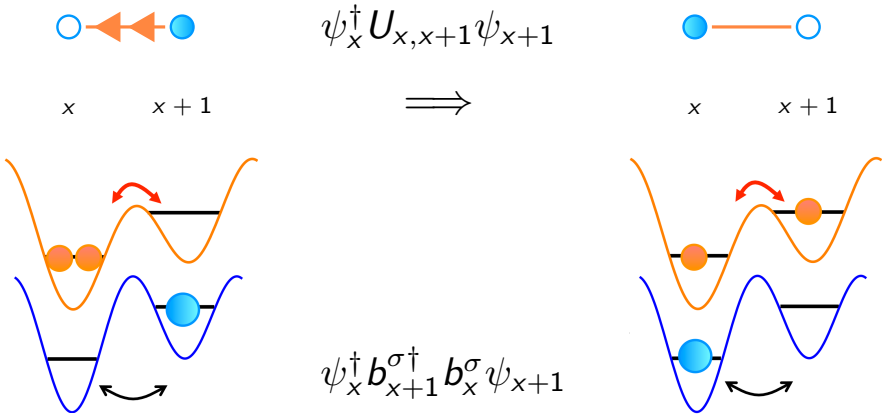

Figure 2.15.: Top part: *Correlated hop induced by the kinetic term in the quantum link model Hamiltonian. The fermion hops from the site $x+1$ to the site x. The spin projection and therefore the electric flux changes from -1 to 0.* Bottom part: *Realization in an ultracold atomic system. The bosonic and the fermionic atoms are confined in optical superlattices. The spin is encoded with $N = 2S$ bosonic atoms.*

Figure 2.15 illustrates how a correlated hop induced by the kinetic term in the Hamiltonian is performed on the optical lattice for a spin $S = 1$ flip. In the quantum link model, the Gauss law is conserved. The fermion hops from the site $x+1$ to the site x (in other words from right to left) while the electric flux changes from -1 to 0.

In the ultracold atomic system the spinless fermion is confined in an optical lattice. Ignoring the Gauss law and the fact that there are other spinless fermions, it is free to successively jump to any site of the system by tunneling between the minima of the optical lattice. The staggered fermion term

$$\sum_x (-1)^x \psi_x^\dagger \psi_x \tag{2.91}$$

can be implemented by an optical superlattice. In other words, the maxima of the optical lattice for the spinless fermions shown in Figure 2.15 all have the same height, while the minima are staggered. Finally this superlattice is populated with the spinless fermionic atoms at half-filling.

The spin on the link is encoded by $N = 2S$ bosonic species. Since they have to be separated from the bosonic species implementing the neighboring links, there are two different species $\sigma = 1, 2$ residing in two different superlattices. Here σ distinguishes

whether the left side of a link corresponds to an even or an odd site

$$\sigma = \begin{cases} 1 & x \text{ odd} \\ 2 & x \text{ even} \end{cases} . \tag{2.92}$$

The quantum link operator corresponds to

$$U_{x,x+1} = b_{x+1}^{\sigma\dagger} b_x^{\sigma} = \begin{cases} b_{x+1}^{1\dagger} b_x^1 & x \text{ odd} \\ b_{x+1}^{2\dagger} b_x^2 & x \text{ even} \end{cases} , \tag{2.93}$$

where $b_x^{\sigma\dagger}$ is the bosonic creation operator for species σ at site x. Pay attention that there is no summation over σ in eq. (2.93). This is a Schwinger representation of the quantum link and the electric flux is defined to be proportional to the population difference

$$E_{x,x+1} = \frac{1}{2}\left(b_{x+1}^{\sigma\dagger} b_{x+1}^{\sigma} - b_x^{\sigma\dagger} b_x^{\sigma}\right) = S - b_x^{\sigma\dagger} b_x^{\sigma} = b_{x+1}^{\sigma\dagger} b_{x+1}^{\sigma} - S\,, \tag{2.94}$$

where

$$2S = N = b_x^{\sigma\dagger} b_x^{\sigma} + b_{x+1}^{\sigma\dagger} b_{x+1}^{\sigma}\,. \tag{2.95}$$

Again, there was no sum over the σ. The confinement of the N bosonic atoms to their corresponding link is realized by double-well potentials with a large amplitude part. A small amplitude part steers the tunneling amplitude on the quantum link. The difference in the minima on the sites lead to spin polarization.

Figure 2.16 illustrates the optical superlattices which create double-well potentials. Depending on how the difference of the minima for species b^1 and b^2 are tuned, a total electric flux contribution and a staggered flux pattern contribution can be induced. As stated in the previous section, for spin $S = 1/2$ the staggered flux pattern has the same effect as the staggered fermion mass because of the Gauss law. The staggered fermion mass is induced by a difference in the minima of the optical superlattices for the fermions.

The distance between the different atomic species is small enough such that they interact with each other. With the setup shown in Figure 2.16, the microscopic 1-d Hamiltonian

$$\widetilde{H} = \triangle\widetilde{H} + \widetilde{H}_U \tag{2.96}$$

with

$$\triangle\widetilde{H} = -t_B \sum_{x \text{ odd}} b_x^{1\dagger} b_{x+1}^1 - t_B \sum_{x \text{ even}} b_x^{2\dagger} b_{x+1}^2 - t_F \sum_x \psi_x^\dagger \psi_{x+1} + \text{H.c.} \tag{2.97}$$

and

$$\widetilde{H}_U = \sum_{x,\alpha,\beta} n_x^\alpha U_{\alpha\beta} n_x^\beta + \sum_{x,\alpha} (-1)^x U_\alpha n_x^\alpha \tag{2.98}$$

can be realized. Here, we introduced the operator

$$n_x^\alpha = b_x^{\alpha\dagger} b_x^\alpha\,, \tag{2.99}$$

which counts the number of atoms of type $\alpha = F, 1, 2$ (fermions, link bosons of species 1, link bosons of species 2). The coefficients U_α describe alternating offsets of the superlattice, and the coefficients $U_{\alpha\beta}$ describe interactions between species α and β (repulsive for

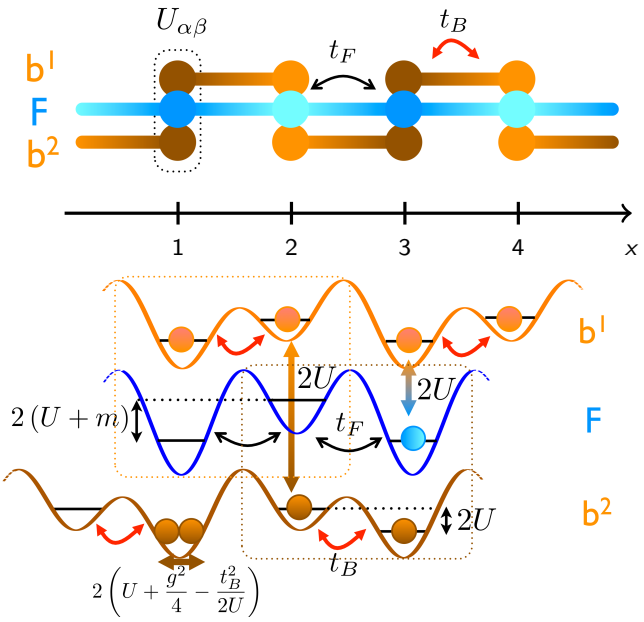

Figure 2.16.: *Illustration of the optical superlattices for a fermionic and two different bosonic species. Two bosonic species are necessary to constrain the bosons on single links.* Top part: *Species* b^1 *and* b^2 *can hop only locally. Species* b^1 *lives on links with odd* x *and even* $x+1$*, while species* b^2 *lives on links with even* x *and odd* $x+1$. Bottom part: *Contributions to the microscopic Hamiltonian by interactions between the individual atoms.*

positive coefficients, attractive for negative ones). The term $\widetilde{H}_U$ can be re-expressed up to a constant as

$$\widetilde{H}_U = \frac{\tilde{g}^2}{2}\sum_x E^2_{x,x+1} + m\sum_x (-1)^x \psi^\dagger_x \psi_x + U\sum_x \widetilde{G}^2_x \,. \tag{2.100}$$

For a large coefficient U at low energies the system remains in the gauge invariant sector.

To work out the relations between eqs. (2.98) and (2.100), we rewrite the gauge generator defined in eq. (2.50) as

$$\begin{aligned}\widetilde{G}_{x\text{ even}} &= n^F_x - E_{x,x+1} + E_{x-1,x} + \frac{1}{2}\left[(-1)^x - 1\right] \\ &= n^F_x - (S - n^2_x) + (n^1_x - S) + \frac{1}{2}\left[(-1)^x - 1\right] \\ &= n^F_x + n^1_x + n^2_x - 2S + \frac{1}{2}\left[(-1)^x - 1\right] \,. \end{aligned} \tag{2.101}$$

Here, we used eq. (2.94) and assumed $\sigma = 1$ for the link which touches the site x from the left and correspondingly $\sigma = 2$ for the link which touches the site x from the right (and the site $x+1$ from the left). The same expression for the gauge generator holds for x odd. Up to a staggered offset, $\widetilde{G}_x$ counts the total number of atoms at site x. Now, let's have a look at the term in eq. (2.100) proportional to $g^2/2$

$$\begin{aligned}\sum_x E^2_{x,x+1} &= \frac{1}{2}\sum_{x\text{ odd}} \left[\left(S - n^1_x\right)^2 + \left(n^1_{x+1} - S\right)^2\right] \\ &\quad + \frac{1}{2}\sum_{x\text{ even}} \left[\left(S - n^2_x\right)^2 + \left(n^2_{x+1} - S\right)^2\right] \\ &= \frac{1}{2}\sum_{x,\sigma=1,2} (n^\sigma_x)^2 + \text{cst}\,, \end{aligned} \tag{2.102}$$

and work out the term

$$\sum_x \widetilde{G}^2_x = \sum_{x,\alpha,\beta} n^\alpha_x n^\beta_x + \sum_{x,\alpha} (-1)^x n^\alpha_x + \text{cst}\,. \tag{2.103}$$

We now rewrite eq. (2.100) as

$$\begin{aligned}\widetilde{H}_U &= \frac{\tilde{g}^2}{4}\sum_{x,\sigma=1,2} (n^\sigma_x)^2 + m\sum_x (-1)^x n^F_x + U\sum_{x,\alpha,\beta} n^\alpha_x n^\beta_x + U\sum_{x,\alpha} (-1)^x n^\alpha_x + \text{cst} \\ &= \left(U + \frac{g^2}{4}\right)\sum_{x,\sigma=1,2} (n^\sigma_x)^2 + (U+m)\sum_x (-1)^x n^F_x \\ &\quad + U\sum_{x,\sigma=1,2} (-1)^x n^\sigma_x + 2U\sum_x \left(n^F_x n^1_x + n^F_x n^2_x + n^1_x n^2_x\right) + \text{cst}\,. \end{aligned} \tag{2.104}$$

Comparing to eq. (2.98) one reads off

$$\begin{aligned} U_{F1} = U_{1F} = U_{F2} = U_{2F} = U_{12} = U_{21} &= U\,, \\ U_{11} = U_{22} &= U + \tilde{g}^2/4\,, \\ U_F &= U + m\,, \\ U_1 = U_2 &= U\,. \end{aligned} \tag{2.105}$$

The factor U_{FF} amounts to a constant contribution. Forcing the system into its gauge invariant sector requires $U \gg g^2, |m|$.

To see how the hopping term

$$-t\psi_x^\dagger U_{x,x+1}\psi_{x+1} = -t\psi_x^\dagger b_{x+1}^{\sigma\dagger} b_x^\sigma \psi_{x+1} \tag{2.106}$$

is enforced by energy conservation, we use second order perturbation theory to reduce the microscopic Hamiltonian in eq. (2.96) to an effective Hamiltonian. For this, let's write the microscopic Hamiltonian as

$$\widetilde{H} = H_0 + V \tag{2.107}$$

with the unperturbed part

$$H_0 = U\sum_x \widetilde{G}_x^2 \tag{2.108}$$

and the perturbation

$$V = \triangle\widetilde{H} + V_{\text{inv}} = \triangle\widetilde{H} + \frac{\tilde{g}^2}{2}\sum_x E_{x,x+1}^2 + m\sum_x (-1)^x \psi_x^\dagger\psi_x\,. \tag{2.109}$$

The unperturbed Hamiltonian has the gauge invariant states as its degenerated zero energy ground states. Let's denote these N ground states as $|\chi_s^{(0)}\rangle$, $s \in \{1, 2, \ldots, N\}$ with $E_s^{(0)} = 0$ and choose them such that they are diagonal in V_{inv}.

The effective Hamiltonian in second order, evaluated between gauge invariant states then has the entries

$$\begin{aligned}
\langle\chi_s^{(0)}|H_{\text{eff}}^{(2)}|\chi_t^{(0)}\rangle &= \langle\chi_s^{(0)}|V|\chi_t^{(0)}\rangle - \langle\chi_s^{(0)}|V\frac{Q_0}{H_0}V|\chi_t^{(0)}\rangle \\
&= \langle\chi_s^{(0)}|V_{\text{inv}}|\chi_t^{(0)}\rangle + \sum_{u=1}^{N}\langle\chi_s^{(0)}|V_{\text{inv}}\frac{|\chi_u^{(0)}\rangle\langle\chi_u^{(0)}|}{H_0}V_{\text{inv}}|\chi_t^{(0)}\rangle \\
&- \langle\chi_s^{(0)}|V_{\text{inv}}\frac{\mathbb{1}}{H_0}V_{\text{inv}}|\chi_t^{(0)}\rangle - \langle\chi_s^{(0)}|(\triangle\widetilde{H})\frac{\mathbb{1}}{H_0}(\triangle\widetilde{H})|\chi_t^{(0)}\rangle \\
&= \langle\chi_s^{(0)}|V_{\text{inv}}|\chi_t^{(0)}\rangle - \langle\chi_s^{(0)}|(\triangle\widetilde{H})\frac{\mathbb{1}}{H_0}(\triangle\widetilde{H})|\chi_t^{(0)}\rangle\,.
\end{aligned} \tag{2.110}$$

Here we used

$$Q_0 = \mathbb{1} - \sum_{s=1}^{N}|\chi_s^{(0)}\rangle\langle\chi_s^{(0)}| \tag{2.111}$$

and the fact that $\triangle\widetilde{H}$ applied on a gauge invariant state $|\chi_s^{(0)}\rangle$ amounts into a gauge variant state. The effective Hamiltonian reads

$$\begin{aligned}
H_{\text{eff}}^{(2)} &= \left(\frac{\tilde{g}^2}{2} + \frac{t_B^2}{U}\right)\sum_x E_{x,x+1}^2 + m\sum_x (-1)^x\psi_x^\dagger\psi_x \\
&- \frac{t_F t_B}{U}\sum_x\left[\psi_x^\dagger U_{x,x+1}\psi_{x+1} + \text{H.c.}\right] - \frac{t_F^2}{U}\sum_x \psi_x^\dagger\psi_x\left(1 - \psi_{x+1}^\dagger\psi_{x+1}\right)\,.
\end{aligned} \tag{2.112}$$

For spin $S = 1/2$ this Hamiltonian matches the initial one defined in eq. (2.36) with

$$t = \frac{t_B t_F}{U} \tag{2.113}$$

and

$$\frac{\tilde{g}^2}{4} = \frac{g^2}{4} - \frac{t_B^2}{2U} \,. \tag{2.114}$$

An additional gauge invariant term with coefficient

$$\delta_F = t_F^2/U \tag{2.115}$$

appeared in eq. (2.112). It's a 4-Fermi term with an additional constant contribution.

Finally, a quantum simulation would consist of an experiment with the following steps repeated several times

- preparation of an initial gauge invariant state
- leaving the system on its own for a certain physical time t
- measurement of some commuting physical observables

This procedure would allow for a quantum simulation of real-time dynamics. The proposed solution is generalizable to 2 and to 3 dimensions and to fermions with spin.

2.6. Conclusions

Our group constructed a quantum simulator of lattice gauge theory to study real-time breaking of a confining string in the $U(1)$ quantum link model at strong coupling in $(1 + 1)$ dimensions using an optical lattice setup.

This simple quantum link model, which couples bosonic gauge fields to fermionic matter, already addresses interesting dynamical questions. It enables demonstration experiments, e.g. for string breaking and for the dynamics after a quench. The calculations of small systems performed in this work would allow to compare the obtained experimental data of a quantum simulator to the theoretical benchmark results.

The basic elements of such a quantum simulator are already individually realized in the laboratory. However, their combination for our simulator has not been realized yet. Also higher dimensions have not been realized yet in the laboratory.

Since full quantum chromodynamics can be formulated in terms of quantum link models [13], approaching it step by step on quantum simulators is promising. However, there is a long list of challenges to implement more QCD like simulators to address e.g. non-zero baryon density.

3. Expansion of a "quark-gluon plasma" in a $U(2)$ gauge theory

The gauge fields in the standard model are non-Abelian. Up to now we worked with an Abelian $U(1)$ quantum link model, which in the following we will extend to the non-Abelian $U(N)$ and $SU(N)$ cases with $N \geq 2$.

This allows us to study the spontaneous breakdown of chiral symmetry, a phenomenon which happens, e.g. in quantum chromodynamics for with quarks.

An appealing fact of the quantum link model also is that fermionic and gauge degrees of freedom are both expressed with quantum variables.

We used the $U(2)$ quantum link model in $(1+1)$-dimensions to address spontaneous symmetry breaking and real-time evolutions with exact diagonalization.

First, in the following three sections, the $U(N)$ and the $SU(N)$ quantum link model is elaborated, closely following what we published in [27] and especially in its supplemental material. The latter contains a pedagogical introduction to the quantum link models and their terminology which were introduced in [13]. However, in this work, as in [27], we specialized to the case where the quarks are represented with staggered fermions.

3.1. Extending the quantum link model to $U(N)$ and $SU(N)$

We describe the $U(N)$ or $SU(N)$ quantum link model residing on a d-dimensional spacial lattice with staggered fermions coupled to a $U(N)$ link variables.

In contrast to chapter 2 we interpret the staggered fermions as quarks, where $\psi_x^{i\dagger}$ is a quark creation operator and ψ_x^i a quark annihilation operator. Here, $i \in \{1, 2, \ldots, N\}$ is the non-Abelian color index of a quark. The operators obey the standard anti-commutation relations

$$\begin{aligned} \{\psi_x^{i\dagger}, \psi_y^j\} &= \delta_{xy}\delta_{ij}\,, \\ \{\psi_x^i, \psi_y^j\} &= \{\psi_x^{i\dagger}, \psi_y^{j\dagger}\} = 0\,. \end{aligned} \tag{3.1}$$

The degrees of freedom associated with the link (x, y) are $N \times N$ matrices

$$U_{xy} = U_{yx}^\dagger \tag{3.2}$$

of quantum link operators, color-neutral Hermitean Abelian electric field operators

$$E_{xy} = -E_{yx}\,, \tag{3.3}$$

and Hermitean non-Abelian electric field operators

$$\begin{aligned} L^a_{xy} &= R^a_{xy}\,, \\ R^a_{yx} &= L^a_{xy} \end{aligned} \tag{3.4}$$

with

$$a \in \{1, 2, \ldots, N^2 - 1\}\,. \tag{3.5}$$

Figure 3.1 shows how the various degrees of freedom are associated with lattice sites and links.

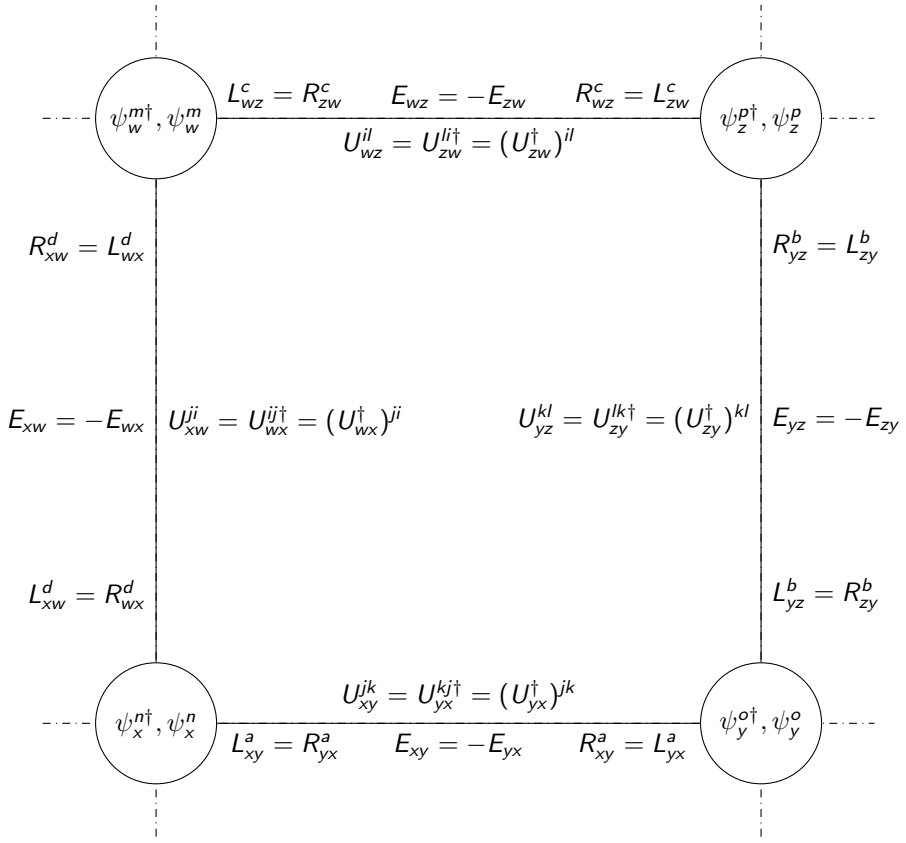

Figure 3.1.: *Assignment of the various degrees of freedom to the four sites w, x, y, z and the four links (w, x), (x, y), (z, y), (w, z) of a plaquette.*

The commutation relations of the bosonic gluonic operators on the same link are the

same as for the standard Hamiltonian formulation of lattice gauge theories:

$$\begin{aligned}
[L^a, L^b] &= 2if_{abc}L^c\,, \\
[R^a, R^b] &= 2if_{abc}R^c\,, \\
[L^a, R^b] &= [E, L^a] = [E, R^a] = 0\,, \\
[L^a, U^{ij}] &= -\lambda^a_{ik}U^{kj}\,, \\
[R^a, U^{ij}] &= U^{ik}\lambda^a_{kj}\,, \\
[E, U^{ij}] &= U^{ij}\,.
\end{aligned} \tag{3.6}$$

Operators on different links commute with each other. The f_{abc} are the structure constants. They contain the full information about the $\mathfrak{su}(N)$ Lie algebra and therefore the full local information about the $SU(N)$ Lie group.

The λ^a which appear in the commutation relations defined in eq. (3.6) are the N^2-1 $SU(N)$ Gell-Mann matrices. They are Hermitean generators of $SU(N)$ which obey the commutation relations

$$[\lambda^a, \lambda^b] = 2if_{abc}\lambda^c\,. \tag{3.7}$$

Since their components are addressed by two indices, their orthogonality is expressed by the scalar product

$$2\delta^{ab} = \lambda^{a*}_{ij}\lambda^b_{ij} = \mathrm{Tr}\,\lambda^a\lambda^b\,. \tag{3.8}$$

There are the $2(N^2-1)$ non-Abelian generators L^a and R^a, the Abelian generator E and the $2N^2$ generators of U. In total these are $4N^2-1$ generators which form the $\mathfrak{su}(2N)$ algebra. A concrete example is given in [13], eq. (2.12).

We again give up the commutativity of the link matrices to obtain Hermitean quantum link operators with a finite-dimensional Hilbert space per link. The link matrices associated with different links have to commute. Additionally we require

$$[U^{ij}_{xy}, U^{kl}_{xy}] = [U^{ij}_{xy}, (U^\dagger_{yx})^{kl}] = [(U^\dagger_{yx})^{ij}, (U^\dagger_{yx})^{kl}] = 0\,. \tag{3.9}$$

Now the operators of a $U(N)$ or an $SU(N)$ quantum link model are embedded in an $\mathfrak{su}(2N)$ algebra. It remains to define the commutation relations for

$$[U^{ij}_{xy}, (U^\dagger_{xy})^{kl}] = [U^{ij}_{xy}, U^{kl}_{yx}]\,. \tag{3.10}$$

These commutation relations In the next section we well see that

$$[U^{ij}_{xy}, (U^\dagger_{xy})^{kl}] = \frac{1}{2}\left(\delta^{il}\lambda^{a*}_{jk}R^a_{xy} - \delta^{jk}\lambda^a_{il}L^a_{xy} + \frac{4}{N}\delta^{il}\delta^{jk}E_{xy}\right) \tag{3.11}$$

is a sensible choice. It also means that the matrix U_{xy} of quantum link operators, in contrast to the link matrix in Wilson's formulation of lattice gauge theory, is no more a unitary object, since, according to eq. (3.11),

$$[U^{ij}_{xy}, (U^\dagger_{xy})^{ji}] = 2NE_{xy} \neq 0\,. \tag{3.12}$$

The Hamiltonian of a d-dimensional $U(N)$ or $SU(N)$ quantum link model with staggered fermions takes the form

$$\begin{aligned} H = & -t \sum_{\langle xy \rangle} (s_{xy} \psi_x^{i\dagger} U_{xy}^{ij} \psi_y^j + \text{H.c.}) + m \sum_x s_x \psi_x^{i\dagger} \psi_x^i \\ & + \frac{g^2}{2} \sum_{\langle xy \rangle} (L_{xy}^a L_{xy}^a + R_{xy}^a R_{xy}^a) + \frac{g'^2}{2} \sum_{\langle xy \rangle} E_{xy}^2 \\ & - \frac{1}{4g^2} \sum_{\langle wxyz \rangle} (\text{Tr}\, U_{wx} U_{xy} U_{yz} U_{zw} + \text{H.c.}) \\ & - \gamma \sum_{\langle xy \rangle} (\det U_{xy} + \text{H.c.}) \,. \end{aligned} \tag{3.13}$$

The sum $\sum_{\langle xy \rangle}$ has to be understood as a summation over all nearest-neighbor pairs of x and y, where $y = x + \hat{q}$ is separated from x in the direction $q \in \{1, 2, ..., d\}$ by one lattice spacing. The Hermitean conjugation in some terms of the Hamiltonian basically switches the role of x and y. The term proportional to m is a staggered mass term with a site-dependent sign-factor

$$s_x = (-1)^{x_1 + ... + x_d} \,. \tag{3.14}$$

The hopping term proportional to t has a link-dependent sign-factor s_{xy}, which for links in the 1-direction is simply $s_{x,x+\hat{1}} = 1$, while in the 2-direction it has the form $s_{x,x+\hat{2}} = (-1)^{x_1}$ and generally, for links in the q-direction, it obeys

$$s_{x,x+\hat{q}} = (-1)^{x_1 + ... + x_{q-1}} \,. \tag{3.15}$$

This factor is inherited from the staggered fermion formalism. From

$$\left(s_{xy} \psi_x^{i\dagger} U_{xy}^{ij} \psi_y^j \right)^\dagger = s_{xy} \psi_y^{j\dagger} U_{yx}^{ji} \psi_x^i \tag{3.16}$$

we expect that

$$s_{yx} = s_{xy} \tag{3.17}$$

and therefore also

$$s_{y,y-\hat{q}} = s_{y-\hat{q},y} = (-1)^{(y-\hat{q})_1 + ... + (y-\hat{q})_{q-1}} = (-1)^{y_1 + ... + y_{q-1}} \,. \tag{3.18}$$

The term proportional to the Abelian gauge coupling g'^2 contains the color-neutral Hermitean Abelian electric field operator E_{xy}, while the term proportional to the non-Abelian gauge coupling g^2 contains the Hermitean non-Abelian electric field operators L_{xy}^a and R_{xy}^a. The term inversely proportional to g^2 is the magnetic field energy. The sum $\sum_{\langle wxyz \rangle}$ goes over all lattice plaquettes with corners as shown in Figure 3.1. The Hamiltonian possesses a $U(N) = SU(N) \times U(1)$ gauge symmetry, which is explicitly broken down to $SU(N)$ by the term

$$\sum_{\langle xy \rangle} (\det U_{xy} + \text{H.c.}) = 2 \sum_{\langle xy \rangle} \Re(\det U_{xy}) \,. \tag{3.19}$$

Beside the Hamiltonian we have the infinitesimal generators of the $SU(N)$ gauge transformations

$$G_x^a = \psi_x^{i\dagger}\lambda_{ij}^a\psi_x^j + \sum_q \left(L_{x,x+\hat{q}}^a + R_{x-\hat{q},x}^a\right) , \tag{3.20}$$

where $\hat{q}$ is a unit-vector in the q-direction. We check, that the definition from above has the right commutation relations

$$\begin{aligned}
[G_x^a, G_y^b] &= \delta_{xy}[\psi_x^{i\dagger}\psi_x^j, \psi_x^{k\dagger}\psi_x^l]\lambda_{ij}^a\lambda_{kl}^b + \delta_{xy}\sum_q \left([L_{x,x+\hat{q}}^a, L_{x,x+\hat{q}}^b] + [R_{x-\hat{q},x}^a, R_{x-\hat{q},x}^b]\right) \\
&= \delta_{xy}\psi_x^{i\dagger}\psi_y^j[\lambda^a, \lambda^b]_{ij} + 2i\delta_{xy}f_{abc}\sum_q \left(L_{x,x+\hat{q}}^c + R_{x-\hat{q},x}^c\right) \\
&= 2i\delta_{xy}f_{abc}G_x^c \, .
\end{aligned} \tag{3.21}$$

The generators are Hermitean since the non-Abelian electric fields are Hermitean and for the fermionic part we explicitly check

$$\left(\lambda_{ij}^a\psi_x^{i\dagger}\psi_x^j\right)^\dagger = \lambda_{ij}^{a*}\psi_x^{j\dagger}\psi_x^i = \psi_x^{j\dagger}\lambda_{ji}^a\psi_x^i \, . \tag{3.22}$$

Since the gauge generators are Hermitean the operator

$$V = \prod_x \exp(i\alpha_x^a G_x^a) \tag{3.23}$$

is unitary and represents a general non-Abelian $SU(N)$ gauge transformation. Hence,

$$V^\dagger = \prod_x \exp(-i\alpha_x^a G_x^a) \, . \tag{3.24}$$

In the following, we use the Hadamard-Lemma

$$\begin{aligned}
Y' = V^\dagger Y V &= \exp(-i\sum_x \alpha_x^a G_x^a) Y \exp(i\sum_x \alpha_x^a G_x^a) \\
&= \mathrm{e}^X \, Y \, \mathrm{e}^{-X} \\
&= \sum_{m=0}^{\infty} \frac{1}{m!}[X, Y]_m \\
&= \sum_{m=0}^{\infty} \frac{1}{m!}[-i\sum_x \alpha_x^a G_x^a, Y]_m \, ,
\end{aligned} \tag{3.25}$$

where

$$\begin{aligned}
[X, Y]_m &= [X, [X, Y]_{m-1}] \, , \\
[X, Y]_0 &= Y \, .
\end{aligned} \tag{3.26}$$

Together with

$$\begin{aligned}
[G^a_x, \psi^i_y] &= \lambda^a_{jk}[\psi^{j\dagger}_x \psi^k_x, \psi^i_y] = -\delta_{xy}\lambda^a_{ij}\psi^j_y\,,\\
[G^a_x, \psi^{i\dagger}_y] &= \lambda^a_{jk}[\psi^{j\dagger}_x \psi^k_x, \psi^{i\dagger}_y] = \delta_{xy}\psi^{j\dagger}_y\lambda^a_{ji}\,,\\
[G^a_x, L^b_{y,y+\hat{q}}] &= \delta_{xy}[L^a_{y,y+\hat{q}}, L^b_{y,y+\hat{q}}] = \delta_{xy}2if_{abc}L^c_{y,y+\hat{q}} = \delta_{xy}2T^a_{bc}L^c_{y,y+\hat{q}}\,,\\
[G^a_x, R^b_{y-\hat{q},y}] &= \delta_{xy}[R^a_{y-\hat{q},y}, R^b_{y-\hat{q},y}] = \delta_{xy}2if_{abc}R^c_{y-\hat{q},y} = \delta_{xy}2T^a_{bc}R^c_{y-\hat{q},y}\,,\\
[G^a_x, E_{y,y+\hat{q}}] &= 0\,,\\
[G^a_x, U_{y,y+\hat{q}}] &= \delta_{xy}[L^a_{y,y+\hat{q}}, U_{y,y+\hat{q}}] + \delta_{x,y+\hat{q}}[R^a_{y,y+\hat{q}}, U_{y,y+\hat{q}}]\,,\\
&= -\delta_{xy}\lambda^a U_{y,y+\hat{q}} + \delta_{x,y+\hat{q}}U_{y,y+\hat{q}}\lambda^a\,,
\end{aligned} \tag{3.27}$$

where we used

$$T^a_{bc} = if_{abc} \tag{3.28}$$

in the adjoint representation, it follows that

$$\begin{aligned}
[-i\sum_x \alpha^a_x G^a_x, \psi^i_y]_m &= ((i\alpha^a_y\lambda^a)^m)_{ij}\psi^j_y\,,\\
[-i\sum_x \alpha^a_x G^a_x, \psi^{i\dagger}_y]_m &= \psi^{j\dagger}_y((-i\alpha^a_y\lambda^a)^m)_{ji}\,,\\
[-i\sum_x \alpha^d_x G^d_x, L^a_{y,y+\hat{q}}]_m &= \left(\left(2i\alpha^b_y T^b\right)^m\right)_{ac} L^c_{y,y+\hat{q}}\,,\\
[-i\sum_x \alpha^d_x G^d_x, R^a_{y-\hat{q},y}]_m &= \left(\left(2i\alpha^b_y T^b\right)^m\right)_{ac} R^c_{y-\hat{q},y}\,,\\
[-i\sum_x \alpha^a_x G^a_x, U^{i_0 j_0}_{y,y+\hat{q}}]_m &= \prod_{l=1}^{m}\left(i\alpha^{a_l}_y\lambda^{a_l}_{i_{l-1}i_l}\delta_{j_{l-1}j_l} - i\alpha^{a_l}_{y+\hat{q}}\delta_{i_l i_{l-1}}\lambda_{j_l j_{l-1}}\right)U^{i_m j_m}_{y,y+\hat{q}}\,,
\end{aligned} \tag{3.29}$$

and therefore the various operators and the U matrices transform as

$$\begin{aligned}
(\psi^i_x)' &= V^\dagger\psi^i_x V = \exp(i\alpha^a_x\lambda^a)_{ij}\psi^j_x\,,\\
(\psi^{i\dagger}_x)' &= V^\dagger\psi^{i\dagger}_x V = \psi^{j\dagger}_x\exp(-i\alpha^a_x\lambda^a)_{ji}\,,\\
(L^a_{x,x+\hat{q}})' &= V^\dagger L^a_{x,x+\hat{q}}V = \left(\exp(2i\alpha^b_x T^b)\right)_{ac} L^c_{x,x+\hat{q}}\,,\\
(R^a_{x-\hat{q},x})' &= V^\dagger R^a_{x-\hat{q},x}V = \left(\exp(2i\alpha^b_x T^b)\right)_{ac} R^c_{x-\hat{q},x}\,,\\
U'_{x,x+\hat{q}} &= V^\dagger U_{x,x+\hat{q}}V = \exp(i\alpha^a_x\lambda^a)U_{x,x+\hat{q}}\exp(-i\alpha^a_{x+\hat{q}}\lambda^a)
\end{aligned} \tag{3.30}$$

under $SU(N)$ gauge transformations. The Abelian electric $U(1)$ field E_{xy} transforms trivially.

For most terms, the non-Abelian $SU(N)$ gauge invariance of the Hamiltonian defined in eq. (3.13) is obvious (and hence $[G^a_x, H] = 0$). For the non-Abelian electric flux term we have e.g.

$$\begin{aligned}
L^a_{x,x+\hat{q}}{}' L^a_{x,x+\hat{q}}{}' &= \left(\exp(2i\alpha^b_x T^b)\right)_{ac} L^c_{x,x+\hat{q}}\left(\exp(2i\alpha^d_x T^d)\right)_{ae} L^e_{x,x+\hat{q}}\\
&= \left(\exp(-2i\alpha^b_x T^b)\right)_{ca}\left(\exp(2i\alpha^d_x T^d)\right)_{ae} L^c_{x,x+\hat{q}}L^e_{x,x+\hat{q}}\\
&= L^a_{x,x+\hat{q}}L^a_{x,x+\hat{q}}\,.
\end{aligned} \tag{3.31}$$

For the determinant we have

$$[G_x^a, \det U_{yz}] = \delta_{xy}[L_{yz}^a, \det U_{yz}] + \delta_{xz}[R_{yz}^a, \det U_{yz}]\,. \tag{3.32}$$

We now explicitly evaluate

$$\begin{aligned}
[L^a, \det U] &= \epsilon_{j_1 j_2 \cdots j_N} \left(L^a U^{1j_1} U^{2j_2} \cdots U^{Nj_N} - U^{1j_1} U^{2j_2} \cdots U^{Nj_N} L^a \right) \\
&= \epsilon_{j_1 j_2 \cdots j_N} \left(\left(-\lambda^a_{1i_1} U^{i_1 j_1} + U^{1j_1} L^a \right) U^{2j_2} \cdots U^{Nj_N} - U^{1j_1} U^{2j_2} \cdots U^{Nj_N} L^a \right) \\
&= -\epsilon_{j_1 j_2 \cdots j_N} \sum_{k=1}^{N} U^{1j_1} \cdots U^{(k-1)j_{k-1}} \lambda_{ki_k} U^{i_k j_k} U^{(k+1)j_{k+1}} \cdots U^{Nj_N} \\
&\overset{*}{=} -\epsilon_{j_1 j_2 \cdots j_N} \sum_{k=1}^{N} U^{1j_1} \cdots U^{(k-1)j_{k-1}} \lambda_{kk} U^{kj_k} U^{(k+1)j_{k+1}} \cdots U^{Nj_N} \\
&= -\det U \, \mathrm{Tr}\, \lambda \\
&= 0\,.
\end{aligned} \tag{3.33}$$

In the step $(*)$ we used, that for $i_k \neq k$, $U^{i_k j_{i_k}}$ and $U^{i_k j_k}$ are symmetric in the coefficients j_{i_k} and j_k. Therefore, the contraction with the total antisymmetric epsilon tensor vanishes. With an analogous calculation we obtain

$$[R^a, \det U] = 0\,. \tag{3.34}$$

Hence, the Hamiltonian in eq. (3.13) is gauge invariant for all choices of parameters.

The infinitesimal generators of the $U(1)$ gauge symmetry

$$G_x = \psi_x^{i\dagger} \psi_x^i - \frac{N}{2} - \sum_q (E_{x,x+\hat{q}} - E_{x-\hat{q},x}) \tag{3.35}$$

are obviously Hermitean. The term $-N/2$ accounts for the filled Dirac sea of staggered fermions. The Abelian generators commute with the non-Abelian one

$$[G_x, G_y^a] = \lambda_{jk}^a [\psi_x^{i\dagger} \psi_x^i, \psi_y^{j\dagger} \psi_y^k] = 0\,. \tag{3.36}$$

To calculate, how the operator

$$W = \prod_x \exp(i\alpha_x G_x) \tag{3.37}$$

which in Hilbert space is unitary and represents a general Abelian $U(1)$ gauge transformation acts on the field operators we again use the Hadamard-Lemma

$$\begin{aligned}
Y' = W^\dagger Y W &= \exp(-i \sum_x \alpha_x G_x) Y \exp(i \sum_x \alpha_x G_x) \\
&= \sum_m [-i \sum_x \alpha_x G_x, Y]_m\,.
\end{aligned} \tag{3.38}$$

Together with

$$\begin{aligned}
[G_x, \psi_y^i] &= [\psi_x^{j\dagger}\psi_x^j, \psi_y^i] = -\delta_{xy}\psi_y^i\,, \\
[G_x, \psi_y^{i\dagger}] &= [\psi_x^{j\dagger}\psi_x^j, \psi_y^{i\dagger}] = \delta_{xy}\psi_y^{i\dagger}\,, \\
[G_x, L^a_{y,y+\hat{q}}] &= [G_x, R^a_{y,y+\hat{q}}] = [G_x, E_{y,y+\hat{q}}] = 0\,, \\
[G_x, U_{y,y+\hat{q}}]^{ij} &= -(\delta_{xy} - \delta_{x,y+\hat{q}})[E_{y,y+\hat{q}}, U_{y,y+\hat{q}}]^{ij}\,, \\
&= (\delta_{x,y+\hat{q}} - \delta_{xy})U^{ij}_{y,y+\hat{q}}\,,
\end{aligned} \tag{3.39}$$

it follows that

$$\begin{aligned}
[-i\sum_x \alpha_x G_x, \psi_y^i]_m &= (i\alpha_y)^m \psi_y^i\,, \\
[-i\sum_x \alpha_x G_x, \psi_y^{i\dagger}]_m &= \psi_y^{i\dagger}(-i\alpha_y)^m\,, \\
[-i\sum_x \alpha_x G_x, U_{y,y+\hat{q}}]^{ij}_m &= (i\alpha_y - i\alpha_{y+\hat{q}})^m\, U^{ij}_{y,y+\hat{q}}\,,
\end{aligned} \tag{3.40}$$

and therefore the various operators transform as

$$\begin{aligned}
\psi_x^{i\,\prime} &= W^\dagger \psi_x^i W = \exp(i\alpha_x)\psi_x^i\,, \\
\psi_x^{i\dagger\prime} &= W^\dagger \psi_x^{i\dagger} W = \psi_x^{i\dagger}\exp(-i\alpha_x)\,, \\
(U'_{x,x+\hat{q}})^{ij} &= (W^\dagger U_{x,x+\hat{q}} W)^{ij} = \exp(i\alpha_x)U^{ij}_{x,x+\hat{q}}\exp(-i\alpha_{x+\hat{q}})
\end{aligned} \tag{3.41}$$

under $U(1)$ gauge transformations. The electric Abelian and non-Abelian fields E_{xy}, L^a_{xy}, and R^a_{xy} transform trivially. For $\gamma = 0$, the Hamiltonian in eq. (3.13) is obviously invariant under Abelian $U(1)$ gauge transformations

$$[H, G_x] = 0\,. \tag{3.42}$$

The determinant term in the Hamiltonian will be zero for some representations. For a representation with a non-zero determinant term, if we choose $\gamma > 0$, this forces the gauge symmetry from $U(N) = SU(N)\times U(1)$ to $SU(N)$. The $U(1)$ gauge generator don't commute with the Hamiltonian in that case. Indeed, if we have a representation with non-zero determinant,

$$[G_x, \det U_{yz}] = (\delta_{xy} - \delta_{xz})\,[E_{yz}, \det U_{yz}] \tag{3.43}$$

is not zero, since

$$\begin{aligned}
[E, \det U] &= \epsilon_{j_1 j_2 \cdots j_N}\left(EU^{1j_1}U^{2j_2}\cdots U^{Nj_N} - U^{1j_1}U^{2j_2}\cdots U^{Nj_N}E\right) \\
&= \epsilon_{j_1 j_2 \cdots j_N}\left(U^{1j_1}\,(1+E)\,U^{2j_2}\cdots U^{Nj_N} - U^{1j_1}U^{2j_2}\cdots U^{Nj_N}E\right) \\
&= N\det U\,.
\end{aligned} \tag{3.44}$$

In other words, if we have a representation with non-zero determinant term, and if we choose $\gamma \neq 0$, we won't apply the $U(1)$ Gauss law, and we obtain a $SU(N)$ model. If the

representation has a vanishing determinant, or if we choose $\gamma = 0$, we obtain a $U(1)$ gauge symmetry and we apply the $U(1)$ Gauss law

$$G_x|\Psi\rangle = 0\,. \tag{3.45}$$

The baryon number generator

$$B = \sum_x \left(\psi_x^{i\dagger}\psi_x^i - \frac{N}{2}\right) \tag{3.46}$$

commutes with the Hamiltonian and therefore generates a global $U(1)_B$ baryon number symmetry in the $SU(N)$ model. In the $U(N)$ model, the additional Gauss law $G_x|\Psi\rangle = 0$ excludes baryons, since

$$B|\Psi\rangle = \sum_x G_x|\Psi\rangle = 0 \tag{3.47}$$

for all physical states. Again, the term $-N/2$ in eq. (3.46) accounts for the filled Dirac sea of staggered fermions.

Physical states $|\Psi\rangle$ obey the $SU(N)$ Gauss law

$$G_x^a|\Psi\rangle = 0\,. \tag{3.48}$$

In a $U(N)$ gauge theory they also obey the $U(1)$ Gauss law

$$G_x|\Psi\rangle = 0\,, \tag{3.49}$$

which eliminates baryons from the physical states.

Next, we discuss the global symmetries of the Hamiltonian in eq. (3.13). The Hamiltonian is symmetric under a shift S_q by one lattice spacing in the direction q

$$\begin{aligned}
{}^{S_q}\psi_x^i &= (-1)^{x_{q+1}+\cdots+x_d}\psi_{x+\hat{q}}^i\,,\\
{}^{S_q}U_{x,x+\hat{r}}^{ij} &= U_{x+\hat{q},x+\hat{q}+\hat{r}}^{ij}\,,\\
{}^{S_q}L_{x,x+\hat{r}}^{a} &= L_{x+\hat{q},x+\hat{q}+\hat{r}}^{a}\,,\\
{}^{S_q}R_{x,x+\hat{r}}^{a} &= R_{x+\hat{q},x+\hat{q}+\hat{r}}^{a}\,,\\
{}^{S_q}E_{x,x+\hat{r}} &= E_{x+\hat{q},x+\hat{q}+\hat{r}}\,.
\end{aligned} \tag{3.50}$$

The sign-factor for shifted fermions accounts for the sign-factor s_{xy} of the hopping term in the Hamiltonian

$$\begin{aligned}
{}^{S_q}\left(s_{x,x+\hat{r}}\psi_x^{i\dagger}U_{x,x+\hat{r}}^{ij}\psi_{x+\hat{r}}^j\right) &= \mathrm{sign}(q-r+1/2)s_{x,x+\hat{r}}\psi_{x+\hat{q}}^{i\dagger}U_{x+\hat{q},x+\hat{q}+\hat{r}}^{ij}\psi_{x+\hat{q}+\hat{r}}^j\\
&= s_{x+\hat{q},x+\hat{q}+\hat{r}}\psi_{x+\hat{q}}^{i\dagger}U_{x+\hat{q},x+\hat{q}+\hat{r}}^{ij}\psi_{x+\hat{q}+\hat{r}}^j\,.
\end{aligned} \tag{3.51}$$

An important exception is the mass term, which breaks this symmetry explicitly, since $s_x = -s_{x+\hat{q}}$. However, the mass term and therefore the whole Hamiltonian commutes for

an even number of shifts in one direction. Therefore, this corresponds to the ordinary translation symmetry. The associated momentum takes values

$$p_q \in \left]-\frac{\pi}{2a}, \frac{\pi}{2a}\right] , \tag{3.52}$$

where a is the lattice spacing. The gauge transformations transform appropriately under shifts by one lattice spacing

$$\begin{aligned} {}^{S_q}G^a_x &= G^a_{x+\hat{q}} \,, \\ {}^{S_q}G_x &= G_{x+\hat{q}} \,. \end{aligned} \tag{3.53}$$

Staggered fermions mix spinor and space-time indices. This distributes quark degrees of freedom on the lattice. For a staggered mass term $|m| \gg t, g^2, (g')^2, 1/g^2, \gamma$ configurations with a staggered fermion number $\psi^{i\dagger}_x \psi^i_x$ are favored. As an example for large positive m, fermions would prefer to sit at sites with an odd value of $x_1 + x_2 + \ldots + x_d$. Let's call this state $|\Psi_{+m}\rangle$. This state is not invariant under the shift symmetry S_q. For large negative m, the fermions would prefer to sit at sites with an even value of $x_1 + x_2 + \ldots + x_d$. We call this state $|\Psi_{-m}\rangle$. However,

$$\begin{aligned} {}^{S_q}|\Psi_{+m}\rangle &= |\Psi_{-m}\rangle \,, \\ {}^{S_q}|\Psi_{-m}\rangle &= |\Psi_{+m}\rangle \,. \end{aligned} \tag{3.54}$$

A concrete example in one dimension will be discussed in section 3.5.

One could imagine that for $m = 0$ and a suitable choice for the remaining Hamiltonian parameters, the shift symmetry breaks spontaneously. The two possible cartoon states would consist of an additive superposition

$$|\Psi_s\rangle = \frac{1}{\sqrt{2}} \left(|\Psi_{+m}\rangle + |\Psi_{-m}\rangle\right) \tag{3.55}$$

with

$${}^{S_q}|\Psi_s\rangle = |\Psi_s\rangle \tag{3.56}$$

and a negative superposition

$$|\Psi_a\rangle = \frac{1}{\sqrt{2}} \left(|\Psi_{+m}\rangle - |\Psi_{-m}\rangle\right) \tag{3.57}$$

with

$${}^{S_q}|\Psi_a\rangle = -|\Psi_a\rangle \,. \tag{3.58}$$

Hence, a single shift in one of the directions q corresponds to the $\mathbb{Z}(2)$ chiral symmetry. In one dimension, this is the only symmetry associated with the shift operator beside the ordinary translations. In more than one dimension, there are more discrete symmetry transformations associated with simultaneous shifts by one lattice spacing. An even number of shifts by one lattice spacing in different directions correspond to flavor transformations. An odd number of shifts in different directions can be decomposed into flavor

transformations and the $\mathbb{Z}(2)$ chiral transformation. Hence, there is a $\mathbb{Z}(2)^{d-1}$ flavor symmetry.

Another symmetry is the charge conjugation C_q which is combined with a shift in the q-direction

$$\begin{aligned}
{}^{C_q}\psi^i_x &= (-1)^{x_1+\ldots+x_q}\psi^{i\dagger}_{x+\hat{q}}\,,\\
{}^{C_q}U^{ij}_{x,x+\hat{r}} &= U^{ij\dagger}_{x+\hat{q},x+\hat{q}+\hat{r}}\,,\\
{}^{C_q}L^a_{x,x+\hat{r}} &= -L^{a*}_{x+\hat{q},x+\hat{q}+\hat{r}}\,,\\
{}^{C_q}R^a_{x,x+\hat{r}} &= -R^{a*}_{x+\hat{q},x+\hat{q}+\hat{r}}\,,\\
{}^{C_q}E_{x,x+\hat{r}} &= -E_{x+\hat{q},x+\hat{q}+\hat{r}}\,.
\end{aligned} \tag{3.59}$$

Again, the sign-factor for the charge conjugated fermion is matched to the sign-factor of the hopping term

$$\begin{aligned}
{}^{C_q}\left(s_{x,x+\hat{r}}\psi^{i\dagger}_x U^{ij}_{x,x+\hat{r}}\psi^j_{x+\hat{r}}\right) &= -\operatorname{sign}(q-r+1/2)s_{x,x+\hat{r}}\psi^i_{x+\hat{q}}U^{ij\dagger}_{x+\hat{q},x+\hat{q}+\hat{r}}\psi^{j\dagger}_{x+\hat{q}+\hat{r}}\\
&= \left(s_{x+\hat{q},x+\hat{q}+\hat{r}}\psi^{i\dagger}_{x+\hat{q}}U^{ij}_{x+\hat{q},x+\hat{q}+\hat{r}}\psi^j_{x+\hat{q}+\hat{r}}\right)^\dagger
\end{aligned} \tag{3.60}$$

The Hamiltonian is invariant under charge conjugation. The mass term remains unbroken

$${}^{C_q}\left(s_x\psi^{i\dagger}_x\psi^i_x\right) = -s_{x+\hat{q}}\left(N-\psi^{i\dagger}_{x+\hat{q}}\psi^i_{x+\hat{q}}\right) = s_{x+\hat{q}}\psi^{i\dagger}_{x+\hat{q}}\psi^i_{x+\hat{q}}\,. \tag{3.61}$$

Due to the complex conjugation involved for the non-Abelian fields $L^a_{x,x+\hat{l}}$ and $R^a_{x,x+\hat{l}}$, the charge conjugation is a symmetry only for real or pseudo-real representations. Then, e.g.

$$\begin{aligned}
{}^{C_q}\left(L^a_{x,x+\hat{r}}L^a_{x,x+\hat{r}}\right) &= SL^a_{x+\hat{q},x+\hat{q}+\hat{r}}S^{-1}SL^a_{x+\hat{q},x+\hat{q}+\hat{r}}S^{-1}\\
&= L^a_{x+\hat{q},x+\hat{q}+\hat{r}}L^a_{x+\hat{q},x+\hat{q}+\hat{r}}
\end{aligned} \tag{3.62}$$

with a suitable unitary transformation S. This amounts to a non-chiral representation of the embedding algebra $\mathfrak{su}(2N)$. The charge conjugated gauge generators are

$$\begin{aligned}
{}^{C_q}G^a_x &= \lambda^{a*}_{ji}\left(\delta^{ij}-\psi^{j\dagger}_{x+\hat{q}}\psi^i_{x+\hat{q}}\right)-\sum_r\left(L^{a*}_{x+\hat{q},x+\hat{q}+\hat{r}}+R^{a*}_{x+\hat{q}-\hat{r},x+\hat{q}}\right)\\
&= -G^{a*}_{x+\hat{q}}
\end{aligned} \tag{3.63}$$

and

$$\begin{aligned}
{}^{C_q}G_x &= \left(N-\psi^{i\dagger}_{x+\hat{q}}\psi^i_{x+\hat{q}}-\frac{N}{2}\right)+\sum_r\left(E_{x+\hat{q},x+\hat{q}+\hat{r}}-E_{x+\hat{q}-\hat{r},x+\hat{q}}\right)\\
&= -G_{x+\hat{q}}\,.
\end{aligned} \tag{3.64}$$

Hence, gauge invariant states remain gauge invariant under charge conjugation. As for the shift symmetry, an even number of charge conjugations C_q in one direction results in an ordinary translation up to a minus-sign for the fermions.

The last symmetry we note is the parity symmetry P with

$$\begin{aligned} {}^P\psi^i_x &= \psi^i_{-x}\,, \\ {}^P U^{ij}_{x,x+\hat{q}} &= U^{ji\dagger}_{-x-\hat{q},-x}\,, \\ {}^P L^a_{x,x+\hat{k}} &= R^a_{-x-\hat{q},-x}\,, \\ {}^P R^a_{x-\hat{q},x} &= L^a_{-x,-x+\hat{q}}\,, \\ {}^P E_{x,x+\hat{q}} &= -E_{-x-\hat{q},-x}\,. \end{aligned} \tag{3.65}$$

The hopping term transforms as

$$\begin{aligned} {}^P\left(s_{x,x+\hat{q}}\psi^{i\dagger}_x U^{ij}_{x,x+\hat{q}}\psi^j_{x+\hat{q}}\right) &= s_{x,x+\hat{q}}\psi^{i\dagger}_{-x}U^{ji\dagger}_{-x-\hat{q},-x}\psi^j_{-x-\hat{q}} \\ &= \left(s_{-x-\hat{q},-x}\psi^{j\dagger}_{-x-\hat{q}}U^{ji}_{-x-\hat{q},-x}\psi^i_{-x}\right)^\dagger . \end{aligned} \tag{3.66}$$

The invariance of the determinant term follows from $\det A^T = \det A$. And the parity transformations of the gauge generators are

$${}^P G^a_x = \psi^{i\dagger}_{-x}\lambda^a_{ij}\psi^j_{-x} + \sum_q \left(R^a_{-x-\hat{q},-x} + L^a_{-x,-x+\hat{q}}\right) = G^a_{-x}\,, \tag{3.67}$$

and

$${}^P G_x = \psi^{i\dagger}_{-x}\psi^i_{-x} - \sum_q \left(-E_{-x-\hat{q},-x} + E_{-x,-x+\hat{q}}\right) = G_{-x}\,. \tag{3.68}$$

The fermion anti-commutation relations in eq. (3.1) remain valid under all symmetry transformations.

3.2. Representing quantum links with rishons

While the quantum spin of the implementation of the $U(1)$ quantum link model in the first chapter of this thesis was realized by Schwinger bosons, remarkably, the non-Abelian gluon (link) fields of the $U(N)$ and the $SU(N)$ model can be represented by fermionic degrees of freedom. In [13] they are called rishons.

Rishons lead to a reformulation of the gauge field operators with interesting insights and serve as an intermediate step to find suitable representations for numerical simulations and for quantum simulations.

The algebraic structure described in the previous section remains unchanged. The description of the rishons can be restricted to a single link, since the Hilbert space is a direct product of the $\mathfrak{su}(2N)$ representations on each link and the (bosonic) generators of different links commute.

Rishons live at the two ends of a link. The notation introduced in [13] assigns them to creation and annihilation operators $c^{i\dagger}_{x,\pm q}$, $c^j_{x,\pm q}$ by specifying a site x and the corresponding

link in direction $+q$ or $-q$. Again, $i, j \in \{1, 2, \ldots, N\}$ are the non-Abelian color indices of the quarks (the fermions described by the creation and annihilation operators $\psi_x^{i\dagger}$, ψ_x^i).

The fermionic rishons also obey the usual anti-commutation relations

$$\begin{aligned} \{c^i_{x,\pm q}, c^{j\dagger}_{y,\pm r}\} &= \delta_{xy}\delta_{\pm q,\pm r}\delta_{ij}\,, \\ \{c^i_{x,\pm q}, c^{j}_{y,\pm r}\} &= \{c^{i\dagger}_{x,\pm q}, c^{j\dagger}_{y,\pm r}\} = 0\,, \end{aligned} \tag{3.69}$$

and they also *anti*-commute with the quarks

$$\{c^{i(\dagger)}_{x,\pm q}, \psi^{j(\dagger)}_y\} = 0\,. \tag{3.70}$$

One now can write the bosonic gluonic operators as

$$\begin{aligned} L^a_{x,x+\hat{q}} &= c^{i\dagger}_{x,+q}\lambda^a_{ij}c^j_{x,+q}\,, \\ R^a_{x-\hat{q},x} &= c^{i\dagger}_{x,-q}\lambda^a_{ij}c^j_{x,-q}\,, \\ E_{x,x+\hat{q}} &= \frac{1}{2}\left(c^{i\dagger}_{x+\hat{q},-q}c^i_{x+\hat{q},-q} - c^{i\dagger}_{x,+q}c^i_{x,+q}\right)\,, \\ U^{ij}_{x,x+\hat{q}} &= c^i_{x,+q}c^{j\dagger}_{x+\hat{q},-q} (= -c^{j\dagger}_{x+\hat{q},-q}c^i_{x,+q})\,. \end{aligned} \tag{3.71}$$

The action of the link operator U on a rishon configuration is shown in Figure 3.2. Since the rishons are fermionic, their relative order is important and can lead to minus signs.

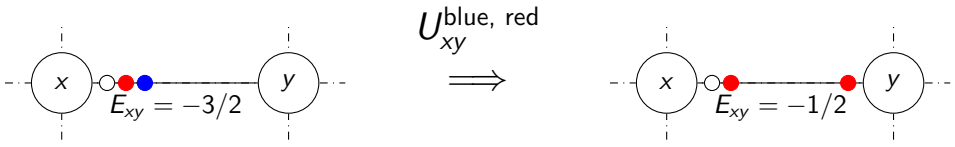

Figure 3.2.: *Action of the link operator U in a model with $N = 3$ rishons on the link. The rishons are represented by white, red, and blue beads.*

As required, the Abelian electric field operator is obviously Hermitean. We check the Hermiticity of the non-Abelian electric field operators

$$\begin{aligned} \left(L^a_{x,x+\hat{q}}\right)^\dagger &= c^{j\dagger}_{x,+q}\lambda^{a*}_{ij}c^i_{x,+q} = L^a_{x,x+\hat{q}}\,, \\ \left(R^a_{x-\hat{q},x}\right)^\dagger &= c^{j\dagger}_{x,-q}\lambda^{a*}_{ij}c^i_{x,-q} = R^a_{x-\hat{q},x}\,. \end{aligned} \tag{3.72}$$

Using $x = w - \hat{q}$ we obtain the identities for the link operators

$$\begin{aligned} L^a_{wx} = L_{w,w+(-\hat{q})} &= c^{i\dagger}_{w,-q}\lambda^a_{ij}c^j_{w,-q} = R^a_{xw}\,, \\ E_{wx} = E_{w,w+(-\hat{q})} &= \frac{1}{2}\left(c^{i\dagger}_{x,-(-q)}c^i_{x,-(-q)} - c^{i\dagger}_{w,-q}c^i_{w,-q}\right) = -E_{xw}\,, \\ (U^\dagger_{wx})^{ij} = U^{ji\dagger}_{wx} = U^{ji\dagger}_{w,w+(-\hat{q})} &= \left(c^j_{w,-q}c^{i\dagger}_{x,-(-q)}\right)^\dagger = U^{ij}_{xw}\,, \end{aligned} \tag{3.73}$$

in agreement with, e.g., Figure 3.1.

All gluonic link operators defined in eq. (3.71) create a rishon for each destroyed one. So they conserve the number of rishons on each individual link. The corresponding rishon number operator is

$$\mathcal{N}_{x,x+\hat{q}} = c^{i\dagger}_{x+\hat{q},-q} c^{i}_{x+\hat{q},-q} + c^{i\dagger}_{x,+q} c^{i}_{x,+q} \,, \tag{3.74}$$

obeying

$$\mathcal{N}_{wx} = \mathcal{N}_{w,w+(-\hat{q})} = c^{i\dagger}_{x,-(-q)} c^{i}_{x,-(-q)} + c^{i\dagger}_{w,-q} c^{i}_{w,-q} = \mathcal{N}_{xw} \,. \tag{3.75}$$

Since this operator also commutes with the quark operators, the rishon number is conserved by the Hamiltonian

$$[H, \mathcal{N}_{xy}] = 0 \,. \tag{3.76}$$

The same arguments hold for the gauge generators

$$\begin{aligned} [G^a_x, \mathcal{N}_{yz}] &= 0 \,, \\ [G_x, \mathcal{N}_{yz}] &= 0 \,. \end{aligned} \tag{3.77}$$

An important consequence of this is that we can study a system in sectors of rishon numbers individually fixed per link. A fixed rishon number on a link corresponds to the choice of an irreducible representation of $\mathfrak{su}(2N)$ on this link.

The definitions in eq. (3.71) fulfill the commutation relations on a link given in eq. (3.6). Using

$$\begin{aligned} [c^{i_1\dagger}_{x_1,\pm q_1} c^{i_2}_{x_2,\pm q_2}, c^{i_3\dagger}_{x_3,\pm q_3} c^{i_4}_{x_4,\pm q_4}] &= \delta_{x_2 x_3} \delta_{\pm q_2, \pm q_3} \delta^{i_2 i_3} c^{i_1\dagger}_{x_1,\pm q_1} c^{i_4}_{x_4,\pm q_4} \\ &\quad - \delta_{x_1 x_4} \delta_{\pm q_1, \pm q_4} \delta^{i_1 i_4} c^{i_3\dagger}_{x_3,\pm q_3} c^{i_2}_{x_2,\pm q_2} \,, \\ [c^{i\dagger}_{x,q} c^{i}_{x,q}, c^{j_1\dagger}_{y_1,\pm r_1} c^{j_2}_{y_2,\pm r_2}] &= \left(\delta_{xy_1} \delta_{q,\pm r_1} - \delta_{xy_2} \delta_{q,\pm r_2}\right) c^{j_1\dagger}_{y_1,\pm r_1} c^{j_2}_{y_2,\pm r_2} \,, \\ [c^{i\dagger}_{x,q} c^{i}_{x,q}, c^{j_1\dagger}_{y,r} c^{j_2}_{y,r}] &= 0 \end{aligned} \tag{3.78}$$

and assuming $q, r > 0$, we obtain, e.g.,

$$\begin{aligned}
[L^a_{x,x+\hat{q}}, L^b_{y,y+\hat{r}}] &= \delta_{xy}\delta_{qr}\lambda^a_{i_1 i_2}\lambda^b_{i_3 i_4}\left(\delta^{i_2 i_3} c^{i_1\dagger}_{x,+q} c^{i_4}_{x,+q} - \delta^{i_1 i_4} c^{i_3\dagger}_{x,+q} c^{i_2}_{x,+q}\right) \\
&= \delta_{xy}\delta_{qr}[\lambda^a, \lambda^b]_{j_1 j_2} c^{j_1\dagger}_{x,+q} c^{j_2}_{x,+q} \\
&= \delta_{xy}\delta_{qr} 2i f_{abc} L^c_{x,x+\hat{q}}\,, \\
[L^a_{x,x+\hat{q}}, R^b_{y-\hat{r},y}] &= \lambda^a_{ij}\lambda^b_{kl}[c^{i\dagger}_{x,+q} c^j_{x,+q}, c^{k\dagger}_{y,-r} c^l_{y,-r}] \\
&= 0\,, \\
[E_{x,x+\hat{q}}, L^a_{y,y+\hat{r}}] &= -\frac{1}{2}\lambda^a_{j_1 j_2}[c^{i\dagger}_{x,+q} c^i_{x,+q}, c^{j_1\dagger}_{y,+r} c^{j_2}_{y,+r}] \\
&= 0\,, \\
[L^a_{x,x+\hat{q}}, U^{ij}_{y,y+\hat{r}}] &= -\lambda^a_{lk}\left[c^{l\dagger}_{x,+q} c^k_{x,+q}, c^{j\dagger}_{y+\hat{r},-r} c^i_{y,+r}\right] \\
&= \lambda^a_{lk}\delta_{xy}\delta_{qr}\delta_{il} c^{j\dagger}_{y+\hat{r},-r} c^k_{x,+q} \\
&= -\delta_{xy}\delta_{qr}\lambda^a_{ik} U^{kj}_{x,x+\hat{q}}\,, \\
[E_{x,x+\hat{q}}, U^{ij}_{y,y+\hat{r}}] &= -\frac{1}{2}[c^{k\dagger}_{x+\hat{q},-q} c^k_{x+\hat{q},-q} - c^{k\dagger}_{x,+q} c^k_{x,+q}, c^{j\dagger}_{y+\hat{r},-r} c^i_{y,+r}] \\
&= -\frac{1}{2}\delta_{xy}\delta_{qr}\left(\delta^{kj} c^{k\dagger}_{x+\hat{q},-q} c^i_{y,+r} + \delta^{ki} c^{j\dagger}_{y+\hat{r},-r} c^k_{x,+q}\right) \\
&= \delta_{xy}\delta_{qr} U^{ij}_{x,x+\hat{q}}\,,
\end{aligned} \tag{3.79}$$

and the commutation relations of the quantum link operator U given in eq. (3.9),

$$\begin{aligned}
[U^{ij}_{x,x+\hat{q}}, (U^\dagger_{y,y+\hat{r}})^{kl}] &= [U^{ij}_{x,x+\hat{q}}, U^{kl}_{y+\hat{r},y}] \\
&= [c^{j\dagger}_{x+\hat{q},-q} c^i_{x,+q}, c^{l\dagger}_{y,+r} c^k_{y+\hat{r},-r}] \\
&= \delta_{xy}\delta_{qr}\left(\delta^{il} c^{j\dagger}_{x+\hat{q},-q} c^k_{x+\hat{q},-q} - \delta^{jk} c^{l\dagger}_{x,+q} c^i_{x,+q}\right)\,.
\end{aligned} \tag{3.80}$$

The last term accounts for the non-commuting cases

$$[U^{ij}_{xy}, (U^\dagger_{xy})^{kl}] = [U^{ij}_{xy}, U^{kl}_{yx}] \tag{3.81}$$

and it is zero for operators assigned to different links. We would like to express this term by linear combinations of electric field operators, since they consist of rishon creation and annihilation of the form $c^{i\dagger}_{x,s} c^j_{x,s}$ too. There are N^2 of these operators, while we have N^2-1 generators λ_a. Therefore, we include the traceful $U(N)$ generator

$$\begin{aligned}
\lambda^0_{ij} &\doteq \delta_{ij}\sqrt{\frac{2}{N}}\,, \\
\operatorname{Tr}\lambda^0 &= \sqrt{2N}\,.
\end{aligned} \tag{3.82}$$

It is orthogonal to all the Gell-Mann matrices λ^a and it fulfills

$$\operatorname{Tr}\lambda^\alpha\lambda^\beta = \lambda^\alpha_{ij}\lambda^\beta_{ji} = 2\delta^{\alpha\beta} \tag{3.83}$$

where $\alpha \in \{0, 1, ..., N^2 - 1\}$ now addresses all the N^2 linearly independent Hermitean matrices. To relate eq. (3.80) with eq. (3.11) it has to be contracted in a sensible way. We first use our notation to write

$$\begin{aligned} L^0_{x,x+\hat{q}} &= c^{i\dagger}_{x,+q}\lambda^0_{ij}c^j_{x,+q} = \sqrt{\frac{2}{N}}c^{i\dagger}_{x,+q}c^i_{x,+q}\,, \\ R^0_{x-\hat{q},x} &= c^{i\dagger}_{x,-q}\lambda^0_{ij}c^j_{x,-q} = \sqrt{\frac{2}{N}}c^{i\dagger}_{x,-q}c^i_{x,-q} \end{aligned} \tag{3.84}$$

to get

$$R^0_{x,x+\hat{q}} - L^0_{x,x+\hat{q}} = 2\sqrt{\frac{2}{N}}E_{x,x+\hat{q}}\,, \tag{3.85}$$

and then derive

$$\begin{aligned} \lambda^\alpha_{li}\lambda^\beta_{jk}[U^{ij}_{xy}, (U^\dagger_{xy})^{kl}] &= \sqrt{2N}\left(\delta^{\alpha 0}R^\beta_{xy} - \delta^{\beta 0}L^\alpha_{xy}\right) \\ &= \sqrt{2N}\left(\delta^{\alpha 0}\delta^{\beta a}R^a_{xy} - \delta^{\beta 0}\delta^{\alpha a}L^a_{xy} + \delta^{\alpha 0}\delta^{\beta 0}\left(R^0_{xy} - L^0_{xy}\right)\right) \\ &= \sqrt{2N}\left(\delta^{\alpha 0}\delta^{\beta a}R^a_{xy} - \delta^{\beta 0}\delta^{\alpha a}L^a_{xy}\right) + 4\delta^{\alpha 0}\delta^{\beta 0}E_{xy} \\ &= \lambda^\alpha_{li}\lambda^\beta_{jk}\frac{1}{2}\left(\delta^{il}\lambda^{a*}_{jk}R^a_{xy} - \delta^{jk}\lambda^a_{il}L^a_{xy} + \frac{4}{N}\delta^{il}\delta^{jk}E_{xy}\right). \end{aligned} \tag{3.86}$$

This indeed agrees with eq. (3.11). There seems to be a misprint in the prefactor we published. It has no consequences, since the result of $[U, U^\dagger]$ seems to be never used in any further derivations. However, let's perform some very explicit checks

$$[U^{ij}_{x,x+\hat{q}}, (U^\dagger_{x,x+\hat{q}})^{ji}] = \delta^{ii}c^{j\dagger}_{x+\hat{q},-q}c^j_{x+\hat{q},-q} - \delta^{jj}c^{i\dagger}_{x,+q}\delta^{jj}c^i_{x,+q} = 2NE_{x,x+\hat{q}} \tag{3.87}$$

in agreement with eq. (3.12), and

$$\lambda^b_{jk}[U^{ij}_{x,x+\hat{q}}, (U^\dagger_{x,x+\hat{q}})^{ki}] = \lambda^b_{jk}\delta^{ii}c^{j\dagger}_{x+\hat{q},-q}c^k_{x+\hat{q},-q} - \lambda^b_{jk}\delta^{jk}c^{i\dagger}_{x,+q}\delta^{jj}c^i_{x,+q} = NR^b_{x,x+\hat{q}} \tag{3.88}$$

agrees with

$$\delta^{il}\lambda^b_{jk}\frac{1}{2}\left(\delta^{il}\lambda^{a*}_{jk}R^a_{xy} - \delta^{jk}\lambda^a_{il}L^a_{xy} + \frac{4}{N}\delta^{il}\delta^{jk}E_{xy}\right) = \frac{1}{2}N\lambda^b_{jk}\lambda^a_{kj}R^a_{xy} = NR^b_{xy}\,. \tag{3.89}$$

Now, let's work out the commutation relations between the gauge generators and the rishon operators. The gauge generators expressed with quarks and rishons are

$$\begin{aligned} G^a_x &= \lambda^a_{ij}\left\{\psi^{i\dagger}_x\psi^j_x + \sum_q\left(c^{i\dagger}_{x,+q}c^j_{x,+q} + c^{i\dagger}_{x,-q}c^j_{x,-q}\right)\right\}, \\ G_x &= \psi^{i\dagger}_x\psi^i_x - \frac{N}{2} + \frac{1}{2}\sum_q\left(c^{i\dagger}_{x,+q}c^i_{x,+q} + c^{i\dagger}_{x,-q}c^i_{x,-q} - c^{i\dagger}_{x-\hat{q},+q}c^i_{x-\hat{q},+q} - c^{i\dagger}_{x+\hat{q},-q}c^i_{x+\hat{q},-q}\right) \\ &= \psi^{i\dagger}_x\psi^i_x - \frac{N}{2} + \sum_q\left(c^{i\dagger}_{x,+q}c^i_{x,+q} + c^{i\dagger}_{x,-q}c^i_{x,-q} - \frac{1}{2}\mathcal{N}_{x-\hat{q},x} - \frac{1}{2}\mathcal{N}_{x,x+\hat{q}}\right). \end{aligned} \tag{3.90}$$

Since the number of rishons on a link $\mathcal{N}_{xy}$ commutes with the Hamiltonian and the gauge generators, the last line accents the locality of the $U(1)$ gauge generator. If we impose the $U(1)$ Gauss law, this is nothing else than fixing the number of rishons assigned to a site together with the number of quarks at that site.

We rewrite the gauge generators as

$$\begin{aligned} G_x^a &= \lambda_{ij}^a \widetilde{G}_x^{ij} \,, \\ G_x &= \delta^{ij} \widetilde{G}_x^{ij} - \frac{N}{2} - \frac{1}{2} \sum_q \left(\mathcal{N}_{x-\hat{q},x} + \mathcal{N}_{x,x+\hat{q}} \right) \end{aligned} \tag{3.91}$$

with

$$\widetilde{G}_x^{ij} = \psi_x^{i\dagger} \psi_x^j + \sum_q \left(c_{x,+q}^{i\dagger} c_{x,+q}^j + c_{x,-q}^{i\dagger} c_{x,-q}^j \right) . \tag{3.92}$$

We now calculate

$$\begin{aligned} [\widetilde{G}_x^{ij}, c_{y,r}^k] &= [c_{x,r}^{i\dagger} c_{x,r}^j, c_{y,r}^k] = -\delta_{xy} \delta^{ik} c_{x,r}^j \,, \\ [\widetilde{G}_x^{ij}, c_{y,r}^{k\dagger}] &= [c_{x,r}^{i\dagger} c_{x,r}^j, c_{y,r}^{k\dagger}] = \delta_{xy} \delta^{jk} c_{x,r}^{i\dagger} \,, \end{aligned} \tag{3.93}$$

which allows us to read off the commutation relations

$$\begin{aligned} [G_x^a, c_{y,r}^k] &= \lambda_{ij}^a [c_{x,r}^{i\dagger} c_{x,r}^j, c_{y,r}^k] = -\delta_{xy} \lambda_{kj}^a c_{x,r}^j \,, \\ [G_x^a, c_{y,r}^{k\dagger}] &= \lambda_{ij}^a [c_{x,r}^{i\dagger} c_{x,r}^j, c_{y,r}^{k\dagger}] = \delta_{xy} c_{x,r}^{i\dagger} \lambda_{ik}^a \,, \\ [G_x, c_{y,r}^k] &= [c_{x,r}^{i\dagger} c_{x,r}^i, c_{y,r}^k] = -\delta_{xy} c_{x,r}^k \,, \\ [G_x, c_{y,r}^{k\dagger}] &= [c_{x,r}^{i\dagger} c_{x,r}^i, c_{y,r}^{k\dagger}] = \delta_{xy} c_{x,r}^{k\dagger} \,. \end{aligned} \tag{3.94}$$

These are the same commutation relations as for the quarks. The derivation of the transformation rules under $U(1)$ and $SU(N)$ gauge transformation are the same. For completeness we explicitly write

$$\begin{aligned} (c_{x,q}^i)' &= V c_{x,q}^i V = \exp(i\alpha_x^a \lambda^a)_{ij} c_{x,q}^j \\ (c_{x,q}^{i\dagger})' &= V c_{x,q}^{i\dagger} V = c_{x,q}^{j\dagger} \exp(-i\alpha_x^a \lambda^a)_{ji} \end{aligned} \tag{3.95}$$

for the $SU(N)$ gauge transformations, and

$$\begin{aligned} (c_{x,q}^i)' &= W c_{x,q}^i W = \exp(i\alpha_x) c_{x,q}^i \\ (c_{x,q}^{i\dagger})' &= W c_{x,q}^{i\dagger} W = c_{x,q}^{i\dagger} \exp(-i\alpha_x) \end{aligned} \tag{3.96}$$

for the $U(1)$ gauge transformations. Hence, rishon and quark annihilation operators $c_{x,q}^i$, ψ_x^i transform in the fundamental representation, while rishon and quark creation operators $c_{x,q}^{i\dagger}$, $\psi_x^{i\dagger}$ transform in the anti-fundamental representation.

If we express the determinant appearing in the Hamiltonian with rishon operators, we obtain

$$\det U_{x,x+\hat{q}} = N!\, c_{x,+q}^1 c_{x+\hat{q},-q}^{1\dagger} c_{x,+q}^2 c_{x+\hat{q},-q}^{2\dagger} \cdots c_{x,+q}^N c_{x+\hat{q},-q}^{N\dagger} \,. \tag{3.97}$$

This operator annihilates all states except those with N rishons of N different colors on this link. Hence, we need $\mathcal{N} = N$ rishons on each link, if we opt for an $SU(N)$ system. The number of states per link then corresponds to the dimension of the $\mathfrak{su}(2N)$ representation

$$\binom{2N}{N} = \frac{(2N)!}{(N!)^2}\,. \tag{3.98}$$

The action of the determinant operator on rishons is shown in Figure 3.3.

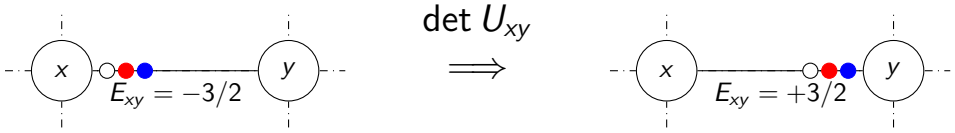

Figure 3.3.: *Action of the determinant operator in an $SU(3)$ quantum link model with $\mathcal{N} = N = 3$ rishons on the link. On the left link, we have a color-neutral object built out of $N = 3$ different rishons sitting on the left side of this link. The action of the determinant operator on that configuration corresponds to a shift of all the rishons to the right side of the link, as shown on the right side. The maximal electric flux is inverted by this operation.*

It remains to list the symmetry transformation rules for the rishon operators

$$\begin{aligned}
{}^{S_q}c^i_{x,\pm r} &= c^i_{x+\hat{q},\pm r}\,,\\
{}^{C_q}c^i_{x,\pm r} &= s_{\pm r}c^{i\dagger}_{x+\hat{q},\pm r}\,,\\
{}^{C_q}c^{i\dagger}_{x,\pm r} &= s_{\pm r}c^{i}_{x+\hat{q},\pm r}\,,\\
{}^{P}c^i_{x,\pm r} &= c^i_{-x,\mp r}\,.
\end{aligned} \tag{3.99}$$

Here we introduced $s_{\pm r} = \mathrm{sign}(\pm r) = \pm 1$, which is the sign in $\pm r$. These rules reproduce the symmetry transformations given in eqs. (3.50), (3.59) and (3.65), e.g., with $y = x + \hat{r}$,

$$\begin{aligned}
{}^{C_q}U^{ij}_{xy} &= -c^{i\dagger}_{x+\hat{q},+r}c^j_{y+\hat{q},-r} = \left(c^i_{x+\hat{q},+r}c^{j\dagger}_{y+\hat{q},-r}\right)^\dagger = U^{ij\dagger}_{x+\hat{q},y+\hat{q}}\,,\\
{}^{C_q}L^a_{xy} &= \lambda^a_{ij}c^i_{x+\hat{q},+r}c^{j\dagger}_{x+\hat{q},+r} = -\lambda^{a*}_{ji}c^{j\dagger}_{x+\hat{q},+r}c^i_{x+\hat{q},+r} = -L^{a*}_{x+\hat{q},y+\hat{q}}\,,\\
{}^{P}U^{ij}_{xy} &= c^i_{-x,-r}c^{j\dagger}_{-y,+r} = \left(c^j_{-y,+r}c^{i\dagger}_{-x,-r}\right)^\dagger = U^{ji\dagger}_{-y,-x}\,,\\
{}^{P}L^a_{xy} &= \lambda^a_{ij}c^{i\dagger}_{-x,-r}c^j_{-x,-r} = R^a_{-y,-x}\,.
\end{aligned} \tag{3.100}$$

Also, the rishon-rishon and rishon-quark anti-commutation relations remain valid under these symmetry transformations. Since

$${}^{C_q}\mathcal{N}_{x,x+\hat{r}} = 2N - \mathcal{N}_{x+\hat{q},x+\hat{q}+\hat{r}}\,, \tag{3.101}$$

only states with $\mathcal{N} = N$ rishons on each link are symmetric under charge conjugation.

3.3. Color-neutral bosonic $U(N)$ gauge invariant operators

As argued in the previous section, rishon and quark annihilation operators transform in the fundamental representation, while the corresponding creation operators transform in the anti-fundamental representation. Hence, if we stick together any of the creation operators on a site with any of the annihilation operators on the same site, we obtain a gauge invariant bosonic operator. If we additionally contract their color indices those operators are color-neutral. We define

$$\begin{aligned} \Phi_{x,\pm q,\pm r} &= c^{i\dagger}_{x,\pm q} c^{i}_{x,\pm r} && \text{“glueball” operators}\,, \\ M_x &= \psi^{i\dagger}_x \psi^i_x && \text{“meson” operators}\,, \\ Q_{x,\pm q} &= c^{i\dagger}_{x,\pm q} \psi^i_x && \text{constituent quark operators} \end{aligned} \tag{3.102}$$

with the properties

$$\begin{aligned} \Phi^\dagger_{x,\pm q,\pm r} &= \Phi_{x,\pm r,\pm q}\,, \\ M^\dagger_x &= M_x\,. \end{aligned} \tag{3.103}$$

While the M_x counts the number of quarks at site x, $\Phi_{x,q,q}$ (two times direction q) counts the number of rishons on the leg of the link in direction q touching site x. Hence, we can write

$$\mathcal{N}_{x,x+\hat{q}} = \Phi_{x,+q,+q} + \Phi_{x+\hat{q},-q,-q}\,. \tag{3.104}$$

The Abelian gauge generator can be trivially rewritten with the gauge invariant operators

$$G_x = M_x - \frac{N}{2} + \sum_q \left(\Phi_{x,+q,+q} + \Phi_{x,-q,-q} - \frac{1}{2}\mathcal{N}_{x-\hat{q},x} - \frac{1}{2}\mathcal{N}_{x,x+\hat{q}} \right)\,. \tag{3.105}$$

This doesn't work out for the non-Abelian gauge generator.

Using, amongst others, eqs. (3.70) and (3.78) we obtain the commutation relations

$$\begin{aligned} [\Phi_{x,\pm q,\pm r}, \Phi_{y,\pm s,\pm t}] &= \delta_{xy} \left(\delta_{\pm r,\pm s} \Phi_{x,\pm q,\pm t} - \delta_{\pm q,\pm t} \Phi_{x,\pm s,\pm r} \right)\,, \\ [\Phi_{x,\pm q,\pm r}, M_y] &= 0\,, \\ [\Phi_{x,\pm q,\pm r}, Q_{y,\pm s}] &= \delta_{xy} \delta_{\pm r,\pm s} \delta^{ij} c^{i\dagger}_{x,\pm q} \psi^j_y = \delta_{xy} \delta_{\pm r,\pm s} Q_{x,\pm q}\,, \\ [\Phi_{x,\pm q,\pm r}, Q^\dagger_{y,\pm s}] &= [Q_{y,\pm s}, \Phi_{x,\pm r,\pm q}]^\dagger = -\delta_{xy} \delta_{\pm q,\pm s} Q^\dagger_{x,\pm r}\,, \\ [M_x, M_y] &= 0\,, \\ [M_x, Q_{y,\pm q}] &= -\delta_{xy} \delta^{ij} c^{j\dagger}_{y,\pm q} \psi^i_x = -\delta_{xy} Q_{x,\pm q}\,, \\ [M_x, Q^\dagger_{y,\pm q}] &= [Q_{y,\pm q}, M_x]^\dagger = \delta_{xy} Q^\dagger_{x,\pm q}\,, \\ [Q_{x,\pm q}, Q^\dagger_{y,\pm r}] &= \delta_{xy} \delta^{ij} c^{i\dagger}_{x,\pm q} c^j_{y,\pm r} - \delta_{xy} \delta_{\pm q,\pm r} \delta^{ij} \psi^{j\dagger}_y \psi^i_x = \delta_{xy} \left(\Phi_{x,\pm q,\pm r} - \delta_{\pm q,\pm r} M_x \right)\,, \\ [Q_{x,\pm q}, Q_{y,\pm r}] &= [Q^\dagger_{x,\pm q}, Q^\dagger_{y,\pm r}] = 0\,. \end{aligned} \tag{3.106}$$

We additionally observe that

$$\begin{aligned} (Q_{x,\pm q})^N &= 0\,, \\ \left(Q^\dagger_{x,\pm q}\right)^N &= 0\,. \end{aligned} \tag{3.107}$$

The symmetry transformation rules for the gauge invariant operators can be deduced from the rules for the quarks in eqs. (3.50), (3.59), (3.65), and for the rishons in eq. (3.99). For the shift symmetry we simply get

$$\begin{aligned} {}^{S_q}\Phi_{x,\pm r,\pm s} &= \Phi_{x+\hat{q},\pm r,\pm s}\,, \\ {}^{S_q}M_x &= M_{x+\hat{q}}\,, \\ {}^{S_q}Q_{x,\pm r} &= (-1)^{x_{q+1}+\cdots+x_d} Q_{x+\hat{q},\pm r}\,. \end{aligned} \tag{3.108}$$

For the charge conjugation we obtain

$$\begin{aligned} {}^{C_q}\Phi_{x,\pm r,\pm s} &= s_{\pm r}s_{\pm s}c^i_{x+\hat{q},\pm r}c^{i\dagger}_{x+\hat{q},\pm s} = s_{\pm r}s_{\pm s}\left(N\delta_{\pm r,\pm s} - \Phi_{x+\hat{q},\pm s,\pm r}\right)\,, \\ {}^{C_q}M_x &= N - M_{x+\hat{q}}\,, \\ {}^{C_q}Q_{x,\pm r} &= (-1)^{x_1+\cdots+x_q} s_{\pm r}c^i_{x+\hat{q},\pm r}\psi^{i\dagger}_{x+\hat{q}} = -s_{\pm r}(-1)^{x_1+\cdots+x_q}Q^\dagger_{x+\hat{q},\pm r}\,, \\ {}^{C_q}Q^\dagger_{x,\pm r} &= -s_{\pm r}(-1)^{x_1+\cdots+x_q}Q_{x+\hat{q},\pm r}\,, \end{aligned} \tag{3.109}$$

and for the parity

$$\begin{aligned} {}^{P}\Phi_{x,\pm r,\pm s} &= \Phi_{-x,\mp r,\mp s}\,, \\ {}^{P}M_x &= M_{-x}\,, \\ {}^{P}Q_{x,\pm r} &= Q_{-x,\mp r}\,. \end{aligned} \tag{3.110}$$

The commutation relations in eq. (3.106) remain valid under the symmetry transformations, e.g.

$$\begin{aligned} {}^{C_q}[M_x, Q_{y,\pm q}] &= [N - M_{x+\hat{q}}, -s_{\pm r}(-1)^{y_1+\cdots+y_q}Q^\dagger_{y+\hat{q},\pm r}] \\ &= s_{\pm r}(-1)^{x_1+\cdots+x_q}\delta_{xy}Q^\dagger_{x+\hat{q},\pm r} \\ &= {}^{C_q}\left(-\delta_{xy}Q_{x,\pm q}\right)\,. \end{aligned} \tag{3.111}$$

Figure 3.4 shows how the glueball operator acts on an initial state. We illustrated

$$\begin{aligned} &\Phi_{x,+1,+2}c^{3\dagger}_{x,+2}c^{2\dagger}_{x,+2}c^{1\dagger}_{x,+2}c^{1\dagger}_{x,+1}|0\rangle_x \\ &= c^{2\dagger}_{x,+2}c^{1\dagger}_{x,+2}c^{3\dagger}_{x,+1}c^{1\dagger}_{x,+1}|0\rangle_x - c^{3\dagger}_{x,+2}c^{1\dagger}_{x,+2}c^{2\dagger}_{x,+1}c^{1\dagger}_{x,+1}|0\rangle_x\,. \end{aligned} \tag{3.112}$$

The states are represented by creating rishons in a certain order out of a state with no rishons and no fermions at this site, called $|0\rangle_x$. In above figure we used white rishons for those with color index 1, red for index 2, and blue for index 3. The rishons are draw from left to right in their creation order. A very similar situation is shown for the constituent quark operator in Figure 3.5.

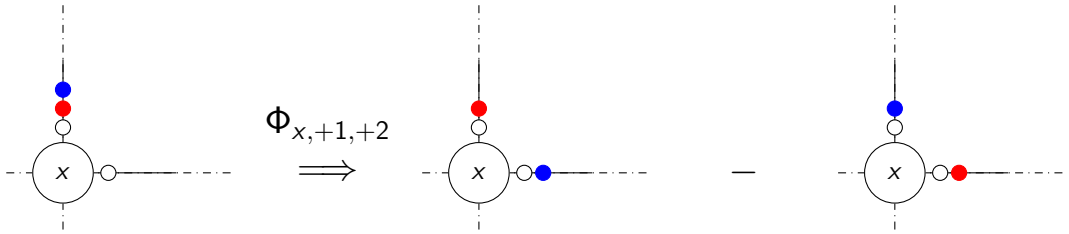

Figure 3.4.: *Action of the glueball operator $\phi_{x,+1,+2}$ on the initial state $c^{3\dagger}_{x,+2}c^{2\dagger}_{x,+2}c^{1\dagger}_{x,+2}c^{1\dagger}_{x,+1}|0\rangle_x$. The colors of the rishons (white, red, blue) correspond to the color indices (1, 2, 3).*

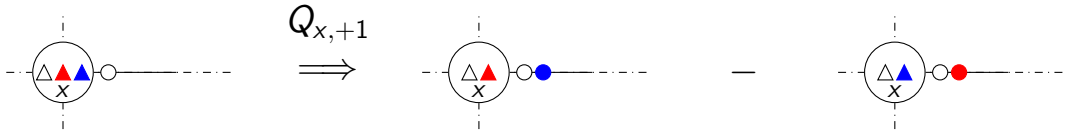

Figure 3.5.: *Action of the constituent quark operator $Q_{x,+1}$ on the initial state $\psi^{3\dagger}_x\psi^{2\dagger}_x\psi^{1\dagger}_x c^{1\dagger}_{x,+1}|0\rangle_x$. The fermions are represented by triangles with the same color encoding as for the rishons.*

The kinetic term of the Hamiltonian in eq. (3.13) (the term proportional to t) now can be rewritten in site-based constituent quark operators Q, since

$$\psi^{i\dagger}_x U^{ij}_{x,x+\hat{q}}\psi^j_{x+\hat{q}} = Q^\dagger_{x,+q}Q_{x+\hat{q},-q}\,. \tag{3.113}$$

This term leads to a correlated hop of rishons and fermions as shown in Figure 3.6. It should be pointed out again, that due to the rishon representation there is no more color interaction between left site of a link and its right side.

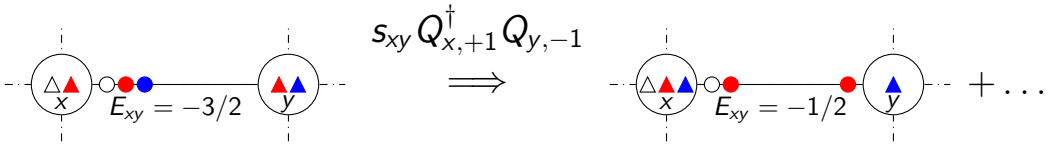

Figure 3.6.: *Action of the kinetic term contribution $s_{xy}Q^\dagger_{x,+1}Q_{y,-1}$ on the initial state $\psi^{3\dagger}_y\psi^{2\dagger}_y|0\rangle_y\psi^{2\dagger}_x\psi^{1\dagger}_x c^{3\dagger}_x c^{2\dagger}_x c^{1\dagger}_x|0_x\rangle$.*

The magnetic plaquette term proportional to $\frac{1}{4g^2}$, which was formulated with link operators U can be rewritten in terms of site-based glueball operators Φ

$$\sum_{\langle wxyz\rangle}(\mathrm{Tr}\,U_{wx}U_{xy}U_{yz}U_{zw} + \mathrm{H.c.}) = \sum_{\langle wxyz\rangle}(\Phi_{w,+q,-r}\Phi_{x,+r,+q}\Phi_{y,-q,+r}\Phi_{z,-r,-q} + \mathrm{H.c.})\,. \tag{3.114}$$

The directions are defined as follows

$$\begin{aligned} r &> q > 0\,, \\ y &= x + \hat{q}\,, \\ z &= x + \hat{q} + \hat{r}\,, \\ w &= x + \hat{r}\,. \end{aligned} \tag{3.115}$$

Defined this way, $\langle xwyz \rangle$ denotes plaquettes with w, x, y, z arranged counter-clockwise as shown in Figures 3.1 and 3.7. If the notation $\langle xwyz \rangle$ would include both orientations, which would correspond to $r > q$ and $r < q$, then we wouldn't need to add the Hermitean conjugation for the plaquette terms.

The above mentioned Figure 3.7 shows the action of the plaquette term. It leads to hops of rishons around the plaquette. Therefore, the numbers of rishons on the links are preserved.

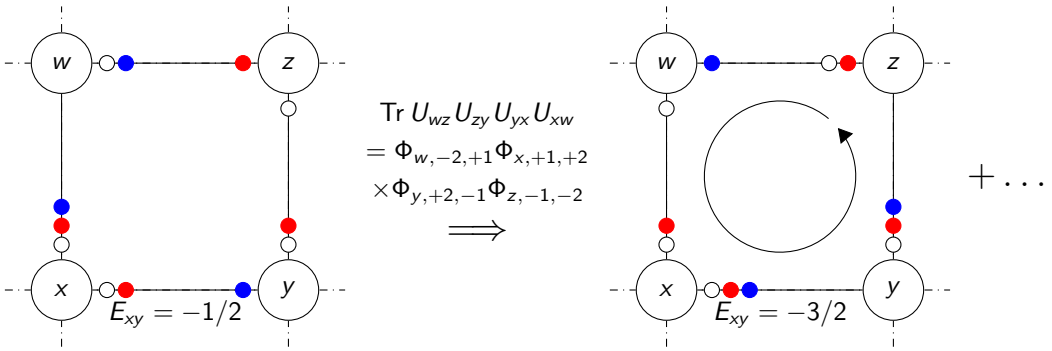

Figure 3.7.: *Action of the plaquette term in a model with $\mathcal{N} = 3$ rishons on each link. On the left plaquette, we have an initial rishon configuration. When the plaquette term is applied on this configuration a superposition of new configurations is created. One of them is shown on the right plaquette. In a model with $N > 3$ this example would include rishon configurations with further colors.*

In section 3.1 we studied different symmetries of the $U(N)$ and $SU(N)$ models (chiral, flavor, charge conjugation, parity) and introduced the baryon number B. Now that we introduced rishons and the vocabulary of "glueballs" and "mesons" it is time to collect phenomena which can be reproduced by these models depending on the dimension d, the number of colors N, the number of rishons on each link $\mathcal{N}$ and if the $U(1)$ symmetry is gauged.

The Mermin-Wagner theorem, which has its origins in [42], states, that there is no spontaneous symmetry breaking of continuous symmetries in less than 3 dimensions at non-zero temperature. At zero temperature, the Euclidean time extends to infinity and counts as an additional dimension. Discrete symmetries can break spontaneously already at two dimensions. Applied to our system, this means that at $(1 + 1)$ dimensions the critical temperature for a chiral phase transition is at $T_c = 0$. At $(2 + 1)$ dimensions, the

spontaneous chiral symmetry breaking can happen for small enough, non-zero temperature ($T_c > 0$).

As argued in section 3.1, there is no flavor symmetry in $(1+1)$ dimensions. In $(2+1)$ dimensions we have one $\mathbb{Z}(2)$ flavor symmetry.

For representations with $\mathcal{N} \neq N$, we obtain a $U(N)$ model, while for representations with $\mathcal{N} = N$ we can choose $\gamma = 0$ and apply the $U(1)$ Gauss law to again get a $U(N)$ model, or we choose $\gamma \neq 0$, have no commuting $U(1)$ gauge generator and get the $SU(N)$ model. In the $SU(N)$ model, the baryon number is not gauged and obtain baryon sectors. If we localize a baryon as much as possible, we obtain a color singlet which consists of N rishons of N different colors sitting near a site. Such a situation was shown in Figure 3.3. The determinant term moves such baryons on a link. For N even the baryons are bosons, for N odd they are fermions. An extensive overview is given in Table 3.1. All models show a glueball spectrum and chiral symmetry breaking can be observed.

dim.	group	emb.	rep.	$\mathcal{N}$	C	baryons	flavor	phenomena
$(1+1)$	$U(2)$	$\mathfrak{su}(4)$	$\{4\}$	1	no	no	no	χSB at $T_c = 0$
$(1+1)$	$U(3)$	$\mathfrak{su}(6)$	$\{6\}$	1	no	no	no	χSB at $T_c = 0$
$(2+1)$	$U(2)$	$\mathfrak{su}(4)$	$\{4\}$	1	no	no	$\mathbb{Z}(2)$	χSB at $T_c > 0$
$(2+1)$	$U(3)$	$\mathfrak{su}(6)$	$\{6\}$	1	no	no	$\mathbb{Z}(2)$	χSB at $T_c > 0$
$(3+1)$	$U(2)$	$\mathfrak{su}(4)$	$\{4\}$	1	no	no	$\mathbb{Z}(2)^2$	χSB at $T_c > 0$
$(3+1)$	$U(3)$	$\mathfrak{su}(6)$	$\{6\}$	1	no	no	$\mathbb{Z}(2)^2$	χSB at $T_c > 0$
$(1+1)$	$SU(2)$	$\mathfrak{su}(4)$	$\{6\}$	2	yes	$U(1)$ bosons	no	χSB at $T_c = 0$ χSR at $n_B > 0$, baryon superfluid
$(1+1)$	$SU(3)$	$\mathfrak{su}(6)$	$\{20\}$	3	yes	$U(1)$ fermions	no	χSB at $T_c = 0$ χSR at $n_B > 0$, "nuclear" physics
$(2+1)$	$SU(2)$	$\mathfrak{su}(4)$	$\{6\}$	2	yes	$U(1)$ bosons	$\mathbb{Z}(2)$	χSB at $T_c > 0$, χSR at $n_B > 0$, baryon superfluid
$(2+1)$	$SU(3)$	$\mathfrak{su}(6)$	$\{20\}$	3	yes	$U(1)$ fermions	$\mathbb{Z}(2)$	χSB at $T_c > 0$ χSR at $n_B > 0$, "nuclear" physics
$(3+1)$	$SU(2)$	$\mathfrak{su}(4)$	$\{6\}$	2	yes	$U(1)$ bosons	$\mathbb{Z}(2)^2$	χSB at $T_c > 0$, χSR at $n_B > 0$, baryon superfluid
$(3+1)$	$SU(3)$	$\mathfrak{su}(6)$	$\{20\}$	3	yes	$U(1)$ fermions	$\mathbb{Z}(2)^2$	χSB at $T_c > 0$ χSR at $n_B > 0$, "nuclear" physics

Table 3.1.: *Overview of symmetries and phenomena in $U(N)$ and $SU(N)$ quantum link models for $N \in \{2, 3\}$, with various representations in various dimensions.*

As already stated, for the $SU(N)$ model, we need a state with exactly $\mathcal{N} = N$ rishons of different colors, such that the determinant term in the Hamiltonian is not strictly zero. For N odd, such a state is fermionic. Since we would like to work with the bosonic glueball,

meson, and constituent quark operators, we prefer to ignore complications with fermionic properties. Hence, in the following we restrict us to the $U(N)$ quantum link models.

A further reason for this decision is, that for $\mathcal{N} = N = 2$ one would already need a 6-dimensional and for $\mathcal{N} = N = 3$ a 20-dimensional representation of $\mathfrak{su}(2N)$.

For the case of only one rishon per link ($\mathcal{N} = 1$) the determinant term is zero, the Abelian electric flux is $E_{xy} = \pm 1/2$, and therefore the Abelian electric flux term in the Hamiltonian in eq. (3.13) proportional to g'^2 is a trivial constant. The non-Abelian flux term proportional to $\frac{g^2}{2}$ is a trivial constant

$$\begin{aligned} L^a_{x,x+\hat{q}} L^a_{x,x+\hat{q}} + R^a_{x,x+\hat{q}} R^a_{x,x+\hat{q}} |\Psi\rangle &= (\lambda^a \lambda^a)_{ij} \left(c^{i\dagger}_{x,+q} c^j_{x,+q} + c^{i\dagger}_{x+\hat{q},-q} c^j_{x+\hat{q},-q} \right) |\Psi\rangle \\ &= \Omega \mathcal{N} |\Psi\rangle = \Omega |\Psi\rangle \,. \end{aligned} \tag{3.116}$$

Here we denoted $|\Psi\rangle$ as any valid state of the system with one rishon per link. We used

$$c^k_{x,q} c^{l\dagger}_{x,q} c^j_{x,q} |\Psi\rangle = \delta_{kl} c^j_{x,q} |\Psi\rangle - c^{l\dagger}_{x,q} c^k_{x,q} c^j_{x,q} |\Psi\rangle = \delta_{kl} c^j_{x,q} |\Psi\rangle \,, \tag{3.117}$$

and the fact that $\lambda^a \lambda^a$ is a quadratic Casimir operator with $\Omega = 3$ for $SU(2)$ and $\Omega = \frac{16}{3}$ for $SU(3)$, since

$$[\lambda^a \lambda^a, \lambda^b] = \lambda^a [\lambda^a, \lambda^b] + [\lambda^a, \lambda^b] \lambda^a = 2i \left(f_{abc} + f_{cba} \right) \lambda^a \lambda^c = 0 \,. \tag{3.118}$$

Hence, for $\mathcal{N} = 1$, the Hamiltonian in eq. (3.13) can be expressed in purely $U(N) = SU(N) \times U(1)$ gauge invariant, color-neutral bosonic operators

$$\begin{aligned} H = &-t \sum_{\langle xy \rangle} \left(s_{xy} Q^\dagger_{x,+q} Q_{y,-q} + \text{H.c.} \right) + m \sum_x s_x M_x \\ &+ \frac{1}{4g^2} \sum_{\langle wxyz \rangle} \left(\Phi_{w,+q,-r} \Phi_{x,+r,+q} \Phi_{y,-q,+r} \Phi_{z,-r,-q} + \text{H.c.} \right) \,. \end{aligned} \tag{3.119}$$

3.4. Implementation of exact diagonalization studies

To achieve interesting system sizes in exact diagonalization studies on classical computers, we work with the $(1+1)$-dimensional $U(2)$ model with $\mathcal{N} = 1$ rishon per link. In one spacial dimension, there is no plaquette term. To force the spontaneous chiral symmetry breaking we are free to add the local 4-fermion term $\sum_x \left(M_x - \frac{N}{2} \right)^2$. So, the Hamiltonian we diagonalize is (remember $s_{xy} = 1$ in one dimension)

$$H = -t \sum_x \left(Q^\dagger_{x,+} Q_{x+1,-} + \text{H.c.} \right) + m \sum_x (-1)^x M_x + V \sum_x \left(M_x - 1 \right)^2 \,. \tag{3.120}$$

Remember that $Q_{x,+}$, $Q_{x,-}$, and M_x are gauge invariant bosonic color-neutral operators. The gauge generators in one dimension with one rishon per link are

$$\begin{aligned} G^a_x &= \sigma^a_{ij} \left\{ \psi^{i\dagger}_x \psi^j_x + c^{i\dagger}_{x,+} c^j_{x,+} + c^{i\dagger}_{x,-} c^j_{x,-} \right\} \,, \\ G_x &= M_x + \Phi_{x,+,+} + \Phi_{x,-,-} - 2 \,, \end{aligned} \tag{3.121}$$

with $i \in \{1,2\}$ and $a \in \{1,2,3\}$. Here we used the Pauli matrices

$$\sigma^1 = \begin{pmatrix} 0 & 1 \\ 1 & 0 \end{pmatrix}, \qquad \sigma^2 = \begin{pmatrix} 0 & -i \\ i & 0 \end{pmatrix}, \qquad \sigma^3 = \begin{pmatrix} 1 & 0 \\ 0 & -1 \end{pmatrix}, \tag{3.122}$$

since they are the $SU(2)$ Gell-Mann matrices. For completeness we write out the non-Abelian $SU(2)$ gauge generators

$$\begin{aligned} G_x^1 &= \psi_x^{1\dagger}\psi_x^2 + \psi_x^{2\dagger}\psi_x^1 + c_{x,+}^{1\dagger}c_{x,+}^2 + c_{x,+}^{2\dagger}c_{x,+}^1 + c_{x,-}^{1\dagger}c_{x,-}^2 + c_{x,-}^{2\dagger}c_{x,-}^1 \,, \\ G_x^2 &= -i\psi_x^{1\dagger}\psi_x^2 + i\psi_x^{2\dagger}\psi_x^1 - ic_{x,+}^{1\dagger}c_{x,+}^2 + ic_{x,+}^{2\dagger}c_{x,+}^1 - ic_{x,-}^{1\dagger}c_{x,-}^2 + ic_{x,-}^{2\dagger}c_{x,-}^1 \,, \\ G_x^3 &= \psi_x^{1\dagger}\psi_x^1 - \psi_x^{2\dagger}\psi_x^2 + c_{x,+}^{1\dagger}c_{x,+}^1 - c_{x,+}^{2\dagger}c_{x,+}^2 + c_{x,-}^{1\dagger}c_{x,-}^1 - c_{x,-}^{2\dagger}c_{x,-}^2 \,. \end{aligned} \tag{3.123}$$

We would like to work directly with gauge invariant states. Hence, we search for local gauge invariant color singlets. Since we work in a 4-dimensional representation of the embedding algebra $\mathfrak{su}(4)$, we should be able to find four orthogonal local gauge invariant color singlets $|1\rangle_x$, $|2\rangle_x$, $|3\rangle_x$, $|4\rangle_x$. We want to work with states which are diagonal in M_x. This means that the states have a definite number of quarks (and by the $U(1)$ gauss law a definite total number of rishons), and that the term proportional to t in the Hamiltonian is the kinetic term.

The $U(1)$ Gauss law $G_x|\Psi\rangle = 0$ tells us, that for a state with two quarks on a site, there are no rishons at this site. The bosonic state

$$|4\rangle_x \doteq \psi_x^{2\dagger}\psi_x^{1\dagger}|0\rangle_x \tag{3.124}$$

is such a local gauge invariant color singlet

$$\begin{aligned} G_x^a|4\rangle_x &= 0 \,, \\ G_x|4\rangle_x &= 0 \,. \end{aligned} \tag{3.125}$$

Here, $|0\rangle_x$ describes a site x with no quarks and no rishons and

$${}_x\langle 0|0\rangle_x = 1 \,. \tag{3.126}$$

The state $|4\rangle_x$ is already normalized

$${}_x\langle 4|4\rangle_x = {}_x\langle 0|\psi_x^1\psi_x^2\psi_x^{2\dagger}\psi_x^{1\dagger}|0\rangle_x = 1 \,. \tag{3.127}$$

Acting with $Q_{x,\pm}$ on $|4\rangle_x$ we find two other bosonic gauge invariant states with one quark and one rishon. Eq. 3.107 tells us, that we can act on $|4\rangle_x$ only once with the same operator. In eq. 3.106 we find

$$[Q_{x,\pm}, Q_{y,\pm}] = [Q_{x,\pm}, Q_{y,\mp}] = [Q_{x,\pm}^\dagger, Q_{y,\pm}^\dagger] = [Q_{x,\pm}^\dagger, Q_{y,\mp}^\dagger] = 0. \tag{3.128}$$

Now we can construct the local bosonic gauge invariant states (already normalized)

$$\begin{aligned} |1\rangle_x &\doteq \frac{1}{\sqrt{2}} Q_{x,+}Q_{x,-}|4\rangle_x = \frac{1}{\sqrt{2}}\left(c_{x,-}^{2\dagger}c_{x,+}^{1\dagger} - c_{x,-}^{1\dagger}c_{x,+}^{2\dagger}\right)|0\rangle_x \,, \\ |2\rangle_x &\doteq \frac{1}{\sqrt{2}} Q_{x,-}|4\rangle_x = \frac{1}{\sqrt{2}}\left(c_{x,-}^{2\dagger}\psi_x^{1\dagger} - c_{x,-}^{1\dagger}\psi_x^{2\dagger}\right)|0\rangle_x \,, \\ |3\rangle_x &\doteq \frac{1}{\sqrt{2}} Q_{x,+}|4\rangle_x = \frac{1}{\sqrt{2}}\left(c_{x,+}^{2\dagger}\psi_x^{1\dagger} - c_{x,+}^{1\dagger}\psi_x^{2\dagger}\right)|0\rangle_x \,. \end{aligned} \tag{3.129}$$

Again, they are color singlets. Their gauge invariance is trivial, since Q and $Q^\dagger$ commute with the gauge generators. The orthogonality of $|2\rangle_x$ and $|3\rangle_x$ follows out of the fact, that for $|2\rangle_x$ the rishons sit on the left side $(-)$ of the site x and for $|3\rangle_x$ they sit on the right side $(+)$. The other orthogonalities are trivial, since there are different numbers of quarks (rishons). Figure 3.8 shows a diagrammatic representation of these states. Applying the

Figure 3.8.: *Diagrammatic representation of the four gauge invariant color singlet states* $|1\rangle_x$, $|2\rangle_x$, $|3\rangle_x$, *and* $|4\rangle_x$. *The rishons and fermions the states* $|1\rangle_x$, $|2\rangle_x$, *and* $|3\rangle_x$ *are drawn with two colors, since these states are superpositions as noted in eq. (3.129).*

shift operator we simply get

$$^{S_1}|i\rangle_x = |i\rangle_{x+1}\,. \tag{3.130}$$

Here, and $|i\rangle_x$ with $i \in \{1,2,3,4\}$ denotes one of the above basis states on site x, and we used the convention $^P|0\rangle_x = |0\rangle_{-x}$. The parity operator acts as

$$\begin{aligned}
^P|4\rangle_x &= \psi^{2\dagger}_{-x}\psi^{1\dagger}_{-x}|0\rangle_{-x} = |4\rangle_{-x}\,,\\
^P|3\rangle_x &= \frac{1}{\sqrt{2}}Q_{-x,-}|4\rangle_{-x} = |2\rangle_{-x}\,,\\
^P|2\rangle_x &= \frac{1}{\sqrt{2}}Q_{-x,+}|4\rangle_{-x} = |3\rangle_{-x}\,,\\
^P|1\rangle_x &= \frac{1}{\sqrt{2}}Q_{-x,-}Q_{-x,+}|4\rangle_{-x} = |1\rangle_{-x}\,.
\end{aligned} \tag{3.131}$$

Remember that the charge conjugation is not a symmetry for $\mathcal{N} = 1$.

Using above states as a basis, we can write the site-based operators of the Hamiltonian as 4×4 matrices

$$Q_{x,+} = \begin{pmatrix} 0 & 1 & 0 & 0 \\ 0 & 0 & 0 & 0 \\ 0 & 0 & 0 & \sqrt{2} \\ 0 & 0 & 0 & 0 \end{pmatrix}, \qquad Q_{x,-} = \begin{pmatrix} 0 & 0 & 1 & 0 \\ 0 & 0 & 0 & \sqrt{2} \\ 0 & 0 & 0 & 0 \\ 0 & 0 & 0 & 0 \end{pmatrix},$$

$$\Phi_{x,+,+} = \begin{pmatrix} 1 & 0 & 0 & 0 \\ 0 & 0 & 0 & 0 \\ 0 & 0 & 1 & 0 \\ 0 & 0 & 0 & 0 \end{pmatrix}, \qquad \Phi_{x,-,-} = \begin{pmatrix} 1 & 0 & 0 & 0 \\ 0 & 1 & 0 & 0 \\ 0 & 0 & 0 & 0 \\ 0 & 0 & 0 & 0 \end{pmatrix}, \qquad M_x = \begin{pmatrix} 0 & 0 & 0 & 0 \\ 0 & 1 & 0 & 0 \\ 0 & 0 & 1 & 0 \\ 0 & 0 & 0 & 2 \end{pmatrix}, \tag{3.132}$$

where

$$\begin{aligned}(Q_{x,\pm})_{ij} &= {}_x\langle i|Q_{x,\pm}|j\rangle_x\,,\\ (\Phi_{x,-,-})_{ij} &= {}_x\langle i|\Phi_{x,-,-}|j\rangle_x\,,\\ (\Phi_{x,+,+})_{ij} &= {}_x\langle i|\Phi_{x,+,+}|j\rangle_x\,,\\ (M_x)_{ij} &= {}_x\langle i|M_x|j\rangle_x\,.\end{aligned} \tag{3.133}$$

The rishon number operators $\Phi_{x,-,-}$, $\Phi_{x,+,+}$, and the fermion number operator M_x are diagonal in the basis $\{|1\rangle_x, |2\rangle_x, |3\rangle_x, |4\rangle_x\}$.

We now have 4 states per site. Naively, the Hilbert space of our 1-dimensional system would be of size 4^L, where L is the number of sites. However, due to the conserved number of rishons

$$\mathcal{N}_{x,x+1} = \Phi_{x,+,+} + \Phi_{x+1,-,-} = 1\,, \tag{3.134}$$

the possible local state combinations of neighboring sites is restricted to (compare also Figure 3.8)

$$A_{x,x+1} = \begin{pmatrix}0 & 0 & 1 & 1\\ 1 & 1 & 0 & 0\\ 0 & 0 & 1 & 1\\ 1 & 1 & 0 & 0\end{pmatrix} \tag{3.135}$$

with

$$(A_{x,x+1})_{ij} = {}_x\langle i|A_{x,x+1}|j\rangle_{x+1}\,. \tag{3.136}$$

Hence, for a state $|i\rangle_x$ at site x exactly two states $|j\rangle_{x+1}$ at site $x+1$ are allowed. Therefore, the number of gauge invariant states in a system of length L is proportional to 2^L.

Observing

$$(A_{x,x+1}A_{x+1,x+2})_{ik} = 1 \tag{3.137}$$

tells us, that every combination of states $|i\rangle_x$ at site x with states $|k\rangle_{x+2}$ at site $x+2$ is allowed. If we fix the state at site x and choose one of the four possible states at site $x+2$, for the state $|j\rangle_{x+1}$ at site $x+1$ there remains only one possibility

$$j = (J_{x,x+2})_{ik} = {}_x\langle i|J_{x,x+2}|k\rangle_{x+2} \tag{3.138}$$

with

$$J_{x,x+2} = \begin{pmatrix}4 & 4 & 3 & 3\\ 2 & 2 & 1 & 1\\ 4 & 4 & 3 & 3\\ 2 & 2 & 1 & 1\end{pmatrix}\,. \tag{3.139}$$

This allows us to directly count up the gauge invariant states of the system. Studying systems with periodic boundary conditions we can encode the gauge invariant state of such a system of size L by an integer number

$$i = \sum_{k=1}^{L/2} 4^{k-1}\,(i_{2k} - 1) \in \{0, 1, \ldots, 2^L - 1\}\,, \tag{3.140}$$

where $i_{2k} = i_x$ encodes the state $|i\rangle_x$ at site $x = 2k$. Exact diagonalizations and real-time evolutions are then performed in a similar way as described in the last chapter (section 2.5).

However, since we will study systems with periodic boundary conditions, the Hamiltonian is block-diagonal in momentum sectors. There are mainly two options to calculate the spectrum (energies and momenta) of the 1-dimensional Hamiltonian.

One way is to first solve the eigenvalue equation of the full Hamiltonian as done in the last chapter. This leads to degenerated solutions, where each state with a momentum $p \neq 0$ is in linear superposition with its parter state with momentum $-p$. The situation gets worse e.g. for almost flat mass shells, were by numerical effects the states of the whole mass shell get mixed. With ad-hoc criteria we identified eigenstates of similar energy. Let's assume we got n of them. These n states are then orthogonalized with the modified Gram-Schmidt method. Let's call this basis $|\Psi_1\rangle, |\Psi_2\rangle, \ldots, |\Psi_n\rangle$. Then the shift by two lattice spacings called T_2 (which corresponds to $S_1 S_1$ introduced in eq. (3.50)) is expressed in the basis of the orthonormalized states as a matrix

$$(T_2)_{ij} \doteq \langle \Psi_i | S_1 S_1 | \Psi_j \rangle \,. \tag{3.141}$$

Here, S_1 was expressed in the basis of gauge invariant states. Finally, the matrix T_2 defined above is diagonalized which yields as eigenvalues the momenta of the identified eigenstates of similar energy. The eigenstates of T_2 are used to recalculate the energies.

While above procedure is easily implemented in a numerical tool like Octave, it is neither very elegant nor very robust. Due to memory and runtime constraints, we only calculate the lowest energy eigenstates of the system. Hence, the mass shells with the highest calculated energies are in most cases not complete and so the the highest calculated energies have to be removed until a gap is found again by ad-hoc criteria.

A cleaner and more robust way is to first build states of definite momentum out of the gauge invariant states. Since

$$(T_2)^{L/2} = \mathbb{1} \,, \tag{3.142}$$

where the system size L is a multiple of two, the momenta are discrete

$$p_{T_2,k} = \frac{2\pi}{aL} \left(k - \lceil L/4 \rceil\right) \tag{3.143}$$

with

$$k \in \{1, 2, \ldots, \frac{L}{2}\} \,. \tag{3.144}$$

For $U(2)$, there are 2^L gauge invariant orthonormal states $|\Psi_l\rangle$, $l \in \{1, 2, \ldots, 2^L\}$. Using

$$2a\frac{L}{2} p_{T_2,k} = 0 \mod 2\pi \,, \tag{3.145}$$

we now define gauge invariant states

$$|\widetilde{\Psi}_{k,l}\rangle \doteq \sum_{n=0}^{L/2-1} \exp\left(-i2anp_{T_2,k}\right) (T_2)^n \, |\Psi_l\rangle \,, \tag{3.146}$$

which have momentum

$$\arg\left(\langle\widetilde{\Psi}_{k,l}|T_2|\widetilde{\Psi}_{k,l}\rangle\right) = \arg\left(\langle\widetilde{\Psi}_{k,l}|\exp\left(i2ap_{T_2,k}\right)\sum_{n=1}^{L/2}\exp\left(-i2anp_{T_2,k}\right)\left(T_2\right)^n|\Psi_l\rangle\right)$$
$$= 2ap_{T_2,k} \in \{0, \frac{4\pi}{L}, \ldots, 2\pi - \frac{4\pi}{L}\} \mod 2\pi\,. \tag{3.147}$$

However, the momentum of $|\widetilde{\Psi}_{k,l}\rangle$ is not always defined, since, depending on the translation symmetries of the chosen gauge invariant state $|\Psi_l\rangle$, $|\widetilde{\Psi}_{k,l}\rangle$ can be zero. As an example, if $T_2|\Psi_l\rangle = |\Psi_l\rangle$, then $|\widetilde{\Psi}_{k,l}\rangle = 0$ for all momenta except for $p_{T_2,k} = 0$. Another trivial effect to account for, is, that if two gauge invariant states are related by one or several translations $|\Psi_{l_2}\rangle = \left(T_2\right)^n|\Psi_{l_1}\rangle$, then $|\widetilde{\Psi}_{k,l_2}\rangle = \exp\left(inp_{T_2,k}2a\right)|\widetilde{\Psi}_{k,l_1}\rangle$. Hence, to build a complete basis in a momentum sector labeled by k out of normalized $|\widetilde{\Psi}_{k,l}\rangle$, only of a subset of $l \in \{1, 2, \ldots, 2^L\}$ is necessary. The Hamiltonian is then re-expressed and diagonalized in this new basis of fixed momentum $p_{T_2,k}$. Since the Hilbert space per momentum sector is smaller, this method allows to diagonalize slightly larger systems. The challenge was to implement the bookkeeping to find minimal sets of $|\widetilde{\Psi}_{k,l}\rangle$.

For $m = 0$, S_1 is a symmetry of the Hamiltonian with associated momentum

$$p_{T_1} \in \left]-\frac{\pi}{a}, \frac{\pi}{a}\right]\,, \tag{3.148}$$

and the techniques described above can be used with

$$\left(T_1\right)_{ij} \doteq \langle\Psi_i|S_1|\Psi_j\rangle \tag{3.149}$$

instead of T_2. Since

$$\left(T_1\right)^L = \mathbb{1}\,, \tag{3.150}$$

the discrete momenta are

$$p_{T_1,k} = \frac{2\pi}{aL}\left(k - L/2\right) \tag{3.151}$$

with

$$k \in \{1, 2, \ldots, L\}\,. \tag{3.152}$$

We define gauge invariant states

$$|\widetilde{\widetilde{\Psi}}_{k,l}\rangle \doteq \sum_{n=0}^{L-1}\exp\left(-ianp_{T_1,k}\right)\left(T_1\right)^n|\Psi_l\rangle \tag{3.153}$$

with momentum

$$\arg\left(\langle\widetilde{\widetilde{\Psi}}_{k,l}|T_1|\widetilde{\widetilde{\Psi}}_{k,l}\rangle\right) = \arg\left(\langle\widetilde{\widetilde{\Psi}}_{k,l}|\exp\left(iap_{T_1,k}\right)\sum_{n=1}^{L}\exp\left(-ianp_{T_1,k}\right)\left(T_1\right)^n|\Psi_l\rangle\right)$$
$$= ap_{T_1,k} \in \{0, \frac{2\pi}{L}, \ldots, 2\pi - \frac{2\pi}{L}\} \mod 2\pi\,, \tag{3.154}$$

if $|\widetilde{\widetilde{\Psi}}_{k,l}\rangle \neq 0$.

An important fact is, that the momenta $p_{T_1,k}$ with their L different realizations carry more information than the momenta $p_{T_2,k}$ with $L/2$ different realizations. If for two states their momenta $p_{T_1,k}$ differs by π they have the same momenta $p_{T_2,k}$.

3.5. Spontaneous chiral symmetry breaking

For a large negative 4-Fermi coupling $|V| \gg t, m$ in the Hamiltonian defined in eq. (3.120) of the 1-dimensional $U(2)$ quantum link model with one rishon per link ($\mathcal{N} = 1$), at zero temperature, the local gauge invariant states $|1\rangle_x$ and $|4\rangle_x$ are favored over $|2\rangle_x$ and $|3\rangle_x$. From the neighboring state matrix in eq. (3.135), which encodes the rishon number conservation, we would expect an at least almost degenerated ground state, which cartoons would look like

$$|\Psi_0\rangle = \frac{1}{\sqrt{2}} \left(|414141 \ldots\rangle + |141414 \ldots\rangle \right) \tag{3.155}$$

and

$$|\Psi_1\rangle = \frac{1}{\sqrt{2}} \left(|414141 \ldots\rangle - |141414 \ldots\rangle \right) . \tag{3.156}$$

Here we introduced the notation

$$|i_1 i_2 \ldots i_{x-1} i_x \ldots\rangle \doteq |i_x\rangle_x |i_{x-1}\rangle_{x-1} \cdots |i_2\rangle_2 |i_1\rangle_1 . \tag{3.157}$$

For an infinite size system, the ground state would be truly degenerated. For a large finite periodic system of length L, the ground state would be almost degenerate with the lowest energy eigenstate cartoon

$$|\Psi_0\rangle = {}^{S_1}|\Psi_0\rangle \tag{3.158}$$

and the first excited state

$$|\Psi_1\rangle = -{}^{S_1}|\Psi_1\rangle . \tag{3.159}$$

Hence, the $\mathbb{Z}(2)$ chiral symmetry would be spontaneously broken and the energy difference of the two almost degenerated states is expected to obey

$$E_1 - E_0 \sim \exp(-L) . \tag{3.160}$$

As a reminder, for $m \neq 0$ the chiral symmetry is explicitly broken to the cartoons

$$\begin{aligned} &|414141 \ldots\rangle \quad m \gg t, V , \\ &|141414 \ldots\rangle \quad m \ll t, V . \end{aligned} \tag{3.161}$$

In contrast, for a large positive 4-Fermi coupling $V \ll t, m$, $|2\rangle_x$ and $|3\rangle_x$ are favored. From the rishon number conservation conservation, in a large periodic system, we would expect the cartoon lowest states

$$\begin{aligned} |\Psi_0\rangle &= |222222 \ldots\rangle + |333333 \ldots\rangle = {}^{P}|\Psi_0\rangle , \\ |\Psi_1\rangle &= |222222 \ldots\rangle - |333333 \ldots\rangle = -{}^{P}|\Psi_1\rangle . \end{aligned} \tag{3.162}$$

Hence, we would expect the spontaneous breakdown of the parity symmetry.

Figure 3.9 shows the spectra calculated with exact diagonalization with momenta $2ap_{T_2}$ according to eq. (3.143). The hopping parameter was set to $t = 1$, and the staggered mass to $m = 0$. For large $|V|$ a band structure appears, as shown in the two panels with

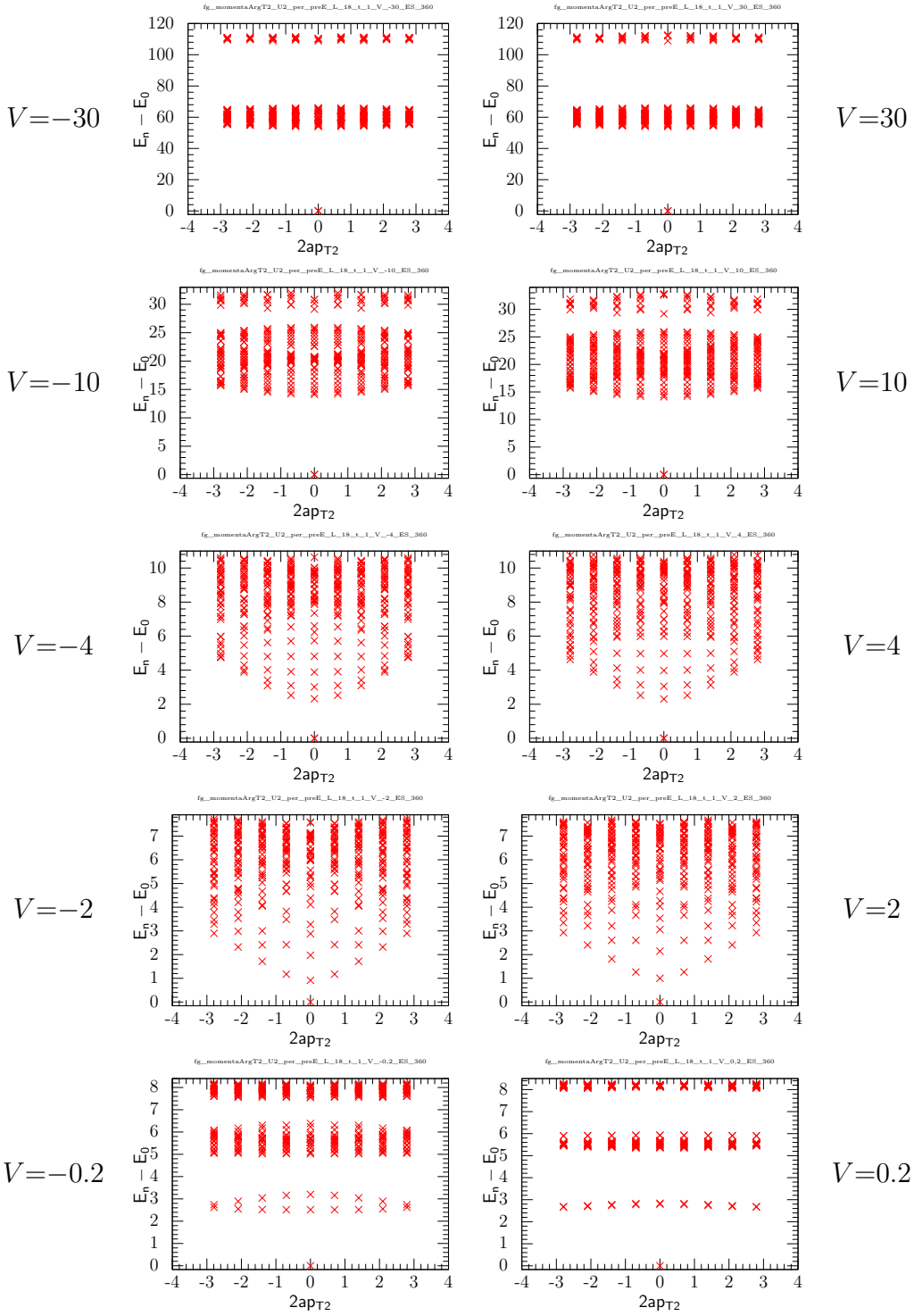

Figure 3.9.: *Spectra for $L = 18$, $t = 1$, $m = 0$, and varying 4-Fermi coupling V. The panels on the left are calculated with negative V, the panels on the right with positive V. The horizontal axis on each panel shows the momenta $2ap_{T_2}$ of the eigenstates, and the vertical axis show their energies E_n relative to the ground state energy E_0 individually for each 4-Fermi coupling V.*

$|V| = 10$. This structure disappears for moderate $|V|$. For $|V|$ around 0, again a band structure appears. For large $|V|$ the ground state is almost degenerated, as visualized for $|V| = 4$ and $|V| = 10$. For smaller $|V|$ the ground state is clearly unique, as visualized for $|V| = 0.2$ and $|V| = 2$.

The same situation is shown in Figure 3.10, but with "chiral" momenta ap_{T_1} according to eq. (3.148). As expected, for $V < 0$, the state which approaches the ground state has chiral momentum $ap_{T_1} = \pi$, while the ground state has $ap_{T_1} = 0$. The parity of both states is positive. For $V = -4$, the ground state energy is almost degenerated, while for $V = -2$ the energy gap is clearly visible. For $V > 0$, the first excited state has chiral momentum $ap_{T_1} = 0$ and negative parity. The ground state has $ap_{T_1} = 0$ too, but positive parity again.

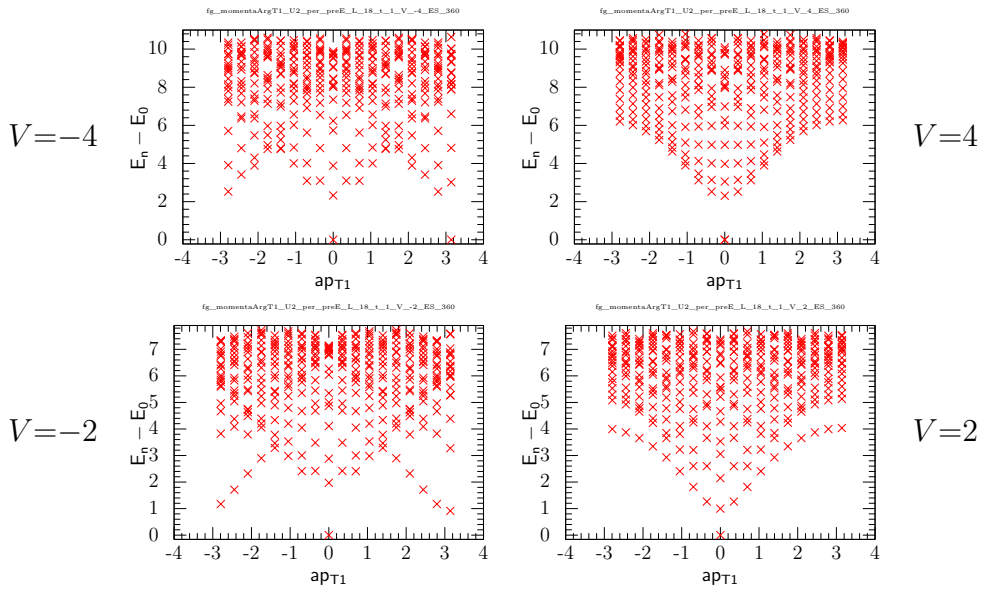

Figure 3.10.: *Spectra for $L = 18$, $t = 1$, $m = 0$, and varying 4-Fermi coupling V. The panels on the left are calculated with negative V, the panels on the right with positive V. The horizontal axis on each panel shows the "chiral" momenta ap_{T_1} of the eigenstates, and the vertical axis show their energies E_n relative to the ground state energy E_0 individually for each 4-Fermi coupling V.*

Figure 3.11 shows the logarithm of the first energy gap $E_1 - E_0$. On the horizontal axis the system size is varied from $L = 2$ to $L = 22$ in steps of 2. The exact diagonalization was performed in the regime with spontaneous chiral symmetry breaking ($V \ll 0$), in the spontaneous parity breaking regime ($V \gg 0$), and in a regime without spontaneous symmetry breaking around $V = 0$. The Hamiltonian parameters were set to $t = 1$ and $m = 0$. The exponential shrinking of the gap with growing system size for $|V| \gtrsim 5$ confirms the expected spontaneous symmetry breaking. For $|V| = 3$, the linear fit obviously does no more match, for $|V| = 2$ the gap is constant for $L \gtrsim 12$ for $|V| < 2$ the size of the gap is constant starting at even smaller system sizes.

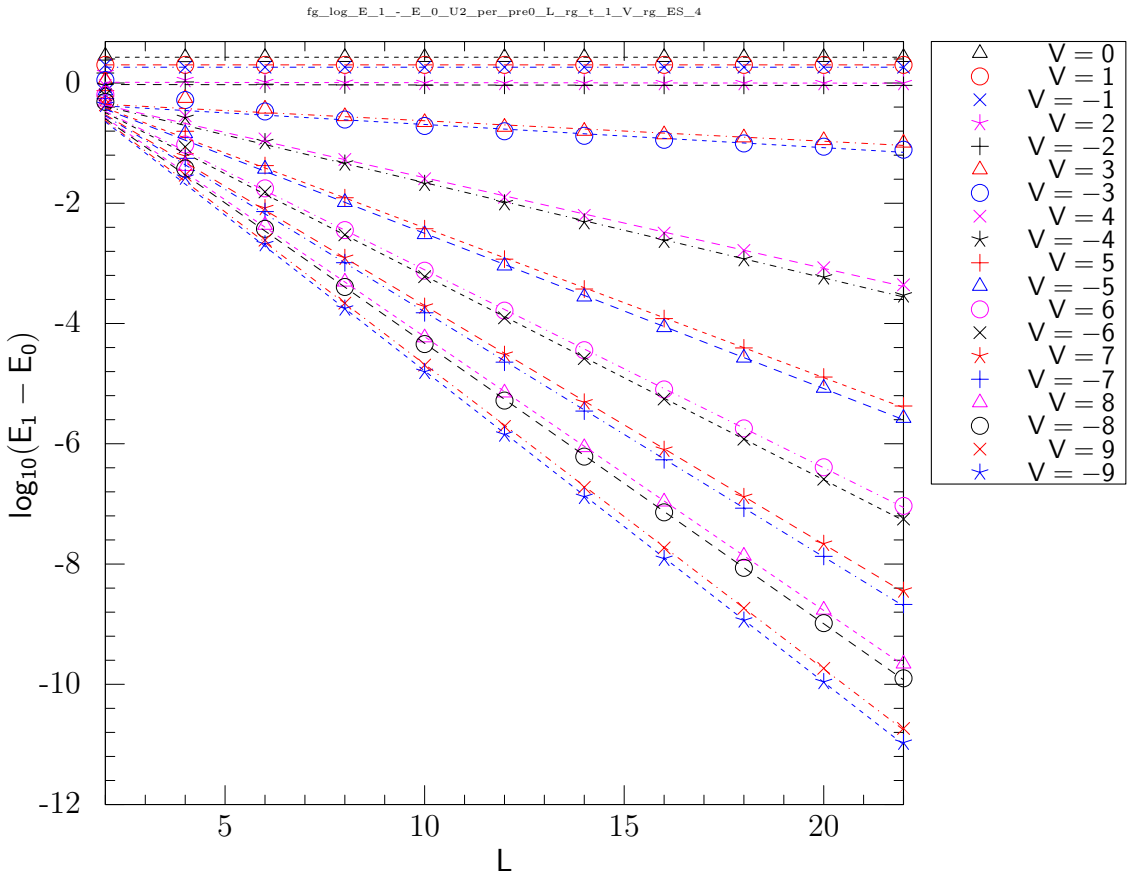

Figure 3.11.: *The vertical axis shows the logarithm to the base* 10 *of the difference of the energy* E_1 *of the first excited state to the ground state energy* E_0 *for* $U(2)$ *systems of length* $L = 2, 4, \ldots, 22$ *(horizontal axis). The parameters of the Hamiltonian defined in eq. (3.120) were set to* $t = 1$ *and* $m = 0$ *with varying local 4-Fermi coupling* V*.*

3.6. Real-time evolution of expansions

We now would like to investigate the real-time evolution of an initial "domain-wall" profile and an initial "hot spot" profile in the 1-dimensional periodic $U(2)$ quantum link model at zero temperature.

For the "domain-wall" profile we use a system of length $L = 20$ with the initial state

$$\Psi_{DW}(\tau = 0) = |14141414\mathbf{1}34141414142\rangle \tag{3.163}$$

at real-time $\tau = 0$ and Hamiltonian parameters $t = 1$, $m = 0$, and $V = -6$. So the ground state of the system is in the phase with spontaneous chiral symmetry breaking at zero temperature. We define the chiral order parameter

$$(\bar{\psi}\psi)_x = s_x \left\langle \psi_x^{i\dagger}\psi_x - \frac{N}{2} \right\rangle \tag{3.164}$$

where for $U(2)$ we have $N = 2$, and $s_x = (-1)^x$ was defined in eq. (3.14). For the above "domain-wall" profile, the chiral order parameter is

$$\langle\Psi_{DW}|(\bar{\psi}\psi)_x|\Psi_{DW}\rangle(\tau = 0) = \begin{cases} 1 & x < L/2 \\ 0 & x \in \{L/2, L\} \\ -1 & L/2 < x < L \end{cases} . \tag{3.165}$$

For $V \gg t, m$ the energy of the ground state of the form described in eq. (3.155) would be

$$E_{\text{ref}} = VL\,. \tag{3.166}$$

The energy of the initial state described in eq. (3.163) would be

$$E_{DW} = E_{\text{ref}} - 2V\,. \tag{3.167}$$

In the spectra in Figure 3.9 we read off that the second excited state has about the same energy for $V \gg t, m$. From Figure 3.11 we read off that the first excited state in a system of size $L = 20$ at $t = 1$, $m = 0$, and $V = -6$ has energy

$$E_1 - E_0 \approx 10^{-6} \ll E_{DW} = E_{\text{ref}} + 12\,. \tag{3.168}$$

Hence, we expect that the system with this initial state has so much energy, that it is no more in the chiral broken phase. Therefore, and since the initial state is very symmetric, the chiral order parameter should vanish for $\tau \gg 0$ which is confirmed by the following numerical simulation.

For the real-time evolution, the initial state described in eq. (3.163) is projected on the first 150 eigenstates of the system. The resulting gauge invariant and therefore valid "physical" state is shown in Figure 3.12 (black triangles). This procedure allows us to perform the real-time evolution for the moderately "large" system size $L = 20$ in much less than an hour even on a standard computer. (The eigenstates use about $2^{20} \times 8 \times$

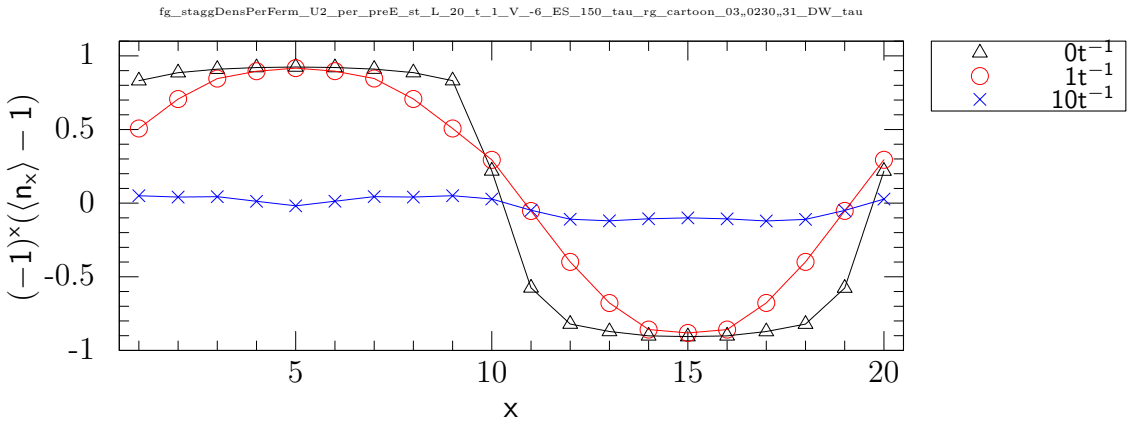

Figure 3.12.: *Real-time evolution of a "domain-wall" profile in a periodic system with* $L = 20$, $t = 1$, $m = 0$, $V = -6$ *at real-times* $\tau = 0, 1/t, 10/t$.

150 Bytes $\approx$ 1.3GB). While at real-time $\tau = 1/t$ the structure of the "domain-wall" is slightly smeared out, at $\tau = 10/t$ the structure has disappeared as expected.

For the "hot spot" profile, again in a periodic system of length $L = 20$ at zero temperature, we use the initial state

$$\Psi_{HS}(\tau = 0) = |14141414\mathbf{33}414141414\rangle \tag{3.169}$$

and again the Hamiltonian parameters $t = 1$, $m = 0$, and $V = -6$. The profile of the chiral order parameter is

$$\langle \Psi_{HS}|(\bar{\psi}\psi)_x|\Psi_{HS}\rangle(\tau = 0) = \begin{cases} 1 & x < L/2 \\ 0 & x \in \{L/2, L/2+1\} \\ 1 & L/2+1 < x \leq L \end{cases} . \tag{3.170}$$

For $V \gg t, m$ the initial state described in eq. (3.169) initial state has also energy

$$E_{HS} = E_{\text{ref}} - 2V . \tag{3.171}$$

The "hot spot" it is mainly in one chiral broken phase. We expect, that this phase remains dominating for $\tau \gg 0$. There is so much energy in the initial state, that the "hot spot" profile should dissolve.

Again, this cartoon profile is projected to the first 150 eigenstates of the system. The real-time evolution of this projected cartoon is shown in Figure 3.13. At real-time $\tau = 1/t$ the "hot spot" has visibly begun to expand and at $\tau = 10/t$ it has almost dissolved as expected.

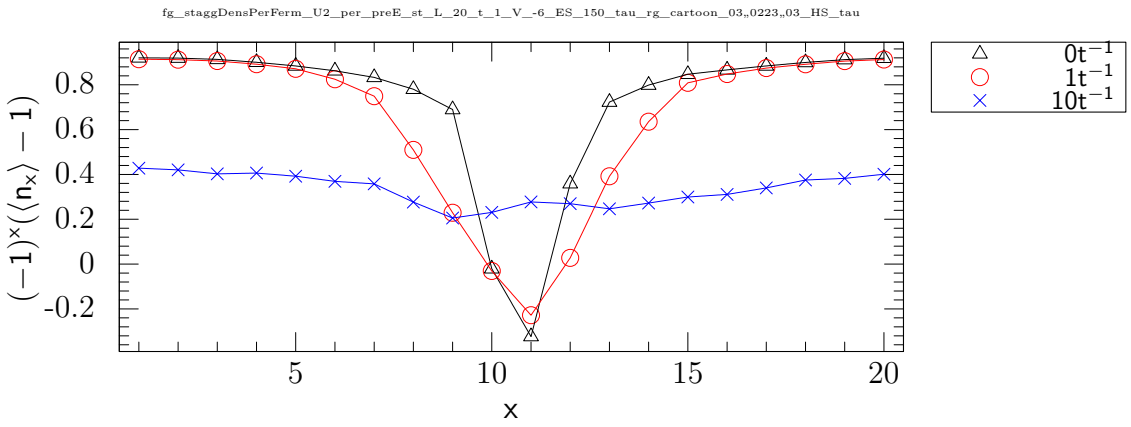

Figure 3.13.: *Real-time evolution of a "hot spot" profile in a periodic system with* $L = 20$, $t = 1$, $m = 0$, $V = -6$ *at real-times* $\tau = 0, 1/t, 10/t$.

3.7. Implementation on a quantum simulator

This section gives an overview of how the discussed $U(N)$ and $SU(N)$ quantum link model could be simulated in an ultracold atom setup in an optical lattice. The ideas are presented in [27] in more details. The implementation relies on a combination of experimental techniques, which were already realized in different laboratories. The individual techniques are tested and proved to work. However, the proposed implementation requires to combine them in a single experimental setup.

The main idea uses the $U(1)$ Gauss law which states that the number of rishons associated with a site together with the number of quarks at this site is a conserved quantity for $U(N)$ quantum link models. This allows the representation of quarks and rishons associated with a site by the same fermionic atoms. If the atom sits on a site, it represents a quark. If it sits on the link, next to that site, it is a rishon belonging to this site. For $(2+1)$ dimensions, this is symbolized as a cross in Figure 3.14. The $(1+1)$-dimensional version of the cross would be realized by a triple-well potential. At the extremities of the cross, the potential has to be high enough, such that the atoms belonging to that site can't escape to a neighboring site. Hence, for $U(N)$ models, the atom is restricted to the cross belonging to one site. This restriction already implements the $U(1)$ Gauss law.

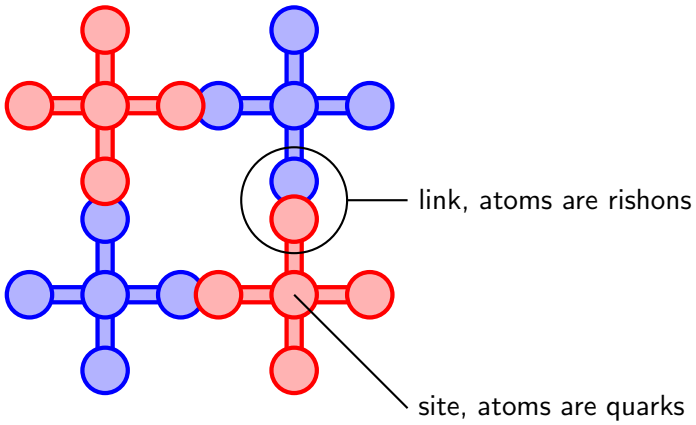

Figure 3.14.: *The red circles symbolize the allowed locations for alkaline-earth atoms with nuclear spin projection $m_I > 0$, while the blue circles symbolize the locations for $m_I < 0$. The atoms are confined to a cross. The center of a cross represents a site. Atoms sitting at the center of the cross model quarks, while atoms sitting at the extremities of a cross model rishons. The quantum links are located between sites, there where two crosses overlap each other. The atoms tunnel between the circles of a cross along the drawn connections.*

The freedom to hop from a quark to a rishon site and vice-versa directly represents the constituent quark operator $Q_{x,\pm q}$. The different colors are encoded by a clever choice of the used ultracold fermionic atoms. Fermionic alkaline-earth isotopes such as ^{87}Sr or ^{173}Yb, have a nuclear spin I with $2I+1$ Zeeman levels $m_I = -I, -I+1, \ldots, +I$. Their

unique property is that the actual Zeeman level of such an atom has almost no influence on its other properties [43, 44]. More precisely, the nuclear spin is decoupled from the electronic angular momentum and they exhibit an $SU(N)$ symmetry with N up to 10 [45]. Hence, the actual color can be encoded in the Zeeman levels.

To construct the full links, spoken in a geometrical picture, the crosses described above are placed such that their ends almost touch (see Figure 3.14). In order to distinguish the left and the right end of a link, e.g. atoms on crosses at even sites are encoded with positive nuclear spin states $m_I > 0$, while atoms associated with odd sites are encoded with negative $m_I < 0$.

At the regions where the ends of a link meet, by an appropriately designed potential the number of rishons on that link is enforced to $\mathcal{N}$.

The microscopic atomic Hamiltonian, which can be addressed by this setup is

$$\widetilde{H} = U \sum_{xy} \left(\mathcal{N}_{xy} - n\right)^2 + \tilde{t} \sum_{x,q} \left(s_{x,x+\hat{q}} Q_{x,+q} Q_{x+\hat{q},-q} + \text{H.c.}\right) + m \sum_{x} M_x \,. \tag{3.172}$$

For $U \gg \tilde{t}, m$ this forces the rishon numbers per link, and therefore the number of atoms per link, to n. In an ultracold atomic setup, this will be implemented by an appropriate design of the potential and using fermion repulsion. The microscopic Hamiltonian in eq. (3.172) induces the hopping term of the target Hamiltonian defined in eq. (3.13) in second order perturbation theory with

$$t = \frac{\tilde{t}^2}{U} \,. \tag{3.173}$$

For the $SU(N)$ model, which requires $\mathcal{N} = N$ atoms per link, the implementation has to be modified, such that if at one end of a link, there are N atoms of N different colors, and on the other side there are no atoms (compare to Figure 3.3), a hop of all atoms with a flip of their nuclear spin is allowed. The case for $N = \mathcal{N} = 2$ is discussed in [27].

3.8. Conclusions

In this project, our group constructed a quantum simulator for $U(N)$ and $SU(N)$ quantum link model in $(1 + 1)$ and $(2 + 1)$ dimensions. The extension to $(3 + 1)$ dimensions is straightforward from a conceptual point of view. However, it will be an additional challenge for the real experimental setup.

Some ingredients are missing to get a full lattice QCD simulator yet, namely a plaquette term, additional link terms and multi-component fermions with the appropriate chiral symmetries. However, the proposed setup provides a robust basis.

The quantum simulator would be realized by an experimental setup with ultracold alkaline-earth atoms in an optical lattice. While the $SU(N)$ Gauss law is implemented

exactly, this time it is the number of rishons on a link which is forced by a dominating coupling in the microscopic Hamiltonian. In practice the implementation of $SU(3)$ will be very challenging. For $SU(2)$ the realization of the $\det U_{xy}$ term, which corresponds to a two-particle transfer, is implemented as a Raman process [27].

As a benchmark, we calculated e.g. spontaneous chiral symmetry breaking and the real-time expansion of a "quark-gluon plasma" in a $(1+1)$-dimensional $U(2)$ gauge theory with exact diagonalization.

4. Ground state Rokhsar-Kivelson wave function for a quantum dimer model

4.1. Introduction

The underlying mechanism of high-T_c superconductivity is poorly understood. Anderson [30] formulated the idea of resonating valance bond (RVB) ground states. These are non-degenerated ground states with an equal weight superposition of nearest neighbor dimer coverings. The underlying idea is that spin 1/2 quantum degrees of freedom are defined on the sites of a 2-dimensional lattice. Nearest-neighbor spins pair up to form singlets. So-called dimers connect two neighboring sites to a singlet. This mechanism could potentially be related to Cooper pair formation.

The quantum dimer models, which were introduced in [29], model the physics of above resonating valence bond states. Their degrees of freedom are the so-called dimers, which live on the links between the sites and encode, if a valence bond is there or not.

Various lattice geometries were studied for this model [46–48]. It has no sign problem. However, there were only limited quantum Monte Carlo calculations. There were long-standing debates about the phase structure [31, 32]. Recently substantial progress was made [33]. A four-component order parameter was developed, which clearly distinguishes the various candidate phases. A new quantum Monte Carlo method for quantum dimer models on large lattices was developed. With these tools the phase diagram for the square lattice quantum dimer model was clarified. It turned out that putting a static charge-anti-charge pair into the periodic system split the flux between the charges into fractionalized flux 1/4 strands. This was analogous to the discovery of the flux 1/2 strands in the square lattice quantum link model [28] shortly before.

The ground state of the quantum dimer model can by constructed analytically at the so-called Rokhsar-Kivelson point [29]. The ground state is an equal weight superposition of all allowed dimer configurations. It is interesting to deform this ground state wave function. In the most general form this was done in [34]. In my work I investigate the properties of the square lattice quantum dimer model at an extended Rokhsar-Kivelson point in terms of its fluxes.

4.2. Quantum dimer model as a special case of the more general (2+1)-d quantum link model

The square lattice quantum dimer model is a (2+1)-dimensional system. A quantum state of the system corresponds to a weighted superposition of so-called dimer configurations. For an undoped system, such a configuration consists of dimers which connect two nearest-neighbor sites such that each site is touched by exactly one dimer. The problem of fully covering such a system by dimers is the same as fully covering an area with dominoes. Figure 4.1 shows a dimer covering with two doped sites. A plaquette with two parallel

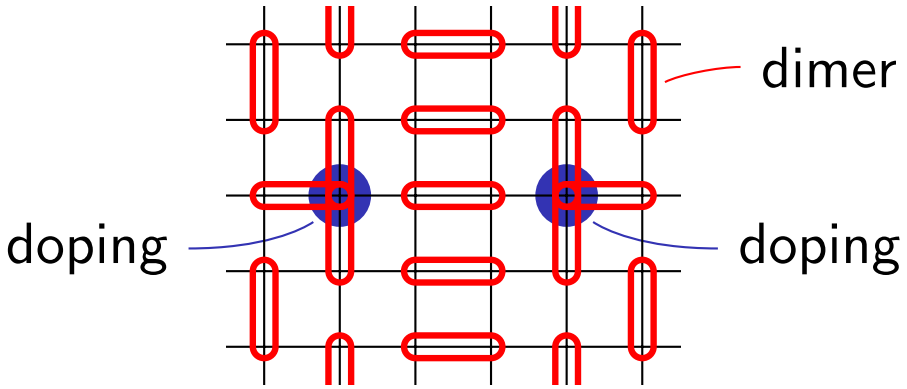

Figure 4.1.: *Quantum dimer model configuration with two doped sites. The black thin lines represent the lattice consisting of sites (where the lines cross) and links between the sites. The red ovals are dimers. A site is touched by one dimer. There are two defects denoted by two blue filled circles which are each touched by three dimers.*

dimers is called flippable. A plaquette flip consists of rotating the two parallel dimers by $\pm\pi/2$ around the center of the plaquette. If the plaquette flip was performed on an allowed dimer covering, the new configuration again will be allowed.

The time-independent local Hamiltonian

$$H = -J \sum_{\square} \left(U_{\square} + U_{\square}^{\dagger} \right) + J\lambda \sum_{\square} \left(U_{\square} + U_{\square}^{\dagger} \right)^2 \tag{4.1}$$

sums over plaquettes $\square$. The off-diagonal kinetic term with factor $-J$ relates dimer coverings which differ by one plaquette flip, where

$$U_{\square} |\,\square\,\rangle = |\,\square\,\rangle \,. \tag{4.2}$$

Up to the dimers on plaquette $\square$ the symbols $|\,\square\,\rangle$ and $|\,\square\,\rangle$ denote the same dimer covering. The diagonal potential term with factor $J\lambda$ counts the number of flippable plaquettes

$$\left(U_{\square} + U_{\square}^{\dagger} \right)^2 = U_{\square} U_{\square}^{\dagger} + U_{\square}^{\dagger} U_{\square} \,. \tag{4.3}$$

The quantum dimer model is a special case of the quantum link model. It corresponds to the $(2+1)$-d $U(1)$ quantum link model with staggered background charges [33]. It's a gauge model with spin 1/2 links and the Hamiltonian has the same form as in eq. (4.1) with $U_\square$ replaced by $\widetilde{U_\square}$. Other mappings of the quantum dimer model to $U(1)$ gauge theories were already worked out earlier [49, 50].

The plaquette operator $\widetilde{U_\square}$ acts on a clockwise around the plaquette flux configuration and flips it to a counter-clockwise around the plaquette configuration

$$\widetilde{U_\square}|\circlearrowright\rangle = |\circlearrowleft\rangle\,. \tag{4.4}$$

The quantum links carrying "electric" flux 1/2 are symbolized by $\longrightarrow$. The exact relation of $U_\square$ in the dimer model to $\widetilde{U_\square}$ in the link model alternates in a checkerboard pattern and is described in appendix A, but finally

$$\widetilde{U_\square} + \widetilde{U_\square}^\dagger = U_\square + U_\square^\dagger\,. \tag{4.5}$$

A dimer configuration can be mapped to a flux configuration by

$$E_{x,i} = (-1)^{x_1+x_2}\left(\frac{1}{2} - D_{x,i}\right), \quad i \in \{1,2\}\,, \quad x = (x_1, x_2) \in \mathbb{Z}\times\mathbb{Z} \tag{4.6}$$

up to an overall charge conjugation. A dimer which touches site x and the neighboring site in direction i is denoted by $D_{x,i} \in \{0,1\}$. The value of the resulting flux starting at site x and flowing in direction i is denoted by $E_{x,i} \in \{-1/2, 1/2\}$. The lattice spacing is put to $a = 1$. Figure 4.2 illustrates the terminology used and Figure 4.3 shows an

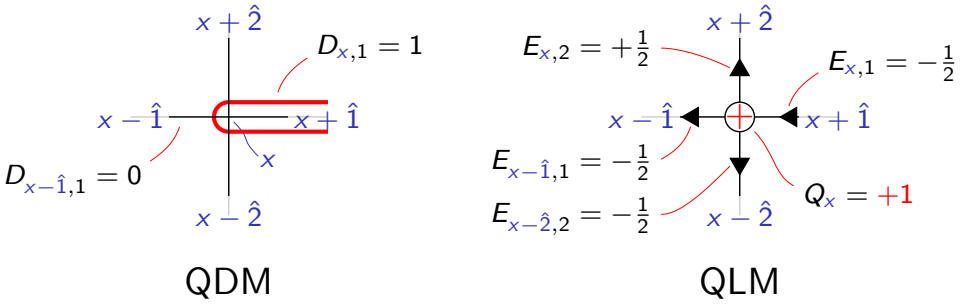

Figure 4.2.: Left panel: *in the quantum dimer model a site x is touched by one dimer (indicated by the truncated red oval). The positions of the neighboring sites are labeled in blue too.* Right panel: *the same corresponding configuration in the quantum link model with charge $Q_x = +1$ at site x, note that positive fluxes flow from left to right or from bottom to top.*

example configuration with dimers and corresponding fluxes.

The local Gauss law of the quantum link model is realized in the quantum dimer model by fixing the number of dimers which touch a site

$$N_x|\psi\rangle = \sum_i \left(D_{x,i} + D_{x-\hat{i},i}\right)|\psi\rangle = n_x|\psi\rangle\,. \tag{4.7}$$

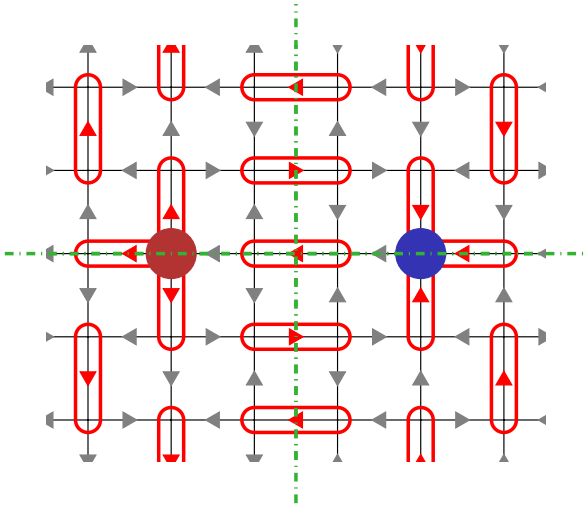

Figure 4.3.: *Example dimer and flux configuration in a system doped with two static double external charges ±2. The green dash dotted lines indicate the remaining reflection symmetries. For the link model the reflection at the vertical axis is accompanied by a charge conjugation.*

The operator N_x counts the number of dimers touching site x. Like N_x, the generator of infinitesimal gauge transformations of the link model

$$\begin{aligned} G_x &= \sum_i \left(E_{x,i} - E_{x-\hat{i},i} \right) \\ &= (-1)^{x_1+x_2} \sum_i \left(1 - D_{x,i} - D_{x-\hat{i},i} \right) \\ &= (-1)^{x_1+x_2} \left(2 - N_x \right) \end{aligned} \tag{4.8}$$

commutes with the Hamiltonian

$$\begin{aligned} [H, N_x] &= 0 \,, \\ [H, G_x] &= 0 \,. \end{aligned} \tag{4.9}$$

In the undoped quantum link model $n_x = 1$ for each site. In the spin 1/2 quantum link model this amounts in a modified local Gauss law with a staggering of the background charges

$$G_x |\psi\rangle = Q_x |\psi\rangle \,, \quad Q_x = (-1)^{(x_1+x_2)} \,. \tag{4.10}$$

Figure 4.4 shows the details of a flip and how the total fluxes

$$E_i := \frac{1}{L_i} \sum_x E_{x,i} \tag{4.11}$$

are conserved. These are fluxes through a horizontal or vertical interface and they are the conserved quantity of the global $U(1)^2$ center symmetry.

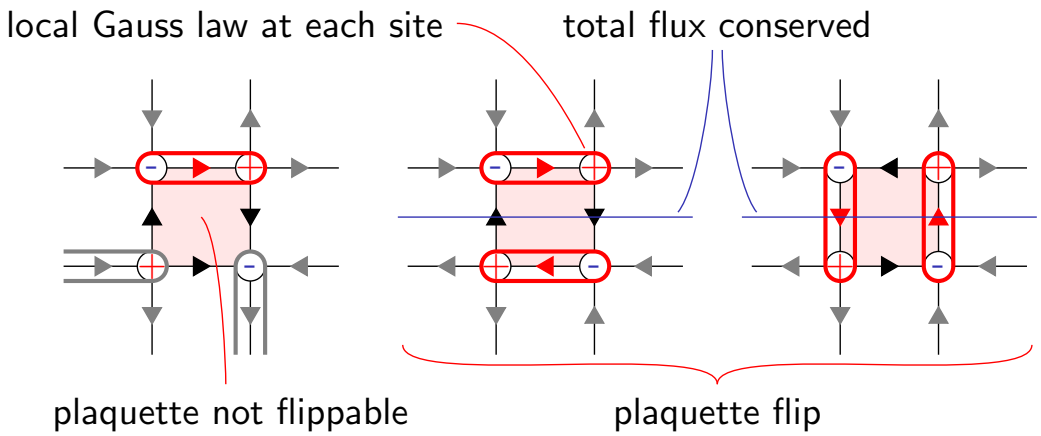

Figure 4.4.: *The local Gauss law is fulfilled on all sites. The plaquette in the* left panel *is not flippable. It has no parallel dimers. The plaquettes in the* center panel *and the* right panel *are flippable. The dimers are parallel which corresponds to an around the plaquette flux. A plaquette flip preserves the local Gauss law and the total flux.*

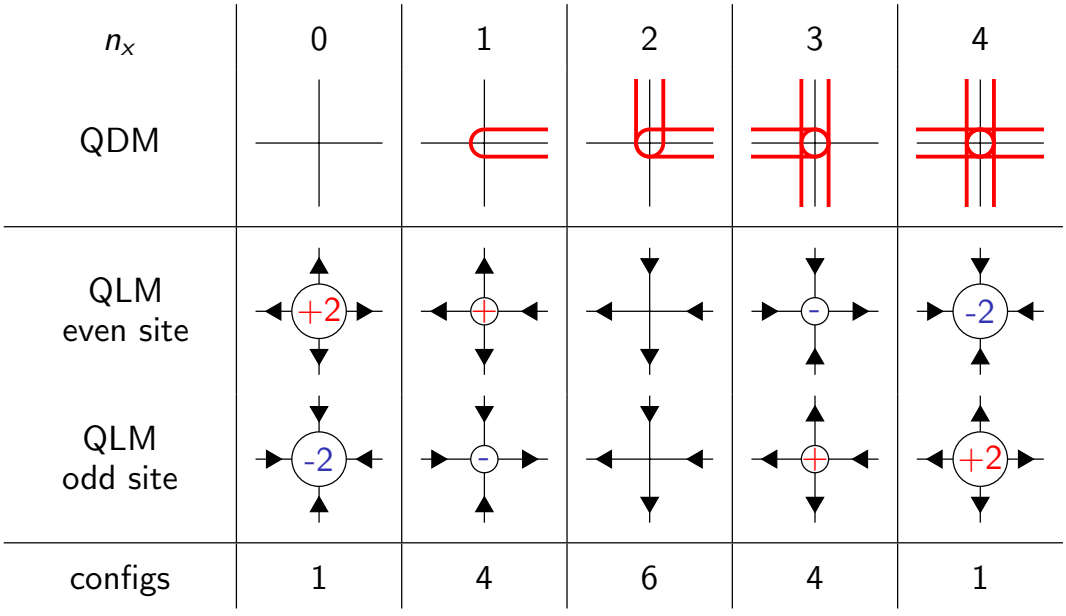

Figure 4.5.: *Relations between quantum dimer (upper part) and quantum link configurations (middle part). The upper part shows dimer configurations on a site for different n_x. The middle part consists of the corresponding flux and charge configurations.*

Figure 4.5 shows the generalized relations between dimers, fluxes and charges of the models. The role of even and odd sites can be interchanged, which corresponds to the mentioned overall charge conjugation. With the same argumentation the quantum dimer model with $n_x = 3$ is equivalent to the one with $n_x = 1$. Rotating the depicted configurations by $\pi/2$ results in additional configurations with the same n_x. In the last row the number of such configurations with the same n_x is denoted.

The quantum dimer model with constant n_x is invariant under translations by one lattice spacing T_1 and T_2

$$^{T_i}D_{x,j} = D_{x+\hat{i},j} \tag{4.12}$$

The associated momentum takes values

$$p_i = \frac{2\pi}{aL_i}\left(k_i - \frac{L_i}{2}\right) \tag{4.13}$$

with

$$k_i \in \{1, 2, \ldots, L_i\}. \tag{4.14}$$

The translations correspond to CT_1 and CT_2 in the quantum link model with staggered background charges, where C denotes charge conjugation

$$^{CT_i}E_{x,j} = -E_{x+\hat{i},j}\,. \tag{4.15}$$

Additional symmetries are spatial rotations by $\pi/2$ around a site and spatial rotations by $\pi/2$ around a plaquette center. We call O the rotation by $\pi/2$ around the origin

$$\begin{aligned}
^{O}D_{x,1} &= D_{(-x_2,x_1),2}\,,\\
^{O}D_{x,2} &= D_{(-x_2,x_1),-1} = D_{(1-x_2,x_1),1}\,,\\
^{O}E_{x,1} &= E_{(-x_2,x_1),2}\,,\\
^{O}E_{x,2} &= E_{(-x_2,x_1),-1} = -E_{(1-x_2,x_1),1}\,,
\end{aligned} \tag{4.16}$$

and O' the rotation by $\pi/2$ around $(\frac{1}{2}, \frac{1}{2})$

$$\begin{aligned}
^{O'}D_{x,1} &= D_{(1-x_2,x_1),2}\,,\\
^{O'}D_{x,2} &= D_{(1-x_2,x_1),-1} = D_{(-x_2,x_1),1}\,.
\end{aligned} \tag{4.17}$$

In the quantum link model, the latter are accompanied by a charge conjugation, which we denote by CO'

$$\begin{aligned}
^{CO'}E_{x,1} &= -E_{(1-x_2,x_1),2}\,,\\
^{CO'}E_{x,2} &= -E_{(1-x_2,x_1),-1} = E_{(-x_2,x_1),1}\,.
\end{aligned} \tag{4.18}$$

Under reflections R_1 and R_2 at an axis in x_1 and x_2 direction the dimers transform as

$$\begin{aligned}
^{R_1}D_{x,1} &= D_{(x_1,-x_2),1}\,,\\
^{R_1}D_{x,2} &= D_{(x_1,-x_2),-2} = D_{(x_1,-x_2-1),2}\,,\\
^{R_2}D_{x,1} &= D_{(-x_1,x_2),-1} = D_{(-x_1-1,x_2),1}\,,\\
^{R_2}D_{x,2} &= D_{(-x_1,x_2),2}\,,
\end{aligned} \tag{4.19}$$

and the electric fluxes as

$$\begin{aligned}
{}^{R_1}E_{x,1} &= E_{(x_1,-x_2),1}\,,\\
{}^{R_1}E_{x,2} &= E_{(x_1,-x_2),-2} = -E_{(x_1,-x_2-1),2}\,,\\
{}^{R_2}E_{x,1} &= E_{(-x_1,x_2),-1} = -E_{(-x_1-1,x_2),1}\,,\\
{}^{R_2}E_{x,2} &= E_{(-x_1,x_2),2}\,.
\end{aligned} \tag{4.20}$$

Under reflections R'_1 at $x_1 = \frac{1}{2}$ and R'_2 at $x_2 = \frac{1}{2}$ the dimer covering transforms as

$$\begin{aligned}
{}^{R'_1}D_{x,1} &= D_{(x_1,1-x_2),1}\,,\\
{}^{R'_1}D_{x,2} &= D_{(x_1,1-x_2),-2} = D_{(x_1,-x_2),2}\,,\\
{}^{R'_2}D_{x,1} &= D_{(1-x_1,x_2),-1} = D_{(-x_1,x_2),1}\,,\\
{}^{R'_2}D_{x,2} &= D_{(1-x_1,x_2),2}\,.
\end{aligned} \tag{4.21}$$

The transformation of the electric fluxes is accompanied by a charge conjugation

$$\begin{aligned}
{}^{CR'_1}E_{x,1} &= -E_{(x_1,1-x_2),1}\,,\\
{}^{CR'_1}E_{x,2} &= -E_{(x_1,1-x_2),-2} = E_{(x_1,-x_2),2}\,,\\
{}^{CR'_2}E_{x,1} &= -E_{(1-x_1,x_2),-1} = E_{(-x_1,x_2),1}\,,\\
{}^{CR'_2}E_{x,2} &= -E_{(1-x_1,x_2),2}\,.
\end{aligned} \tag{4.22}$$

A flux string can be created by adding a double positive and a double negative static external charge to the system. One charge is located at an $(x_1 + x_2)$ even and the other at an $(x_1 + x_2)$ odd site such that the background charge in the link model is just inverted at these two sites. In the dimer model this results in two sites which are touched by three dimers. The situation is shown in Figure 4.3.

4.3. Candidate phases

There are two known (and two speculated) phases in the quantum dimer model. For systems with large negative $J\lambda$ (see Hamiltonian in eq. (4.1)) the columnar phase with a maximal number of flippable plaquettes is realized (first row in Figure 4.7). Half of the plaquettes are flippable and the total flux in the columnar phase is $(0, 0)$. So the ground state of the system is in the flux $(0, 0)$ sector for $J\lambda \ll 0$.

For systems with large positive $J\lambda$ a staggered phase without flippable plaquettes has minimal energy. The total flux in the staggered phase is maximal in one direction. In the total flux $(0, 0)$ sector various local staggered phase realization separated by domain-walls could be expected.

The plaquettes which reside on the dual lattice

$$\widetilde{x} = \left(x_1 + \frac{1}{2}, x_2 + \frac{1}{2}\right)\,, \tag{4.23}$$

are divided into sublattices A, B, C, and D. The association of the individual plaquettes with the sublattices consistent with [33] is listed in Table 4.1 and is also shown in Figure 4.6.

sublattice	$\widetilde{x}_1 - \frac{1}{2}$	$\widetilde{x}_2 - \frac{1}{2}$	$\widetilde{x}_1 + \widetilde{x}_2$
$\widetilde{x} \in A$	odd	even	even
$\widetilde{x} \in B$	even	even	odd
$\widetilde{x} \in C$	odd	odd	odd
$\widetilde{x} \in D$	even	odd	even

Table 4.1.: *Sublattices A, B, C, and D.*

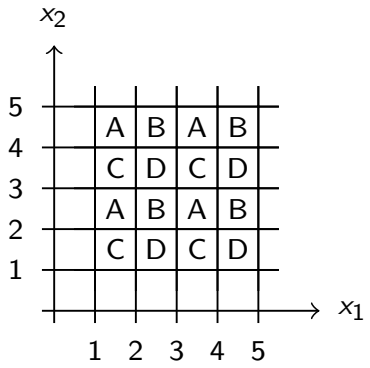

Figure 4.6.: *Sublattices A, B, C, and D.*

The candidate phase configurations of each row of Figure 4.7 are related from left to right by rotations by $\pi/2$ around a site with $x_1 + x_2$ even. The naming conventions for the phases were introduced in [33]. While the columnar phase could appear as a superposition of the four pure columnar cartoon phases, each staggered phase lives in a different topological sector of the quantum dimer model.

There was a misinterpreted numerical evidence of an additional so-called plaquette phase which is shown in the last row of Figure 4.7. A plaquette cartoon configuration can be achieved by starting out of a columnar cartoon configuration and flipping half of the plaquettes in a checkerboard pattern. There are four possible bulk realizations with individually resonating dimers on one of the sublattices. If for example the dimers resonate on sublattice A, there is no correlation between the plaquettes on this sublattice. While in the columnar phase half of the plaquettes are flippable, in the plaquette phase only a quarter of them are. The plaquette phase seemed to appear for lattices with sizes up to 48×48 [31]. Other groups came to the conclusion that a mixed phase interpolating between columnar and plaquette states appears [32]. As already mentioned, due to the introduction of a new Monte Carlo method and a four-component order parameter which is discussed in the next section our group came to the conclusion that there is no mixed phase [33].

A further observation which can be made in Figure 4.7 is, that the plaquette phases, at

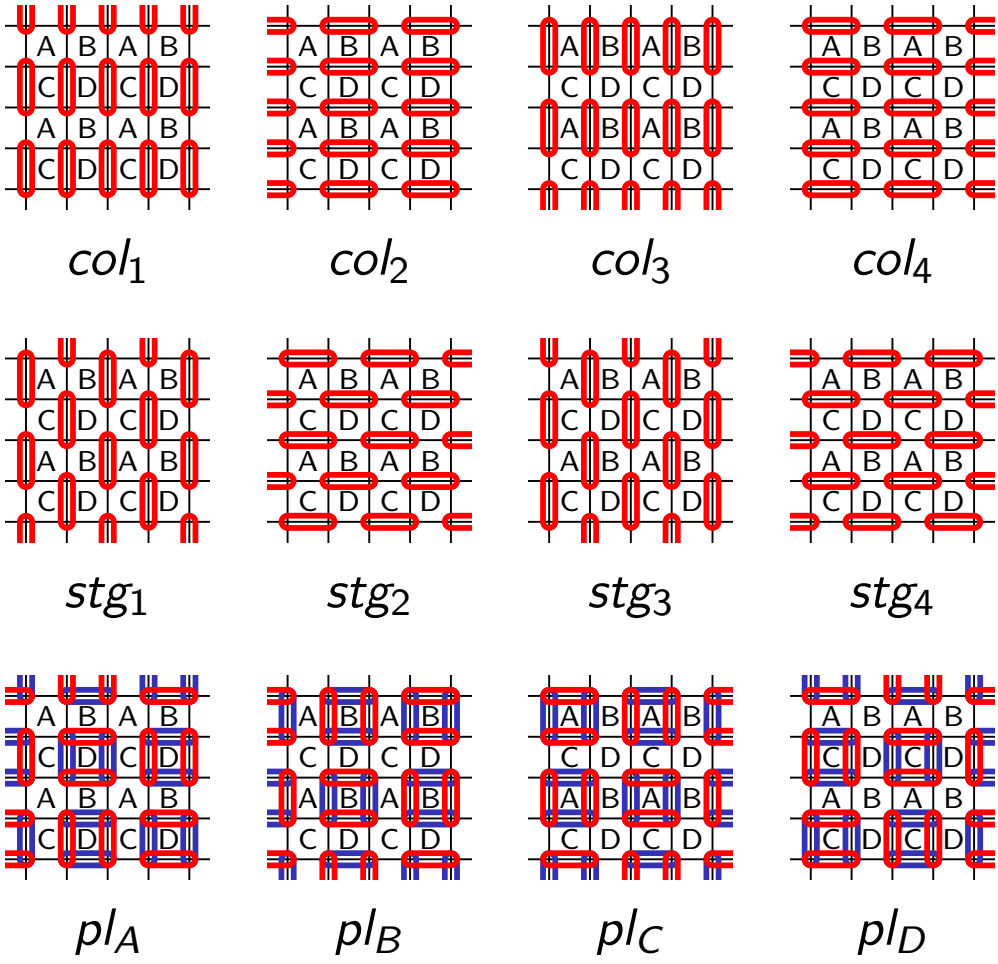

Figure 4.7.: *Cartoon configurations of the various candidate phases in the quantum dimer model. The individual configurations are uniquely named. The sublattices denoted by A, B, C, and D are shown as a guide to the eye. The configurations in each row are related by rotations O by $\pi/2$ around a site with $x_1 + x_2$ even.* Top panel: *columnar phase cartoon configurations col_1, col_2, col_3, col_4, with total fluxes zero.* Center panel: *staggered phase cartoon configurations stg_1, stg_2, stg_3, stg_4, with maximal flux in a different direction each.* Bottom panel: *bulk plaquette phase configurations pl_A, pl_B, pl_C, pl_D. The overlap of red and blue parallel dimers symbolize individually resonating pairs of dimers.*

least from a graphical point of view, are related to the columnar phases. The plaquette phase realization pl_A has graphical contributions from the columnar phases col_1 and col_2. On the other hand, the graphical intersection of the columnar phases pl_A and pl_B results in the columnar phase col_2. The columnar and plaquette candidate phase realizations can be ordered in a circular structure

$$\ldots\ ,\ col_1\ ,\ pl_A\ ,\ col_2\ ,\ pl_B\ ,\ col_3\ ,\ pl_C\ ,\ col_4\ ,\ pl_D\ ,\ col_1\ ,\ \ldots \tag{4.24}$$

Table 4.2 lists how the various symmetry transformations act on columnar and on plaquette phases.

S	CT_1	CT_2	O	CO'	R_1	R_2
${}^S col_1$	col_1	col_3	col_2	col_4	col_3	col_1
${}^S col_2$	col_4	col_2	col_3	col_3	col_2	col_4
${}^S col_3$	col_3	col_1	col_4	col_2	col_1	col_3
${}^S col_4$	col_2	col_4	col_1	col_1	col_4	col_2
${}^S pl_A$	pl_D	pl_B	pl_B	pl_C	pl_B	pl_D
${}^S pl_B$	pl_C	pl_A	pl_C	pl_B	pl_A	pl_C
${}^S pl_C$	pl_B	pl_D	pl_D	pl_A	pl_D	pl_B
${}^S pl_D$	pl_A	pl_C	pl_A	pl_D	pl_C	pl_A

Table 4.2.: *This table corresponds to Tables II and III in [33]. It shows how the symmetry transformations $S = CT_1$, CT_2, O, CO', R_1, and R_2 act on the columnar phases col_1, col_2, col_3, col_4, and on the plaquette phases pl_A, pl_B, pl_C, and pl_D.*

4.4. Four-component order parameter

We want to be able to distinguish the four cartoon realizations of the columnar phase and the plaquette phase. Therefore, we will construct a four-component order parameter based on a dual height representation associated with a dimer configuration. Each plaquette gets decorated by a degree of freedom which is known as a height variable

$$h_{\widetilde{x}} \in \{-1, 1\}\,. \tag{4.25}$$

The dual height representation was already used in [28] to construct a two-component order parameter for the quantum link model. The heights used in this document are related to the ones in [33] by

$$h_{\widetilde{x}} = 2h^{A,D}_{\widetilde{x}} - 1 = 2h^{B,C}_{\widetilde{x}}\,. \tag{4.26}$$

For each dimer covering there are exactly two height coverings which are related by inverting all heights together. The actual rules work if each site is touched by one or three dimers. So configurations with external static charges can be decorated with heights too.

The rules of decoration depend on an arbitrarily chosen background of Dirac strings. These strings can be interpreted as a flux of value one which connects each charge of the quantum link model background charges to an anti-charge of the background. The Dirac string covering obeys the same rules as a dimer covering with one string touching each site. We choose a staggered Dirac string pattern in direction 2. The strings are located on vertical links $(x, x+\hat{2})$ with $x_1 + x_2$ odd and are denoted by a green box in Figure 4.8.

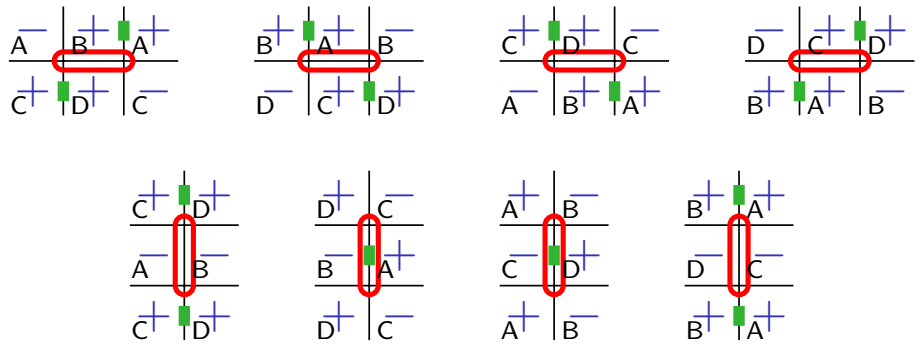

Figure 4.8.: *Realizations of the height covering rules for sites touched by one dimer. The green rectangles indicate Dirac strings.*

The height variables are related to the dimers by

$$\begin{aligned} D_{x,1} &= \frac{1}{2}\left(1 + h_{\widetilde{x}} h_{\widetilde{x}-\hat{2}}\right) , \\ D_{x,2} &= \frac{1}{2}\left(1 + (-1)^{x_1+x_2} h_{\widetilde{x}} h_{\widetilde{x}-\hat{1}}\right) , \end{aligned} \tag{4.27}$$

which corresponds to

$$\begin{aligned} E_{x,1} &= -\frac{1}{2}(-1)^{x_1+x_2} h_{\widetilde{x}} h_{\widetilde{x}-\hat{2}} \\ &\quad \left(= \left(h^{X}_{\widetilde{x}} - h^{X'}_{\widetilde{x}-\hat{2}}\right) \mod 2\right) , \\ E_{x,2} &= -\frac{1}{2} h_{\widetilde{x}} h_{\widetilde{x}-\hat{1}} \\ &\quad \left(= (-1)^{x_1+x_2} \left(h^{X}_{\widetilde{x}} - h^{X'}_{\widetilde{x}-\hat{1}}\right) \mod 2\right) . \end{aligned} \tag{4.28}$$

This system results in consistent height coverings as shown in Figure 4.8.

In Figure 4.9 all 16 possible height coverings around a single site are shown. For 8 of them, one dimer touches the site, for the remaining 8 height coverings three dimers touch the site. This Figure 4.9 illustrates that a dimer pattern has to rotate two times around a site to reproduce the initial height pattern. The consequence is that the repeating phase sequence, which was given in eq. (4.24), for height-based order parameters has to be extended to

$$\begin{aligned} &\ldots , col_1 , pl_A , col_2 , pl_B , col_3 , pl_C , col_4 , pl_D , \\ &\quad col'_1 , pl'_A , col'_2 , pl'_B , col'_3 , pl'_C , col'_4 , pl'_D , col_1 , \ldots \end{aligned} \tag{4.29}$$

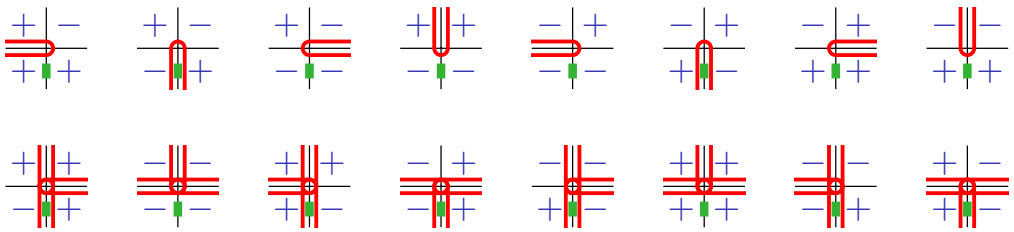

Figure 4.9.: *These are all 16 possible height coverings around a site. The green rectangle indicates a Dirac string. In the first row one dimer touches the site. In the second row three dimers touch the site. From left to right the dimer pattern is rotated by $\pi/2$ for each drawing. The pattern has to rotate two times around the site to reproduce the initial height covering.*

Due to the staggered background Dirac strings the symmetry transformations on the heights are endowed with alternating sign factors. There are additional sign factors which we will fix later on.

$$\begin{aligned}
{}^{CR'_1}h_{\widetilde{x}} &= h_{(\widetilde{x}_1,-\widetilde{x}_2)+\hat{2}}\,,\\
{}^{CR'_2}h_{\widetilde{x}} &= (-1)^{\widetilde{x}_1-\frac{1}{2}}\,h_{(-\widetilde{x}_1,\widetilde{x}_2)+\hat{1}}\,,\\
{}^{R_1}h_{\widetilde{x}} &= s_{R_1}(-1)^{\widetilde{x}_1+\frac{1}{2}}\,h_{(\widetilde{x}_1,-\widetilde{x}_2)}\,,\\
{}^{R_2}h_{\widetilde{x}} &= h_{(-\widetilde{x}_1,\widetilde{x}_2)}\,,\\
{}^{O}h_{\widetilde{x}} &= s_O(x_1,x_2)h_{(-\widetilde{x}_2,\widetilde{x}_1)}\,.
\end{aligned} \tag{4.30}$$

In appendix B we check whether these height transformation rules are indeed correct. There also the sign

$$s_O(x_1,x_2) = \begin{cases} s_{O_0}(-1)^{(x_1+x_2)/2} & \text{if } x_1+x_2 \text{ is even,}\\ s_{O_0}(-1)^{(x_1+x_2+1)/2} & \text{if } x_1+x_2 \text{ is odd.}\end{cases} \tag{4.31}$$

is derived. This matches with Figure 4.9 for

$$s_{O_0} = -1\,. \tag{4.32}$$

We reformulate the sign of the rotation O as

$$\begin{aligned}
s'_O(y) &= \begin{cases} s_{O_0}(-1)^{(y-1)/2} & \text{if } y \text{ is odd,}\\ s_{O_0}(-1)^{y/2} & \text{if } y \text{ is even.}\end{cases}\\
&= \begin{cases} (-1)^{(y+1)/2} & \text{if } y \text{ is odd,}\\ (-1)^{y/2+1} & \text{if } y \text{ is even.}\end{cases}.
\end{aligned} \tag{4.33}$$

We rewrite

$${}^{O}h_{\widetilde{x}} = s'_O(\widetilde{x}_1+\widetilde{x}_2)h_{(-\widetilde{x}_2,\widetilde{x}_1)}\,. \tag{4.34}$$

Applying two times a reflection leads back to the initial dimer covering

$${}^{(CR'_1)^2}h_{\widetilde{x}} = {}^{(CR'_2)^2}h_{\widetilde{x}} = {}^{R_1^2}h_{\widetilde{x}} = {}^{R_2^2}h_{\widetilde{x}} = h_{\widetilde{x}}\,. \tag{4.35}$$

We use relations between the symmetry transformations

$$\begin{aligned} CT_1 &= CR_2' R_2 \,, \\ CT_2 &= CR_1' R_1 \,, \\ O^2 &= s_{O^2}(\widetilde{x}_1 + \widetilde{x}_2) R_1 R_2 \,, \\ (CO')^2 &= s_{(CO')^2}(\widetilde{x}_1 + \widetilde{x}_2) CR_1' \, CR_2' \,, \end{aligned} \tag{4.36}$$

such that

$$\begin{aligned} {}^{CT_1}h_{\widetilde{x}} &= {}^{CR_2'}h_{(-\widetilde{x}_1,\widetilde{x}_2)} = (-1)^{\widetilde{x}_1+\frac{1}{2}} \, h_{\widetilde{x}+\hat{1}} \,, \\ {}^{CT_2}h_{\widetilde{x}} &= s_{R_1}(-1)^{\widetilde{x}_1+\frac{1}{2}} \, {}^{CR_1'}h_{(\widetilde{x}_1,1-\widetilde{x}_2)} = s_{R_1}(-1)^{\widetilde{x}_1+\frac{1}{2}} \, h_{\widetilde{x}+\hat{2}} \,, \\ {}^{(CT_1)^2}h_{\widetilde{x}} &= -h_{\widetilde{x}+2\hat{1}} \,, \\ {}^{(CT_2)^2}h_{\widetilde{x}} &= h_{\widetilde{x}+2\hat{2}} \,, \\ {}^{CT_1CT_2}h_{\widetilde{x}} &= s_{R_1}(-1)^{\widetilde{x}_1+\frac{1}{2}} \, {}^{CT_1}h_{\widetilde{x}+\hat{2}} = s_{R_1} h_{\widetilde{x}+\hat{1}+\hat{2}} \,, \\ {}^{CT_2CT_1}h_{\widetilde{x}} &= (-1)^{\widetilde{x}_1+\frac{1}{2}} \, {}^{CT_2}h_{\widetilde{x}+\hat{1}} = -s_{R_1} h_{\widetilde{x}+\hat{1}+\hat{2}} \,, \\ {}^{(CT_1CT_2)^2}h_{\widetilde{x}} &= -{}^{(CT_1)^2(CT_2)^2}h_{\widetilde{x}+\hat{1}+\hat{2}} = h_{\widetilde{x}+2\hat{1}+2\hat{2}} \,. \end{aligned} \tag{4.37}$$

The last line is a check, since CT_1CT_2 maps the background Dirac string pattern on itself, and therefore the sign of $(CT_1CT_2)^2$ has to be positive. We continue to use the symmetry relations

$$\begin{aligned} s_{O^2}(\widetilde{x}_1 + \widetilde{x}_2) \, {}^{O^2}h_{\widetilde{x}} &= {}^{R_1}h_{(-\widetilde{x}_1,\widetilde{x}_2)} = s_{R_1}(-1)^{\widetilde{x}_1-\frac{1}{2}} \, h_{-\widetilde{x}} \,, \\ {}^{O^4}h_{\widetilde{x}} &= -s_{O^2}(\widetilde{x}_1 + \widetilde{x}_2) s_{O^2}(-\widetilde{x}_1 - \widetilde{x}_2) \, h_{\widetilde{x}} \,, \\ s_{(CO')^2}(\widetilde{x}_1 + \widetilde{x}_2) \, {}^{(CO')^2}h_{\widetilde{x}} &= (-1)^{\widetilde{x}_1-\frac{1}{2}} \, {}^{CR_1'}h_{(-\widetilde{x}_1,\widetilde{x}_2)+\hat{1}} = (-1)^{\widetilde{x}_1-\frac{1}{2}} h_{-\widetilde{x}+\hat{1}+\hat{2}} \,, \\ {}^{(CO')^4}h_{\widetilde{x}} &= s_{(CO')^2}(\widetilde{x}_1 + \widetilde{x}_2) s_{(CO')^2}(2 - \widetilde{x}_1 - \widetilde{x}_2) h_{\widetilde{x}} \,. \end{aligned} \tag{4.38}$$

The double covering of dimer configurations with height configurations as shown in Figure 4.9 and as expressed in the sequence in eq. (4.29) leads to

$$O^4 = -1 \,, \tag{4.39}$$

and it follows

$$s_{O^2}(y) s_{O^2}(-y) = 1 \,. \tag{4.40}$$

The rotation $(CO')^2$ leads to the same dimer covering, such that

$$(CO)^4 = 1 \,, \tag{4.41}$$

and therefore

$$s_{(CO')^2}(y) s_{(CO')^2}(2 - y) = 1 \,. \tag{4.42}$$

From

$$\begin{aligned} {}^{O^2}h_{\widetilde{x}} &= s_O'(\widetilde{x}_1 + \widetilde{x}_2) \, {}^{O}h_{(-\widetilde{x}_2,\widetilde{x}_1)} \\ &= s_O'(\widetilde{x}_1 + \widetilde{x}_2) s_O'(\widetilde{x}_1 - \widetilde{x}_2) h_{-\widetilde{x}} = (-1)^{\widetilde{x}_1-\frac{1}{2}} h_{-\widetilde{x}} \\ &\stackrel{!}{=} s_{O^2}(\widetilde{x}_1 + \widetilde{x}_2) s_{R_1}(-1)^{\widetilde{x}_1-\frac{1}{2}} h_{-\widetilde{x}} \end{aligned} \tag{4.43}$$

we conclude that

$$s_{O^2}(\widetilde{x}_1 + \widetilde{x}_2) = s_{R_1} \,. \tag{4.44}$$

With the remaining relations between the symmetry transformations

$$\begin{aligned} CO' &= CT_1\, O \,, \\ O &= CO'\, CT_2 \end{aligned} \tag{4.45}$$

we calculate

$$\begin{aligned} {}^{CO'}h_{\widetilde{x}} &= s'_O(\widetilde{x}_1 + \widetilde{x}_2)^{CT_1} h_{(-\widetilde{x}_2,\widetilde{x}_1)} = s'_O(\widetilde{x}_1 + \widetilde{x}_2)(-1)^{\widetilde{x}_2 - \frac{1}{2}} h_{(-\widetilde{x}_2,\widetilde{x}_1)+\hat{1}} \,, \\ {}^{(CO')^2}h_{\widetilde{x}} &= -(-1)^{\widetilde{x}_1+\widetilde{x}_2} s'_O(\widetilde{x}_1 + \widetilde{x}_2) s'_O(1 + \widetilde{x}_1 - \widetilde{x}_2) h_{-\widetilde{x}+\hat{1}+\hat{2}} \\ &= -(-1)^{2\widetilde{x}_1+\widetilde{x}_2+\frac{1}{2}} h_{-\widetilde{x}+\hat{1}+\hat{2}} \\ &\stackrel{!}{=} s_{(CO')^2}(\widetilde{x}_1 + \widetilde{x}_2)(-1)^{\widetilde{x}_1 - \frac{1}{2}} h_{-\widetilde{x}+\hat{1}+\hat{2}} \,, \end{aligned} \tag{4.46}$$

from which

$$s_{(CO')^2}(\widetilde{x}_1 + \widetilde{x}_2) = (-1)^{\widetilde{x}_1+\widetilde{x}_2} \,. \tag{4.47}$$

For consistency we check

$$\begin{aligned} {}^{O}h_{\widetilde{x}} &= s_{R_1}(-1)^{\widetilde{x}_1 + \frac{1}{2}} {}^{CO'} h_{\widetilde{x}+\hat{2}} \\ &= s_{R_1}(-1)^{\widetilde{x}_1+\widetilde{x}_2+1} s'_O(\widetilde{x}_1 + \widetilde{x}_2 + 1) h_{(-\widetilde{x}_2,\widetilde{x}_1)} \\ &= -s_{R_1} s'_O(\widetilde{x}_1 + \widetilde{x}_2) h_{(-\widetilde{x}_2,\widetilde{x}_1)} \,, \end{aligned} \tag{4.48}$$

which fixes the sign

$$s_{R_1} = -1 \,. \tag{4.49}$$

Now that we have the symmetry transformations for the heights, let's have a look at Figure 4.10 where the candidate phases shown in Figure 4.7 are decorated with heights. In all realizations of the columnar and the plaquette phase, a repeated height pattern appears. This motivates the introduction of magnetization-like order parameters

$$M_X = \sum_{\widetilde{x} \in X} s^X_{\widetilde{x}} h_{\widetilde{x}} \tag{4.50}$$

which are defined on the corresponding sublattice $X \in \{A, B, C, D\}$. The sign factor $s^X_{\widetilde{x}}$ is defined as

$$\begin{aligned} s^A_{\widetilde{x}} = s^C_{\widetilde{x}} &= (-1)^{(\widetilde{x}_1 + \frac{1}{2})/2} && \text{if } \widetilde{x}_1 + \frac{1}{2} \text{ is even,} \\ s^B_{\widetilde{x}} = s^D_{\widetilde{x}} &= (-1)^{(\widetilde{x}_1 - \frac{1}{2})/2} && \text{if } \widetilde{x}_1 + \frac{1}{2} \text{ is odd.} \end{aligned} \tag{4.51}$$

Figure 4.11 visualizes the geometric structure of the sign factors. The flipped partners (red, blue) of each cartoon plaquette configuration pl_i in Figure 4.10 amount to the same values of the order parameter.

The transition between the columnar phases col_1 and col_2 in Figure 4.10 is related by an inversion of M_D, between col_2 and col_3 an inversion of M_B, and between col_3 and col_4

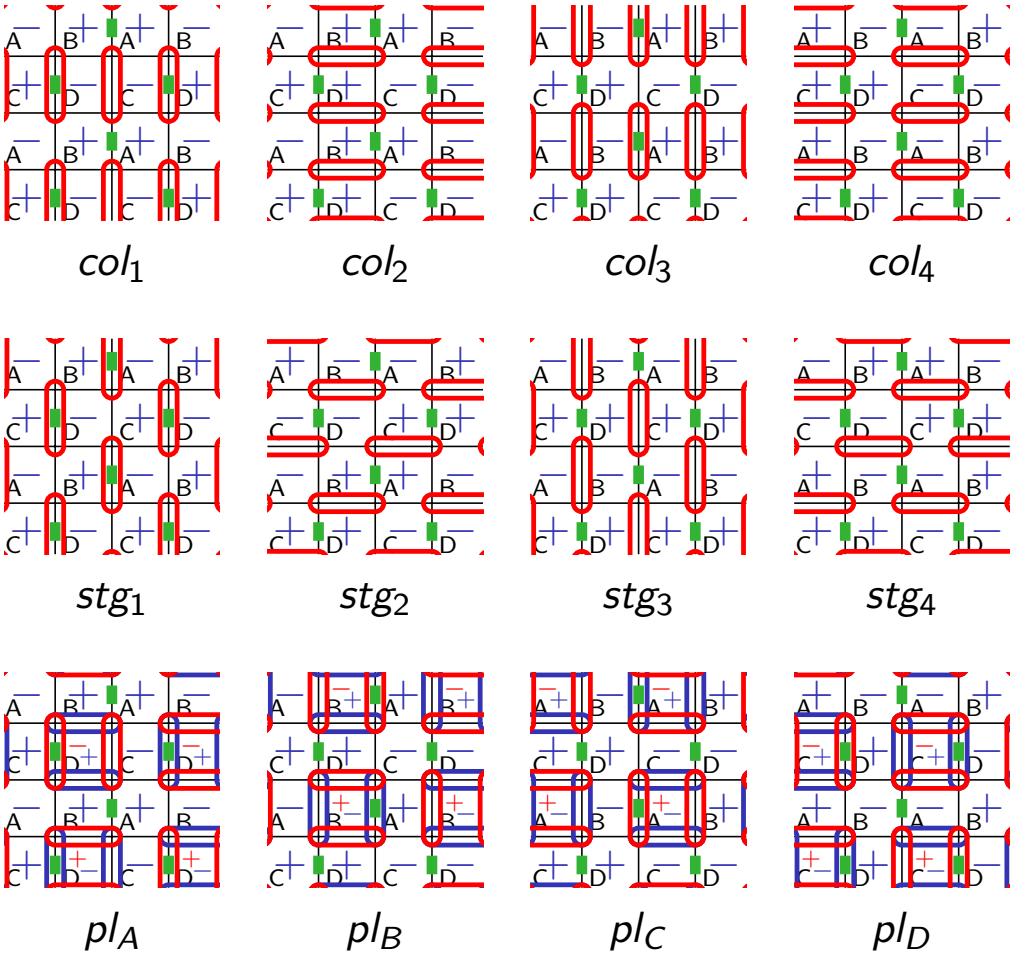

Figure 4.10.: *Same situation as in Figure 4.7. The cartoon configurations are now decorated with heights. Inverting all heights of a configuration inverts the signs of the order parameter values too, but it amounts to the same physical dimer covering. Those partner height coverings are denoted by an apostrophe (col_i', stg_i', pl_i').*

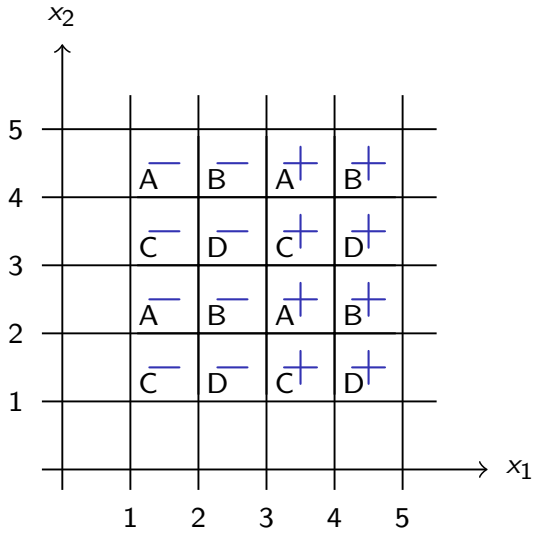

Figure 4.11.: *Geometrical structure of the sign factor* $s^X_{\widetilde{x}}$.

an inversion of M_A. Inverting M_C in col_4 depicted in Figure 4.10 results in the dimer covering of col_1. However, compared to col_1 in the Figure, all heights will be inverted. There is no way to switch between the height coverings of col_1 and col_4 shown in the figure by an inversion of a single M_X.

We derive the symmetry transformation rules for the magnetization-like order parameter M_X first for CR'_1 and CR'_2

$$
\begin{aligned}
{}^{CR'_1}M_{X=A,C} &= \sum_{\widetilde{x}\in X}(-1)^{(\widetilde{x}_1+\frac{1}{2})/2}h_{(\widetilde{x}_1,1-\widetilde{x}_2)} = M_{X=A,C}\,,\\
{}^{CR'_1}M_{X=B,D} &= \sum_{\widetilde{x}\in X}(-1)^{(\widetilde{x}_1-\frac{1}{2})/2}h_{(\widetilde{x}_1,1-\widetilde{x}_2)} = M_{X=B,D}\,,\\
{}^{CR'_2}M_{X=A,C} &= \sum_{\widetilde{x}\in X}(-1)^{(\widetilde{x}_1+\frac{1}{2})/2}(-1)^{\widetilde{x}_1-\frac{1}{2}}h_{(1-\widetilde{x}_1,\widetilde{x}_2)}\,,\\
&= \sum_{\widetilde{x}\in X}(-1)^{(1-\widetilde{x}_1+\frac{1}{2})/2+2(\widetilde{x}_1-\frac{1}{2})}h_{(1-\widetilde{x}_1,\widetilde{x}_2)} = M_{X=A,C}\,,\\
{}^{CR'_2}M_{X=B,D} &= \sum_{\widetilde{x}\in X}(-1)^{(\widetilde{x}_1-\frac{1}{2})/2}(-1)^{\widetilde{x}_1-\frac{1}{2}}h_{(1-\widetilde{x}_1,\widetilde{x}_2)}\,,\\
&= \sum_{\widetilde{x}\in X}(-1)^{(1-\widetilde{x}_1-\frac{1}{2})/2+2(\widetilde{x}_1-\frac{1}{2})}h_{(1-\widetilde{x}_1,\widetilde{x}_2)} = M_{X=B,D}\,,
\end{aligned}
\tag{4.52}
$$

which results in

$$
{}^{CR'_i}M_X = M_X\,. \tag{4.53}
$$

For R_1 and R_2 we obtain

$$\begin{aligned}
{}^{R_1}M_{X=A,C} &= \sum_{\widetilde{x}\in X}(-1)^{(\widetilde{x}_1+\frac{1}{2})/2}(-1)^{\widetilde{x}_1-\frac{1}{2}}h_{\widetilde{x}_1,-\widetilde{x}_2}\,,\\
&= -\sum_{\widetilde{x}\in X}(-1)^{(\widetilde{x}_1+\frac{1}{2})/2}h_{\widetilde{x}_1,-\widetilde{x}_2} = -M_{X=C,A}\,,\\
{}^{R_1}M_{X=B,D} &= \sum_{\widetilde{x}\in X}(-1)^{(\widetilde{x}_1-\frac{1}{2})/2}(-1)^{\widetilde{x}_1-\frac{1}{2}}h_{\widetilde{x}_1,-\widetilde{x}_2}\,,\\
&= \sum_{\widetilde{x}\in X}(-1)^{(\widetilde{x}_1-\frac{1}{2})/2}h_{\widetilde{x}_1,-\widetilde{x}_2} = M_{X=D,B}\,,\\
{}^{R_2}M_{X=A,C} &= \sum_{\widetilde{x}\in X}(-1)^{(\widetilde{x}_1+\frac{1}{2})/2}h_{-\widetilde{x}_1,\widetilde{x}_2}\\
&= \sum_{\widetilde{x}\in X}(-1)^{(-\widetilde{x}_1-\frac{1}{2})/2+\widetilde{x}_1+\frac{1}{2}}h_{-\widetilde{x}_1,\widetilde{x}_2} = M_{X=B,D}\,,\\
{}^{R_2}M_{X=B,D} &= \sum_{\widetilde{x}\in X}(-1)^{(\widetilde{x}_1-\frac{1}{2})/2}h_{-\widetilde{x}_1,\widetilde{x}_2}\\
&= \sum_{\widetilde{x}\in X}(-1)^{(-\widetilde{x}_1+\frac{1}{2})/2+\widetilde{x}_1-\frac{1}{2}}h_{-\widetilde{x}_1,\widetilde{x}_2} = M_{X=A,C}\,.
\end{aligned} \tag{4.54}$$

For the rotations O and CO' Table 4.1 helps to find the correct relations

$$\begin{aligned}
{}^{O}M_{A} &= \sum_{\widetilde{x}\in A}(-1)^{(\widetilde{x}_1+\frac{1}{2})/2}s'_O(\widetilde{x}_1+\widetilde{x}_2)h_{-\widetilde{x}_2,\widetilde{x}_1}\\
&= \sum_{\widetilde{x}\in A}(-1)^{(\widetilde{x}_1+\frac{1}{2})/2}(-1)^{(\widetilde{x}_1+\widetilde{x}_2)/2+1}h_{-\widetilde{x}_2,\widetilde{x}_1}\\
&= \sum_{\widetilde{x}\in A}(-1)^{(-\widetilde{x}_2+\frac{1}{2})/2+\widetilde{x}_1+\widetilde{x}_2+1}h_{-\widetilde{x}_2,\widetilde{x}_1}\\
&= -\sum_{\widetilde{x}\in A}(-1)^{(-\widetilde{x}_2+\frac{1}{2})/2}h_{-\widetilde{x}_2,\widetilde{x}_1} = -M_C\,,
\end{aligned} \tag{4.55}$$

$$\begin{aligned}
{}^{O}M_{B} &= \sum_{\widetilde{x}\in B}(-1)^{(\widetilde{x}_1-\frac{1}{2})/2}s'_O(\widetilde{x}_1+\widetilde{x}_2)h_{-\widetilde{x}_2,\widetilde{x}_1}\\
&= \sum_{\widetilde{x}\in B}(-1)^{(\widetilde{x}_1-\frac{1}{2})/2}(-1)^{(\widetilde{x}_1+\widetilde{x}_2+1)/2}h_{-\widetilde{x}_2,\widetilde{x}_1}\\
&= \sum_{\widetilde{x}\in B}(-1)^{(-\widetilde{x}_2+\frac{1}{2})/2+\widetilde{x}_1+\widetilde{x}_2}h_{-\widetilde{x}_2,\widetilde{x}_1}\\
&= -\sum_{\widetilde{x}\in B}(-1)^{(-\widetilde{x}_2+\frac{1}{2})/2}h_{-\widetilde{x}_2,\widetilde{x}_1} = -M_A
\end{aligned} \tag{4.56}$$

$$
\begin{aligned}
{}^{O}M_C &= \sum_{\widetilde{x}\in C}(-1)^{\left(\widetilde{x}_1+\frac{1}{2}\right)/2}s'_O(\widetilde{x}_1+\widetilde{x}_2)h_{-\widetilde{x}_2,\widetilde{x}_1} \\
&= \sum_{\widetilde{x}\in C}(-1)^{\left(\widetilde{x}_1+\frac{1}{2}\right)/2}(-1)^{(\widetilde{x}_1+\widetilde{x}_2+1)/2}h_{-\widetilde{x}_2,\widetilde{x}_1} \\
&= \sum_{\widetilde{x}\in C}(-1)^{\left(-\widetilde{x}_2-\frac{1}{2}\right)/2+\widetilde{x}_1+\widetilde{x}_2+1}h_{-\widetilde{x}_2,\widetilde{x}_1} \\
&= \sum_{\widetilde{x}\in C}(-1)^{\left(-\widetilde{x}_2-\frac{1}{2}\right)/2}h_{-\widetilde{x}_2,\widetilde{x}_1} = M_D\,, \qquad (4.57)
\end{aligned}
$$

$$
\begin{aligned}
{}^{O}M_D &= \sum_{\widetilde{x}\in D}(-1)^{\left(\widetilde{x}_1-\frac{1}{2}\right)/2}s'_O(\widetilde{x}_1+\widetilde{x}_2)h_{-\widetilde{x}_2,\widetilde{x}_1} \\
&= \sum_{\widetilde{x}\in D}(-1)^{\left(\widetilde{x}_1-\frac{1}{2}\right)/2}(-1)^{(\widetilde{x}_1+\widetilde{x}_2)/2+1}h_{-\widetilde{x}_2,\widetilde{x}_1} \\
&= \sum_{\widetilde{x}\in D}(-1)^{\left(-\widetilde{x}_2-\frac{1}{2}\right)/2+\widetilde{x}_1+\widetilde{x}_2+1}h_{-\widetilde{x}_2,\widetilde{x}_1} \\
&= -\sum_{\widetilde{x}\in D}(-1)^{\left(-\widetilde{x}_2-\frac{1}{2}\right)/2}h_{-\widetilde{x}_2,\widetilde{x}_1} = -M_B \qquad (4.58)
\end{aligned}
$$

We want to use M_X as a order parameter. However, ${}^{S}M_X$, where S is a symmetry transformation, transforms the measure itself and we are interested in the measure of transformed configurations too. Using

$$M_X\left[\mathcal{C}\right] = {}^{S}M_X\left[{}^{S}\mathcal{C}\right] = M_Y\left[{}^{S}\mathcal{C}\right]\,, \qquad (4.59)$$

where $\mathcal{C}$ denotes a height configuration, ${}^{S}\mathcal{C}$ the transformed configuration, and ${}^{S}M_X\left[{}^{S}\mathcal{C}\right]$ the transformed operator applied on the transformed configuration we collect the results in Table 4.3. The translations CT_1, CT_2, and the rotation CO' listed in the table are

S	CT_1	CT_2	O	CO'	R_1	R_2	CR'_1	CR'_2
$M_A\left[{}^{S}\mathcal{C}\right]$	$M_B\left[\mathcal{C}\right]$	$-M_C\left[\mathcal{C}\right]$	$-M_B\left[\mathcal{C}\right]$	$-M_D\left[\mathcal{C}\right]$	$-M_C\left[\mathcal{C}\right]$	$M_B\left[\mathcal{C}\right]$	$M_A\left[\mathcal{C}\right]$	$M_A\left[\mathcal{C}\right]$
$M_B\left[{}^{S}\mathcal{C}\right]$	$M_A\left[\mathcal{C}\right]$	$M_D\left[\mathcal{C}\right]$	$-M_D\left[\mathcal{C}\right]$	$-M_B\left[\mathcal{C}\right]$	$M_D\left[\mathcal{C}\right]$	$M_A\left[\mathcal{C}\right]$	$M_B\left[\mathcal{C}\right]$	$M_B\left[\mathcal{C}\right]$
$M_C\left[{}^{S}\mathcal{C}\right]$	$M_D\left[\mathcal{C}\right]$	$-M_A\left[\mathcal{C}\right]$	$-M_A\left[\mathcal{C}\right]$	$M_C\left[\mathcal{C}\right]$	$-M_A\left[\mathcal{C}\right]$	$M_D\left[\mathcal{C}\right]$	$M_C\left[\mathcal{C}\right]$	$M_C\left[\mathcal{C}\right]$
$M_D\left[{}^{S}\mathcal{C}\right]$	$M_C\left[\mathcal{C}\right]$	$M_B\left[\mathcal{C}\right]$	$M_C\left[\mathcal{C}\right]$	$-M_A\left[\mathcal{C}\right]$	$M_B\left[\mathcal{C}\right]$	$M_C\left[\mathcal{C}\right]$	$M_D\left[\mathcal{C}\right]$	$M_D\left[\mathcal{C}\right]$

Table 4.3.: *This table relates the order parameters $M_X\left[{}^{S}\mathcal{C}\right]$ of a configuration which was transformed by the symmetry operator $S = CT_1$, CT_2, O, CO', R_1, R_2, CR'_1, and CR'_2 to the corresponding order parameters $M_X\left[\mathcal{C}\right]$ of the original configuration $\mathcal{C}$.*

composed out of

$$
\begin{aligned}
M_X\left[{}^{CT_1}\mathcal{C}\right] &= M_X\left[{}^{CR'_2R_2}\mathcal{C}\right] = M_{Y_1}\left[{}^{CR'_2}\mathcal{C}\right] = M_{Y_1}\left[\mathcal{C}\right]\,, \\
M_X\left[{}^{CT_2}\mathcal{C}\right] &= M_X\left[{}^{CR'_1R_1}\mathcal{C}\right] = M_{Y_2}\left[{}^{CR'_1}\mathcal{C}\right] = M_{Y_2}\left[\mathcal{C}\right]\,, \\
M_X\left[{}^{CO'}\mathcal{C}\right] &= M_X\left[{}^{CT_1O}\mathcal{C}\right] = M_{Z_1}\left[{}^{O}\mathcal{C}\right] = M_{Z_2}\left[\mathcal{C}\right]\,. \qquad (4.60)
\end{aligned}
$$

The staggered phase realizations all transform trivially since $M_X\,[stg_i] = 0$.

Table 4.4 lists the values for M_X for the candidate phase realizations in a (4×4) system. The values correspond to the graphical representations in Figure 4.10. The values of M_X

	col_1	pl_A	col_2	pl_B	col_3	pl_C	col_4	pl_D	col'_1	pl'_A	stg_i
M_A	4	4	4	4	4	0	-4	-4	-4	-4	0
M_B	-4	-4	-4	0	4	4	4	4	4	4	0
M_C	-4	-4	-4	-4	-4	-4	-4	0	4	4	0
M_D	4	0	-4	-4	-4	-4	-4	-4	-4	0	0

Table 4.4.: *Values of the four-component order parameter components in a* (4×4) *system for different cartoon phases. Note that inverting all values of the order parameter at once results in the same physical dimer configuration.*

for the partner height coverings are just inverted. Each candidate phase leads to a distinct set of M_X. We remember, that the rotation O by $\pi/2$ advances us by two items in the sequence written in eq. (4.29). As a check the transformation rules of Table 4.3 match with Table 4.4.

A further property we can read out from the Table 4.4 is that for each columnar phase there is a unique way to add up the values of M_X given in the table to a maximum. Let M_{11} be the combination which is maximal for the columnar phase col_1. This combination is at the same time zero for the two times rotated columnar phase $col_3 = {}^{OO}col_1$. Using the definition

$$\begin{aligned} M_{12}\left[{}^{O}\mathcal{C}\right] &= M_{11}\left[\mathcal{C}\right], \\ M_{22}\left[{}^{O}\mathcal{C}\right] &= M_{12}\left[\mathcal{C}\right], \\ M_{21}\left[{}^{O}\mathcal{C}\right] &= M_{22}\left[\mathcal{C}\right], \end{aligned} \tag{4.61}$$

we obtain a magnetization-like order parameter M_{ij}

$$\begin{aligned} M_{11} &= +M_A - M_B - M_C + M_D\,, \\ M_{12} &= +M_A - M_B - M_C - M_D\,, \\ M_{22} &= +M_A + M_B - M_C - M_D\,, \\ M_{21} &= -M_A + M_B - M_C - M_D\,. \end{aligned} \tag{4.62}$$

Inverting all heights amounts to inverting all four components and results in the same physical state. The order parameter distinguishes all three columnar and all three plaquette phases. In a cartoon staggered phase $M_1 = M_2 = M_3 = M_4 = 0$ and $M_{11} = M_{12} = M_{21} = M_{22} = 0$. The values of the four-component order parameter for the different phases in a (4×4) system are listed in Table 4.5. Obviously, M_{11} and M_{22} are in a sense orthogonal, since maximizing the absolute value of one of them the other is zero. The same holds for M_{12} and M_{21}. Table 4.6 collects the transformation properties of the order parameter M_X.

In Figure 4.12 the four-component order parameter is projected into two dimensions. The pure staggered phase (which is not in the same flux sector as the pure columnar or

	col_1	pl_A	col_2	pl_B	col_3	pl_C	col_4	pl_D	col'_1	pl'_A	stg_i
M_{11}	16	12	8	4	0	-4	-8	-12	-16	-12	0
M_{12}	8	12	16	12	8	4	0	-4	-8	-12	0
M_{22}	0	4	8	12	16	12	8	4	0	-4	0
M_{21}	-8	-4	0	4	8	12	16	12	8	4	0

Table 4.5.: *Values of the four-component order parameter components in a* (4×4) *system for different cartoon phases. Note that inverting all values of the order parameter at once would result in the same physical dimer configuration.*

S	CT_1	CT_2	O	CO'	R_1	R_2	CR'_1	CR'_2
$M_{11}\left[{}^S\mathcal{C}\right]$	$-M_{11}\left[\mathcal{C}\right]$	$M_{22}\left[\mathcal{C}\right]$	$-M_{21}\left[\mathcal{C}\right]$	$M_{21}\left[\mathcal{C}\right]$	$M_{22}\left[\mathcal{C}\right]$	$-M_{11}\left[\mathcal{C}\right]$	$M_{11}\left[\mathcal{C}\right]$	$-M_{11}\left[\mathcal{C}\right]$
$M_{12}\left[{}^S\mathcal{C}\right]$	$M_{21}\left[\mathcal{C}\right]$	$M_{12}\left[\mathcal{C}\right]$	$M_{11}\left[\mathcal{C}\right]$	$M_{22}\left[\mathcal{C}\right]$	$M_{12}\left[\mathcal{C}\right]$	$M_{21}\left[\mathcal{C}\right]$	$M_{12}\left[\mathcal{C}\right]$	$-M_{12}\left[\mathcal{C}\right]$
$M_{22}\left[{}^S\mathcal{C}\right]$	$M_{22}\left[\mathcal{C}\right]$	$M_{11}\left[\mathcal{C}\right]$	$M_{12}\left[\mathcal{C}\right]$	$M_{12}\left[\mathcal{C}\right]$	$M_{11}\left[\mathcal{C}\right]$	$M_{22}\left[\mathcal{C}\right]$	$M_{22}\left[\mathcal{C}\right]$	$-M_{22}\left[\mathcal{C}\right]$
$M_{21}\left[{}^S\mathcal{C}\right]$	$M_{12}\left[\mathcal{C}\right]$	$-M_{21}\left[\mathcal{C}\right]$	$M_{22}\left[\mathcal{C}\right]$	$M_{11}\left[\mathcal{C}\right]$	$-M_{21}\left[\mathcal{C}\right]$	$M_{12}\left[\mathcal{C}\right]$	$M_{21}\left[\mathcal{C}\right]$	$-M_{21}\left[\mathcal{C}\right]$

Table 4.6.: *This table corresponds to Tables I in [33]. It relates the order parameters* $M_{ij}\left[{}^S\mathcal{C}\right]$ *of a configuration which was transformed by the symmetry operator* $S = CT_1$, CT_2, O, CO', R_1, R_2, CR'_1, *and* CR'_2 *to the corresponding order parameters* $M_{ij}\left[\mathcal{C}\right]$ *of the original configuration* $\mathcal{C}$.

pure plaquette phases) would appear as a point at the origin of the diagrams. The choice of the flipped height partners in Figure 4.10 together with the ordering of the projection axes was such that the order of the phases shown in each diagram of Figure 4.12 in counterclockwise order is described by the periodic sequence in eq. (4.29). As already mentioned, inverting all heights results in the same physical dimer covering ($col'_i \hat{=} col_i$, $pl'_i \hat{=} pl_i$).

Table 4.6 differs in the overall signs of CT_2, O, CO', and R_1 compared to [33]. Note that the tables don't have the same order. The differences could be caused by the choice of different conventions.

The two above mentioned projections (M_{11}, M_{22}) and (M_{12}, M_{21}) are motivation to define two angles φ_1 and φ_2 such that

$$\begin{aligned} M_{11} + \mathrm{i}M_{22} &= M_1\, \mathrm{e}^{\mathrm{i}\varphi_1} \\ M_{12} + \mathrm{i}M_{21} &= M_2\, \mathrm{e}^{\mathrm{i}\varphi_2}\ . \end{aligned} \tag{4.63}$$

These angles will turn out to parametrize a soft pseudo-Goldstone mode. The relative orientation of the phases between the two projections (M_{11}, M_{22}) and (M_{12}, M_{21}) (see also green line in Figure 4.12) are motivation to rotate the definition of (M_{12}, M_{21}) by an angle $\pi/4$:

$$\widetilde{\varphi}_2 = \varphi_2 + \frac{\pi}{4}\,. \tag{4.64}$$

With

$$\widetilde{M}_{12} + \mathrm{i}\widetilde{M}_{21} = M_2\, \mathrm{e}^{\mathrm{i}\widetilde{\varphi}_2} = (M_{12} + \mathrm{i}M_{21})\, \mathrm{e}^{\mathrm{i}\frac{\pi}{4}} \tag{4.65}$$

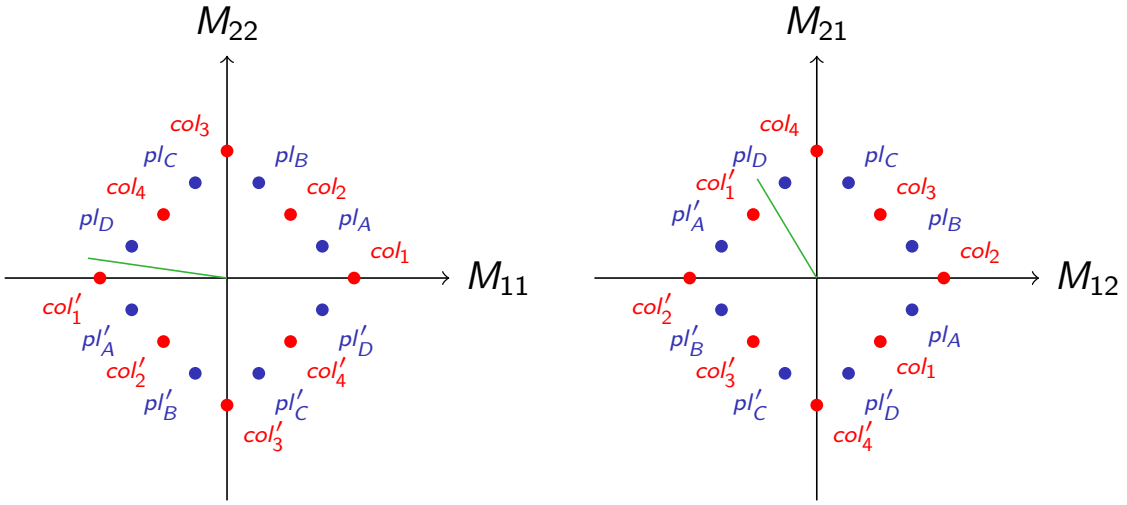

Figure 4.12.: *Projection of the four-component order parameter into two dimensions. Phases with an apostrophe are related to their partner without apostrophe by an inversion of all heights. A partner pair corresponds to the same physical dimer covering.*

this amounts into

$$\begin{aligned}\widetilde{M}_{12} &= \Re\left((M_{12}+\mathrm{i}M_{21})\,\mathrm{e}^{\mathrm{i}\frac{\pi}{4}}\right) = \frac{1}{\sqrt{2}}\,(M_{12}-M_{21}) = \sqrt{2}\,(M_A-M_B)\\ \widetilde{M}_{21} &= \Im\left((M_{12}+\mathrm{i}M_{21})\,\mathrm{e}^{\mathrm{i}\frac{\pi}{4}}\right) = \frac{1}{\sqrt{2}}\,(M_{12}+M_{21}) = -\sqrt{2}\,(M_C+M_D)\ .\end{aligned} \tag{4.66}$$

The different realizations of a phase are then treated on equal footing as shown in Figure 4.13. We can now define

$$\varphi = \frac{1}{2}\,(\varphi_1+\widetilde{\varphi}_2) = \frac{1}{2}\left(\varphi_1+\varphi_2+\frac{\pi}{4}\right)\ . \tag{4.67}$$

The cartoon phases are then related by

φ	0	$\pi/8$	$\cdots$	$7\pi/8$	$-\pi$	$-7\pi/8$	$\cdots$	$-\pi/8$
cartoon phase	col_1	pl_A	$\cdots$	pl_D	col'_1	pl'_A	$\cdots$	pl'_D

Without external charges, the realizations of a phase are related by geometrical rotations by $\pi/2$ around a site. In the projected order parameter space this corresponds to a rotation by $\pi/4$. We will see only later in the results that at the Rokhsar-Kivelson point $\lambda = 1$ the projections of the order parameter appear as an almost perfect ring without any staggered phase realization. So in that case the angle φ parametrizes a massless Goldstone boson field.

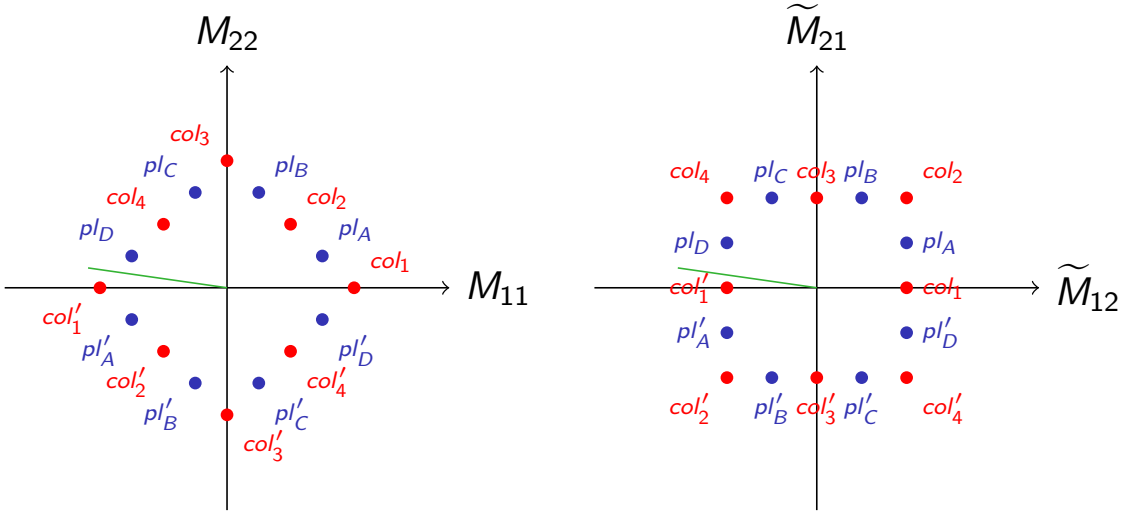

Figure 4.13.: Left panel: *projection* (M_{11}, M_{22}). Right panel: *projection* $(\widetilde{M}_{12}, \widetilde{M}_{21})$ *which is the projection* (M_{12}, M_{21}) *rotated by* $\frac{\pi}{4}$.

4.5. The Rokhsar-Kivelson point $\lambda = 1$

At $\lambda = 1$ the quantum dimer model has a ground state that can be constructed analytically. The solution is the equal weight superposition of all allowed dimer coverings of a flux sector. This was already known since [29].

Let's again take a look at the time-independent standard quantum dimer model Hamiltonian again

$$H = T + V = \sum_{\square} (t_{\square} + v_{\square}) \tag{4.68}$$

with

$$\begin{aligned} t_{\square} &= -J \left(U_{\square} + U_{\square}^{\dagger} \right) \\ v_{\square} &= J\lambda \left(U_{\square} + U_{\square}^{\dagger} \right)^2 = J\lambda \left(U_{\square} U_{\square}^{\dagger} + U_{\square}^{\dagger} U_{\square} \right) . \end{aligned} \tag{4.69}$$

In a basis of cartoon dimer coverings $\mathcal{C}, \mathcal{C}'$ the local kinetic term $t_{\square}$ behaves as

$$\langle \mathcal{C} | t_{\square} | \mathcal{C}' \rangle = \begin{cases} -J & \text{if } (\mathcal{C}, \mathcal{C}') \text{ differ by flip of plaquette } \square, \\ 0 & \text{else.} \end{cases} \tag{4.70}$$

The diagonal local potential term $v_{\square}$ detects flippable plaquettes

$$\langle \mathcal{C} | v_{\square} | \mathcal{C}' \rangle = \delta_{\mathcal{C},\mathcal{C}'} \cdot \begin{cases} J\lambda & \text{if plaquette } \square \text{ flippable in configuration } \mathcal{C}, \\ 0 & \text{else.} \end{cases} \tag{4.71}$$

It has the important property

$$\begin{aligned} J\langle\mathcal{C}|v_\square|\mathcal{C}\rangle &= J^2\lambda\langle\mathcal{C}|\left(U_\square + U_\square^\dagger\right)^2|\mathcal{C}\rangle \\ &= J^2\lambda\sum_{\mathcal{C}'}\langle\mathcal{C}|\left(U_\square + U_\square^\dagger\right)|\mathcal{C}'\rangle\langle\mathcal{C}'|\left(U_\square + U_\square^\dagger\right)|\mathcal{C}\rangle \\ &= J^2\lambda\sum_{\mathcal{C}'}\langle\mathcal{C}|\left(U_\square + U_\square^\dagger\right)|\mathcal{C}'\rangle \\ &= -J\lambda\sum_{\mathcal{C}'}\langle\mathcal{C}|t_\square|\mathcal{C}'\rangle \end{aligned} \tag{4.72}$$

which at the so-called Rokhsar-Kivelson point $\lambda = 1$, makes the model analytically solvable Its ground state wave function is the equal-weight superposition of all allowed dimer coverings

$$|\psi_0\rangle = \mathcal{N}\sum_{\mathcal{C}}|\mathcal{C}\rangle \tag{4.73}$$

with a normalization factor $\mathcal{N}$ such that the wave function is normalized. To see that this really is the ground state, let's have a look at a general normalized wave function in the dimer basis

$$|\psi\rangle = \sum_{\mathcal{C}}|\mathcal{C}\rangle\langle\mathcal{C}|\psi\rangle \tag{4.74}$$

and first apply the local potential

$$\begin{aligned} \langle\psi|v_\square|\psi\rangle &= \sum_{\mathcal{C},\mathcal{C}'}\langle\psi|\mathcal{C}\rangle\langle\mathcal{C}|v_\square|\mathcal{C}'\rangle\langle\mathcal{C}'|\psi\rangle \\ &= \sum_{\mathcal{C}}\langle\psi|\mathcal{C}\rangle\langle\mathcal{C}|v_\square|\mathcal{C}\rangle\langle\mathcal{C}|\psi\rangle \\ &= -\lambda\sum_{\mathcal{C},\mathcal{C}'}\langle\psi|\mathcal{C}\rangle\langle\mathcal{C}|t_\square|\mathcal{C}'\rangle\langle\mathcal{C}|\psi\rangle \end{aligned} \tag{4.75}$$

and then the whole local Hamiltonian of a plaquette

$$\begin{aligned} \langle\psi|h_\square|\psi\rangle &= \sum_{\mathcal{C},\mathcal{C}'}\langle\psi|\mathcal{C}\rangle\langle\mathcal{C}|t_\square|\mathcal{C}'\rangle\left\{\langle\mathcal{C}'|\psi\rangle - \lambda\langle\mathcal{C}|\psi\rangle\right\} \\ &= \frac{1}{2}\sum_{\mathcal{C},\mathcal{C}'}\langle\psi|\mathcal{C}\rangle\langle\mathcal{C}|t_\square|\mathcal{C}'\rangle\left\{\langle\mathcal{C}'|\psi\rangle - \lambda\langle\mathcal{C}|\psi\rangle\right\} \\ &\quad - \frac{1}{2}\sum_{\mathcal{C},\mathcal{C}'}\langle\psi|\mathcal{C}'\rangle\langle\mathcal{C}'|t_\square|\mathcal{C}\rangle\left\{\lambda\langle\mathcal{C}'|\psi\rangle - \langle\mathcal{C}|\psi\rangle\right\} \end{aligned} \tag{4.76}$$

Since $\langle\mathcal{C}'|t_\square|\mathcal{C}\rangle = \langle\mathcal{C}|t_\square|\mathcal{C}'\rangle \leq 0$ and at the Rokhsar-Kivelson point $\lambda = 1$, this leads to

$$\begin{aligned} \langle\psi|h_\square|\psi\rangle &= -\frac{1}{2}\sum_{\mathcal{C},\mathcal{C}'}\left\{\langle\psi|\mathcal{C}'\rangle - \langle\psi|\mathcal{C}\rangle\right\}\langle\mathcal{C}|t_\square|\mathcal{C}'\rangle\left\{\langle\mathcal{C}'|\psi\rangle - \langle\mathcal{C}|\psi\rangle\right\} \\ &= -\frac{1}{2}\sum_{\mathcal{C},\mathcal{C}'}\left|\langle\psi|\mathcal{C}\rangle - \langle\psi|\mathcal{C}'\rangle\right|^2\langle\mathcal{C}|t_\square|\mathcal{C}'\rangle \\ &\geq 0\,. \end{aligned} \tag{4.77}$$

So eq. (4.73) not only describes the ground state ($\langle\psi_0|\mathcal{C}\rangle = \mathcal{N} \quad \forall\mathcal{C}$), but even its local energy density is zero

$$h_\square|\psi_0\rangle = 0\,, \quad H|\psi_0\rangle = 0\,. \tag{4.78}$$

Since flipping dimers doesn't change the total fluxes, the Hamiltonian is block-diagonal in sectors of total fluxes. The ground state wave functional remains the same for all sectors, therefore fluxes don't cost energy, they condense in the vacuum. This leads to deconfinement even for $(2+1)$ dimensions at zero temperature. A massless Goldstone boson appears which manifests itself as a ring in the projection of the order parameters.

For general $(2+1)$ dimensional $U(1)$ models (with above exception at the Rokhsar-Kivelson point $\lambda = 1$) a string costs energy and therefore the model is confined. Only when there is enough energy in those system ($T > T_C$) they deconfine. Near, but not exactly at the Rokhsar-Kivelson point $\lambda = 1$ the quantum dimer model possesses a weak first order phase transition.

4.6. Previous results

This work will be compared with to results obtained for the standard quantum dimer model on a periodic square lattice [33]. For $\lambda < 1$ Figure 4.14 shows the angular distribution of the order parameter with φ defined in eq. (4.67). The horizontal axis is folded from $[0, 2\pi]$ into $[0, \pi/4]$ such that angles near 0 or $\pi/4 \approx 0.79$ indicate a columnar phase while angles near $\pi/8 \approx 0.39$ would indicate a plaquette phase. Obviously there is no other than the columnar phase, no plaquette phase and no peak splitting which would indicate a mixed phase. For λ near the Rokhsar-Kivelson point $\lambda = 1$, the angular distribution becomes flat and the above mentioned pseudo-Goldstone boson mode becomes exactly massless.

Figure 4.15 shows the linear rise of the potential (vertical axis) of a double positive static charge with distance r (horizontal axis) from a double negative static charge in the periodic system for $\lambda < 1$. The system is confined.

For Figure 4.16 two static external charges ± 2 were separated by 49 lattice spacings in a periodic volume of 144^2 lattice sites. The system is in a deep columnar phase $\lambda = -0.2$ and the temperature is rather low ($\beta J = 72$). The figure shows that the local energy density encoded by colors doesn't show a Coulomb flux but rather strands of flux $1/4$. The interior of the strands display plaquette order and are interfaces separating distinct columnar phases.

The simulations became more difficult near the Rokhsar-Kivelson point $\lambda = 1$. There confinement gets lost at zero temperature even in $(2+1)$ dimensions.

Figure 4.17 shows the first few excited states with zero momentum for the quantum dimer model. We will use this figure later on as a reference for the exact diagonalization studies at the Rokhsar-Kivelson point $\lambda = 1$ and at its proximity.

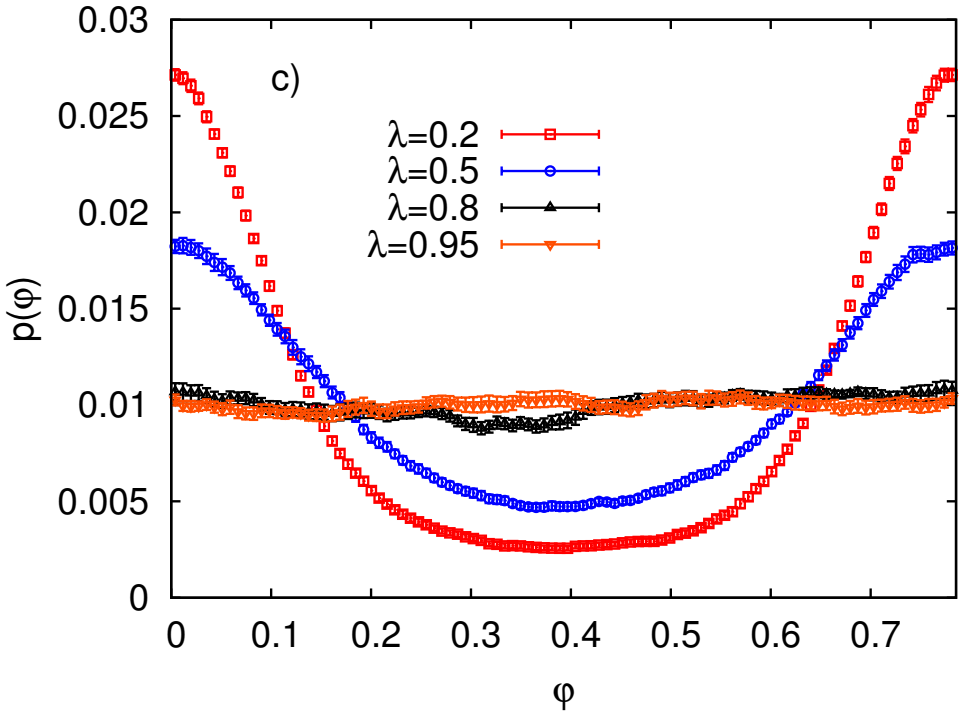

Figure 4.14.: *From [33]. Angular distribution of the projected order parameters. The angle φ is folded from $[0, 2\pi]$ into $[0, \pi/4]$. High densities at the extrema of the horizontal axis indicate columnar phases. High densities in the center would indicate plaquette phases.*

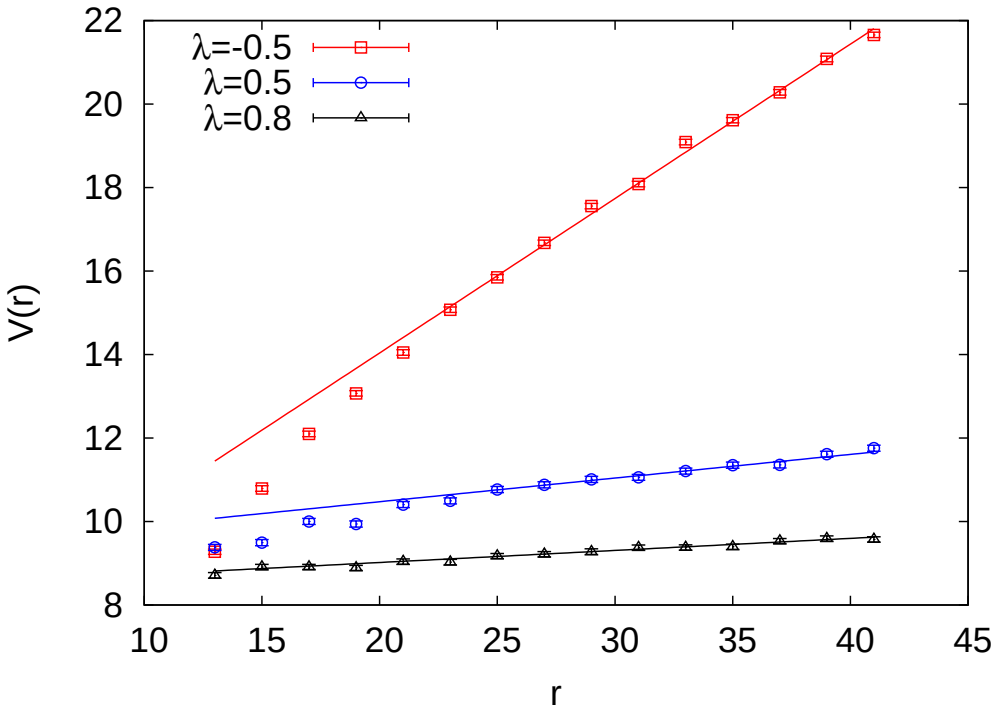

Figure 4.15.: *From [33]. Linear rise of the potential $V(r)$ (horizontal axis) for two static external charges ± 2 separated by a distance r (vertical axis).*

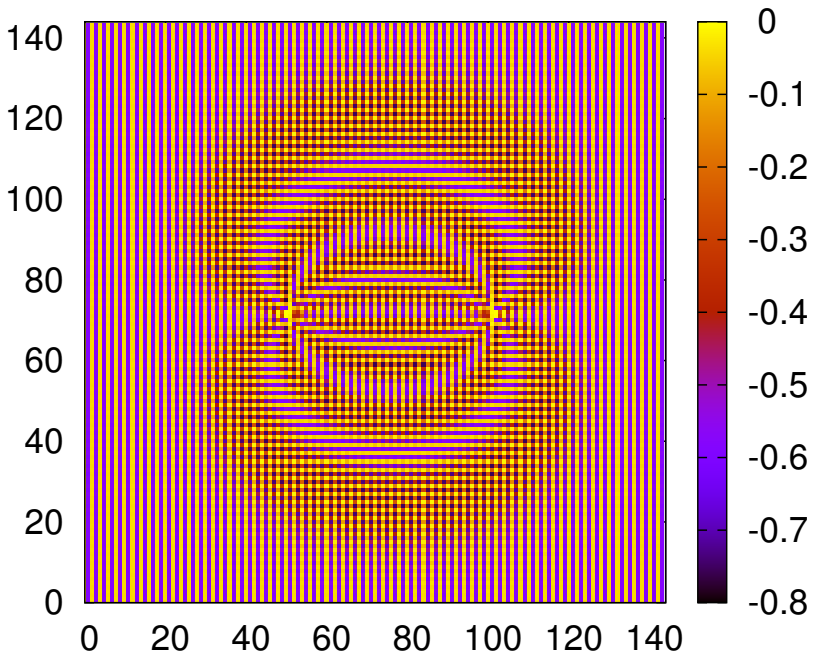

Figure 4.16.: *From [33]. Local energy density encoded in colors. The horizontal and vertical axis correspond to the geometrical x_1 and x_2 axis of the system.*

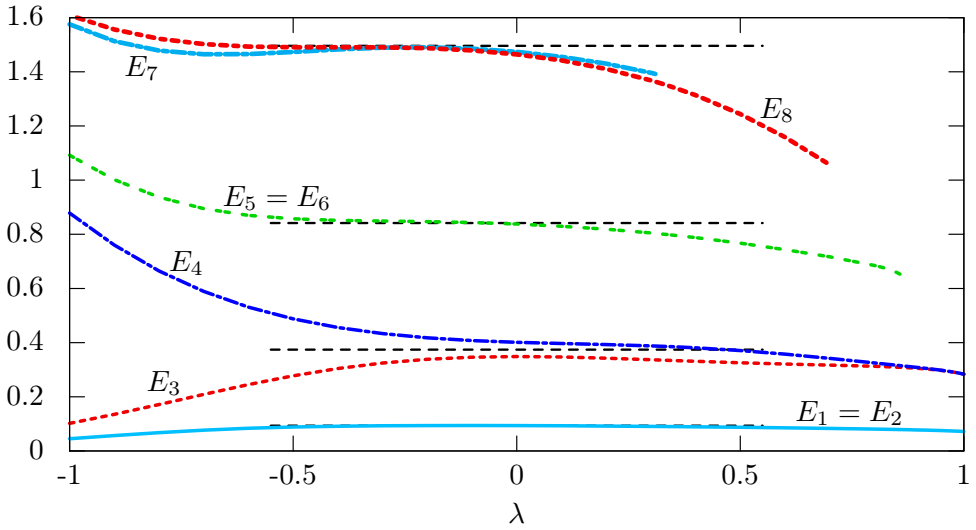

Figure 4.17.: *From [33]. Energy spectrum of the* (8×8) *quantum dimer model as a function of the Rokhsar-Kivelson coupling* λ.

4.7. Modified ground state Rokhsar-Kivelson wave function

A wave function is a solution of a family of so-called parent Hamiltonians. The wave function defined in eq. (4.73) can be locally deformed in many ways [34] still being a solution of some modified parent Hamiltonian. We choose the following minimally entangled ground state wave function

$$|\widetilde{\psi}_0\rangle = \sum_{\mathcal{C}} |\mathcal{C}\rangle\langle\mathcal{C}|\widetilde{\psi}_0\rangle \tag{4.79}$$

with

$$\langle\mathcal{C}|\widetilde{\psi}_0\rangle := \widetilde{\mathcal{N}} \prod_{\square} \widetilde{\psi}_0\left(\square, \mathcal{C}\right) \tag{4.80}$$

and

$$\widetilde{\psi}_0\left(\square, \mathcal{C}\right) := \begin{cases} \phi_1 & \text{if } \square \text{ flippable for } \mathcal{C} \\ \phi_2 & \text{else} \end{cases} \tag{4.81}$$

where $\phi_1, \phi_2 > 0$. Again $\widetilde{\mathcal{N}}$ is a normalization factor such that $\langle\widetilde{\psi}_0|\widetilde{\psi}_0\rangle = 1$. Since this ground state wave function is translation invariant, it has zero momentum, as it should be for a ground state. Obviously for $\phi_1 \gg \phi_2 > 0$ flippable plaquettes are favored and we get into a columnar phase. However, it is a deconfined columnar phase as we see later. For $\phi_2 \gg \phi_1 > 0$ flippable plaquettes are suppressed and a staggered phase is formed. Because of the normalization factor only the ratio ϕ_1/ϕ_2 is relevant. For $\phi_1 = \phi_2$ it is equal to eq. (4.73) and therefore it is the ground state of the standard quantum dimer Hamiltonian in eq. (4.1) with $\lambda = 1$. For $\phi_1 \neq \phi_2$ the ground state wave function extends the Rokhsar-Kivelson point to a line of Rokhsar-Kivelson points. We want to derive a Hamiltonian for which the above wave function is the ground state.

In general, if a Hamiltonian is given, we can try to obtain its spectrum by solving the eigenvalue equation

$$H|\psi_i\rangle = E_i|\psi_i\rangle\,. \tag{4.82}$$

For general Hamiltonians the wave functions ψ_i will be highly non-trivial and entangled. If, in contrast, a set of time-independent wave functions ψ_i with energies E_i is given, we could construct their parent Hamiltonian as

$$H = \sum_i E_i|\psi_i\rangle\langle\psi_i|\,. \tag{4.83}$$

However, in general these Hamiltonians wouldn't be local.

Using the dimer covering basis we write the eigenvalue equation (4.82) as

$$\langle\mathcal{C}|T|\psi_i\rangle + \langle\mathcal{C}|V|\mathcal{C}\rangle\langle\mathcal{C}|\psi_i\rangle = E_i\langle\mathcal{C}|\psi_i\rangle \quad \forall\mathcal{C}\,. \tag{4.84}$$

Here we separated the Hamiltonian into a diagonal potential part V and an off-diagonal kinetic part T. This can formally be cast in the local form

$$\sum_\square \langle\mathcal{C}|v_\square|\mathcal{C}\rangle = E_i - \sum_\square \frac{\langle\mathcal{C}|t_\square|\psi_i\rangle}{\langle\mathcal{C}|\psi_i\rangle} \quad \forall\mathcal{C}\,. \tag{4.85}$$

The energies of the system can be shifted by an overall constant. Hence, we are free to set the ground state energy to zero ($E_0 = 0$). Now we can define

$$\langle\mathcal{C}|\widetilde{v}_\square|\mathcal{C}\rangle \coloneqq -\frac{\langle\mathcal{C}|t_\square|\widetilde{\psi}_0\rangle}{\langle\mathcal{C}|\widetilde{\psi}_0\rangle} = -\sum_{\mathcal{C}'}\langle\mathcal{C}|t_\square|\mathcal{C}'\rangle\frac{\langle\mathcal{C}'|\widetilde{\psi}_0\rangle}{\langle\mathcal{C}|\widetilde{\psi}_0\rangle} \tag{4.86}$$

which then automatically fulfills eq. (4.84) for the ground state. In general a $\widetilde{v}_\square$ defined in this way would be highly non-local. However, it has the remarkable feature that the energy density of its ground state is zero:

$$\widetilde{v}_\square|\widetilde{\psi}_0\rangle = \sum_{\mathcal{C}}|\mathcal{C}\rangle\langle\mathcal{C}|\widetilde{v}_\square|\mathcal{C}\rangle\langle\mathcal{C}|\widetilde{\psi}_0\rangle = -\sum_{\mathcal{C}}|\mathcal{C}\rangle\frac{\langle\mathcal{C}|t_\square|\widetilde{\psi}_0\rangle}{\langle\mathcal{C}|\widetilde{\psi}_0\rangle}\langle\mathcal{C}|\widetilde{\psi}_0\rangle = -t_\square|\widetilde{\psi}_0\rangle\,, \tag{4.87}$$

and hence

$$\widetilde{h}_\square|\widetilde{\psi}_0\rangle = (t_\square + \widetilde{v}_\square)\,|\widetilde{\psi}_0\rangle = 0\,. \tag{4.88}$$

For the modified wave function we want to keep the local kinetic term of the parent Hamiltonian unchanged

$$t_\square = -J\left(U_\square + U_\square^\dagger\right)\,. \tag{4.89}$$

Using the ground state wave function defined in eq. (4.80) and the fact that a plaquette flip only affects neighboring plaquettes (see Figure 4.18) we can work out

$$\langle\mathcal{C}|\widetilde{v}_\square|\mathcal{C}\rangle = -\sum_{\mathcal{C}'}\langle\mathcal{C}|t_\square|\mathcal{C}'\rangle\prod_{\widetilde{\square}=\square\pm\hat{i}}\frac{\widetilde{\psi}_0\left(\widetilde{\square},\mathcal{C}'\right)}{\widetilde{\psi}_0\left(\widetilde{\square},\mathcal{C}\right)}\,. \tag{4.90}$$

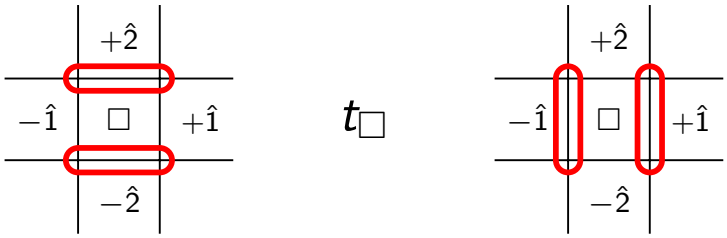

Figure 4.18.: *A plaquette flip only affects neighboring plaquettes.*

This potential is obviously local and for $\phi_1 = \phi_2$ it simplifies to the standard case described in eq. (4.72) with $\lambda = 1$. Hence, eq. (4.86) is a sensible definition in our case. The potential term can be rewritten in the flux basis of the corresponding quantum link model

$$\langle \mathcal{C}|\widetilde{v}_\square|\mathcal{C}\rangle = J \left(\; + \; \right) \left(\frac{\phi_1}{\phi_2}\right)^{k_\square(\mathcal{C})} \tag{4.91}$$

with

$$k_\square(\mathcal{C}) = \left(\; - \; \right) \times \left(\; - \; + \; - \; + \; - \; + \; - \; \right) . \tag{4.92}$$

The above symbols , , , …, denote products of delta functions of fluxes in the noted direction. The Hamiltonian obviously depends on the ratio of ϕ_1 to ϕ_2 only. The potential is defined for arbitrary flux patterns, so external charges and different flux sectors are already incorporated. No way was found to decompose this local potential into a sum of simpler ones.

There is also no way to add an additional local potential which could distinguish different flux sectors. Hence, finally all flux sectors in the ground state have energy $E_0 = 0$. This means that fluxes don't cost energy and the system is deconfined. The $U(1) = SO(2)$ center symmetry is spontaneously broken, even on finite lattices. The local energy density of the ground state is zero for all flux sectors.

The question arises whether the choosen wave function really is the ground state of the system for all ratios $\phi_1/\phi_2 > 0$. Again we consider the general normalized wave function defined in eq. (4.74). First let's apply the local potential defined in eq. (4.86)

$$\begin{aligned}
\langle\psi|\widetilde{v}_\square|\psi\rangle &= \sum_{\mathcal{C},\mathcal{C}'} \langle\psi|\mathcal{C}\rangle\langle\mathcal{C}|\widetilde{v}_\square|\mathcal{C}'\rangle\langle\mathcal{C}'|\psi\rangle \\
&= \sum_{\mathcal{C}} \langle\psi|\mathcal{C}\rangle\langle\mathcal{C}|\widetilde{v}_\square|\mathcal{C}\rangle\langle\mathcal{C}|\psi\rangle \\
&= -\sum_{\mathcal{C},\mathcal{C}'} \langle\psi|\mathcal{C}\rangle\langle\mathcal{C}|t_\square|\mathcal{C}'\rangle \frac{\langle\mathcal{C}'|\widetilde{\psi}_0\rangle}{\langle\mathcal{C}|\widetilde{\psi}_0\rangle}\langle\mathcal{C}|\psi\rangle
\end{aligned} \tag{4.93}$$

and then the whole local Hamiltonian of a plaquette

$$\begin{aligned}
\langle\psi|\widetilde{h}_{\square}|\psi\rangle &= \sum_{\mathcal{C},\mathcal{C}'}\langle\psi|\mathcal{C}\rangle\langle\mathcal{C}|t_{\square}|\mathcal{C}'\rangle\left\{\langle\mathcal{C}'|\psi\rangle - \frac{\langle\mathcal{C}'|\widetilde{\psi}_0\rangle}{\langle\mathcal{C}|\widetilde{\psi}_0\rangle}\langle\mathcal{C}|\psi\rangle\right\} \\
&= \sum_{\mathcal{C},\mathcal{C}'}\frac{\langle\widetilde{\psi}_0|\mathcal{C}'\rangle\langle\psi|\mathcal{C}\rangle}{\langle\widetilde{\psi}_0|\mathcal{C}'\rangle\langle\mathcal{C}|\widetilde{\psi}_0\rangle}\langle\mathcal{C}|t_{\square}|\mathcal{C}'\rangle\left\{\langle\mathcal{C}'|\psi\rangle\langle\mathcal{C}|\widetilde{\psi}_0\rangle - \langle\mathcal{C}|\psi\rangle\langle\mathcal{C}'|\widetilde{\psi}_0\rangle\right\} \\
&= \frac{1}{2}\sum_{\mathcal{C},\mathcal{C}'}\frac{\langle\widetilde{\psi}_0|\mathcal{C}'\rangle\langle\psi|\mathcal{C}\rangle}{\langle\widetilde{\psi}_0|\mathcal{C}'\rangle\langle\mathcal{C}|\widetilde{\psi}_0\rangle}\langle\mathcal{C}|t_{\square}|\mathcal{C}'\rangle\left\{\langle\mathcal{C}'|\psi\rangle\langle\mathcal{C}|\widetilde{\psi}_0\rangle - \langle\mathcal{C}|\psi\rangle\langle\mathcal{C}'|\widetilde{\psi}_0\rangle\right\} \\
&- \frac{1}{2}\sum_{\mathcal{C},\mathcal{C}'}\frac{\langle\widetilde{\psi}_0|\mathcal{C}\rangle\langle\psi|\mathcal{C}'\rangle}{\langle\widetilde{\psi}_0|\mathcal{C}\rangle\langle\mathcal{C}'|\widetilde{\psi}_0\rangle}\langle\mathcal{C}'|t_{\square}|\mathcal{C}\rangle\left\{\langle\mathcal{C}'|\psi\rangle\langle\mathcal{C}|\widetilde{\psi}_0\rangle - \langle\mathcal{C}|\psi\rangle\langle\mathcal{C}'|\widetilde{\psi}_0\rangle\right\} \\
&= -\frac{1}{2}\sum_{\mathcal{C},\mathcal{C}'}\frac{\left|\langle\mathcal{C}'|\psi\rangle\langle\mathcal{C}|\widetilde{\psi}_0\rangle - \langle\mathcal{C}|\psi\rangle\langle\mathcal{C}'|\widetilde{\psi}_0\rangle\right|^2}{\langle\widetilde{\psi}_0|\mathcal{C}'\rangle\langle\mathcal{C}|\widetilde{\psi}_0\rangle}\langle\mathcal{C}|t_{\square}|\mathcal{C}'\rangle \\
&\geq 0\,. \qquad (4.94)
\end{aligned}$$

Here we used the facts that $\langle\mathcal{C}'|t_{\square}|\mathcal{C}\rangle = \langle\mathcal{C}|t_{\square}|\mathcal{C}'\rangle \leq 0$ and $\langle\widetilde{\psi}_0|\mathcal{C}\rangle = \langle\mathcal{C}|\widetilde{\psi}_0\rangle > 0$. So the wave function defined in eq. (4.80) is the ground state and its local energy density is zero

$$\widetilde{h}_{\square}|\widetilde{\psi}_0\rangle = 0|\widetilde{\psi}_0\rangle\,. \qquad (4.95)$$

Since now we constructed a valid parent Hamiltonian whose ground state wave function is given by eq. (4.80), we can analyze its excited states by exact diagonalization of small systems. The ground state properties can be examined for larger systems by Monte Carlo methods.

4.8. Observables

At zero temperature with periodic boundary conditions, there is no tunneling between flux sectors (E_1, E_2). An observable can be calculated as

$$\langle\mathcal{O}\rangle_{T=0,\vec{E}} = \langle\widetilde{\psi}_0|\hat{\mathcal{O}}|\widetilde{\psi}_0\rangle_{\vec{E}} = \sum_{\mathcal{C},\mathcal{C}'|_{(E_1,E_2)}}\langle\widetilde{\psi}_0|\mathcal{C}\rangle\langle\mathcal{C}|\hat{\mathcal{O}}|\mathcal{C}'\rangle\langle\mathcal{C}'|\widetilde{\psi}_0\rangle\,. \qquad (4.96)$$

For observables diagonal in the dimer basis (or equivalently in flux configurations) we can write

$$\langle\mathcal{O}\rangle_{T=0,\vec{E}} = \sum_{\mathcal{C}|_{(E_1,E_2)}}\left|\langle\mathcal{C}|\widetilde{\psi}_0\rangle\right|^2\langle\mathcal{C}|\hat{\mathcal{O}}|\mathcal{C}\rangle = \sum_{\mathcal{C}|_{(E_1,E_2)}}\rho\left(\mathcal{C}\right)O\left(\mathcal{C}\right)\,. \qquad (4.97)$$

with the probability density

$$\rho\left(\mathcal{C}\right) = \left|\langle\mathcal{C}|\widetilde{\psi}_0\rangle\right|^2 = \mathcal{N}^2\prod_{\square}\left|\widetilde{\psi}_0\left(\square,\mathcal{C}\right)\right|^2 \geq 0 \qquad (4.98)$$

and the value of the observable for a cartoon configuration

$$O\left(\mathcal{C}\right) = \langle \mathcal{C}|\hat{\mathcal{O}}|\mathcal{C}\rangle \,. \tag{4.99}$$

Despite the fact that the ground state is analytically known, for systems larger than 8×8 the observable can't be computed exactly since the Hilbert space is exponentially large. However, one can still perform Monte Carlo sampling with the probability density $\rho\left(\mathcal{C}\right)$ as a Boltzmann weight.

As a side remark we note that the quantum dimer model with the modified wave function can be mapped to a system of classical statistical physics [51]

$$\begin{aligned}
\langle \mathcal{O} \rangle_{T=0,\vec{E}} &= \mathcal{N}^2 \sum_{\mathcal{C}|_{(E_1,E_2)}} O\left(\mathcal{C}\right) \prod_{\square} \left(\widetilde{\psi}_0\left(\square, \mathcal{C}\right)\right)^2 \\
&= \mathcal{N}^2 \sum_{\mathcal{C}|_{(E_1,E_2)}} O\left(\mathcal{C}\right) \exp\left(2 \sum_{\square} \ln\left(\widetilde{\psi}_0\left(\square, \mathcal{C}\right)\right)\right) \\
&= \mathcal{N}^2 \phi_2^{(2V)} \sum_{\mathcal{C}|_{(E_1,E_2)}} O\left(\mathcal{C}\right) \mathrm{e}^{2\ln\left(\frac{\phi_1}{\phi_2}\right) F_{\mathcal{C}}} \,,
\end{aligned} \tag{4.100}$$

where $F_{\mathcal{C}}$ is the number of flippable plaquettes in configuration $\mathcal{C}$. It is known that quantum dimer models undergo a Kosterlitz-Thouless transition [52–54]. There the term $2\ln\left(\frac{\phi_1}{\phi_2}\right)$ would play the role of an inverse temperature. In contrast to this existing literature and also to [55], in our quantum interpretation of the system we analyze each flux sector individually.

4.9. Effective theory

To generate a total flux in an otherwise columnar phase it is sufficient to move one row of dimers by one lattice spacing. For a well defined height covering and therefore a well defined order parameter in a periodic system the flux has to be of unit 2. Such a configuration with simple dimer shifts is shown in the top panel of Figure 4.19. Two vertical rows of staggered flux pattern appear around the translated dimers. These dimers belong to the narrowest realization of a local columnar configuration which is shown in the mid panel for the same amount of total flux. This transition can be performed by just flipping the 5^{th}, 6^{th}, 15^{th}, and 16^{th} vertical rows denoted with "col_1" two times with alternating flipping center. At the bottom of each panel of the figure the contribution to the total flux is noted, where

$$\overline{E}_2(x_1 + 1/2, x_2) \coloneqq \frac{1}{2L_2} \sum_{x_2} \left[E_2(x_1, x_2) + E_2(x_1 + 1, x_2)\right] \,. \tag{4.101}$$

Just by flipping the rows of plaquettes left to those labeled "stg_1" in the mid panel of Figure 4.19 one reaches the configuration at the bottom panel of the same figure. There

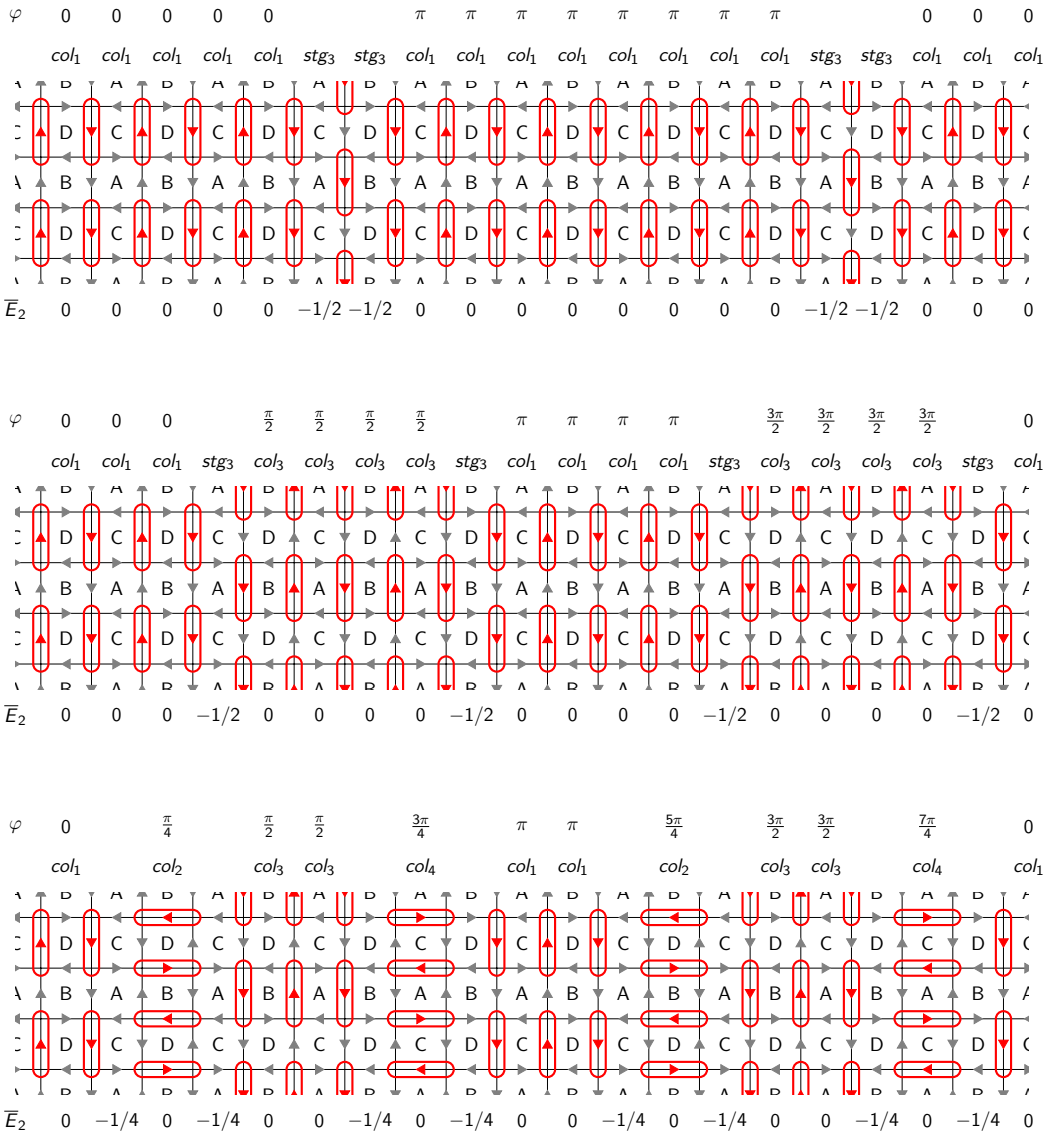

Figure 4.19.: *A periodic system with* 20×4 *lattice sites. The definition of the blocked electric flux* $\overline{E}_2$ *is given in eq. (4.101). In words it is the mean of all fluxes on the links at the left and at the right of the vertical column associated with a value of* $\overline{E}_2$*. Summing up the individual contributions* $\overline{E}_2$ *at the bottom of an individual panel amounts to a negative total flux of unit* 2 *in the* x_2 *direction. Above each panel the corresponding phase realization of each column of plaquettes is indicated if applicable. The sublattices are pointed out to easily identify the different local phase realizations. Additionally the corresponding value of* φ *is noted. The* top panel *shows a configuration where the total flux is created by a shift of two dimer rows relative to the bulk columnar* col_1 *configuration. At the* center panel *these two rows are enlarged to columnar* col_3 *configurations. Finally in the* bottom panel *which belongs to the same flux sector as the first two panels there is no more staggered structure.*

are more possibilities to realize configurations of this type than those of the first two panels. For large ϕ_1/ϕ_2 deep in the deconfined columnar phase such configurations will be more probable first due to statistics and second because they contain no more staggered structures and therefore more flippable plaquettes.

These were configurations without superpositions as an example for the flux $(0, -2)$ sector. One can smear out the boundaries of the local columnar configurations with local resonating dimer configurations and therefore generate local plaquette phase configurations as shown in Figure 4.20. If one imagines to project the resonating dimer plaquettes to

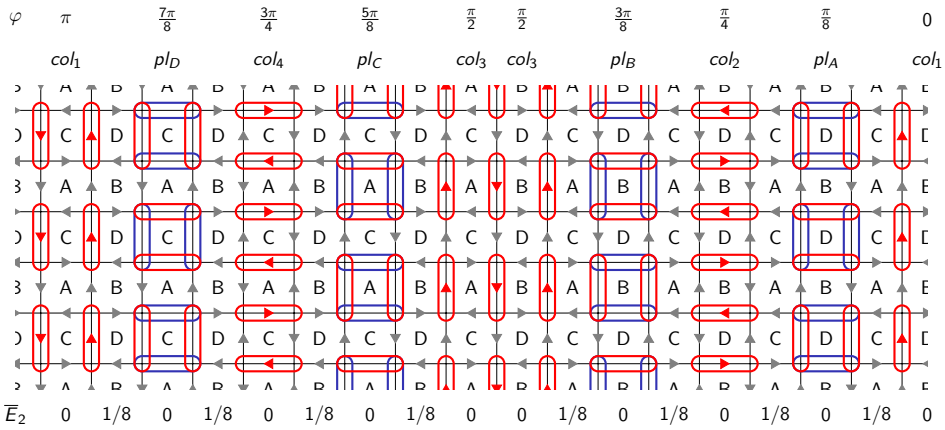

Figure 4.20.: *A periodic system with* 36×6 *lattice sites and total flux of unit* 2 *in the* x_2 *direction. Here only half of the system is visualized. Imagine a copy of the same system on the right with* φ *continuing from 0 to* $-\pi = \pi$*. Again, the sublattices are pointed out to easily identify the different local phase realizations. Local plaquette configurations separate the local columnar configurations. On top the corresponding phase realization of each column of plaquettes is indicated with the corresponding value of* φ*. Remember that adding* π *to* φ *results in the same physical configuration. The definition of the blocked electric flux* $\overline{E}_2$ *is given in the text.*

either horizontal parallel dimers or vertical parallel dimers a configuration similar to the bottom panel of Figure 4.19 appears. Figure 4.20 shall give us an illustration how a flux is generated by a monotonically growing φ. The angle φ defined in eq. (4.67) parametrizes the massless Goldstone boson field appearing at the Rokhsar-Kivelson point. For a flux of unit 1, φ has to change by π. Remember that a change of π results in the same physical phase. A growing φ in the x_1 direction corresponds to a negative flux in the x_2 direction while a growing φ in the x_2 direction corresponds to a positive flux in the x_1 direction. The latter is visualized in Figure 4.21, where

$$\overline{E}_1(x_1, x_2 + 1/2) := \frac{1}{2L_1} \sum_{x_1} \left[E_2(x_1, x_2) + E_2(x_1, x_2 + 1) \right] . \tag{4.102}$$

Putting a defect into the quantum dimer model corresponds to putting an additional charge into the quantum link model with staggered static background charges. Charges

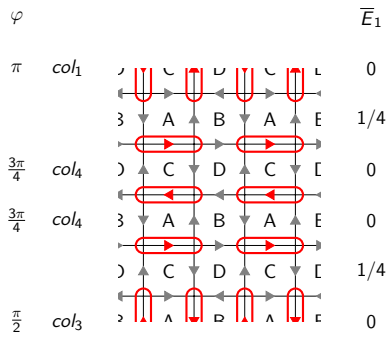

Figure 4.21.: *Section of a system with a positive total flux contribution of unit* 1 *in the* x_1 *direction. Again, the sublattices are pointed out to easily identify the different local phase realizations. On the left the corresponding phase realization of each row of plaquettes is indicated with the corresponding value of* φ*. The definition of the blocked electric flux* $\overline{E}_1$ *is given in the text.*

appear as a vortex where the different local columnar phase realizations meet. For a charge of unit 2 a vortex appears around which φ changes by 2π. This is shown in Figure 4.22.

The above observations are captured

$$F_{\mu\nu} = \frac{1}{\pi}\epsilon_{\mu\nu\rho}\partial_\rho f\left(\varphi(x)\right) = \frac{1}{\pi}\epsilon_{\mu\nu\rho}\frac{\partial f}{\partial\varphi}\partial_\rho\varphi(x) \tag{4.103}$$

with $f(\varphi)$ real, $E_i = F_{0i}$, and $B = F_{12}$. For twice differentiable φ fields eq. (4.103) fulfills

$$\partial_i E_i = \partial_i F_{0i} = \frac{1}{\pi}\partial_i\epsilon_{0ij}\partial_j f\left(\varphi(x)\right) = 0\,. \tag{4.104}$$

Assume $\partial_2\varphi(x) = 0$ as in Figures 4.19 and 4.20. Then

$$E_1(x) = \frac{1}{\pi}\frac{\partial f}{\partial\varphi}\partial_2\varphi(x) = 0 \tag{4.105}$$

and

$$\begin{aligned}\int_{x_A}^{x_B} dx_1 E_2(x_1,x_2) &= -\frac{1}{\pi}\int_{x_A}^{x_B} dx_1\,\partial_1 f\left(\varphi(x_1,x_2)\right)\\ &= \frac{1}{\pi}\left[f\left(\varphi(x_A,x_2)\right) - f\left(\varphi(x_B,x_2)\right)\right]\,.\end{aligned} \tag{4.106}$$

Comparing this result with Figure 4.20 we obtain

$$f\left(\frac{k\pi}{8}+\frac{l\pi}{8}\right) = f\left(\frac{k\pi}{8}\right) + \frac{l\pi}{8}\,,\quad k,l\in\mathbb{Z} \tag{4.107}$$

The Hamiltonian of the quantum dimer model is invariant under geometrical rotations by $\pi/2$. Such a rotation changes φ by $\pi/4$, so

$$\frac{\partial f}{\partial\varphi}\left(\varphi+\frac{\pi}{4}\right) = \frac{\partial f}{\partial\varphi}\left(\varphi\right)\,. \tag{4.108}$$

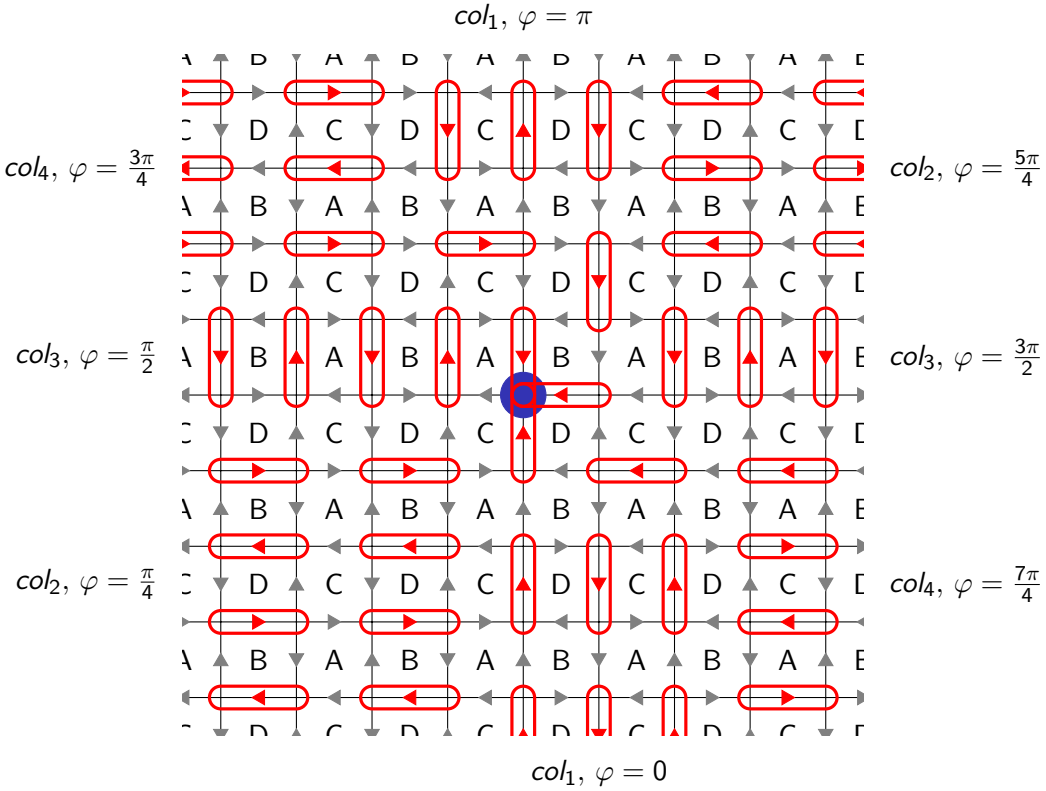

Figure 4.22.: *Going once around the static double negative charge, which sits in the center, each columnar configuration realization appears two times. Double negative is understood relative to the staggered background charge. The static charge appears as a vortex at which the local columnar phase realizations meet. Going counter-clockwise around the double negative charge the angle φ decreases. Analogous to Figure 4.20 local plaquette configurations between the columnar configurations could have been inserted.*

The most general solution of the last equation is

$$f(\varphi) = f_0 + f_1\,\varphi + \sum_{k=1}^{\infty}\left[a_k \sin(8k\varphi) + \tilde{b}_k \cos(8k\varphi)\right] . \tag{4.109}$$

The constant f_0 is irrelevant. Because of eq. (4.107), $f_1 = 1$ and $\tilde{b}_k = 0$ for k odd, finally

$$f(\varphi) = \varphi + \sum_{k=1}^{\infty}\left[a_k \sin(8k\varphi) + b_k \cos(16k\varphi)\right] . \tag{4.110}$$

If there is an integer charge of value k in a region Ω according to Figure 4.22 the angle φ changes by an amount of $k\pi$ and we consistently get

$$\begin{aligned} Q_\Omega &= \int_\Omega d^2x\,\partial_i E_i = \int_{\partial\Omega} d\sigma_i\, E_i = \int_{\varphi_0}^{\varphi_0+k\pi} d\varphi\,\frac{(\partial\vec{x}\times\hat{e}_3)_i}{\partial\varphi}\,E_i \\ &= \frac{1}{\pi}\int_{\varphi_0}^{\varphi_0+k\pi} d\varphi\,\epsilon_{ij3}\frac{\partial x_j}{\partial\varphi}\frac{\partial f}{\partial\varphi}\epsilon_{0ik}\frac{\partial\varphi}{\partial x_k} = \frac{1}{\pi}\int_{\varphi_0}^{\varphi_0+k\pi} d\varphi\,\frac{\partial f}{\partial\varphi} \\ &= \frac{1}{\pi}\left[f(\varphi_0+k\pi) - f(\varphi_0)\right] = k\,. \end{aligned} \tag{4.111}$$

Here we assumed a boundary $\partial\Omega$ with monotonically growing φ. The gradient of φ is orthogonal to the electric flux

$$\left(\vec{\nabla}\varphi\right)\cdot\vec{E} = \partial_i\varphi E_i = \partial_\varphi\frac{1}{\pi}\epsilon_{0i\rho}\partial_\rho f\left(\varphi(x)\right) = \frac{1}{\pi}f'(\varphi)\epsilon_{0ij}\partial_i\varphi\partial_j\varphi = 0\,. \tag{4.112}$$

Following the gradient of φ, in eq. (4.111) tells us that

$$\frac{dQ_\Omega}{d\varphi} = \frac{1}{\pi}\frac{\partial f}{\partial\varphi}\,. \tag{4.113}$$

We would like to build an effective theory with the Goldstone mode parameterized by the angle φ. The Lagrange density then has the form

$$\begin{aligned} \mathcal{L}(\varphi,\dot{\varphi},\partial_i\varphi,\partial_i\partial_i\varphi) &= \rho_t\,\dot{\varphi}^2 + \rho\,\partial_i\varphi\,\partial_i\varphi + \kappa\left(\partial_i\partial_i\varphi\right)^2 \\ &\quad + \xi\sum_i \partial_i\partial_i\varphi\,\partial_i\partial_i\varphi + V(\varphi)\,. \end{aligned} \tag{4.114}$$

The equation of motion is then given by

$$\begin{aligned} 0 &\overset{!}{=} \frac{\partial\mathcal{L}}{\partial\varphi} - \frac{d}{dt}\frac{\partial\mathcal{L}}{\partial\dot{\varphi}} - \partial_i\left(\frac{\partial\mathcal{L}}{\partial(\partial_i\varphi)}\right) + \partial_i\partial_i\left(\frac{\partial\mathcal{L}}{\partial(\partial_i\partial_i\varphi)}\right) \\ &= V'(\varphi) - 2\rho_t\ddot{\varphi} - 2\rho\partial_i\partial_i\varphi + 2\kappa\partial_i\partial_i\partial_j\partial_j\varphi + 2\xi\sum_i\partial_i\partial_i\partial_i\partial_i\varphi\,. \end{aligned} \tag{4.115}$$

If we assume a periodic system with a flux in the x_2 direction wrapping over the boundaries and no static external charges, for symmetry reasons $E_2(x)$ will be constant and $E_1(x) = 0$. An analogous situation arises for a flux in the x_1 direction. In such a situation

$$0 = \partial_i E_j = \frac{1}{\pi}\epsilon_{0jk}\frac{\partial f}{\partial\varphi}\partial_i\partial_k\varphi(x)\,, \quad i,j\in\{1,2\}\,. \tag{4.116}$$

In section 4.7 we saw that for the modified ground state wave function the local energy density is zero for all flux sectors. Hence the Lagrange density has to be zero for fields φ which fulfill

$$\partial_i \partial_k \varphi(x) = 0\,, \quad i,k \in \{1,2\}\,. \tag{4.117}$$

In other words such fields are solutions of the classical equation of motion. From this it follows that $\rho = 0$ since a constant non-zero $\partial_i \varphi$ satisfies eq. (4.117).

As we already observed at the beginning of this section, in a system with a total flux of value 2 in one direction, the value of φ has to cover the whole range from 0 to 2π. Since this doesn't cost energy, it immediately follows that $V(\varphi) = 0$ in the Lagrange density. For static configurations and with $\rho = 0$ this amounts into

$$\mathcal{L}(\partial_i \partial_i \varphi) = \kappa \left(\partial_i \partial_i \varphi\right)^2 + \xi \sum_i \partial_i \partial_i \varphi \, \partial_i \partial_i \varphi \tag{4.118}$$

with the equation of motion

$$0 \stackrel{!}{=} \kappa \partial_i \partial_i \partial_j \partial_j \varphi + \xi \sum_i \partial_i \partial_i \partial_i \partial_i \varphi\,. \tag{4.119}$$

While this is an interesting path to follow, we will first pursue another attempt. The quantum dimer model respects the Gauss law. If one coarse grains the microscopic model, its staggered background charges average to zero. Putting static external charges ± 2 in a periodic system should in a first approximation be equivalent to putting static charges ± 2 in classical electrodynamics in a periodic manner.

In classical electrodynamics the static electric field of a point charge Q in two spatial dimensions with

$$\vec{x} = r \begin{pmatrix} \cos(\alpha) \\ \sin(\alpha) \end{pmatrix} \tag{4.120}$$

is

$$\vec{E} = \frac{Q}{2\pi r} \begin{pmatrix} \cos(\alpha) \\ \sin(\alpha) \end{pmatrix} = \frac{Q}{2\pi} \frac{\vec{x}}{|\vec{x}|^2}\,. \tag{4.121}$$

The gradient of $\alpha = \arg(x_1, x_2)$ is

$$\vec{\nabla}\alpha = \begin{pmatrix} \partial_1 \\ \partial_2 \end{pmatrix} \arg(x_1, x_2) = \frac{1}{r^2} \begin{pmatrix} x_2 \\ x_1 \end{pmatrix}\,. \tag{4.122}$$

As it was the case for the gradient of φ, also the gradient of α is orthogonal to the electric field

$$\left(\vec{\nabla}\alpha\right) \vec{E} = 0\,. \tag{4.123}$$

With $\partial_i E_i = 0$ (except for $\vec{x} = (0,0)$) we obtain

$$\begin{aligned} \int_\Omega d^2x \, \partial_i E_i = \int_{\partial\Omega} d\sigma_i \, E_i &= \int_0^{2\pi} d\alpha \, r \begin{pmatrix} \cos(\alpha) \\ \sin(\alpha) \end{pmatrix} \frac{Q}{2\pi r} \begin{pmatrix} \cos(\alpha) \\ \sin(\alpha) \end{pmatrix} \\ &= \int_0^{2\pi} d\alpha \, \frac{Q}{2\pi} = Q\,. \end{aligned} \tag{4.124}$$

We conclude that

$$\frac{dQ}{d\alpha} = \frac{Q}{2\pi}\,. \tag{4.125}$$

Using this and eq. (4.113), we now identify the Goldstone boson field φ

$$\frac{Q}{2\pi}d\alpha = dQ \stackrel{!}{=} dQ_\Omega = \frac{1}{\pi}f'(\varphi)d\varphi\,. \tag{4.126}$$

Assuming the simplest case $f(\varphi) = \varphi$ ($a_k = b_k = 0$ in eq. (4.110)) this simply amounts to

$$\varphi = \varphi_0 + \frac{Q}{2}\alpha\,. \tag{4.127}$$

Now let's put a static external charge $Q_l = -2$ located at $(q_{l,1}, q_{l,2})$ and a static external charge $Q_r = +2$ at $(q_{r,1}, q_{r,2})$ into a periodic system of size $L_1 \times L_2$. This amounts into

$$E_i(\vec{x}) = E_{l,i}(\vec{x}) + E_{r,i}(\vec{x}) \tag{4.128}$$

with

$$E_{p,i}(\vec{x}) = \frac{Q_p}{2\pi}\sum_{n_1,n_2\in\mathbb{Z}}\frac{x_i - q_{p,i} - n_iL_i}{\sum_{j=1,2}\left(x_j - q_{p,j} - n_jL_j\right)^2}\,. \tag{4.129}$$

Equation (4.128) is defined only for vanishing total charge, The contribution of one charge to the electric flux in the x_1 direction through a cut of the system in the x_2 direction is given by

$$\begin{aligned}
\varepsilon_{p,1}(x_1) &= \int_0^{L_2} dx_2 E_{p,1}(x_1, x_2) \\
&= \frac{Q_p}{2\pi}\int_{-\infty}^{\infty} dx_2 \sum_{n_1\in\mathbb{Z}}\frac{x_1 - q_{p,1} - n_1L_1}{\left(x_1 - q_{p,1} - n_1L_1\right)^2 + \left(x_2\right)^2} \\
&= \frac{Q_p}{2\pi}\sum_{n_1\in\mathbb{Z}}\left[\arctan\left(\frac{x_2}{x_1 - q_{p,1} - n_1L_1}\right)\right]_{x_2=-\infty}^{\infty} \\
&= \frac{Q_p}{2}\sum_{n_1\in\mathbb{Z}}\operatorname{sign}\left(x_1 - q_{p,1} - n_1L_1\right)\,.
\end{aligned} \tag{4.130}$$

The analogous expression, with the roles of indices 1 and 2 interchanged, holds for $\varepsilon_{p,2}(x_2)$. Assuming $0 < l_1 < r_1 < L_1$ this amounts to

$$\begin{aligned}
\varepsilon_1(0 \le x_1 < L_1) &= \operatorname{sign}\left(x_1 - q_{r,1}\right) - \operatorname{sign}\left(x_1 - q_{l,1}\right) \\
&= 2\Theta\left(x_1 - q_{l,1}\right)\Theta\left(q_{r,1} - x_1\right)\,.
\end{aligned} \tag{4.131}$$

Hence, there is a flux of unit 2 for $x_1 \in\,]q_{l,1}, q_{r,1}[$ and no flux for $x_1 \in\,]0, q_{l,1}[$ and $x_1 \in\,]q_{r,1}, L_1[$ as we would expect in the flux $(0,0)$ sector. We have to discretize this continuum result to compare it with the quantum dimer model which lives on a lattice.

To compare to a flux in the x_1 direction in a quantum link between the sites (x_1, x_2) and $(x_1 + a, x_2)$ we have to integrate the flux in the x_1 direction of the continuum model which

flows through the 1-dimensional surface defined by the dual link connecting the dual sites $(x_1+\frac{a}{2}, x_2-\frac{a}{2})$ and $(x_1+\frac{a}{2}, x_2+\frac{a}{2})$

$$\begin{aligned}\varepsilon_{p,1}(x_1,x_2) &= \int_{x_2-\frac{a}{2}}^{x_2+\frac{a}{2}} dx_2' E_{p,1}(x_1+\frac{a}{2}, x_2') \\ &= \frac{Q_p}{2\pi}\int_{x_2-\frac{a}{2}}^{x_2+\frac{a}{2}} dx_2' \sum_{n_1,n_2\in\mathbb{Z}} \frac{x_1+\frac{a}{2}-q_{p,1}-n_1L_1}{\left(x_1+\frac{a}{2}-q_{p,1}-n_1L_1\right)^2+\left(x_2'-q_{p,2}-n_2L_2\right)^2} \\ &= \frac{Q_p}{2\pi}\sum_{n_1,n_2\in\mathbb{Z}}\left[\arctan\left(\frac{x_2'-q_{p,2}-n_2L_2}{x_1+\frac{a}{2}-q_{p,1}-n_1L_1}\right)\right]_{x_2'=x_2-\frac{a}{2}}^{x_2+\frac{a}{2}}. \end{aligned} \tag{4.132}$$

From this we obtain

$$\begin{aligned}\pi\varepsilon_1(x_1,x_2) = &\sum_{n_1,n_2\in\mathbb{Z}} \arctan\left(\frac{x_2+\frac{a}{2}-q_{r,2}-n_2L_2}{x_1+\frac{a}{2}-q_{r,1}-n_1L_1}\right) \\ &- \sum_{n_1,n_2\in\mathbb{Z}} \arctan\left(\frac{x_2-\frac{a}{2}-q_{r,2}-n_2L_2}{x_1+\frac{a}{2}-q_{r,1}-n_1L_1}\right) \\ &- \sum_{n_1,n_2\in\mathbb{Z}} \arctan\left(\frac{x_2+\frac{a}{2}-q_{l,2}-n_2L_2}{x_1+\frac{a}{2}-q_{l,1}-n_1L_1}\right) \\ &+ \sum_{n_1,n_2\in\mathbb{Z}} \arctan\left(\frac{x_2-\frac{a}{2}-q_{l,2}-n_2L_2}{x_1+\frac{a}{2}-q_{l,1}-n_1L_1}\right)\end{aligned} \tag{4.133}$$

and analogously

$$\begin{aligned}\varepsilon_{p,2}(x_1,x_2) &= \int_{x_1-\frac{a}{2}}^{x_1+\frac{a}{2}} dx_1' E_{p,2}(x_1', x_2+\frac{a}{2}) \\ &= \frac{Q_p}{2\pi}\int_{x_1-\frac{a}{2}}^{x_1+\frac{a}{2}} dx_1' \sum_{n_1,n_2\in\mathbb{Z}} \frac{x_2+\frac{a}{2}-q_{p,2}-n_2L_2}{\left(x_2+\frac{a}{2}-q_{p,2}-n_2L_2\right)^2+\left(x_1'-q_{p,1}-n_1L_1\right)^2} \\ &= \frac{Q_p}{2\pi}\sum_{n_1,n_2\in\mathbb{Z}}\left[\arctan\left(\frac{x_1'-q_{p,1}-n_1L_1}{x_2+\frac{a}{2}-q_{p,2}-n_2L_2}\right)\right]_{x_1'=x_1-\frac{a}{2}}^{x_1+\frac{a}{2}}. \end{aligned} \tag{4.134}$$

which results in

$$\begin{aligned}\pi\varepsilon_2(x_1,x_2) = &\sum_{n_1,n_2\in\mathbb{Z}} \arctan\left(\frac{x_1+\frac{a}{2}-q_{r,1}-n_1L_1}{x_2+\frac{a}{2}-q_{r,2}-n_2L_2}\right) \\ &- \sum_{n_1,n_2\in\mathbb{Z}} \arctan\left(\frac{x_1-\frac{a}{2}-q_{r,1}-n_1L_1}{x_2+\frac{a}{2}-q_{r,2}-n_2L_2}\right) \\ &- \sum_{n_1,n_2\in\mathbb{Z}} \arctan\left(\frac{x_1+\frac{a}{2}-q_{l,1}-n_1L_1}{x_2+\frac{a}{2}-q_{l,2}-n_2L_2}\right) \\ &+ \sum_{n_1,n_2\in\mathbb{Z}} \arctan\left(\frac{x_1-\frac{a}{2}-q_{l,1}-n_1L_1}{x_2+\frac{a}{2}-q_{l,2}-n_2L_2}\right).\end{aligned} \tag{4.135}$$

It will turn out that these predictions very well account for the situation at the standard Rokhsar-Kivelson point with $\lambda = \phi_1/\phi_2 = 1$ as we will see in the results.

4.10. Algorithms

The Metropolis algorithm used to examine the ground state properties was rather trivial and follows standard textbook procedures. Nevertheless it is listed as pseudo code in Figure 4.23 for completeness. Possible initial dimer coverings with external charges in

```
program QdmMetropolis:
  • initialize the system with a valid dimer covering
  • perform N_t thermalization sweeps
  • perform N_p production sweeps

in each sweep:
  • perform V Metropolis steps
    (where V is the number of plaquettes)
  • if in production:  measure

in each Metropolis step:
  • call the actual configuration C
  • randomly pick one of the plaquettes and call it □
  • if □ is flippable:
    – call the configuration with □ flipped C'
    – with probability p(C'|C) = min(1, ρ(C')/ρ(C)) accept C' as the
      new actual configuration, otherwise retain C
```

Figure 4.23.: *Metropolis algorithm used for the quantum dimer model with ground state wave function ansatz.*

columnar phases are shown in Figure 4.24.

For systems up to 8×8 lattice sites the partition function can be completely evaluated for each flux sector by exploring all dimer coverings of a Hamiltonian sector by flipping plaquettes. These results have been used to check the Monte Carlo implementation and whether latter is ergodic. In this brute force approach, dimer coverings are encoded by 64-bit integers which we call dimer covering codes. A direct encoding of the dimer states would need two bits per plaquette which would result in a 128-bit integer for an 8×8 system. The used encoding, which on average uses one bit per plaquette, is shown in Figure 4.25. The brute force algorithm is listed as pseudo code in Figure 4.26

It is an open question whether we identified all symmetries up to now. The reason for this question is that there is an emergent $U(1)$ symmetry at the Rokhsar-Kivelson point. It is the question whether the Hamiltonian has sub-sectors beyond the flux sectors.

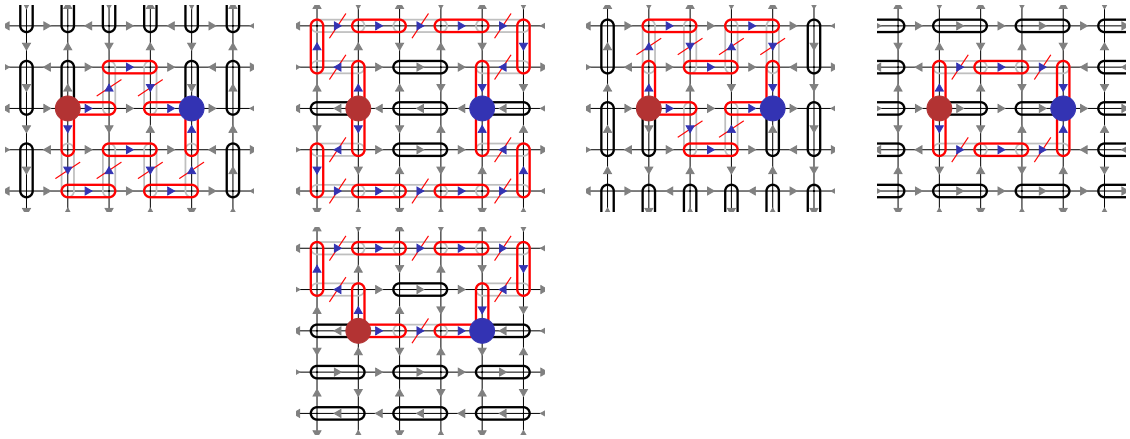

Figure 4.24.: *Possible initial dimer coverings with external charges in columnar phases.*

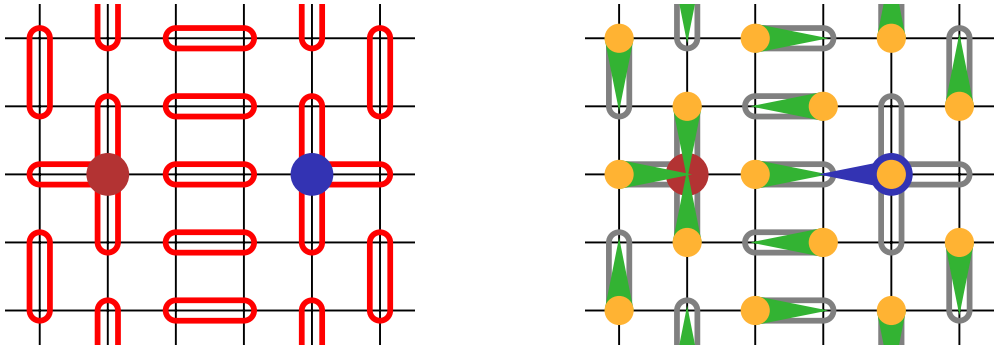

Figure 4.25.: Left panel: *an example dimer configuration with two external charges (defects).* Right panel: *encoding of the dimer configuration on the left for the brute force algorithm. At every second site (yellow dots) the direction (green arrow) of the touching dimer is stored. This results in two bits (four directions) for every second plaquette. The site with the blue defect is encoded inversely (blue arrow in the direction without a dimer).*

Need two initially empty lists for dimer covering codes:

detected-list Configurations detected by the algorithm. This list will finally hold all configurations of a sector.

todo-list Configurations to be explored by flipping them. These are detected but not explored yet. This list will finally be empty.

program QdmBruteForce:

- initialize the system with a valid dimer covering $\mathcal{C}_I$
- measure with weight $\rho(\mathcal{C}_I)$
- put $\mathcal{C}_I$ in both lists
- while the todo-list is not empty:
  - take one configuration out of the todo-list and name it $\mathcal{C}_t$
  - process $\mathcal{C}_t$

processing $\mathcal{C}_t$ means:

- for each flippable plaquette $\square$ in configuration $\mathcal{C}_t$:
  - flip $\square$ in $\mathcal{C}_t$ and name the new configuration $\mathcal{C}_d$
  - if $\mathcal{C}_d$ is not in detected-list yet:
    * measure with weight $\rho(\mathcal{C}_d)$
    * put $\mathcal{C}_d$ in both lists

Figure 4.26.: *Brute force algorithm for a small quantum dimer model with ground state wave function ansatz.*

The algorithm in Figure 4.27 systematically detects all valid dimer coverings and groups them to sectors where a sector consists of coverings which are connected by one ore more plaquette flips. Note that going through all 2^{64} codes explicitly would take years for an ordinary CPU. So the search of the next larger valid dimer covering code c was performed by modifying the dimers directly and rejecting whole groups of configurations as early as possible when one of the several constraints was violated. This method works for systems up to 64 sites with and without external charges. Note that the exact form of the potential doesn't play a role as long as it is diagonal in dimer coverings. So the analysis holds for the standard quantum dimer model and for the modified one with ground state wave function ansatz.

The finding was that the flux sectors are unique up to two exceptions. The trivial exceptions consists of sectors without flippable plaquettes. Another exception were certain flux sectors on systems with external charges where a plaquette pair in some sense moved along a line which was connected to the external charges. So there is no final answer, since one could imagine that additional symmetries could only be observed for systems larger than 8×8.

Small systems are accessible by exact diagonalization too. This reveals information about the spectrum (the excited states). Especially it allows a deformation of the potential which mixes the properties of the standard quantum dimer model with those of the wave function ansatz by simply defining the local potential

$$\begin{aligned} v_{\square,ED}(\mathcal{C}) &= \lambda v_{\square,WF}(\mathcal{C}) \\ &= J\lambda \left(\quad + \quad \right) \left(\frac{\phi_1}{\phi_2} \right)^{k_\square(\mathcal{C})} \end{aligned} \tag{4.136}$$

with $k_\square(\mathcal{C})$ defined in eq. (4.92). For $\phi_1/\phi_2 = 1$ we obtain the standard quantum dimer model, for $\lambda = 1$ we obtain the ground state wave function ansatz used in the Metropolis algorithm. Again arpack was used to perform the exact diagonalizations.

4.11. Results

4.11.1. Statistics of the order parameter

Figure 4.28 shows projected histograms of the order parameters for the Hamiltonian parameter $\phi_1/\phi_2 \in \{0.4, 1, 2, 2.2\}$. About 10^7 Metropolis sweeps were performed, where a sweep is defined in Figure 4.23. This figure is compared to the predicted patterns in Table 4.5 and in the left column of Figure 4.12. As expected, for $\phi_1/\phi_2 = 0.4$ the system is in a staggered phase which manifests itself as narrow bumps around zero in the first row of Figure 4.28. For $\phi_1/\phi_2 = 1$ (second row), which is the Rokhsar-Kivelson point of the standard quantum dimer model, the picture has changed to almost perfectly circular rings which indicate an emergent $U(1)$ symmetry. The rotation by $\pi/4$ described in eq. (4.67) is nicely visible in the dark shadings. For larger ϕ_1/ϕ_2 the rings become deformed to diamonds. For $\phi_1/\phi_2 = 2.2$ the system clearly got into a deconfined columnar phase.

Uses brute force algorithm with detected-list, todo-list. Dimer coverings $\mathcal{C}$ are represented by covering codes c.

program QdmSubSector:

- put covering code c to zero
- if $c(=0)$ represents a valid dimer covering:
  - explore c
- repeat until BREAK occurs:
  - try to find the next larger covering code c which represents a valid dimer covering
  - if there was no more valid dimer covering:
    - BREAK
  - else if c is not in the detected-list yet:
    - explore c

exploring c means:

- put c in both lists (detected-list and todo-list)
- explore the whole actual sector with the brute force algorithm starting with the configuration represented by c
- print out useful informations on this sub-sector including
  - c
  - flux sector
  - minimal and maximal number of flippable plaquettes of the configurations in this sub-sector

Figure 4.27.: *Algorithm to search sub-sectors in flux sectors of a small quantum dimer model. The above algorithm uses the brute force algorithm listed in Figure 4.26. However, no measurements of observables are performed. This way, the exact form of the potential doesn't play a role as long as it is diagonal in the dimer covering basis. The covering codes c are 64-bit values encoded as indicated in Figure 4.25.*

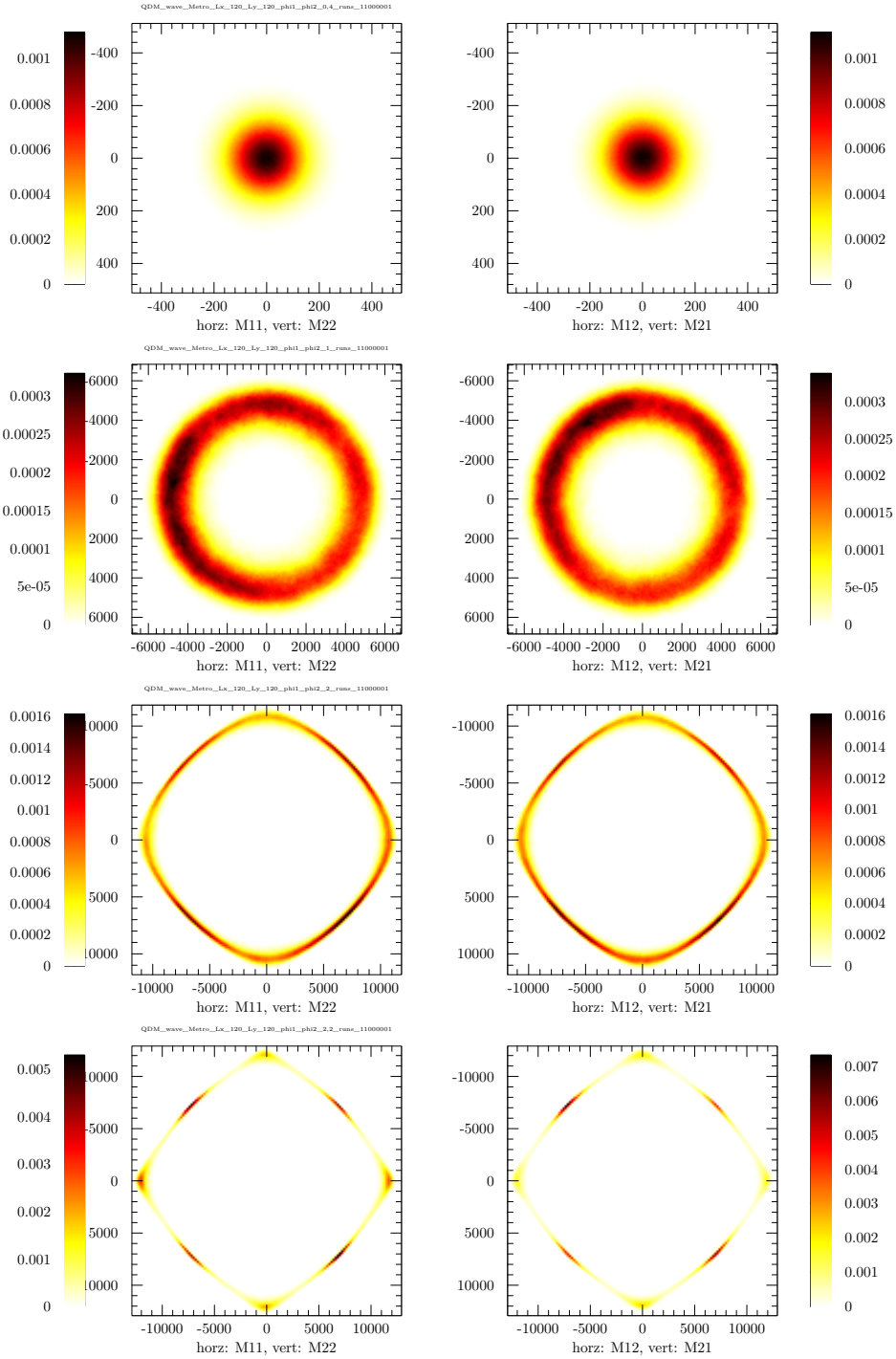

Figure 4.28.: *Projected histograms of the order parameters. The left panels show M_{11} on the horizontal axis and M_{22} on the vertical axis. The right panels show M_{12} on the horizontal axis and M_{21} on the vertical axis. The system has a volume of $L_1 \times L_2 = 120 \times 120$. The value of the Hamiltonian parameter is (from top to down): $\phi_1/\phi_2 = 0.4, 1, 2, 2.2$. The scales depend on ϕ_1/ϕ_2.*

Figure 4.29 shows the angular distribution of the projected order parameters shown in Figure 4.28. The angle φ is defined in eq. (4.67) (compare to Figure 4.13). Let's denote the probability density to find the order parameter projected to (M_{11}, M_{22}) with $p_a(M_{11}, M_{22})$ and for the projection to $(\widetilde{M}_{12}, \widetilde{M}_{21})$ with $p_b(\widetilde{M}_{12}, \widetilde{M}_{21})$. The densities are normalized such that

$$\int dM_{11}\, dM_{22}\, p_a(M_{11}, M_{22}) = \int d\widetilde{M}_{12}\, d\widetilde{M}_{21}\, p_b(\widetilde{M}_{12}, \widetilde{M}_{21}) = 1\,. \tag{4.137}$$

The probability densities $p_a(\varphi)$ and $p_b(\varphi)$ of the argument φ of the projections (M_{11}, M_{22}) and $(\widetilde{M}_{12}, \widetilde{M}_{21})$

$$p_k(\varphi) = \int_0^\infty dr\, r\, p_k(r\cos\varphi, r\sin\varphi) \tag{4.138}$$

are normalized to 1

$$\int_0^{2\pi} p_k(\varphi) d\varphi = 1\,. \tag{4.139}$$

The top panel in Figure 4.29 shows the probability densities $p_a(\varphi)$ and $p_b(\varphi)$ folded from $[0, 2\pi]$ into $[0, \pi/4]$ and normalized to $\pi/4$

$$p(\varphi) = \frac{1}{2}\left(p_a(\varphi) + p_b(\varphi)\right) \tag{4.140}$$

$$\widetilde{p}(\varphi) = \frac{\pi}{4}\sum_{l=0}^{3}\left[p\left(\frac{l\pi}{2} + \varphi\right) + p\left(\frac{l\pi}{2} - \varphi\right)\right]\,. \tag{4.141}$$

The angle φ is on the horizontal axis such that a φ near 0 or $\pi/4 \approx 0.79$ indicates a deconfined columnar phase while angles near $\pi/8 \approx 0.39$ would indicate a plaquette phase. Obviously no plaquette phase appears for different Hamiltonian parameters ϕ_1/ϕ_2. The bottom panel in Figure 4.29 shows a variant of the standard deviation

$$\sigma = \sqrt{\int_0^{2\pi}\left(p(\varphi) - \frac{1}{2\pi}\right)^2 d\varphi} \tag{4.142}$$

of the probability density over the angle φ for different Hamiltonian parameters ϕ_1/ϕ_2.

The top panel of Figure 4.30 shows the mean radius of the projected order parameters illustrated in Figure 4.28 as a function of their assigned angle φ. The radius is defined as

$$R(\varphi) = \frac{1}{2}\left(R_a(\varphi) + R_b(\varphi)\right) \tag{4.143}$$

$$R_k(\varphi) = \frac{1}{p_k(\varphi)}\int_0^\infty dr\, r^2\, p_k(r\cos\varphi, r\sin\varphi)\,. \tag{4.144}$$

Again the angle was folded analogous to eq. (4.140). The figure visualizes how the ring appearing in Figure 4.28 gets deformed for $\phi_1/\phi_2 > 1$. There the approximate $U(1)$ symmetry disappears. The bottom panel of Figure 4.30 shows the mean radius

$$R = \int_0^{2\pi} R(\varphi) p(\varphi) d\varphi \tag{4.145}$$

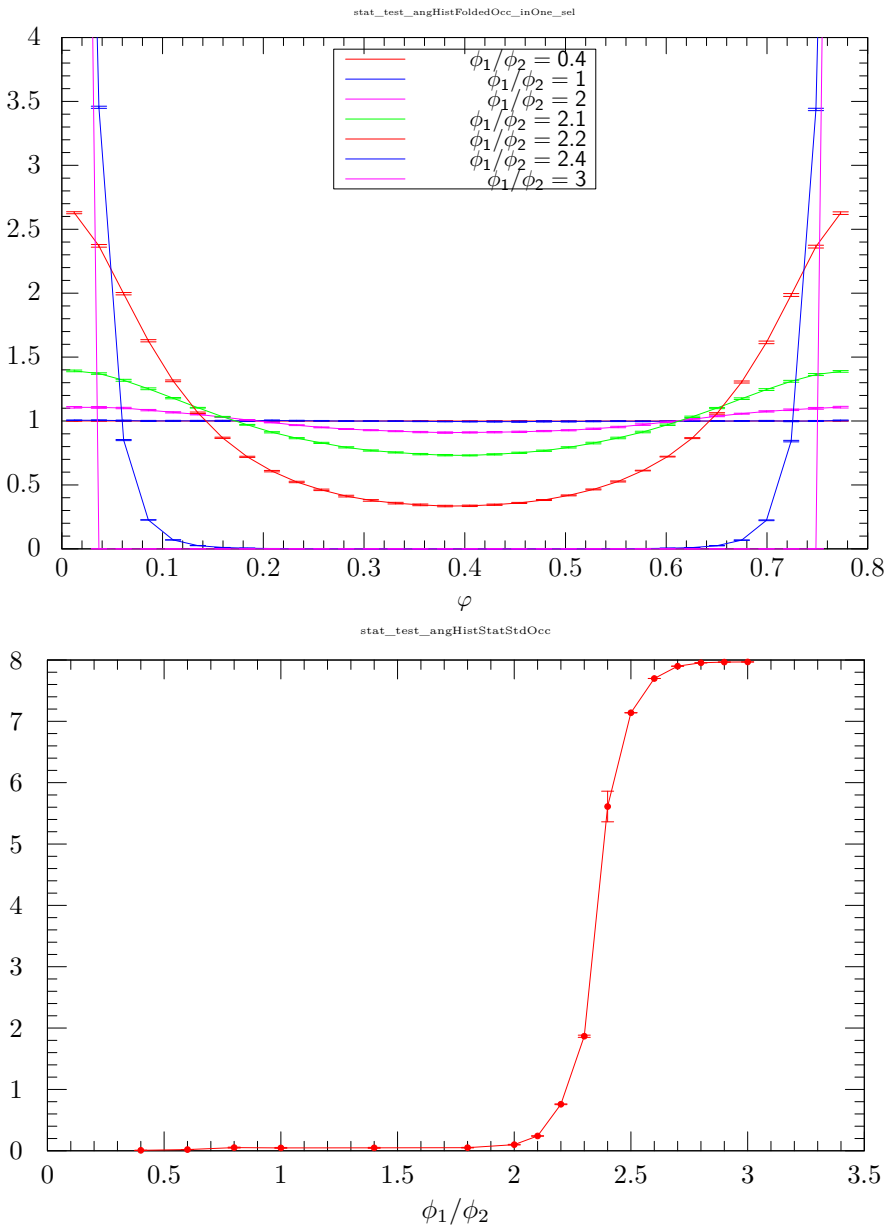

Figure 4.29.: Top panel: *Angular distribution of the projected order parameters shown in Figure 4.28. The probability density with error bars (vertical axis) is normalized to $\pi/4$). The angle φ is folded from $[0, 2\pi]$ into $[0, \pi/4]$. High densities at the extrema of the horizontal axis indicate columnar phases. High densities in the center would indicate plaquette phases.* Bottom panel: *Standard deviation over the angle φ (with error bars) of the above probability density for different Hamiltonian parameters ϕ_1/ϕ_2. For both panels the system size was fixed to $L_1 \times L_2 = 120 \times 120$.*

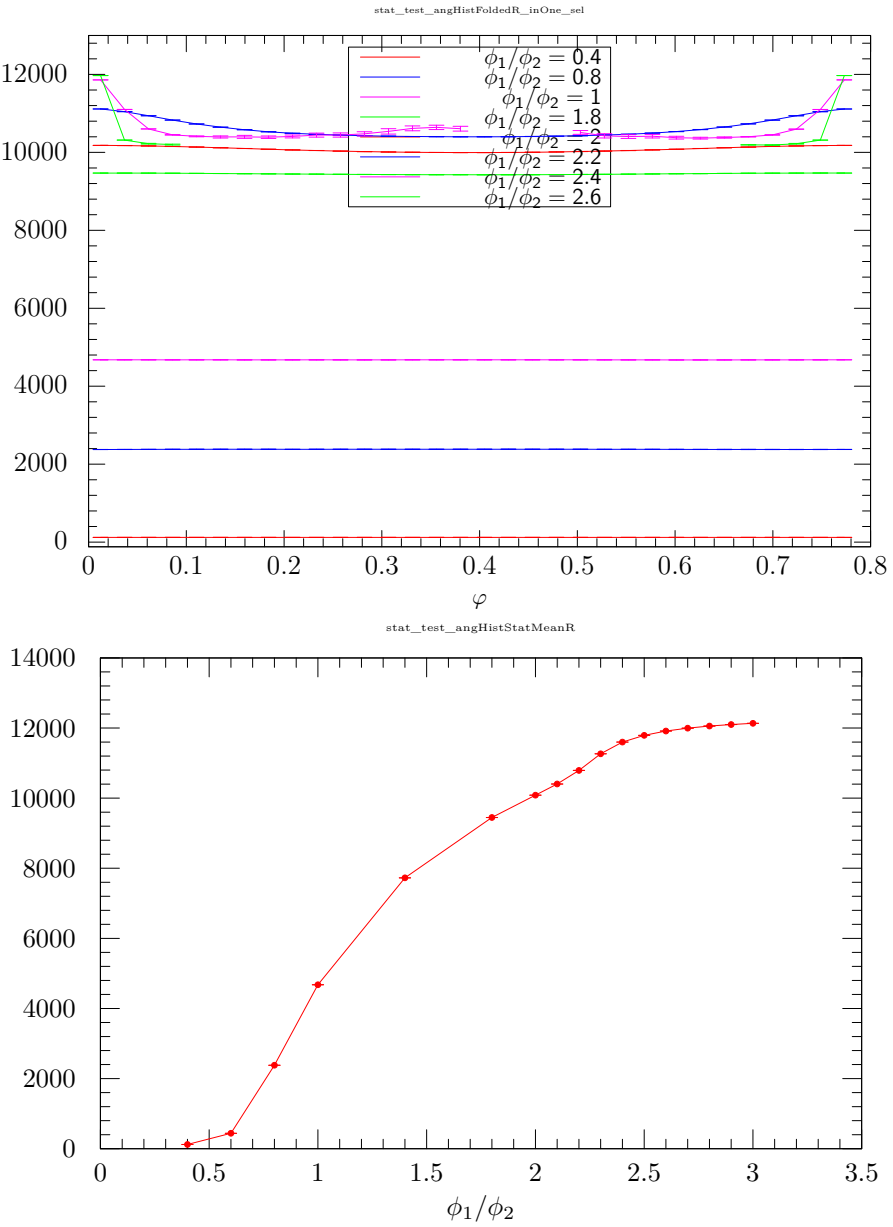

Figure 4.30.: Top panel: *Mean radius with error bars of the projected order parameters shown in Figure 4.28 as a function of their assigned angle φ. The angle φ is again folded from $[0, 2\pi]$ into $[0, \pi/4]$.* Bottom panel: *Mean of above radius over the angle φ with error bars for different Hamiltonian parameters ϕ_1/ϕ_2. For both panels the system size was fixed to $L_1 \times L_2 = 120 \times 120$.*

for different ϕ_1/ϕ_2. In terms of order parameter values this corresponds to

$$\begin{aligned} R_a &= \int_0^{2\pi} d\varphi \int_0^{\infty} dr\, r^2\, p_a(r\cos\varphi, r\sin\varphi) \\ &= \int dM_{11}\, dM_{22}\, p_a(M_{11}, M_{22}) \sqrt{M_{11}^2 + M_{22}^2}\,. \end{aligned} \tag{4.146}$$

This radius is related to the square root of the susceptibility of the order parameter. Without external charges for symmetry reasons (compare definition in eq. (4.50))

$$\left\langle M_A^k \right\rangle = \left\langle M_B^k \right\rangle = \left\langle M_C^k \right\rangle = \left\langle M_D^k \right\rangle , \tag{4.147}$$

and

$$\langle M_I M_J \rangle_{I \neq J} = 0\,. \tag{4.148}$$

Using the definition of the order parameter in eq. (4.62) this leads to

$$\begin{aligned} \langle M_{11} \rangle = \langle M_{12} \rangle = \langle M_{21} \rangle = \langle M_{22} \rangle = 4 \langle M_A \rangle = 0\,, \\ \left\langle M_{11}^2 \right\rangle = \left\langle M_{12}^2 \right\rangle = \left\langle M_{21}^2 \right\rangle = \left\langle M_{22}^2 \right\rangle = 4 \left\langle M_A^2 \right\rangle . \end{aligned} \tag{4.149}$$

For the susceptibility of the order parameter we have

$$\begin{aligned} \chi &= \langle \chi_{11} + \chi_{22} + \chi_{12} + \chi_{21} \rangle = \left\langle M_{11}^2 + M_{22}^2 + M_{12}^2 + M_{21}^2 \right\rangle \\ &= 2 \left\langle M_{11}^2 + M_{22}^2 \right\rangle = 2 \int dM_{11}\, dM_{22}\, p_a(M_{11}, M_{22}) \left(M_{11}^2 + M_{22}^2 \right) . \end{aligned} \tag{4.150}$$

Despite the fact that the expressions are not the same, the square root of half of the susceptibility is empirically very similar to the above radius

$$\begin{aligned} &\sqrt{\int dM_{11}\, dM_{22}\, p_a(M_{11}, M_{22}) \left(M_{11}^2 + M_{22}^2 \right)} = \sqrt{\frac{\chi}{2}} \\ &\approx R = \int dM_{11}\, dM_{22}\, p_a(M_{11}, M_{22}) \sqrt{M_{11}^2 + M_{22}^2} \end{aligned} \tag{4.151}$$

as shown in Figure 4.31.

4.11.2. Local phase structure with static external charges

It was already pointed out that putting two static external charges ± 2 in the deep columnar phase results in strands of flux 1/4 [33]. These strands are visible in the local potential energy density as shown in Figure 4.16. A close look at this figure shows the different columnar and plaquette phase realizations the system has to go through to allow a net flux.

In the following we are several times interested in observables evaluated in one external columnar phase realization. One ad-hoc way to get such results would be to run several Monte Carlo simulations starting in the desired external columnar phase realization and

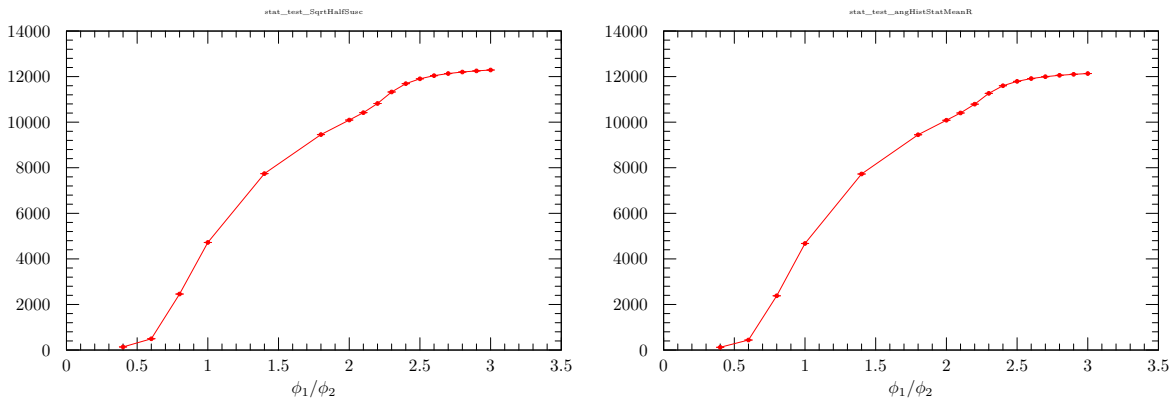

Figure 4.31.: *Comparison of* $\sqrt{\frac{\chi(\phi_1/\phi_2)}{2}}$ (left panel) *to* $R(\phi_1/\phi_2)$ (right panel) *for a system of volume* $L_1 \times L_2 = 120 \times 120$.

using only those runs which don't tunnel to another phase realization. Since our Algorithm allows for high Monte Carlo statistics with many tunnel events, we use another approach. The statistics of the observables is gathered in four different variants, each associated to one external columnar phase realization.

For each generated configuration, the four-component order parameter and the corresponding phase angle φ as defined in eq. (4.67) is calculated. The configuration is then associated to the cartoon columnar phase realization whose angle differs the least from the measured angle φ. The corresponding statistics is then updated. In the following we will speak about "the wave function was evaluated for one external columnar phase".

For the modified ground state wave function the local potential energy density is zero for all values of ϕ_1/ϕ_2. To reveal the phase structure, the local parallelism of dimers is shown in Figure 4.32. These are Monte Carlo results for a periodic 120×120 system away from the standard Rokhsar-Kivelson point. The static external charges were separated by 51 lattice spacings and $3.3 \cdot 10^7$ sweeps were performed. A similar structure like for the standard quantum dimer model appears. It has to be like this, since around each charge the angle φ, which parameterizes the soft pseudo-Goldstone mode, changes by 2π. So each columnar and each plaquette phase is realized two times around the charge. However, this doesn't mean that the flux has to be fractionalized. A first hint into this direction is the observation of plaquette phases (grayish) which seem to be realized in smaller regions compared to the structure that appears in the standard quantum dimer model (see Figure 4.16).

Figure 4.33 shows the local parallelism of dimers for static external charges ± 2 separated by $(\triangle x, \triangle y) = (24, 25)$ lattice spacings at $\phi_1/\phi_2 = 2.4$. Again the measure was built with Monte Carlo results for one external columnar phase. The structure looks the same as those in Figure 4.32.

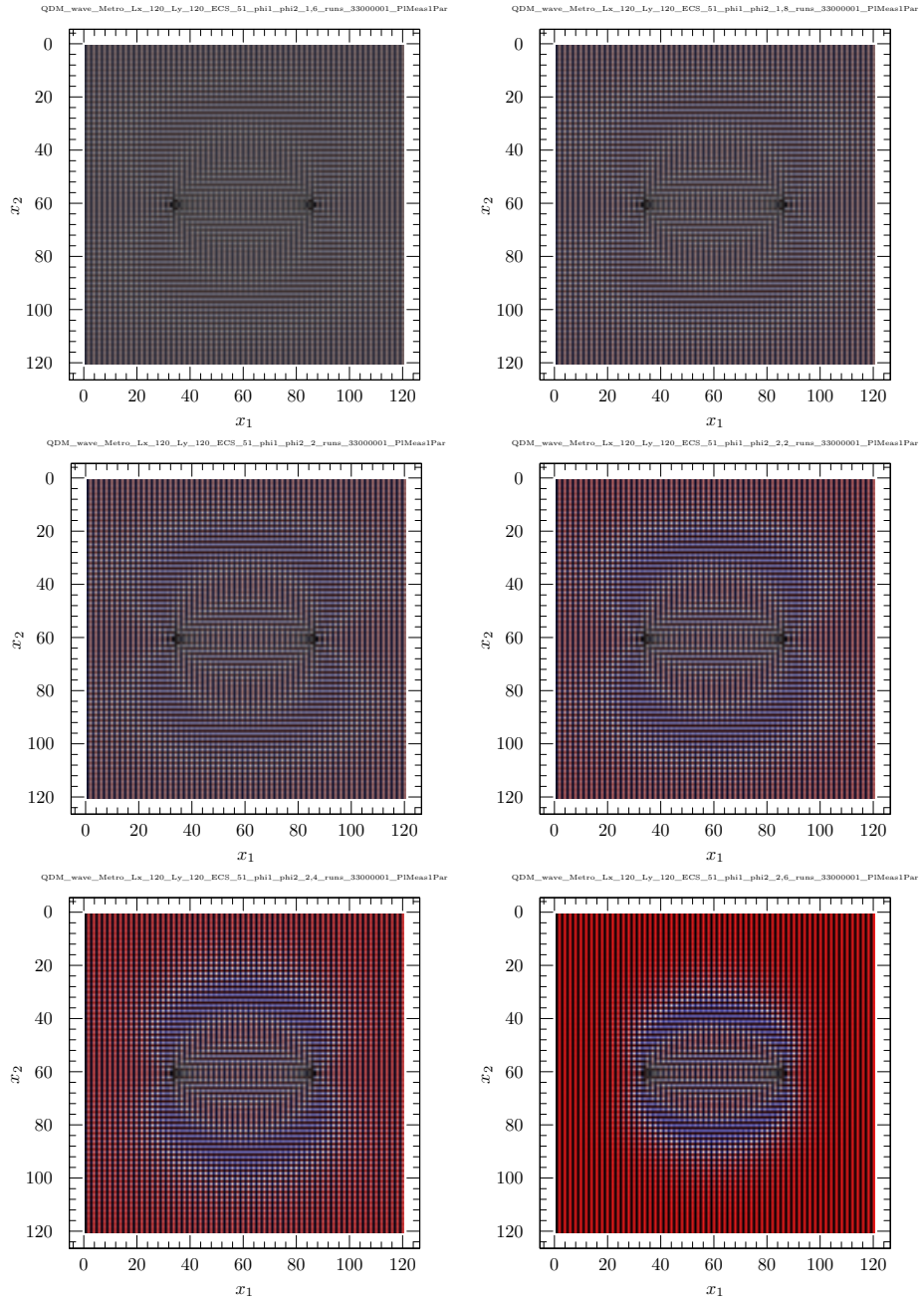

Figure 4.32.: *Local parallelism of dimers. Two static external charges* ± 2 *separated by* 51 *lattice units are put in a periodic system of volume* 120×120*. The horizontal and vertical axes correspond to the geometrical* x_1 *and* x_2 *axis of the system. The figure shows Monte Carlo results of the modified wave function evaluated for one external columnar phase for* $\phi_1/\phi_2 = 1.6$ *(top left),* $1.8, \ldots, 2.6$ *(top right). Dark plaquettes are not flippable. Light plaquettes are resonant, they are in the plaquette phase. Blueish plaquettes have horizontal parallel dimers and reddish have vertical parallel dimers, they both are in a local columnar phase.*

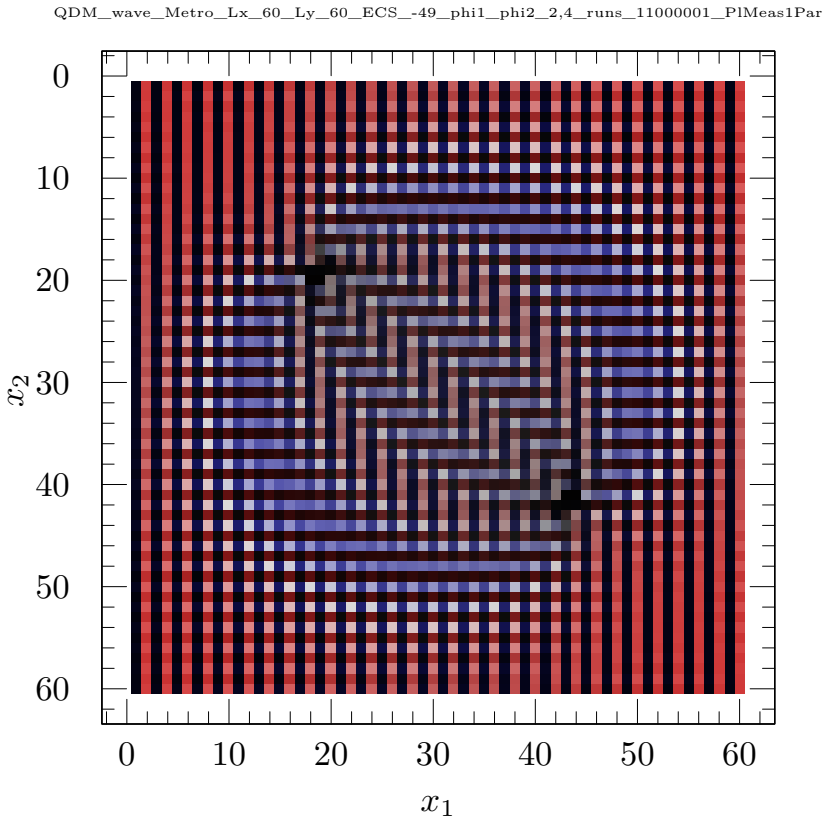

Figure 4.33.: *Local parallelism of dimers. Two static external charges* ± 2 *diagonally separated by* $(\triangle x, \triangle y) = (24, 25)$ *lattice spacings are put in a periodic system of volume* 60×60*. The horizontal and vertical axes correspond to the geometrical* x_1 *and* x_2 *axis of the system. The figure shows Monte Carlo results of the modified wave function evaluated for one external columnar phase for* $\phi_1/\phi_2 = 2.4$*.*

4.11.3. Electric fluxes

For static external charges ±2 the question arises, whether the fluxes get fractionalized as deep in the columnar phase of the standard quantum dimer model. Because of the staggered background charges the local fluxes are wildly pointing in different directions, see Figure 4.34, left panel. These results are for $\phi_1/\phi_2 = 2.5$. $1.1 \cdot 10^7$ Monte Carlo sweeps were performed. In the right panel of Figure 4.34 the wave function was evaluated

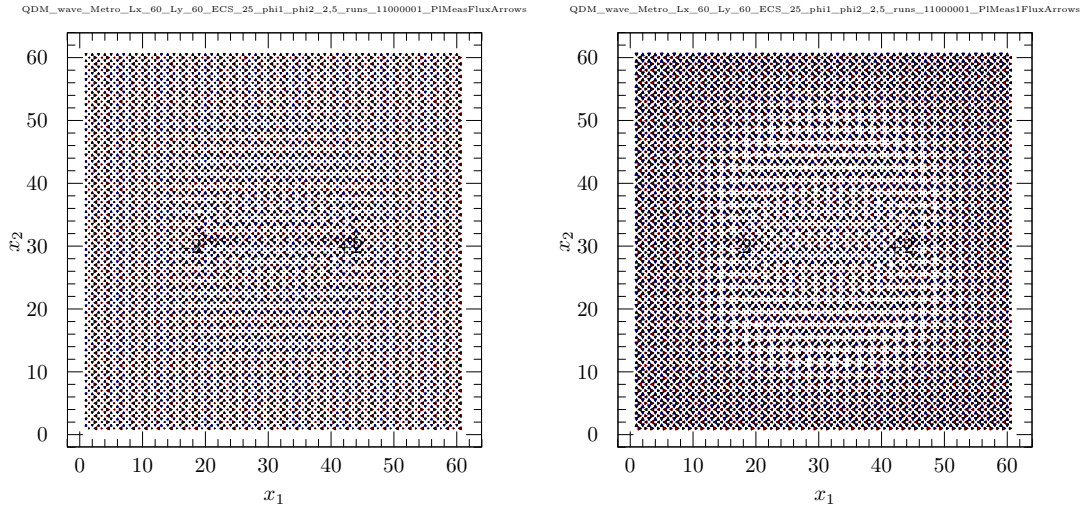

Figure 4.34.: *Two static external charges ±2 separated by 25 lattice units are put in a periodic system of volume* 60×60. *The picture shows the local flux pattern as a result of a Monte Carlo simulation for* $\phi_1/\phi_2 = 2.5$. *The horizontal and vertical axis correspond to the geometrical* x_1 *and* x_2 *axes of the system. The fluxes are visualized with arrows whose sizes are proportional to the absolute value of the flux. Fluxes in or against the* x_1 *direction are red, fluxes in or against the* x_2 *direction are blue. The* left panel *shows the results of the full ground state wave function ansatz, while the* right panel *shows the results of the wave function evaluated for one external columnar phase, as described in the main text.*

for one external columnar phase. It shows the typical background pattern of alternating fluxes E_1 in the x_1 direction whose direction depend on x_2 only. Remember there are four columnar phase realizations. Two of them lead to alternating fluxes E_2 whose direction would depend on x_1 only.

To get rid of the disturbing flux alternations the electric flux is blocked and averaged as discussed in Appendix C. The final result is shown in Figure 4.35. The artifacts which disturbed Figure 4.34 are almost gone.

At the Rokhsar-Kivelson point the electric flux should correspond to a Coulomb potential in a periodic volume as described by eqs. (4.133) and (4.135). Figure 4.36 shows the blocked and averaged flux values at a cut between two static external charges predicted by

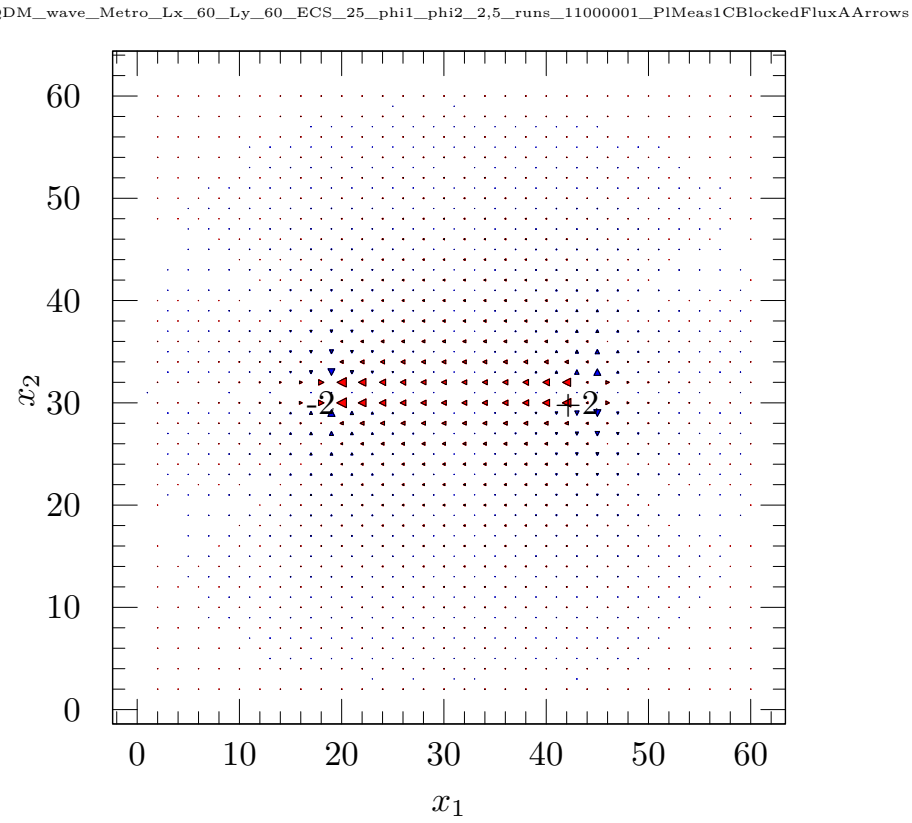

Figure 4.35.: *Here the local pattern of blocked and additionally averaged fluxes is shown under the same conditions as in the right panel of Figure 4.34. The wave function was evaluated for one external columnar phase. This figure is the same as the one in the top left panel of Figure C.3.*

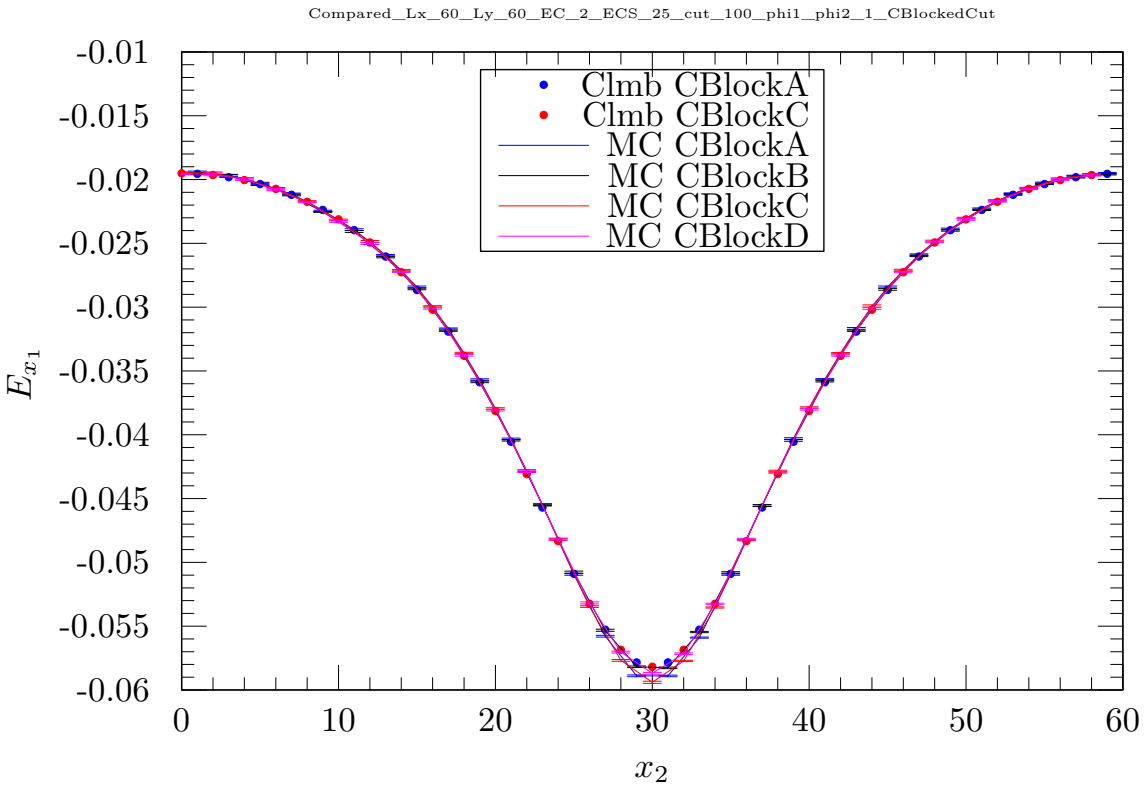

Figure 4.36.: *This picture shows the local flux pattern at a cut through the perpendicular bisection between two static external charges* ± 2 *which were put into a periodic system of volume* 60×60*. The horizontal axis shows the* x_2 *position. The vertical axis shows the electric flux in the* x_1 *direction. The round dots show blocked and averaged electric flux values calculated in the effective theory at the standard Rokhsar-Kivelson point* $\phi_1/\phi_2 = 1$*,* $\lambda = 1$*. They are shown as a guide to the eye. The line segments are linear interpolations between the measured blocked and averaged electric flux values of the full wave function (without any restrictions to the external phase) at the standard Rokhsar-Kivelson point generated by Monte Carlo. For both cases all four possible choices of the blocking scheme are shown.*

the effective theory (round dots) and compared the Monte Carlo results of the full wave function (without any restrictions to the external phase) at the standard Rokhsar-Kivelson point. There is a deviation from the prediction near $x_2 = 30$ which could be caused by lattice artifacts.

In Figure 4.37 the same situation is shown as in Figure 4.36 but for $\phi_1/\phi_2 = 1$, 1.4, 1.8, 2, 2.2, and 2.6. The results of the effective theory are for $\phi_1/\phi_2 = 1$ only. The flux pattern of the modified wave function gets squeezed to the connecting line between the static external charges at $x_2 = 30$. Independent of the values of ϕ_1/ϕ_2 there is a good match of the Monte Carlo results to the effective theory at the Rokhsar-Kivelson point $\lambda = 1$ in the regions around $x_2 = 20$ and $x_2 = 40$. Between these two values the dependence of the chosen blocking center has a strong influence for larger ϕ_1/ϕ_2. The most important result here is that, even for large positive ϕ_1/ϕ_2 deep in the deconfined columnar phase, the flux doesn't split into strings. This is in contrast to the standard quantum dimer model which deep in the columnar phase ($\lambda < 0$) shows flux strands [33].

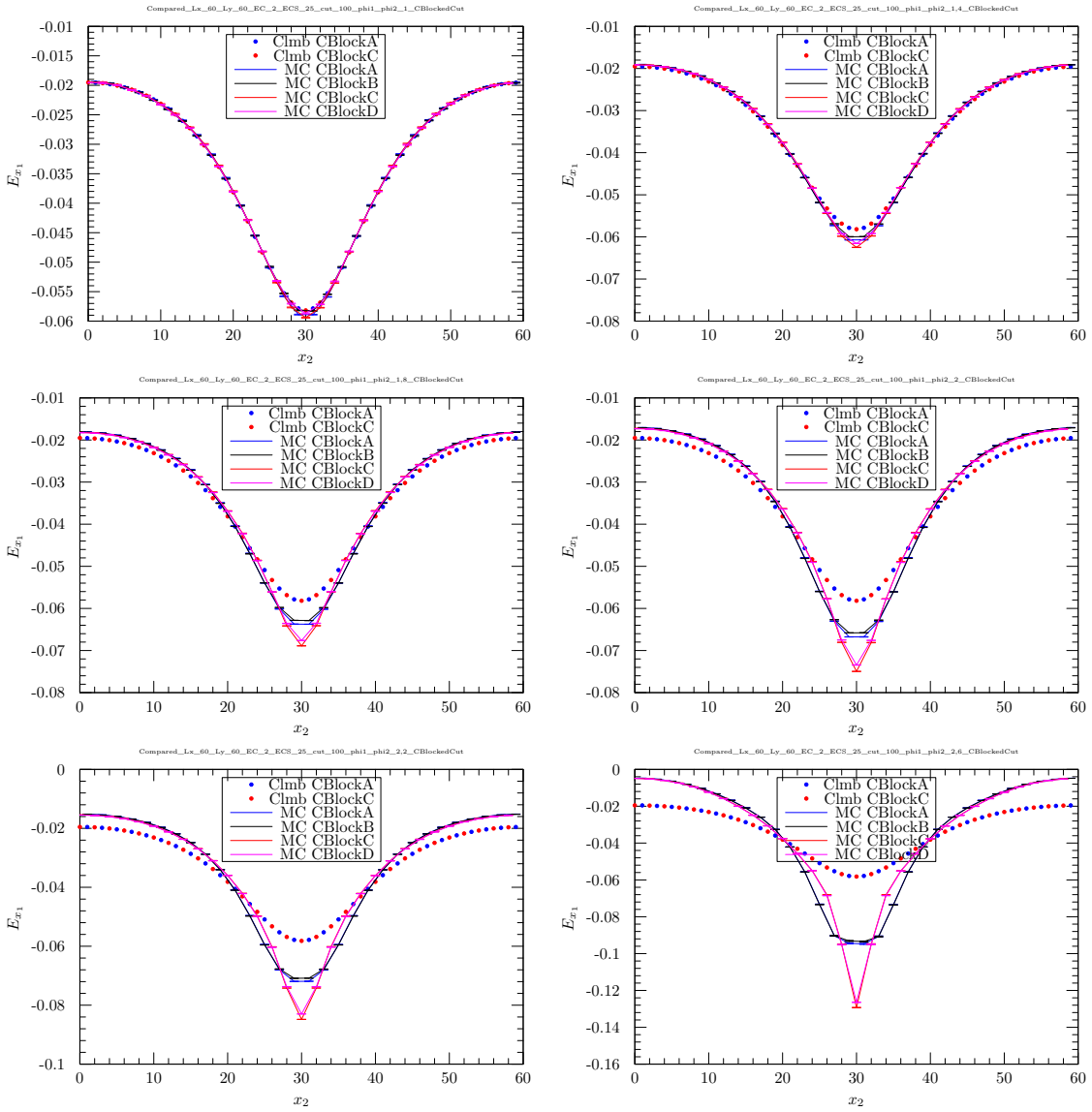

Figure 4.37.: *The upper left panel ($\phi_1/\phi_2 = 1$) is the same as shown in Figure 4.36. The other panels show the same situation generated by Monte Carlo at $\phi_1/\phi_2 =$ 1.4, 1.8, 2, 2.2, and 2.6. However, the results of the effective theory are at the standard Rokhsar-Kivelson point $\phi_1/\phi_2 = 1$ in each panel. The flux pattern gets squeezed for large ϕ_1/ϕ_2.*

4.11.4. Exact diagonalization

While Monte Carlo results for varying λ at low temperature were presented in [33], I presented results at an extended Rokhsar-Kivelson line for varying ϕ_1/ϕ_2 at zero temperature with a distinct Monte Carlo method. With exact diagonalization both regimes can be combined with some arbitrary choice how both potential terms are combined to one term. An example is given with the potential described in eq. (4.136).

Exact diagonalization was performed for systems with 4×4 and 6×6 lattice sites. The 6×6 system has "only" 44176 dimer coverings. The sparse Hamiltonian matrix consists of an order of $2 \cdot 10^5$ non-zero entries. To obtain the momenta of the eigenstates one could use a Gram-Schmidt orthogonalization followed by a re-diagonalization.

Using translation symmetries one can construct dimer covering sets which belong to distinct momentum sectors. So each momentum sector can be diagonalized separately as already explained in chapter 3. In the flux zero sector $\vec{E} = 0$ the 6×6 system has 1256 of such dimer covering sets. For general observables one would need to reconstruct the original dimer coverings. This would be realized by a sparse matrix which has as many non-zero entries as the number of valid dimer coverings (44176 in the case of a 6×6 system).

The 8×8 system would already have about $1.5 \cdot 10^8$ valid dimer coverings. It is possible to access energies and momenta of such a system by using the translation symmetries. This was shown for the standard quantum dimer model in [33].

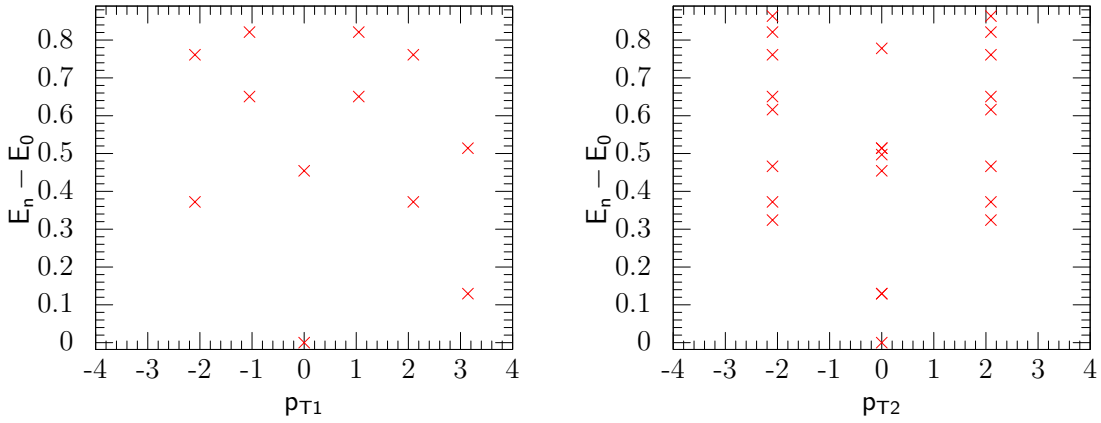

Figure 4.38.: *Spectra of the* 6×6 *quantum dimer model at the Rokhsar-Kivelson point* $\lambda = 1$ *for momenta* $p_{T_1,2} = p_{T_2,2} = 0$ *in the zero flux sector* $\vec{E} = 0$. Left panel*: Momenta* $\vec{p}_{T_1} = (0,0)$, $(\pm\pi/3, 0)$, $(\pm 2\pi/3, 0)$, *and* $(\pi, 0)$ *at the horizontal axis, associated with the translation by one lattice spacing in the* x_1 *direction.* Right panel*: Momenta* $\vec{p}_{T_2} = (0,0)$ *and* $(\pm 2\pi/3, 0)$ *at the horizontal axis, associated with the translation by two lattice spacings in the* x_1 *direction.*

Figure 4.38 shows spectra of the 6×6 square lattice quantum dimer model with periodic boundary conditions at the Rokhsar-Kivelson point $\lambda = 1$, $\phi_1/\phi_2 = 1$ in the flux zero sector

$\vec{E} = 0$. Only eigenstates with momenta $p_{T_1,2} = p_{T_2,2} = 0$ are shown. The vertical axis show the energy. In the left panel, the horizontal axis shows momenta $p_{T_1,1}$ associated with the translation by one lattice spacing in the x_1 direction. This corresponds to the combined charge conjugation and translation by one lattice spacing CT in the quantum link model. In the right panel, the horizontal axis shows momenta $p_{T_2,1}$ associated with the translation by two lattice spacings in the x_1 direction.

Using T_i (CT_i) to plot spectra seems unphysical. In chapter 3 this was related to the chiral symmetry and its spontaneous breaking. In the quantum dimer model, e.g. the single columnar phase patterns are not CT symmetric on their own. For the ground state all possible dimer coverings contribute with the same positive weight. Hence, it has momentum $\vec{p}_{T_1} = 0$.

Figure 4.39 shows the spectra with absolute momenta. where in the left panel the horizontal axis shows the absolute momenta $|p_{T_1}|$. In the right panel, the horizontal axis shows the absolute momenta $|p_{T_2}|$. The first two degenerated excited states have momen-

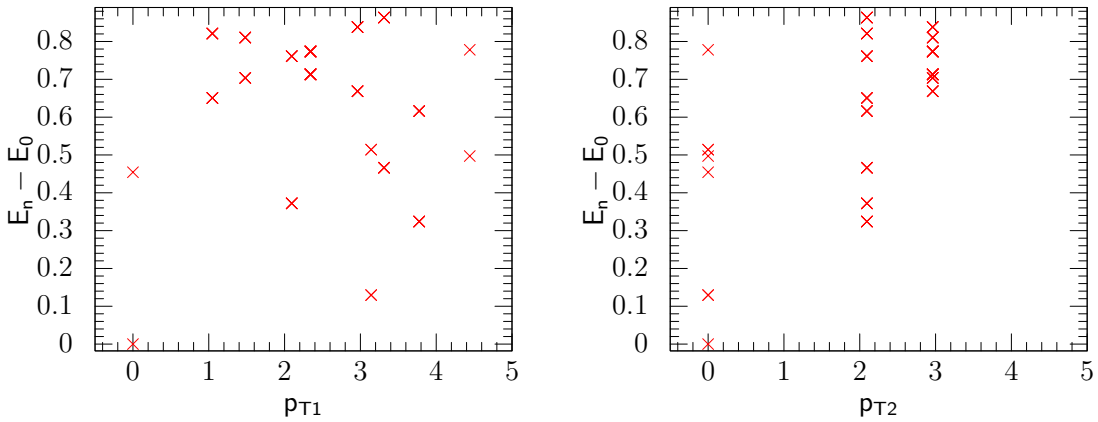

Figure 4.39.: *Spectra of the* 6×6 *quantum dimer model at the Rokhsar-Kivelson point* $\lambda = 1$ *for all possible momenta in the zero flux sector* $\vec{E} = 0$. Left panel*: Momenta* $|p_{T_1}| = 0,\ \pi/3,\ \sqrt{2}\pi/3,\ 2\pi/3,\ \sqrt{5}\pi/3,\ 2\sqrt{2}\pi/3,\ \pi,\ \sqrt{10}\pi/3,\ \sqrt{13}\pi/3,$ *and* $\sqrt{2}\pi$ *at the horizontal axis.* Right panel*: Momenta* $|p_{T_2}| = 0,\ 2\pi/3,$ *and* $2\sqrt{2}\pi/3$ *at the horizontal axis.*

tum $\vec{p}_{T_1} = (\pi, 0)$ and $(0, \pi)$. It would be nice to be able to perform exact diagonalizations on much larger lattices to check if the gap vanishes exponentially, which would indicate spontaneous symmetry breaking.

Figure 4.40 shows the spectra of the standard ($\phi_1/\phi_2 = 1$) quantum dimer model for $\lambda \in [-1.1, 1.1]$ in the flux zero sector $\vec{E} = 0$. Only momenta $\vec{p}_{T_2} = 0$ are shown. The previous spectra in Figures 4.38 and 4.39, calculated at the Rokhsar-Kivelson point $\lambda = 1$, correspond to the right end of the right panel in Figure 4.40. The left panel for the 4×4 system suffers from large artifacts caused by the small system size. In contrast, the right panel for the 6×6 system is very similar to the spectrum shown in Figure 4.17 which was a 8×8 system [33].

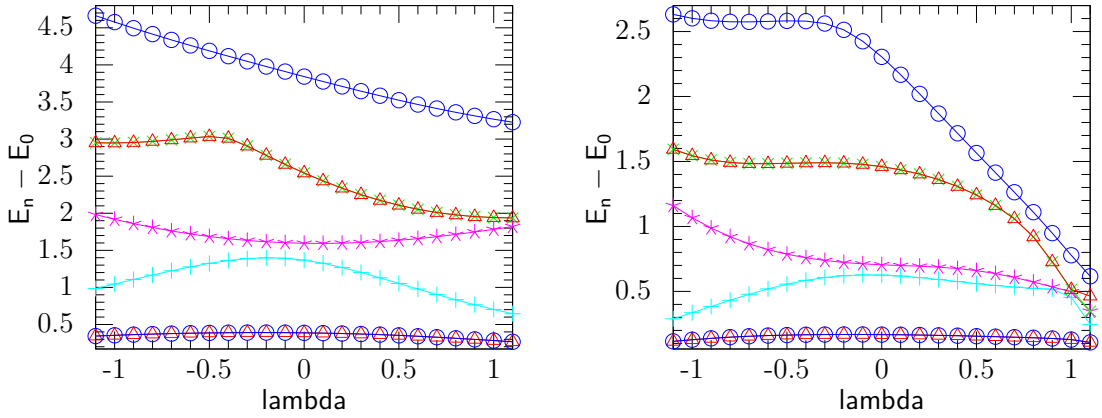

Figure 4.40.: *Spectra of the standard quantum dimer model ($\phi_1/\phi_2 = 1$) for $\lambda \in [-1.1, 1.1]$ in the zero flux sector $\vec{E} = 0$. The energies are relative to the ground state energy E_0. This zero line ($E_0 - E_0 = 0$) is suppressed. Only momenta $\vec{p}_{T_2} = 0$ are shown. In both panels, for $\lambda \in [-1.1, 1[$, the momenta associated with the translation of one lattice spacing are read from bottom to top $\vec{p}_{T_1} = \{(0,\pi),(\pi,0)\}$, $(0,0)$, (π,π), $\{(0,\pi),(\pi,0)\}$, and (π,π). The ground state always has $\vec{p}_{T_1} = 0$ and is not shown, as already stated.* Left panel: 4×4 *system.* Right panel: 6×6 *system.*

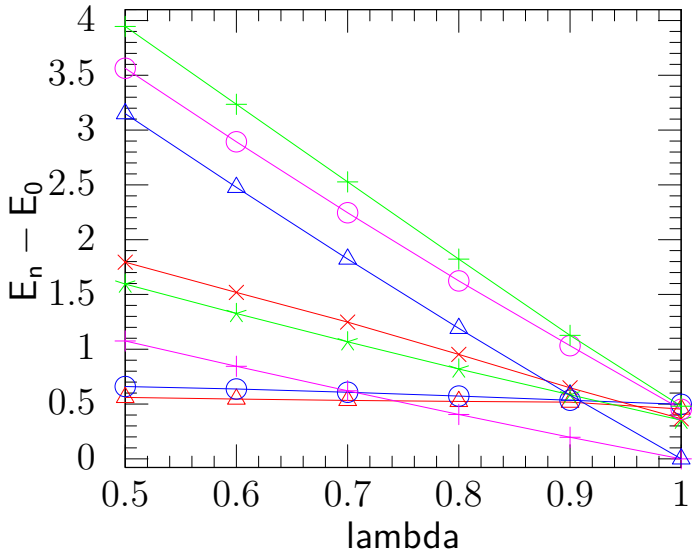

Figure 4.41.: *Spectra of the 6×6 standard quantum dimer model ($\phi_1/\phi_2 = 1$) for $\lambda \in [0.5, 1]$. The energy lines shown are relative to the ground state energies of the zero flux sector $\vec{E} = 0$ for each value of λ. The flux sectors are $\vec{E} = (0,0)$, $(0,1)$, and $(0,2)$. The zero line of the ground state in the zero flux sector is suppressed. The CT states of the zero flux sector are suppressed too, because they have no correspondence in the non-zero flux sectors. At $\lambda = 0.5$ the energies belong to the following flux sectors (again read from bottom to top) $\vec{E} = 2 \times (0,0)$, $3 \times (0,1)$, and $3 \times (0,2)$.*

Figure 4.41 shows the spectra of the 6×6 standard quantum dimer model ($\phi_1/\phi_2 = 1$). The two degenerated states of the flux zero sector $\vec{E} = 0$ with $\vec{p}_{T_1} = (0, \pi)$ and $(\pi, 0)$ have no correspondence in the sectors with flux since there CT is explicitly broken. They are therefore suppressed. The 6×6 square lattice model has 25 valid flux sectors. From those only 13 are non-trivial: $\vec{E} = (0,0)$, $(0, \pm 1)$, $(\pm 1, 0)$, $(\pm 1, \pm 1)$, $(0, \pm 2)$, and $(\pm 2, 0)$. The figure shows the flux sectors $\vec{E} = (0,0)$, $(0,1)$, and $(0,2)$. The case $\vec{E} = (1,1)$ is not treated. One can read off the condensation of fluxes in the vacuum at the Rokhsar-Kivelson point $\lambda = 1$. (The ground state is not shown for the zero flux sector $\vec{E} = 0$).

Up to this point, these diagonalization results are all known and served as a check of the diagonalization routines and as a summary.

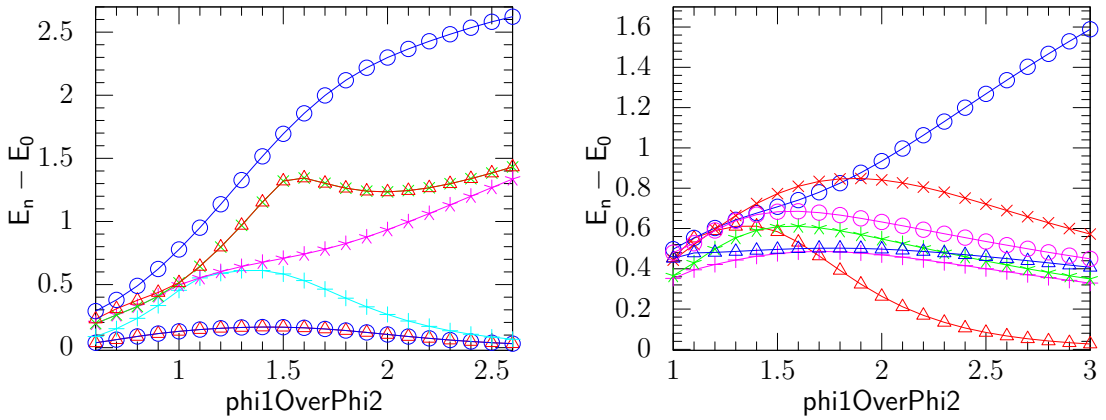

Figure 4.42.: *Spectra of the modified ground state wave function ($\lambda = 1$) for varying ϕ_1/ϕ_2 in a 6×6 system. The ground state of each flux sector has energy zero. So these zero lines are not shown. Only momenta $\vec{p}_{T_2} = 0$ are shown. For technical reasons, the colors and marks of the same state do not agree comparing the two panels.* Left panel: *Zero flux sector $\vec{E} = 0$ for $\phi_1/\phi_2 \in [0.6, 2.6]$. For $\phi_1/\phi_2 \in [1, 2.6]$ the momenta $\vec{p}_{T_1}$ have the same values and order as already stated (read from bottom to top): $\vec{p}_{T_1} = \{(0,\pi),(\pi,0)\}$, $(0,0)$, (π,π), $\{(0,\pi),(\pi,0)\}$, and (π,π).* Right panel: *$\vec{E} = (0,0)$, $(0,1)$, and $(0,2)$ for $\phi_1/\phi_2 \in [1, 2.6]$. The CT states of the zero flux sector $\vec{E} = 0$ are suppressed again in this panel. At $\phi_1/\phi_2 = 1$ the energies belong to the flux sectors (from bottom to top) $\vec{E} = 3 \times (0,1)$, $(0,2)$, $(0,0)$, $(0,2)$, and $(0,0)$. At $\phi_1/\phi_2 = 1.8$ the order is $\vec{E} = (0,0)$, $(0,1)$, $(0,2)$, $(0,1)$, $(0,2)$, $(0,0)$, and $(0,1)$. And at $\phi_1/\phi_2 = 2.6$ the order is $\vec{E} = (0,0)$, $2 \times (0,1)$, $2 \times (0,2)$, $(0,1)$, and $(0,0)$.*

Figure 4.42 shows the spectra corresponding to the modified ground state wave function. The corresponding potential is described in eqs. (4.91) and (4.92). The periodic system again had a size of 6×6 lattice spacings with periodic boundary conditions. On the horizontal axis the extended Rokhsar-Kivelson line ($\lambda = 1$, ϕ_1/ϕ_2 varying) was explored. Only momenta $\vec{p}_{T_2} = 0$ are shown. In the left panel the zero flux sector $\vec{E} = 0$ is shown. This sector is CT symmetric so momenta associated with translations by one lattice spacing are defined. In the right panel the flux sectors $\vec{E} = (0,0)$, $(0,1)$ and $(0,2)$ are shown. The ground states of the different flux sectors all have zero energy and are

therefore not shown. Remember that for $\phi_1/\phi_2 = 1$ we are at the standard Rokhsar-Kivelson point $\lambda = 1$. Due to lack of time, these spectra are not investigated further. At least, in contrast to the standard quantum dimer model examined in [33] we can no more recognize the rotor spectrum found in Figure 4.17. This is no surprise. As stated in section 4.9 for the modified ground state wave function the local energy density is zero for all flux sectors. This resulted in $\rho = 0$ for the term $\rho\partial_i\varphi\partial_i\varphi$ in the effective Lagrange density defined in eq. (4.114). A rotor spectrum would only appear for $\rho \neq 0$.

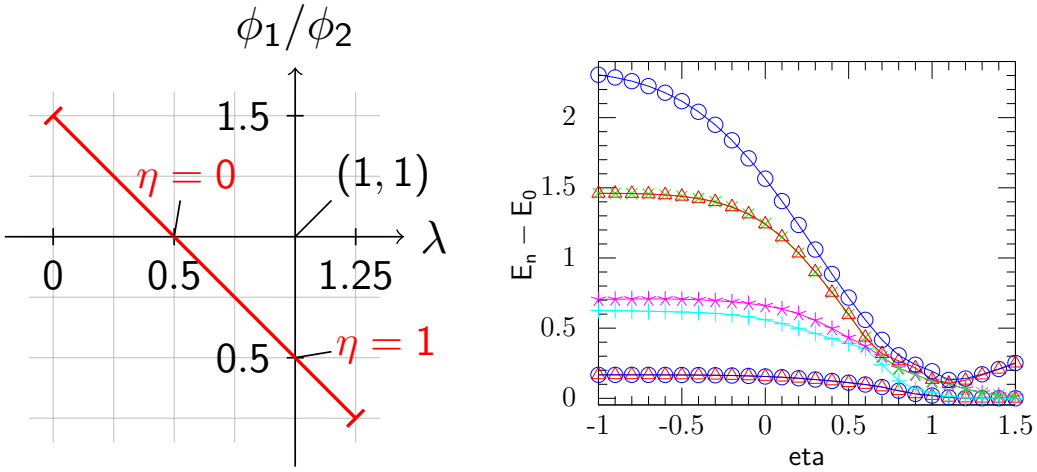

Figure 4.43.: Left panel: *Parametrization of λ and ϕ_1/ϕ_2 for the exact diagonalization shown in the right panel.* Right panel: *Spectrum of the combined wave function defined in eq. (4.136) in a 6×6 system. The energies are relative to the ground state. The zero line of the latter is not shown. The momenta associated with translations by one lattice spacing for $\eta \in [-1, 0.5]$ read from bottom to top $\vec{p}_{T_1} = \{(0,\pi),(\pi,0)\}$, $(0,0)$, (π,π), $\{(0,\pi),(\pi,0)\}$, and (π,π).*

As an outlook Figure 4.43 shows an example for the exact diagonalization of the combined wave function defined in eq. (4.136) along the red parametrization line depicted in the left panel. In this generalization $\lambda \neq 1$ in general. Hence, the ground state wave function can't be described exactly. For $\eta = 0$ we are at the standard quantum dimer model and for $\eta = 1$ we obtain the modified ground state wave function. We can freely interpolate between the models, since both parameters λ and ϕ_1/ϕ_2 can be tuned arbitrarily in the combined wave function defined in eq. (4.136).

4.12. Conclusions

In this chapter we treated the quantum dimer model at an extended Rokhsar-Kivelson line. First, the dimer model was re-expressed as a $(2+1)$ dimensional quantum link model and by a careful symmetry analysis a four-component order parameter was constructed. This was already done by our group [33].

Then the ground state wave function at the Rokhsar-Kivelson point $\lambda = 1$ was gener-

alized, which extended the point to a line. A simple Metropolis algorithm was used to investigate the ground state properties of the system at exactly zero temperature $T = 0$. There the system doesn't tunnel between the different electric flux sectors. This motivated the investigation of individual flux sectors which is in contrast to existing work.

A clean but empiric blocking and averaging scheme was developed to visualize the local electric flux patterns. An important result is that even for large positive ϕ_1/ϕ_2 deep in the deconfined columnar phase the net flux remains homogeneous in contrast to the standard quantum dimer model which deep in the columnar phase shows flux strands [33]. These strands were observed in the local energy density which on the extended Rokhsar-Kivelson line, as a further result of this work, is strictly zero.

The effective theory developed in [33] is no longer valid for the Rokhsar-Kivelson line, and there seems to be no rotor spectrum appearing in the corresponding exact diagonalizations. Hence, a new effective theory has to be developed yet. First steps were performed in section 4.9. The diagonalizations were performed as a basis for future analysis. As an outlook, an interpolation between standard quantum dimer model ($\phi_1/\phi_2 = 1$) and modified ground state wave function ($\lambda = 1$) was proposed.

5. Summary and Outlook

The quantum link model is a lattice gauge theory with discrete quantum degrees of freedom on the links in a finite-dimensional Hilbert space. It is a versatile model exhibiting phenomena like spontaneous symmetry breaking and its restoration, baryon superfluidity, "nuclear" physics (binding), and string breaking known from high-energy as well as from condensed matter physics. Its study leads to new insights and ideas for models and algorithms.

The quantum link model was reviewed for an Abelian $U(1)$ and for a non-Abelian $U(N)$ and $SU(N)$ gauge theory coupled to staggered fermions. In the $U(N)$ quantum link model the Abelian Gauss law is imposed and the links have an associated electric flux represented by spin degrees of freedom.

Living in a finite-dimensional Hilbert space, the quantum link model is perfectly suited to be implemented in a quantum simulator. The required conceptual components are already realized as individual experimental setups. We proposed quantum simulators for the Abelian $U(1)$ and for a non-Abelian $U(N)$ and $SU(N)$ quantum link model based on ultracold alkaline-earth atoms trapped in an optical lattice. The concepts support up to $(3+1)$-dimensional models. Nevertheless, it remains a long way to implement all ingredients of a full QCD lattice gauge theory.

Since the quantum dimer model which originates form condensed matter physics also can be rewritten as a $U(1)$ quantum link model coupled to staggered fermions with staggered static background charges, this allowed us to treat the dimer model as a gauge theory and to interpret dimer configurations as electric flux configurations realized as spin $\frac{1}{2}$ degrees of freedom.

In $(1+1)$-dimensions the quantum link model is accessible to exact diagonalization studies for moderate system sizes. This allowed us to investigate models for string breaking and spontaneous chiral symmetry breaking. It was even possible to compute the real-time evolution of the latter phenomena. Theses studies serve as a benchmark for ultracold atomic simulations.

In $(2+1)$-dimensions exact diagonalizations were performed for small system sizes in the quantum dimer model. However, the ground state for moderately large systems is accessible by Monte Carlo methods.

At the Rokhsar-Kivelson point the ground state of the quantum dimer models can be constructed analytically. The local energy density is zero and electric fluxes don't cost energy. The system remains deconfined even at zero temperature. We choose an extension

of this point to a parametrized family of deconfined systems by constructing a modified ground state wave function. Even deep in the columnar phase the system does not confine.

The ground state wave function can be evaluated with a Metropolis Monte Carlo algorithm directly at zero temperature. We used the four-dimensional order parameter introduced in [33] to reliable distinguish the different candidate phases. There were no signs of a plaquette or a mixed phase on the extended Rokhsar-Kivelson line as it was the case in the standard quantum dimer model [33].

In contrast to the standard quantum dimer model the electric flux pattern created by a static charge-anti-charge pair does not fractionalize in stands even deep in the columnar phase. However, the flux pattern which corresponds to a Coulomb distribution in the standard dimer model becomes squeezed deep in the columnar phase, approaching the straight line between the static charge-anti-charge pair. The effective theory which predicts such a behavior is not elaborated yet.

The spectrum of a small-size quantum dimer model was calculated for the modified ground state wave function, however, due to lack of time without any interpretation. As an outlook, an interpolation between standard quantum dimer model and modified ground state wave function was performed. However, for this interpolation, the ground state wave function can no longer be constructed analytically.

Quantum link models are well suited to implement non-perturbative quantum simulation e.g. with ultracold atoms trapped in an optical lattice. Quantum simulation remains the most promising way to address currently unsolved problems like the real-time and high density dynamics of strongly coupled systems. The proposed quantum simulators are a first step on a long and interesting way.

Acknowledgements

First of all I would like to thank Uwe-Jens Wiese to offer me this great opportunity to write my Ph.D. thesis, for his pleasant patient substantial support, for the extensive proof-reading of this thesis. Thank you very much for challenging me with tasks like working on lattice gauge models, in particular quantum link models, developing algorithms, and implementing and performing the numerical analysis.

In particular me, my wife Madlen Stebler, and my daughter Cindy Stebler would like to thank him for his invitation to Cambridge (Massachusetts) in June 2013 where he accommodated us for two weeks in his temporary home during his research sabbatical at the Massachusetts Institute of Technology. We were very warmly housed by him and his daughter Christina Wiese.

I will never forget the inspiring talks about our work during the daily walks from their home to his office in the MIT. It was a great experience to discuss our work on the blackboard which I enjoyed the whole day long almost only interrupted by lunch or by the meetings of the theory group.

I would like to thank Andreas Läuchli the current head of the Institute for Theoretical Physics at the University of Innsbruck for interesting discussions at occasional meetings, for his willingness to work through my thesis as a co-referee, and to serve as an examiner at my Ph.D. defense.

For the great collaboration between our research groups I would like to thank Peter Zoller and his collaborators Marcello Dalmonte and Enrique Rico Ortega of the Institute for Quantum Optics and Quantum Information (IQOQI) of the Austrian Academy.

Many thanks go to the (former) colleagues of our group Debasish Banerjee, Michael Bögli, Philippe Widmer, Therkel Olesen, Nadiia Vlasii, Florian Hebenstreit, and Wynne Evans for interesting discussions on physics and private topics and for the pleasant working atmosphere.

In particular I would like to thank Debasish and Michael for our intense, challenging and fruitful collaboration. At this point a cordially thank you goes to Philippe and our former office mate Kyle Steinhauer for hours of discussion on software implementation topics and to Therkel for sharing handicraft and engineering work ideas with me.

I would like to thank Urs Wenger whose exercises of his lecture I tutored several times for many helpful informal discussions, Esther Fiechter, secretary of our institute for all her help, support and informal discussions too, and Markus Moser for keeping our IT

infrastructure alive and for many discussions about bits and bytes. This work is supported partially by the Schweizer Nationalfonds and partially by the European Research Council under the European Union' Seventh Framework Programme (FP7/2007-2013)/ERC Grant Agreement No. 339220.

All this would not have happened, had my former supervisor Reinhold Krause, retired head of the Institute for Mechatronic Systems at the university of applied science in Burgdorf, not put the idea into my head that I should find a way an area and a passion to perform Ph.D. studies. Thank you very much for your encouragement.

However, the most important person for this process is my beloved wife Madlen Stebler. She fully supported the decision to start my studies more than ten years ago. Many lovely thanks for your appreciation and your support. I owe you so much.

I would also like to thank my parents. My mother Paula Stebler takes care of our daughter on a regular basis which allows us to manage our jobs. Thank you very much.

A. Plaquette operator of the quantum dimer model in dimer and flux bases

In agreement with eq. (4.2) we have

$$U_\square|\square\rangle = |\square\rangle\,, \qquad U_\square|\square\rangle = 0\,,$$
$$U_\square^\dagger|\square\rangle = 0\,, \qquad U_\square^\dagger|\square\rangle = |\square\rangle\,. \tag{A.1}$$

However, eq. (4.6) defines a staggered mapping between dimers and fluxes which, as illustrated in Figure A.1, in agreement with eqs. (4.2) and (4.4), results in a staggered mapping of $\widetilde{U_\square}$ and $\widetilde{U_\square}^\dagger$ to $U_\square$ and $U_\square^\dagger$:

$$\widetilde{U_I}|\square\rangle = |\square\rangle \iff U_\square|\square\rangle = |\square\rangle\,,$$
$$\widetilde{U_J}^\dagger|\square\rangle = |\square\rangle \iff U_\square^\dagger|\square\rangle = |\square\rangle\,,$$
$$\widetilde{U_K}|\square\rangle = |\square\rangle \iff U_\square^\dagger|\square\rangle = |\square\rangle\,,$$
$$\widetilde{U_L}^\dagger|\square\rangle = |\square\rangle \iff U_\square|\square\rangle = |\square\rangle\,. \tag{A.2}$$

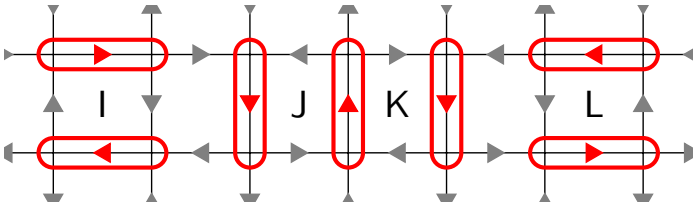

Figure A.1.: *Staggered mapping between parallelism of fluxes and around the plaquette fluxes illustrated with a valid dimer configuration with four flippable plaquettes I, J, K, and L.*

B. Check of the height symmetries in the quantum dimer model

Here we check whether the symmetry transformation rules for the heights in eq. (4.30) are correct by calculating the dimer transformation relations listed in eq. (4.27). Remember

$$\begin{aligned} D_{x,-1} &= D_{x-\hat{1},1}\,, \\ D_{x,-2} &= D_{x-\hat{2},2}\,. \end{aligned} \tag{B.1}$$

For the reflections R_1, R_2 we obtain

$$\begin{aligned} {}^{R_1}D_{x,1} &= \frac{1}{2}\left(1 + {}^{R_1}h_{\widetilde{x}}{}^{R_1}h_{\widetilde{x}-\hat{2}}\right) \\ &= \frac{1}{2}\left(1 + h_{(\widetilde{x}_1,-\widetilde{x}_2)}h_{(\widetilde{x}_1,1-\widetilde{x}_2)}\right) \\ &= D_{(x_1,-x_2),1}\,, \\ {}^{R_1}D_{x,2} &= \frac{1}{2}\left(1 + (-1)^{x_1+x_2\,R_1}h_{\widetilde{x}}{}^{R_1}h_{\widetilde{x}-\hat{1}}\right) \\ &= \frac{1}{2}\left(1 - (-1)^{x_1-x_2}h_{(\widetilde{x}_1,-\widetilde{x}_2)}h_{(\widetilde{x}_1-1,-\widetilde{x}_2)}\right) \\ &= D_{(x_1,-x_2-1),2}\,, \end{aligned} \tag{B.2}$$

and

$$\begin{aligned} {}^{R_2}D_{x,1} &= \frac{1}{2}\left(1 + {}^{R_2}h_{\widetilde{x}}{}^{R_2}h_{\widetilde{x}-\hat{2}}\right) \\ &= \frac{1}{2}\left(1 + h_{(-\widetilde{x}_1,\widetilde{x}_2)}h_{(-\widetilde{x}_1,\widetilde{x}_2-1)}\right) \\ &= D_{(-x_1-1,x_2),1}\,, \\ {}^{R_2}D_{x,2} &= \frac{1}{2}\left(1 + (-1)^{x_1+x_2\,R_2}h_{\widetilde{x}}{}^{R_2}h_{\widetilde{x}-\hat{1}}\right) \\ &= \frac{1}{2}\left(1 + (-1)^{-x_1+x_2}h_{(-\widetilde{x}_1,\widetilde{x}_2)}h_{(1-\widetilde{x}_1,\widetilde{x}_2)}\right) \\ &= D_{(-x_1,x_2),2}\,. \end{aligned} \tag{B.3}$$

B. Check of the height symmetries in the quantum dimer model

For the reflections CR'_1, CR'_2 we obtain

$$\begin{aligned}
{}^{R'_1}D_{x,1} &= \frac{1}{2}\left(1 + {}^{CR'_1}h_{\widetilde{x}}{}^{CR'_1}h_{\widetilde{x}-\hat{2}}\right) \\
&= \frac{1}{2}\left(1 + h_{(\widetilde{x}_1,1-\widetilde{x}_2)}h_{(\widetilde{x}_1,2-\widetilde{x}_2)}\right) \\
&= D_{(x_1,1-x_2),1}\,, \\
{}^{R'_1}D_{x,2} &= \frac{1}{2}\left(1 + (-1)^{x_1+x_2}{}^{CR'_1}h_{\widetilde{x}}{}^{CR'_1}h_{\widetilde{x}-\hat{1}}\right) \\
&= \frac{1}{2}\left(1 + (-1)^{x_1-x_2}h_{(\widetilde{x}_1,1-\widetilde{x}_2)}h_{(\widetilde{x}_1-1,1-\widetilde{x}_2)}\right) \\
&= D_{(x_1,-x_2),2}\,,
\end{aligned} \tag{B.4}$$

and

$$\begin{aligned}
{}^{R'_2}D_{x,1} &= \frac{1}{2}\left(1 + {}^{CR'_2}h_{\widetilde{x}}{}^{CR'_2}h_{\widetilde{x}-\hat{2}}\right) \\
&= \frac{1}{2}\left(1 + h_{(1-\widetilde{x}_1,\widetilde{x}_2)}h_{(1-\widetilde{x}_1,\widetilde{x}_2-1)}\right) \\
&= D_{(-x_1,x_2),1}\,, \\
{}^{R'_2}D_{x,2} &= \frac{1}{2}\left(1 + (-1)^{x_1+x_2}{}^{CR'_2}h_{\widetilde{x}}{}^{CR'_2}h_{\widetilde{x}-\hat{1}}\right) \\
&= \frac{1}{2}\left(1 - (-1)^{-x_1+x_2}h_{(1-\widetilde{x}_1,\widetilde{x}_2)}h_{(2-\widetilde{x}_1,\widetilde{x}_2)}\right) \\
&= D_{(1-x_1,x_2),2}\,.
\end{aligned} \tag{B.5}$$

This is in agreement with the symmetries discussed in section 4.2. For the rotation O we derive

$$\begin{aligned}
{}^{O}D_{x,1} &= \frac{1}{2}\left(1 + {}^{O}h_{\widetilde{x}}{}^{O}h_{\widetilde{x}-\hat{2}}\right) \\
&= \frac{1}{2}\left(1 + s_O(x_1,x_2)s_O(x_1,x_2-1)h_{(-\widetilde{x}_2,\widetilde{x}_1)}h_{(1-\widetilde{x}_2,\widetilde{x}_1)}\right) \\
&\overset{!}{=} \frac{1}{2}\left(1 + (-1)^{-x_2+x_1}h_{(-\widetilde{x}_2,\widetilde{x}_1)}h_{(1-\widetilde{x}_2,\widetilde{x}_1)}\right) \\
&= D_{(-x_2,x_1),2}\,, \\
{}^{O}D_{x,2} &= \frac{1}{2}\left(1 + (-1)^{x_1+x_2}{}^{O}h_{\widetilde{x}}{}^{O}h_{\widetilde{x}-\hat{1}}\right) \\
&= \frac{1}{2}\left(1 + (-1)^{x_1+x_2}s_O(x_1,x_2)s_O(x_1-1,x_2)h_{(-\widetilde{x}_2,\widetilde{x}_1)}h_{(-\widetilde{x}_2,\widetilde{x}_1-1)}\right) \\
&\overset{!}{=} \frac{1}{2}\left(1 + h_{(-\widetilde{x}_2,\widetilde{x}_1)}h_{(-\widetilde{x}_2,\widetilde{x}_1-1)}\right) \\
&= D_{(-x_2-1,x_1),1}\,.
\end{aligned} \tag{B.6}$$

We read off constraints for the sign $s_O(x_1,x_2)$

$$\begin{aligned}
s_O(x_1,x_2)s_O(x_1,x_2-1) &= (-1)^{x_1-x_2} = (-1)^{x_1+x_2} \\
s_O(x_1,x_2)s_O(x_1-1,x_2) &= (-1)^{x_1+x_2}\,.
\end{aligned} \tag{B.7}$$

The simplest solution is

$$s_O(x_1, x_2) = \begin{cases} s_{O_0}(-1)^{(x_1+x_2)/2} & \text{if } x_1 + x_2 \text{ is even,} \\ s_{O_0}(-1)^{(x_1+x_2+1)/2} & \text{if } x_1 + x_2 \text{ is odd.} \end{cases} \tag{B.8}$$

Hence, all check worked and we determined the sign $s_O(x_1, x_2)$ up to an overall sign s_{O_0}.

C. Empiric blocking and averaging of the electric fluxes in the quantum dimer model

To cure the effects of the background staggering, the fluxes are blocked

$$\begin{aligned} \widetilde{E}_1(\vec{x} - (1/2, 1/2)) &= E_1(\vec{x}) + E_1(\vec{x} - \hat{2}) \\ \widetilde{E}_2(\vec{x} - (1/2, 1/2)) &= E_2(\vec{x}) + E_2(\vec{x} - \hat{1}) \\ \widetilde{E}_i &\in \{-1, 0, 1\} \end{aligned} \tag{C.1}$$

as illustrated in Figure C.1.

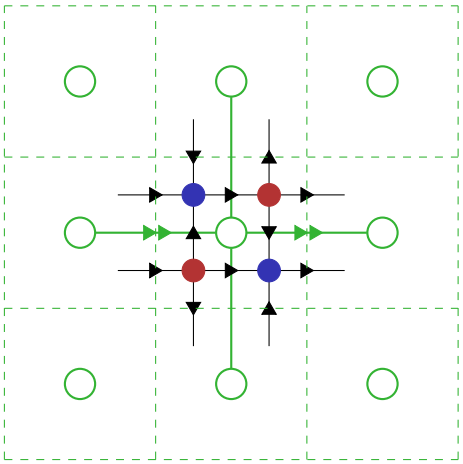

Figure C.1.: *Blocking of fluxes. The staggered background charges are explicitly indicated by blue and red dots. The boundaries of the blocks are denoted with green dashed lines. Blocked flux links (green solid lines) are connecting the centers of the blocks, which are indicated by green circles. The blocked fluxes have values in* $\{-1, 0, 1\}$ *which is indicated by double green arrows or missing arrows. The net charge of each block is zero and the Gauss law is respected.*

The spacial positions $\vec{x}$ are restricted to one of the following four possibilities: Either x_1 is even only or x_1 is odd only and either x_2 is even only or x_2 is odd only. The net charge of each block is zero. The fluxes $(\widetilde{E}_1, \widetilde{E}_2)$ going through the surface of a block respect the

Gauss law

$$\begin{aligned}\sum_{i=1,2}\Big[\widetilde{E}_i(\vec{x}-(1/2,1/2))-\widetilde{E}_i(\vec{x}-(1/2,1/2)-2\hat{i})\Big]=\\ E_1(\vec{x})+E_1(\vec{x}-\hat{2})-E_1(\vec{x}-2\,\hat{1})-E_1(\vec{x}-\hat{2}-2\,\hat{1})\\ +E_2(\vec{x})+E_2(\vec{x}-\hat{1})-E_2(\vec{x}-2\,\hat{2})-E_2(\vec{x}-\hat{1}-2\,\hat{2})=\\ \sum_{i=1,2;\,\vec{y}=0,\hat{1},\hat{2},\hat{1}+\hat{2}}\Big[E_i(\vec{x}-\vec{y})-E_i(\vec{x}-\vec{y}-\hat{i})\Big]=\\ \sum_{\vec{y}=0,\hat{1},\hat{2},\hat{1}+\hat{2}}Q(\vec{x}-\vec{y})=0\,.\end{aligned}\tag{C.2}$$

The blocking generates two artifacts. First the static external charges are not in the center of a block (note the positions of the staggered background charges in Figure C.1). The second artifact is a beat which is discussed and cured in what follows.

Now let's take a look at Figure 4.32. The exterior (red) around the static charges shows a columnar phase with horizontal parallel dimers. This corresponds to electric fluxes E_1 in the horizontal x_1 direction. The sign of these fluxes alternate depending on if the vertical position x_2 of the flux is even or odd. However, the direction of the local fluxes E_1 doesn't depend on x_1. The same situation (for smaller volume) is shown in the right panel of Figure 4.34.

If we would move between the charges from the top centers of the figures to the bottom centers, the local phase realizations change, going once through the sequence in eq. (4.29), compare also to Figure 4.21.

Advancing further down to the next plaquette phase (blue in Figure 4.32), the sign of the local fluxes E_1 now depend if x_1+x_2 is even or odd. In the next columnar phase (red) the sign of E_1 again only depends on x_2, but this time, the staggering is inverted to the one in the top centers in Figure 4.32).

The next columnar phase, located in the center between the static charges, is the same as in the exterior domain. Continuing to the bottom the situation repeats itself and we met each columnar phase two times, therefore the phase angle φ changed by 2π.

If we assume a large charge separation in direction x_1 (large compared to L_2), we can model the above behavior roughly with (compare to eq. (4.103) in section 4.9)

$$E_1(L_1/2,\,x_2)=\frac{1}{\pi}\frac{\partial\varphi(L_1/2,x_2)}{\partial x_2}+A\sin\left(2\,\varphi(L_1/2,x_2)\right)\cos\left(\pi x_2\right)\tag{C.3}$$

The first term is the flux we would like to measure. It would be constant according to our assumption (large separation of the charges). The second term accounts for the staggered flux pattern described above. The factor A is the amplitude of the disturbing alternating flux. In a pure columnar phase $|A|=1/2$. The term $\sin(\varphi)$ accounts for the phase change and therefore for the superposed "slower" sign change in the "fast" alternation. From $x_2=1$ to $x_2=L_2$, the phase angle φ changes by 2π and therefore the first term gets zero

four times. The term $\cos(\pi x_2)$ corresponds to the flux alternation caused by horizontal parallel dimers. With our assumption of a constant flux the phase pattern changes with

$$\varphi(x_2) \approx \frac{2\pi x_2}{L_2} + \varphi_0 \,. \tag{C.4}$$

The surrounding columnar phase we look at has $\varphi_0 = \pi/4$.

In one dimension we could simply filter the disturbing term away choosing a filter frequency which suppresses the "fast" $\cos(\pi x_2)$ term enough and doesn't affect slower variations. However, in our case we have to pay attention to preserve the Gauss law. This was the motivation to use the blocking scheme in a first step. But it is now this scheme defined in eq. (C.1) which picks out every second x_2-value out of eq. (C.3) only. If we choose the scheme with x_2 even, we obtain

$$\begin{aligned} \widetilde{E}_1\left(\frac{L_1-1}{2},\, 2k-\frac{1}{2}\right) &= E_1\left(\frac{L_1}{2},\, 2k\right) + E_1\left(\frac{L_1}{2},\, 2k-1\right) \\ &= \varphi'(2k) + \varphi'(2k-1) \\ &\quad + A\left(\sin\left(2\,\varphi(2k-1)\right) - \sin\left(2\,\varphi(2k)\right)\right) \,. \end{aligned} \tag{C.5}$$

The last term proportional to A appears as a large unwanted contribution. Around $\varphi(2k) = n\pi/2$ the difference of the two sin terms gets most pronounced. For $\varphi(2k) = 0$ the error in the blocked flux is about $4\pi|A|/L_2$ for large L_2. This is to be compared to the expected blocked flux which for large charge separation is $4/L_2$. So the relative error could become as large as $\pi|A| \approx 1.57$. The result is shown in Figure C.2. There is a clear asymmetry in each panel with respect to a reflection at a straight line in direction x_1 at $x_2 = L/2$. The statistics is rather high, so the algorithm has tunneled between all the external columnar phase realizations. So if there would have been a symmetry breaking which could manifest itself as an asymmetric pattern it would not be visible in the panels because of the frequent tunneling. Additionally, the blocked fluxes very heavily depend on the choice of the exact blocking coordinates which is unphysical.

Since each of the four blocking choices respect the Gauss law, the result of these blockings can be averaged

$$\widetilde{\widetilde{E}}_k(\vec{y}) = \frac{1}{4}\left(\widetilde{E}_k(\vec{y}) + \widetilde{E}_k(\vec{y}-\hat{1}) + \widetilde{E}_k(\vec{y}-\hat{2}) + \widetilde{E}_k(\vec{y}-\hat{1}-\hat{2})\right) \tag{C.6}$$

with $\vec{y} = \vec{x} - (1/2, 1/2)$. Again there are four choices for the $\vec{x}$ which again amounts to the choice of taking the even or the odd indices of a component. After the blocking and averaging, the center of such a cell falls on the original lattice sites. The result is shown in Figure C.3. Now the artifacts are almost gone. This can be understood for

$$(\widetilde{x}_1,\, \widetilde{x}_2) = \left(\frac{L_1-1}{2},\, 2k-\frac{1}{2}\right) \tag{C.7}$$

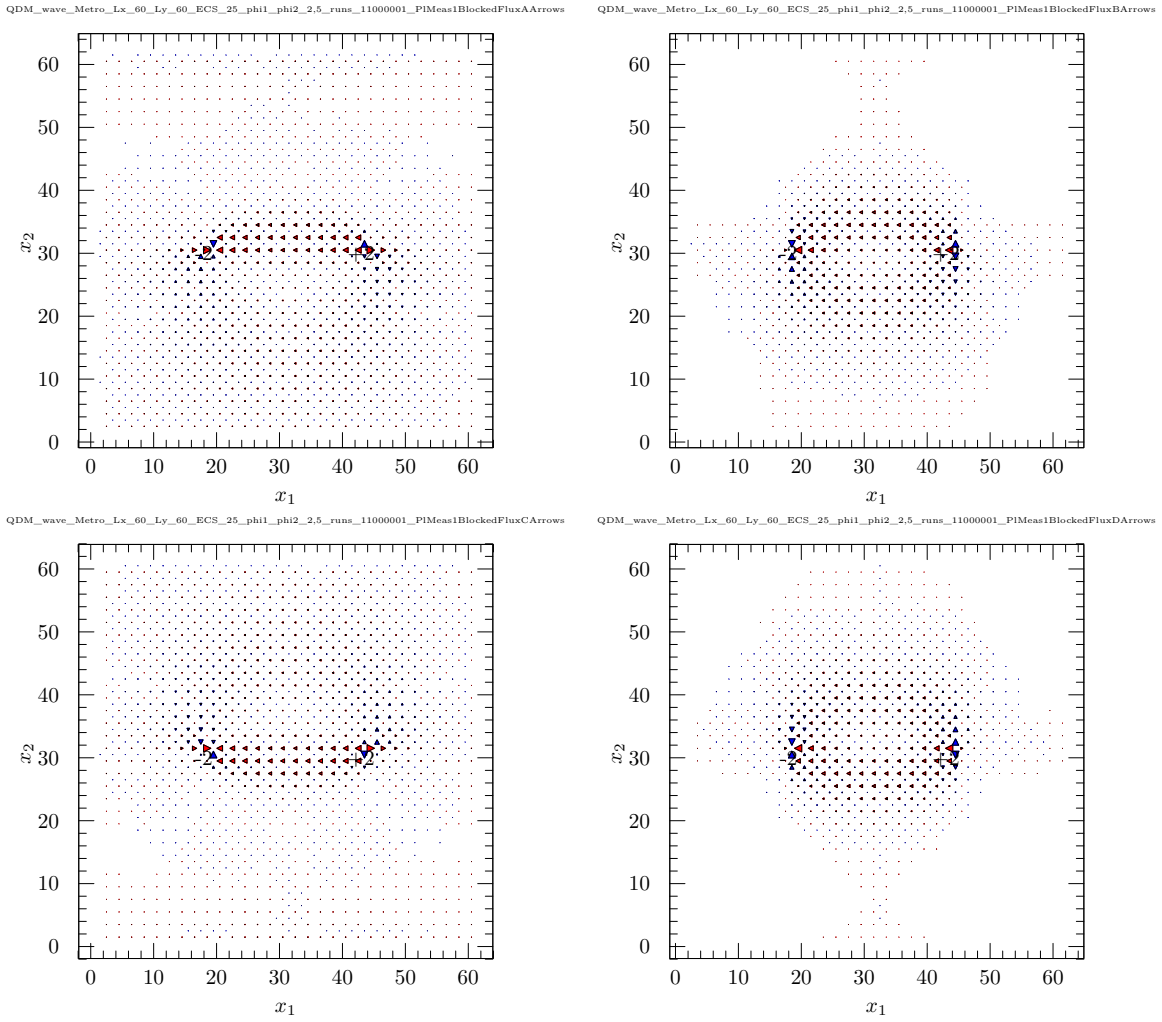

Figure C.2.: *This Figure shows the local pattern of blocked fluxes under the same conditions as in the right panel of Figure 4.34. Again, the wave function was evaluated for one external columnar phase. The blocked fluxes are clearly not symmetric under reflection on a straight line in direction x_1 at $x_2 = L/2$. The four panels correspond to the four different choices for the blocking scheme (Even or odd x_1 and even or odd x_2).*

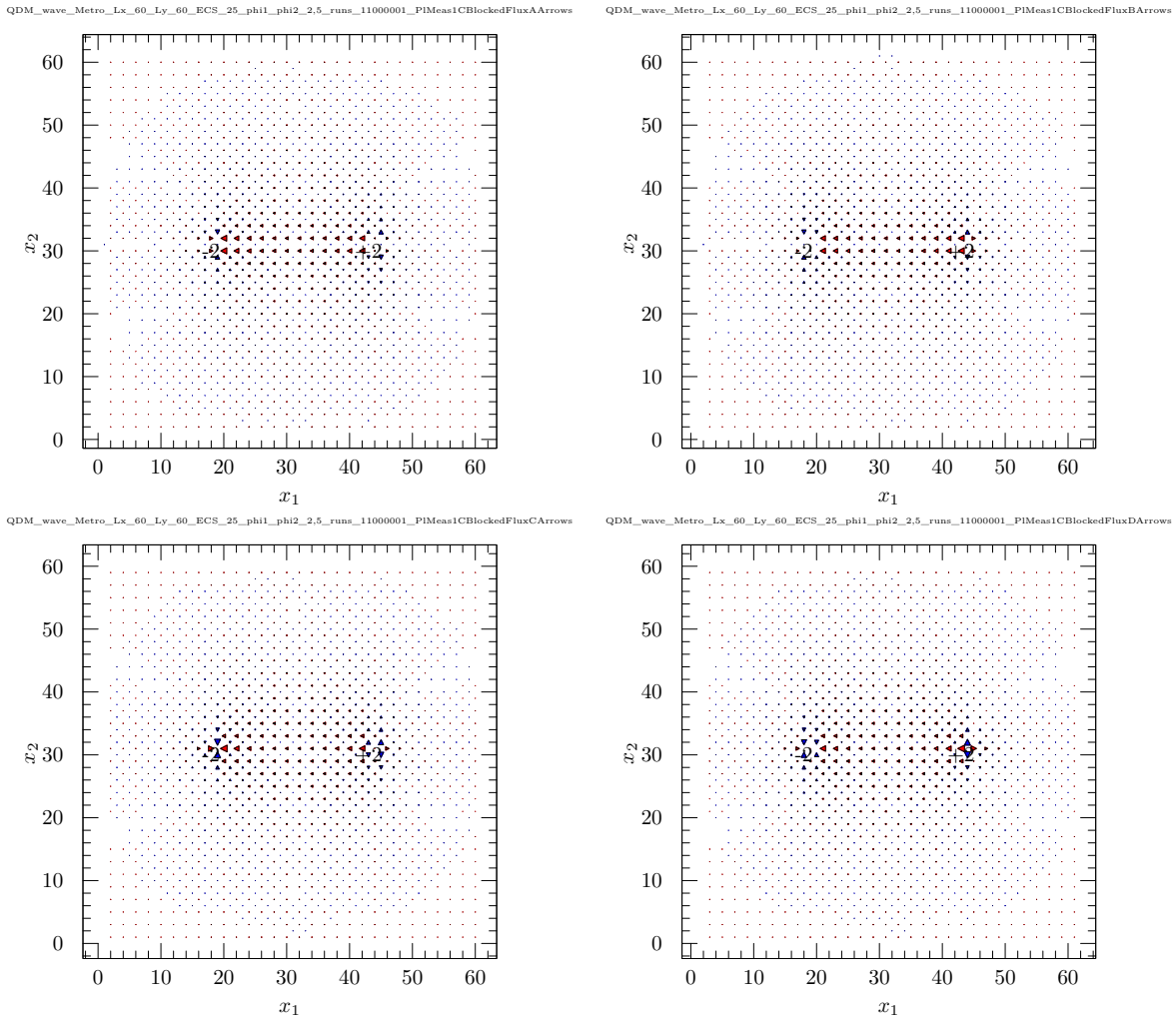

Figure C.3.: *Here the local pattern of blocked and additionally averaged fluxes is shown under the same conditions as in the right panel of Figure 4.34. The wave function was evaluated for one external columnar phase. The four panels again correspond to the four different choices for the blocking scheme. The result now depends much less on this choice.*

by looking at

$$\begin{aligned}
2\widetilde{\widetilde{E}}_2\left(\widetilde{x}_1,\,\widetilde{x}_2\right) &= \frac{1}{2}\left(\widetilde{E}_2\left(\widetilde{x}_1,\,\widetilde{x}_2\right)+\widetilde{E}_2\left(\widetilde{x}_1-1,\,\widetilde{x}_2\right)+\widetilde{E}_2\left(\widetilde{x}_1,\,\widetilde{x}_2-1\right)+\widetilde{E}_2\left(\widetilde{x}_1-1,\,\widetilde{x}_2-1\right)\right)\\
&\approx \widetilde{E}_2\left(\widetilde{x}_1,\,\widetilde{x}_2\right)+\widetilde{E}_2\left(\widetilde{x}_1,\,\widetilde{x}_2-1\right)\\
&= E_2\left(\frac{L_1}{2},\,2k\right)+2E_2\left(\frac{L_1}{2},\,2k-1\right)+E_2\left(\frac{L_1}{2},\,2k-2\right)\\
&= \varphi'(2k)+2\varphi'(2k-1)+\varphi'(2k-2)\\
&+ A\left(2\sin\left(2\,\varphi(2k-1)\right)-\sin\left(2\,\varphi(2k)\right)-\sin\left(2\,\varphi(2k-2)\right)\right)\,. \qquad \text{(C.8)}
\end{aligned}$$

For $\varphi(2k-1)=0$ and large L_2 and charges separated even more than L_2 the flux is almost constant over x_2 and eq. (C.4) is a good approximation. Then the last term with factor A becomes

$$\begin{aligned}
2\sin\left(2\,\varphi(2k-1)\right)-\sin\left(2\,\varphi(2k)\right)-\sin\left(2\,\varphi(2k-2)\right) &\approx -2\varphi(2k)-2\varphi(2k-2)\\
&\approx -\frac{4\pi}{L_2}+\frac{4\pi}{L_2}=0\,. \qquad \text{(C.9)}
\end{aligned}$$

Figure C.4 summarizes again what happened. The lines are linear interpolations between the measured values. The blue curve shows the original alternating flux pattern. One could try to naively subtract the influence of the ± 1 background charges by subtraction of the "classical" quarter fluxes generated by the background charges. The black curve shows that this fails dramatically. The magenta line shows the blocked fluxes. It is obviously not symmetric under reflections at $x_2 = 30$. However, the oscillations disappeared. The red curve finally shows the desired blocked and averaged flux.

In Figure C.5 the influence of the chosen blocking center is shown for the wave function at $\phi_1/\phi_2 = 2$ evaluated for different external columnar phases. The influence of the blocking center gets more pronounced compared to the full wave function (no restrictions to the external phase) shown in the mid right panel of Figure 4.37. For the wave function evaluated in distinct external columnar phases even the regions from $x_2 = 0$ to $x_2 = 20$ and from $x_2 = 40$ to $x_2 = 59$ become affected. Nevertheless this form of restricted wave function evaluation could be slightly unphysical since the system tunneled through all columnar phases during the simulation but the measures were cumulated separately depending on the external columnar phase (as described in section 4.11.2).

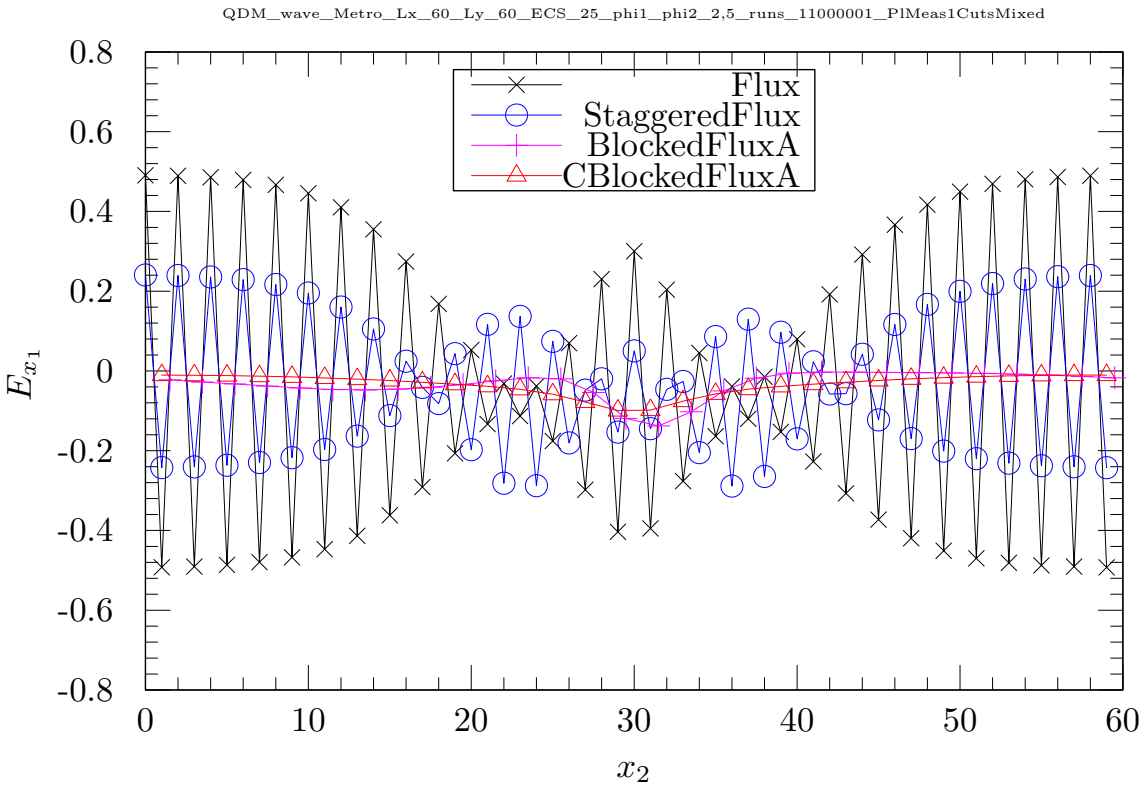

Figure C.4.: *Cut through the perpendicular bisection between the external charges ±2 under the same conditions as in Figures 4.34 (right panel), C.2 and C.3. The horizontal axis shows the x_2 position. The vertical axis shows the electric flux in the x_1 direction. The line segments are linear interpolations between the measured electric flux values. The blue curve is the original flux. The black curve is a naive attempt to subtract the background charges, as described in the text. The magenta curve shows the blocked flux with large remaining artifacts. The red curve shows the smooth blocked and averaged flux which is almost symmetric around $x_2 = 30$. Only one of the four possible blocking choices is shown for the last two curves. Again the wave function was evaluated for one external columnar phase.*

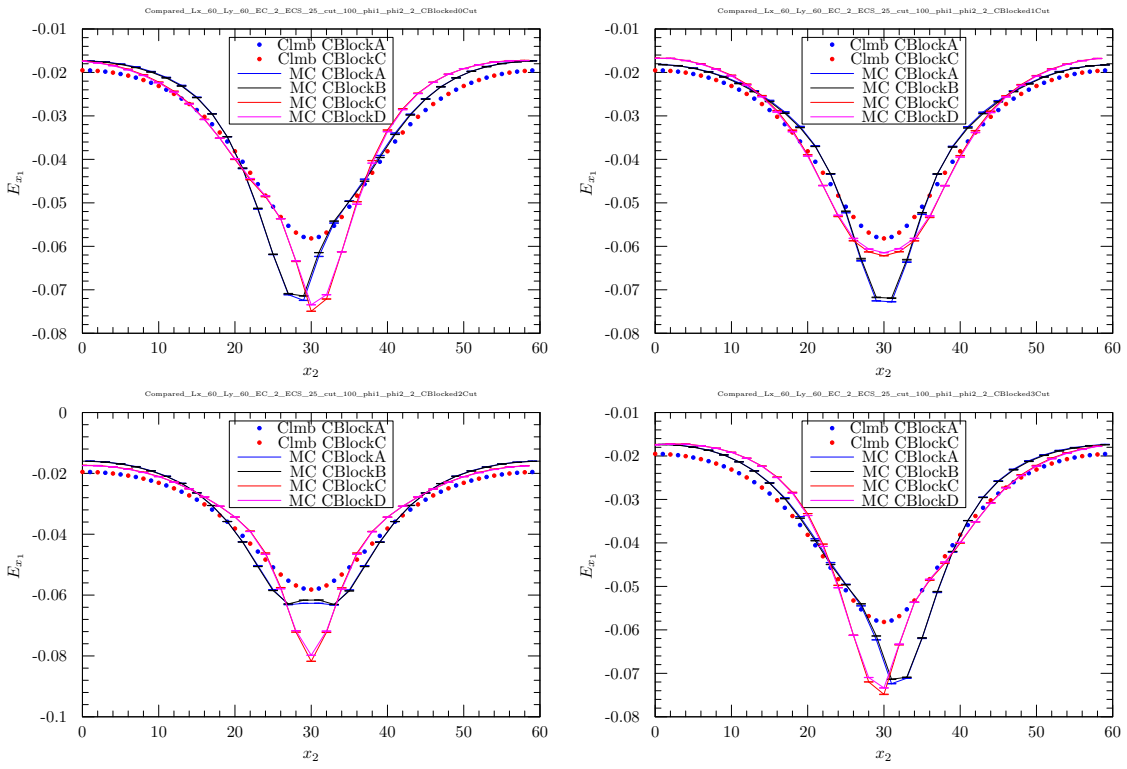

Figure C.5.: *Local blocked and averaged flux pattern at a cut through the perpendicular bisection between two static external charges for $\phi_1/\phi_2 = 2$. In each panel the wave function was evaluated for a different external columnar phase. Again the dots indicate the results of the effective theory as a guide to the eye.*

Bibliography

[1] R. P. Feynman, *Simulating physics with computers*, International Journal of Theoretical Physics **21** 6-7 (1982) pp. 467–488.

[2] S. Lloyd, *Universal Quantum Simulators*, Science **273** 5278 (1996) pp. 1073–1078.

[3] J. I. Cirac and P. Zoller, *Quantum Computations with Cold Trapped Ions*, Phys. Rev. Lett. **74** (1995) pp. 4091–4094.

[4] H. Haffner, W. Hansel, C. F. Roos, J. Benhelm, D. Chek-al kar, M. Chwalla, T. Korber, U. D. Rapol, M. Riebe, P. O. Schmidt, C. Becher, O. Guhne, W. Dur, and R. Blatt, *Scalable multiparticle entanglement of trapped ions*, Nature **438** 7068 (2005) pp. 643–646, 10.1038/nature04279.

[5] T. Monz, P. Schindler, J. T. Barreiro, M. Chwalla, D. Nigg, W. A. Coish, M. Harlander, W. Hänsel, M. Hennrich, and R. Blatt, *14-Qubit Entanglement: Creation and Coherence*, Phys. Rev. Lett. **106** (2011) p. 130506.

[6] D. Jaksch, C. Bruder, J. I. Cirac, C. W. Gardiner, and P. Zoller, *Cold Bosonic Atoms in Optical Lattices*, Phys. Rev. Lett. **81** (1998) pp. 3108–3111.

[7] M. Greiner, O. Mandel, T. Esslinger, T. W. Hänsch, and I. Bloch, *Quantum phase transition from a superfluid to a Mott insulator in a gas of ultracold atoms*, Nature **415** 6867 (2002) pp. 39–44, 10.1038/415039a.

[8] S. DÃijrr, Z. Fodor, J. Frison, C. Hoelbling, R. Hoffmann, S. D. Katz, S. Krieg, T. Kurth, L. Lellouch, T. Lippert, K. K. Szabo, and G. Vulvert, *Ab Initio Determination of Light Hadron Masses*, Science **322** 5905 (2008) pp. 1224–1227.

[9] K. G. Wilson, *Confinement of quarks*, Phys. Rev. D **10** (1974) pp. 2445–2459.

[10] D. Horn, *Finite matrix models with continuous local gauge invariance*, Physics Letters B **100** 2 (1981) pp. 149 – 151.

[11] P. Orland and D. Rohrlich, *Lattice gauge magnets: Local isospin from spin*, Nuclear Physics B **338** 3 (1990) pp. 647 – 672.

[12] S. Chandrasekharan and U.-J. Wiese, *Quantum link models: A discrete approach to gauge theories*, Nuclear Physics B **492** 1-2 (1997) pp. 455 – 471.

[13] R. Brower, S. Chandrasekharan, and U.-J. Wiese, *QCD as a quantum link model*, Phys. Rev. D **60** (1999) p. 094502.

[14] R. Brower, S. Chandrasekharan, S. Riederer, and U.-J. Wiese, *D-theory: field quantization by dimensional reduction of discrete variables*, Nuclear Physics B **693** 1-3 (2004) pp. 149 – 175.

[15] H. P. Büchler, M. Hermele, S. D. Huber, Matthew P. A. Fisher, and P. Zoller, *Atomic Quantum Simulator for Lattice Gauge Theories and Ring Exchange Models*, Phys. Rev. Lett. **95** (2005) p. 040402.

[16] S. Tewari, V. W. Scarola, T. Senthil, and S. D. Sarma, *Emergence of Artificial Photons in an Optical Lattice*, Phys. Rev. Lett. **97** (2006) p. 200401.

[17] L.-M. Duan, E. Demler, and M. D. Lukin, *Controlling Spin Exchange Interactions of Ultracold Atoms in Optical Lattices*, Phys. Rev. Lett. **91** (2003) p. 090402.

[18] H. Weimer, M. Muller, I. Lesanovsky, P. Zoller, and H. P. Buchler, *A Rydberg quantum simulator*, Nat Phys **6** 5 (2010) pp. 382–388, 10.1038/nphys1614.

[19] J. I. Cirac, P. Maraner, and J. K. Pachos, *Cold Atom Simulation of Interacting Relativistic Quantum Field Theories*, Phys. Rev. Lett. **105** (2010) p. 190403.

[20] E. Kapit and E. Mueller, *Optical-lattice Hamiltonians for relativistic quantum electrodynamics*, Phys. Rev. A **83** (2011) p. 033625.

[21] S. Nascimbène, N. Navon, K. J. Jiang, F. Chevy, and C. Salomon, *Exploring the thermodynamics of a universal Fermi gas*, Nature **463** 7284 (2010) pp. 1057–1060, 10.1038/nature08814.

[22] S. Trotzky, L. Pollet, F. Gerbier, U. Schnorrberger, I. Bloch, N. V. Prokof'ev, B. Svistunov, and M. Troyer, *Suppression of the critical temperature for superfluidity near the Mott transition*, Nat Phys **6** 12 (2010) pp. 998–1004, 10.1038/nphys1799.

[23] K. Van Houcke, F. Werner, E. Kozik, N. Prokof'ev, B. Svistunov, M. J. H. Ku, A. T. Sommer, L. W. Cheuk, A. Schirotzek, and M. W. Zwierlein, *Feynman diagrams versus Fermi-gas Feynman emulator*, Nat Phys **8** 5 (2012) pp. 366–370, 10.1038/nphys2273.

[24] X. Zhang, C.-L. Hung, S.-K. Tung, and C. Chin, *Observation of Quantum Criticality with Ultracold Atoms in Optical Lattices*, Science **335** 6072 (2012) pp. 1070–1072.

[25] S. Trotzky, Y-A. Chen, A. Flesch, I. P. McCulloch, U. Schollwock, J. Eisert, and I. Bloch, *Probing the relaxation towards equilibrium in an isolated strongly correlated one-dimensional Bose gas*, Nat Phys **8** 4 (2012) pp. 325–330, 10.1038/nphys2232.

[26] D. Banerjee, M. Dalmonte, M. Müller, E. Rico, P. Stebler, U.-J. Wiese, and P. Zoller, *Atomic Quantum Simulation of Dynamical Gauge Fields Coupled to Fermionic Matter: From String Breaking to Evolution after a Quench*, Phys. Rev. Lett. **109** (2012) p. 175302.

[27] D. Banerjee, M. Bögli, M. Dalmonte, E. Rico, P. Stebler, U.-J. Wiese, and P. Zoller, *Atomic Quantum Simulation of* $\mathrm{U}(N)$ *and* $\mathrm{SU}(N)$ *Non-Abelian Lattice Gauge Theories*, Phys. Rev. Lett. **110** (2013) p. 125303.

[28] D. Banerjee, P. Widmer, F.-J. Jiang, and U.-J. Wiese, *Crystalline Confinement*, in processdings of "31st International Symposium on Lattice Field Theory" p. PoS(LATTICE 2013)333.

[29] D. S. Rokhsar and S. A. Kivelson, *Superconductivity and the Quantum Hard-Core Dimer Gas*, Phys. Rev. Lett. **61** (1988) pp. 2376–2379.

[30] P. W. Anderson, *The Resonating Valence Bond State in La_2CuO_4 and Superconductivity*, Science **235** 4793 (1987) pp. 1196–1198.

[31] O. F. Syljuåsen, *Plaquette phase of the square-lattice quantum dimer model: Quantum Monte Carlo calculations*, Phys. Rev. B **73** (2006) p. 245105.

[32] A. Ralko, D. Poilblanc, and R. Moessner, *Generic Mixed Columnar-Plaquette Phases in Rokhsar-Kivelson Models*, Phys. Rev. Lett. **100** (2008) p. 037201.

[33] D. Banerjee, M. Bögli, C. P. Hofmann, F.-J. Jiang, P. Widmer, and U.-J. Wiese, *Interfaces, strings, and a soft mode in the square lattice quantum dimer model*, Phys. Rev. B **90** (2014) p. 245143.

[34] C. Castelnovo, C. Chamon, C. Mudry, and P. Pujol, *From quantum mechanics to classical statistical physics: Generalized Rokhsar-Kivelson Hamiltonians and the "Stochastic Matrix Form" decomposition*, Annals of Physics **318** 2 (2005) pp. 316 – 344.

[35] M. Troyer and U.-J. Wiese, *Computational Complexity and Fundamental Limitations to Fermionic Quantum Monte Carlo Simulations*, Phys. Rev. Lett. **94** (2005) p. 170201.

[36] J. Kogut and L. Susskind, *Hamiltonian formulation of Wilson's lattice gauge theories*, Phys. Rev. D **11** (1975) pp. 395–408.

[37] T. Banks, L. Susskind, and J. Kogut, *Strong-coupling calculations of lattice gauge theories: (1 + 1)-dimensional exercises*, Phys. Rev. D **13** (1976) pp. 1043–1053.

[38] R. B. Lehoucq and D. C. Sorensen, *Deflation Techniques for an Implicitly Restarted Arnoldi Iteration*, SIAM Journal on Matrix Analysis and Applications **17** (1996) pp. 789–821.

[39] W. E. Arnoldi, *The principle of minimized iterations in the solution of the matrix eigenvalue problem*, Quarterly of Applied Mathematics **9** (1951) pp. 17–29.

[40] C. Lanczos, *An iteration method for the solution of the eigenvalue problem of linear differential and integral operators*, J. Res. Nat'l Bur. Std. **45** (1950) pp. 225–282.

[41] M. Pepe and U.-J. Wiese, *From Decay to Complete Breaking: Pulling the Strings in $SU(2)$ Yang-Mills Theory*, Phys. Rev. Lett. **102** (2009) p. 191601.

[42] N. D. Mermin and H. Wagner, *Absence of Ferromagnetism or Antiferromagnetism in One- or Two-Dimensional Isotropic Heisenberg Models*, Phys. Rev. Lett. **17** (1966) pp. 1133–1136.

[43] M. A. Cazalilla, A. F. Ho, and M. Ueda, *Ultracold gases of ytterbium: ferromagnetism and Mott states in an $SU(6)$ Fermi system*, New Journal of Physics **11** 10 (2009) p. 103033.

[44] S. Taie, R. Yamazaki, S. Sugawa, and Y. Takahashi, *An SU(6) Mott insulator of an atomic Fermi gas realized by large-spin Pomeranchuk cooling*, Nat Phys **8** 11 (2012) pp. 825–830.

[45] A. V. Gorshkov, M. Hermele, V. Gurarie, C. Xu, P. S. Julienne, J. Ye, P. Zoller, E. Demler, M. D. Lukin, and A. M. Rey, *Two-orbital $SU(N)$ magnetism with ultracold alkaline-earth atoms*, Nat Phys **6** 4 (2010) pp. 289–295.

[46] G. Misguich, D. Serban, and V. Pasquier, *Quantum Dimer Model on the Kagome Lattice: Solvable Dimer-Liquid and Ising Gauge Theory*, Phys. Rev. Lett. **89** (2002) p. 137202.

[47] A. F. Albuquerque and F. Alet, *Critical correlations for short-range valence-bond wave functions on the square lattice*, Phys. Rev. B **82** (2010) p. 180408.

[48] C. A. Lamas, A. Ralko, M. Oshikawa, D. Poilblanc, and P. Pujol, *Hole statistics and superfluid phases in quantum dimer models*, Phys. Rev. B **87** (2013) p. 104512.

[49] E. Fradkin and S. Kivelson, *Short range resonating valence bond theories and superconductivity*, Modern Physics Letters B **04** 03 (1990) pp. 225–232.

[50] L. B. Ioffe and A. I. Larkin, *Superconductivity in the liquid-dimer valence-bond state*, Phys. Rev. B **40** (1989) pp. 6941–6947.

[51] C. L. Henley, *From classical to quantum dynamics at Rokhsar-Kivelson points*, Journal of Physics: Condensed Matter **16** 11 (2004) p. S891.

[52] S. Chandrasekharan and C. G. Strouthos, *Kosterlitz-Thouless universality in dimer models*, Phys. Rev. D **68** (2003) p. 091502.

[53] F. Alet, J. L. Jacobsen, G. Misguich, V. Pasquier, F. Mila, and M. Troyer, *Interacting Classical Dimers on the Square Lattice*, Phys. Rev. Lett. **94** (2005) p. 235702.

[54] F. Alet, Y. Ikhlef, J. L. Jacobsen, G. Misguich, and V. Pasquier, *Classical dimers with aligning interactions on the square lattice*, Phys. Rev. E **74** (2006) p. 041124.

[55] A. M. Läuchli, S. Capponi, and F. F. Assaad, *Dynamical dimer correlations at bipartite and non-bipartite Rokhsar-Kivelson points*, Journal of Statistical Mechanics: Theory and Experiment **2008** (2008) p. P01010.

Erklärung

gemäss Art. 28 Abs. 2 RSL 05

Name/Vorname: Stebler Pascal

Matrikelnummer: 99-278-848

Studiengang: Physik

Bachelor ☐ Master ☐ Dissertation ☑

Titel der Arbeit: Quantum Link and Quantum Dimer Models:
From Classical to Quantum Simulation

LeiterIn der Arbeit: Prof. Dr. U.-J. Wiese

Ich erkläre hiermit, dass ich diese Arbeit selbständig verfasst und keine anderen als die angegebenen Quellen benutzt habe. Alle Stellen, die wörtlich oder sinngemäss aus Quellen entnommen wurden, habe ich als solche gekennzeichnet. Mir ist bekannt, dass andernfalls der Senat gemäss Artikel 36 Absatz 1 Buchstabe r des Gesetzes vom 5. September 1996 über die Universität zum Entzug des auf Grund dieser Arbeit verliehenen Titels berechtigt ist. Ich gewähre hiermit Einsicht in diese Arbeit.

Bern,

Ort/Datum

Unterschrift

Pascal Stebler

Lebenslauf

Eichenweg 2
3177 Laupen
☎ 031 505 10 47
079 303 39 11
✉ pascal.stebler@gmx.ch

Persönliche Daten

Geboren am	1. November 1972
Staatsangehörigkeit	Schweiz
Zivilstand	Verheiratet / 1 Kind (Cindy 2010)

Profil

– Elektroingenieur HTL mit Titelumwandlung FH
– Industrieerfahrung als Projektleiter (Hardware- und Softwareentwicklung)
– Nachdiplomstudien in IT und Betriebswirtschaft
– Mehrjährige Erfahrung mit technischen Innovationsprojekten für die Industrie
– Mehrjährige Erfahrung in der Entwicklung von Algorithmen und Software
– Master in Physik

Aus- und Weiterbildungen

10/2011 – 02/2016 **Ph.D. in Physics**, *Universität Bern*.
– Dissertation "Quantum Link and Quantum Dimer Models: From Classical to Quantum Simulation" betreut durch Prof. Dr. U.-J. Wiese

10/2009 – 09/2011 **Master of Science in Physics**, *Universität Bern*.
– Masterarbeit "Constraint Effective Potential of the Magnetization in the Quantum XY Model" betreut durch Prof. Dr. U.-J. Wiese
wurde mit dem Fakultätspreis ausgezeichnet
– Vollzeitstudium in theoretischer Physik neben 40% Berufstätigkeit
– Zusätzliche Vorlesungen aus dem Master angewandte Physik und dem Master Informatik

10/2004 – 09/2009 **Bachelor of Science in Physics**, *Universität Bern*.
– Vollzeitstudium neben 50% Berufstätigkeit
– Minor Mathematik, zusätzliche Vorlesungen aus dem Bachelor Informatik

01/2001 – 12/2002 **Nachdiplomstudium Softwareschule Schweiz (SWS)**, *Berner Fachhochschule*, Bern.
– Berufsbegleitendes Nachdiplomstudium in Software Engineering

04/1999 – 03/2000 **Nachdiplomstudium Unternehmensführung**, *Berner Fachhochschule*, Burgdorf.
– Vollzeitstudium neben eigener Firma (GmbH, Entwicklung einer integrierten Schaltung (ASIC))

11/1992 – 10/1995 **Elektroingenieur HTL**, *Hochschule für Technik und Architektur Freiburg*.
– Vollzeitstudium, Fachrichtung Elektronik, Unterrichtssprache überwiegend Französisch

04/1989 – 03/1992 **Berufsmittelschule**, *Gewerblich Industrielle Berufsschule Bern (GIBB)*.

04/1988 – 03/1992 **Eidgenössisches Fähigkeitszeugnis**, *Ascom Hasler AG*, Bümpliz und Bern.
– Berufslehre als Elektroniker, Fachrichtung Informatik

Berufserfahrungen

10/2011 – 08/2015 **Assistenz und Dissertation**, *Universität Bern*.
- Modellieren von Quantensystemen, entwickeln von Quanten Monte Carlo Algorithmen
- Implementieren der Simulationen (in C++/Boost)
- Erzeugen der Simulationsdaten mit Linux-Clustern
- Statistische Analyse und Visualisierung der Daten (mit Octave, einem MATLAB Klon)
- Übungsbetreuung, Vorlesungsvertretung

10/2004 – 09/2011 **Wissenschaftlicher Mitarbeiter 40%**, *Berner Fachhochschule*, Burgdorf.
- Selbständige Bearbeitung von mittleren und grösseren Forschungs- und Entwicklungsprojekten
- Entwurf der Softwarearchitektur in mittleren bis grösseren Projekten
  - Sortieranlage mit Bildverarbeitung für die Fischzucht
  - GPS gestützter Grossflächendrucker (grosse Druckanlage auf Anhänger) mit fahrtabhängigen Druckalgorithmen
- Entwurf und Entwicklung von Schnittstellenelektronik
- Simulation und Entwurf neuartiger Mikromotoren und Aktoren inklusive Versuchsaufbauten
- Weitergabe von Projekt- und Entwicklungswissen an jüngere Mitarbeiter
- Mitbetreuen von Semester-, Diplom- und Bachelorarbeiten
- Ideenfindung in Innovationsprojekten
- Mithilfe bei Dienstleistungsaufträgen und bei der Durchführung von Expertisen
- Mithilfe bei der Ausarbeitung von Projektanträgen

04/2004 – 09/2004 **Ingenieur**, *AMMANN Langenthal AG*, Langenthal.
- Weiterentwicklung und Dokumentation des Maschinenleitsystems für Vibrationswalzen
- Versuchsdurchführungen im Strassenbau

05/2000 – 03/2004 **Projektassistent**, *Berner Fachhochschule*, Burgdorf.
- Entwicklung eines Maschinenleitsystems für Vibrationswalzen mit Echtzeit-Darstellung von GPS-gestützten Messdaten in Geländekarten, Verteilung der Daten an benachbarte Vibrationswalzen und webbasiertem Analysesystem (UML, C++/Qt, Java und SQL)
- Zugehörige Versuchsdurchführungen im Strassenbau
- Produktentwicklung der temperaturstabilisierten Sensorbox eines Gleismesswagen
- Zugehörige Versuchsdurchführungen auf stillgelegten Gleisen
- Beraten von Studenten im Rahmen von Semester- und Diplomarbeiten

10/1995 – 04/1999 **Projektleiter**, *Zbinden Posieux SA*, Posieux.
- Produktentwicklung der elektronischen Steuerungen eines Anhängerbremssystems
- Entwicklung der zugehörigen Echtzeit Steuersoftware (in Assembler)
- Versuchsdurchführung auf Prüfständen, auf Fahrzeugen und auf der Strasse
- Abwickeln der externen Prüfung auf elektromagnetische Verträglichkeit (EMV)
- Verhandeln mit Herstellern und Lieferanten
- Koordinieren der externen Serienproduktion
- Präsentation an internationalen Messen (Genf, Hannover)
- Zweisprachiges Arbeitsumfeld (Deutsch/Französisch)

08/1992 – 10/1992 **Elektroniker**, *Ascom Hasler AG*, Bern.
- Entwicklung einer objektorientierten Konfigurationssoftware (in Turbo Pascal)

Arbeitstreffen, Sommerschule, Seminar, Konferenz

2012 – 2014 **Regelmässige Arbeitstreffen**, *Gruppe von Prof. Dr. Peter Zoller, Universität Innsbruck*.

22. – 26.09.2014 **Sommerschule**, *ComplexQuantumSystems*, Wien.
– Aktualisiertes Poster zusammen mit U.-J. Wiese:
Ground state Rokhsar-Kivelson wave function for a Quantum Dimer Model

18. – 23.08.2014 **Seminar**, *Quantum Critical Matter – from Atoms to Bulk*, Obergurgl.
– Poster zusammen mit U.-J. Wiese:
Ground state Rokhsar-Kivelson wave function for a Quantum Dimer Model

3. – 14.06.2013 **Arbeitstreffen**, *Massachusetts Institute of Technology*, Cambridge.
– Besuch meines Doktorvaters in seinem Forschungssemester am MIT

22. – 25.09.2012 **Konferenz**, *Quantum Information meets Statistical Mechanics*, Innsbruck.
– Poster zusammen mit D. Banerjee und U.-J. Wiese:
Quantum Simulation of String Breaking and Evolution after a Quench in a $U(1)$ Gauge Theory

Publikationen

– D. Banerjee, M.Bögli, M. Dalmonte, E. Rico, PS, U.-J. Wiese, P. Zoller,
Atomic Quantum Simulation of U(N) and SU(N) Non-Abelian Lattice Gauge Theories,
Phys. Rev. Lett. 110, 125303 (2013), (`arXiv:1211.2242`)

– D. Banerjee, M. Dalmonte, M. Müller, E. Rico, PS, U.-J. Wiese, P. Zoller,
Atomic Quantum Simulation of Dynamical Gauge Fields coupled to Fermionic Matter:
From String Breaking to Evolution after a Quench,
Phys. Rev. Lett. 109, 175302 (2012), (`arXiv:1205.6366`)

– U. Gerber, C. P. Hofmann, F.-J. Jiang, G. Palma, PS, U.-J. Wiese,
Constraint Effective Potential of the Magnetization in the Quantum XY Model,
J.Stat.Mech.1106:P06002,2011, (`arXiv:1102.3317`)

IT Kompetenzen

Sprachen	C/C++ (Boost, Qt 5), Octave/MATLAB, Java (J2EE, JSP), XML, SQL, Assembler, Grundkenntnisse in Python und LabVIEW
Elektrotechnik	Altium Designer, ngspice, Mentor Graphics
Versionsverwaltung	Apache Subversion, Concurrent Versions System (CVS)
Entwurf	Unified Modeling Language (UML)
Entwicklungsumg.	KDevelop, Eclipse, Arduino, Microsoft Visual Studio
Betriebssysteme	Ubuntu Linux, Android, Microsoft Windows XP
Textsatz	LaTeX, LibreOffice Writer, Microsoft Word
Tabellenkalkulation	LibreOffice Calc, Microsoft Excel
Präsentation	LaTeX, Microsoft PowerPoint
Algebra	Grundkenntnisse in Mathematica, Maple und Maxima

Sprachkenntnisse

Deutsch: Muttersprache, Englisch: B2, Französisch: B1

Privat

Interessen	Familie, Technik und exakte Wissenschaften, Heimwerken, Eigenbau, Modellflug